Western University
Scholarship@Western

Electronic Thesis and Dissertation Repository

12-12-2012 12:00 AM

Novel Control and Harmonics Impact of PV Solar Farms

Byomakesh Das, *The University of Western Ontario*

Recommended Citation

NOVEL CONTROL AND HARMONICS IMPACT OF PV SOLAR FARMS

(Spine title: Novel Control and Harmonics Impact of PV Solar Farms)

(Thesis format: Monograph)

by

Byomakesh Das

Graduate Program

in

Engineering Science

A thesis submitted in partial fulfillment
of the requirements for the degree of
Master of Engineering Science

The School of Graduate and Postdoctoral Studies
Western University
London, Ontario, Canada

© Byomakesh Das 2012

Western University
School of Graduate and Postdoctoral Studies

CERTIFICATE OF EXAMINATION

<u>Supervisor</u>   <u>Examiners</u>

_____   _____
Dr. Rajiv K. Varma   Dr. Gerry Moschopoulos

<u>Supervisory Committee</u>
                                                               _____
                                                               Dr. Quazi Mehbubar Rahman

_____

                                                               _____
                                                               Dr. Samuel F. Asokanthan

_____

The thesis by

Byomakesh Das

entitled:

Novel Control and Harmonics Impact of PV Solar Farms

is accepted in partial fulfillment of the
requirements for the degree of
Master of Engineering Science

_____   _____
            Date   Chair of the Thesis Examination Board

ii

ABSTRACT

This thesis presents a novel application of Photovoltaic (PV) solar system inverter, both during night and day, as a dynamic reactive power compensator STATCOM. This technology, termed PV-STATCOM, is designed and developed for power factor correction in the networks of two utilities: Bluewater Power, Sarnia, and London Hydro. This thesis further describes for the first time, the harmonic impact studies on a utility distribution network in presence of the largest PV solar farm in Canada.

This novel utilization of a PV-STATCOM for power factor correction of induction motor loads is demonstrated with (i) electromagnetic transient simulation in PSCAD/EMTDC software, (ii) real-time simulation studies in a Real Time Digital Simulator (RTDS), and (iii) Hardware-in-the-Loop (HIL) simulation studies of the PV-STATCOM controller implemented in a Digital Signal Processor based dSPACE system. Two different inverter control methods are employed - Hysteresis control and Pulse Width Modulation (PWM) control. The effectiveness of the PV-STATCOM controller is verified with different PV power outputs and at different loading conditions of the induction motor. The PV-STATCOM is able to improve the motor power factor to unity both during night and in the day even while generating real power.

The harmonic impact studies of the 20 MW large scale PV solar farm and a 10 kW PV solar system are performed with the PSCAD/EMTDC model of two distribution feeders connecting to the solar farm in Bluewater Power, Sarnia. The models are validated with load flow results obtained from the CYME load flow software and Supervisory Control and Data Acquisition (SCADA) data available from the utility. The network resonance behaviors of the two feeders are analyzed using frequency scanning method in PSCAD/EMTDC. The measured harmonics data provided by Hydro One for three different power levels from the solar farm are utilized for harmonic impact studies. It is shown that even with worst case harmonics injection from both the large scale PV solar farm and a small PV solar system, the voltage harmonic distortion is within the limits specified by IEEE Standard 519.

Keywords

Photovoltaic Solar system, Distribution system, STATCOM, Hysteresis Control, PWM Control, Induction Motor, Power Factor Correction, Real-time Digital Simulation, Hardware-in-the-Loop Simulation, Load Flow, Network Resonance, Frequency Scanning, Total Harmonics Distortion (THD), Total Demand Distortion (TDD), Short Circuit Level

ACKNOWLEDGMENTS

TABLE OF CONTENTS

LIST OF TABLES

LIST OF FIGURES

xiv

LIST OF APPENDICES

LIST OF ABBREVIATIONS

PV	Photovoltaic
STATCOM	Static Synchronous Compensator
FACTS	Flexible AC Transmission System
VSI	Voltage Source Inverter
CSI	Current Source Inverter
PWM	Pulse Width Modulation
RTDS	Real Time Digital Simulator
HIL	Hardware-in-the-Loop
CHIL	Controller Hardware-in-the-Loop
GTDI	Giga Transceiver Digital Input
DDAC	Digital to Digital Analog Converter
PCC	Point of Common Coupling
SCL	Short Circuit Level
THD	Total Harmonic Distortion
TDD	Total Demand Distortion
SCADA	Supervisory Control and Data Acquisition
GIS	Geographical Information System

<h1>Chapter 1</h1>

INTRODUCTION

1.1 GENERAL

Photovoltaic energy has attracted significant attention around the world due to its technical, economical, and environmental benefits, with annual growth rate of 25-35% over the last 10 years and a substantial growth of 54% alone in the year 2011 [1]-[2]. With 67.4 GW of Photovoltaic (PV) installations by the end of 2011, photovoltaic solar energy is going mainstream [1]. Although PV is expensive, according to the European Photovoltaic Industry Association, PV solar module prices have dropped significantly by 40% over the last two years, and a further drop of 50% is expected in the next three years, according to the market survey [1]-[5]. The advancements in power electronics have placed the PV system as a competitive alternative to other renewable energy sources. Different PV incentive programs have been introduced in various countries to encourage the residential and commercial use of PV systems. As of July 2012, the largest grid connected solar farm is the Agua Caliente Solar Project in Arizona, USA with a nominal power output of 247 MW [4], [5], [8]. Similarly, other mega solar projects are the Charanka Solar Park in India, with a nominal power output of 214 MW, and the Golmud Solar Park in China, with a nominal power output of 200 MW [6], [8]. The Sarnia Photovoltaic Solar Farm in Ontario, Canada has a nominal capacity of 80 MW, with installed capacity of 97 MW. Sault Ste Marie Solar Park in Ontario, Canada is the second largest photovoltaic solar farm, with an installed capacity of 68 MW. Canada is expected to achieve a solar PV installation from 9000 MW to 15000 MW by 2025 [7], [8].

1.2 MODELING OF GRID CONNECTED PV SOLAR SYSTEM

A grid connected PV solar system consists of a PV solar array, a Voltage Source Inverter (VSI), a filter which is typically a part of the VSI, and a coupling transformer to interconnect to high voltage system. Figure 1.1 depicts a grid connected PV solar system.
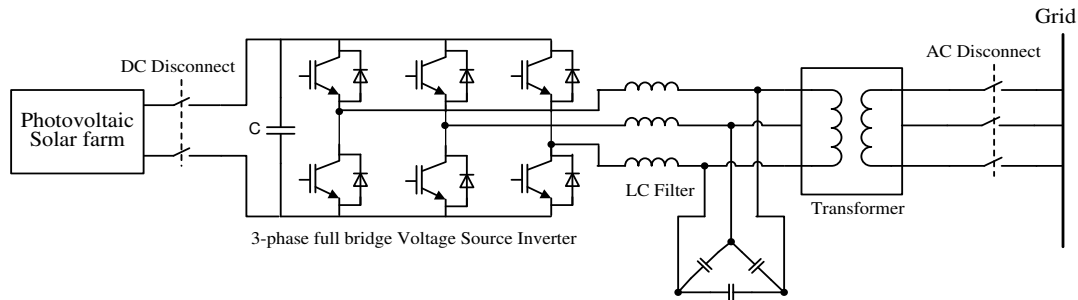
Figure 1.1 Grid connected Photovoltaic Solar System

PV arrays consist of series/parallel connections of a number of PV modules, where a module comprises a series connection of a number of PV cells. The PV Solar arrays are connected in parallel to the dc-link capacitor, C, and the DC side terminals of the VSI. The main function of the dc-link capacitor is to maintain a constant DC bus voltage. The VSI is the core of the grid connected PV system that transforms DC power from the PV arrays into AC power via a set of solid-state switches such as IGBTs [9]. Each leg of the VSI has two semiconductor switches that produce one phase of the AC-side voltage. The switches in each leg are turned ON/OFF in a complementary manner to convert DC power from the PV array to AC power to the grid. The switching action of these semiconductor valves is governed by the control system implemented in a microcontroller on the VSI inverter [9]. The LC filter keeps harmonic currents at low levels and ensures a low voltage distortion at the PCC. Typically, an interconnected transformer is used in a grid connected PV system in order to step up VSI terminal AC voltage to that of the grid PCC voltage. The type of transformer configuration depends upon the interconnection standards utilized by the utilities [9]-[11]. A DC disconnect switch is required ahead of the inverter to isolate the PV array from the network. Similarly, AC disconnect switches are used to disconnect the entire PV solar system from the grid [11].

1.2.1   Modeling of PV panel

In order to simulate the behavior of a solar panel, different models are developed in various softwares [12]-[15]. Among the different models, the single-diode circuit is the most commonly used model in power system simulation studies since it offers a reasonably good trade-off between simplicity and accuracy, and can be efficiently included in many power system simulation platforms. Figure 1.2 shows the single-diode equivalent model of a PV

cell. The circuit is composed of a diode in parallel with the current source, the series resistance and a parallel resistance. I_g, R_s, and R_p represent the current source and series resistances of the PV cell, and the leakage resistance of the PV cell [16].
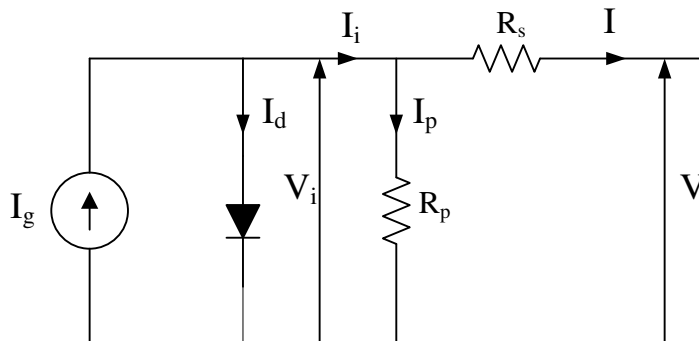
Figure 1.2 Single-diode equivalent circuit of a PV module

The basic equation describing the nonlinear current-voltage relationship of the PV cell is

$$I = I_g - I_o \left(e^{\frac{\beta(V + R_s I)}{\alpha}} - 1\right) - \left(\frac{V + R_s I}{R_p}\right) \qquad (1.1)$$

Where, I and V are the terminal current and voltage of the PV cell. I_o, β, and α, represent the diode reverse saturation current, inverse thermal voltage, and diode ideality factor respectively [16]-[17].

1.2.2 Modeling of PV Inverter

Photovoltaic inverters use self-commutated inverters due to advances in IGBTs and MOSFETs. Self-commutated inverters can be of two types: voltage source inverters (VSI), and current source inverters (CSI). A VSI uses a capacitor on the DC side to maintain a constant voltage at the DC link. A terminal voltage of the constant amplitude and variable width is obtained at the AC side. Similarly, a CSI uses an inductor on the DC side to maintain a constant current [18]-[19]. A current waveform of the constant amplitude and variable width is obtained at the AC side. These two different topologies have their own advantages, yet, the present practice of a PV inverter is to use the VSI topology due to its better efficiency, better dynamic response, and due to low output current harmonics as compared to CSI [19]-[22].

Two-level and three-level three-phase VSI are the most commonly used topologies in power systems [23]. A two level VSI system is a preferred configuration for medium and low power grid connected PV applications because of cost effectiveness and the option for utilizing high switching frequencies according to different PV inverter manufacturers [24]-[25]. Theoretically, the DC input bus voltage (V_{dc}) of a two-level VSI inverter needs to follow the relationship $V_{dc} \geq 1.633\ V_{L-L}$ [23], while some of the manufactures specify $V_{dc} \geq 1.414\ V_{L-L}$ [20]. The operable range of the DC voltage differs according to the rated power of the inverter, and rated voltage of the AC utility grid system, etc. According to a survey conducted by International Energy Agency (IEA) on PV systems and different PV inverters, the operational DC voltage range for a capacity of 1kW to 10 kW PV system includes 40-95V, 72-145V, 75-225V, 100-350V, 125-375V, 139-400V, 150-500V, 250-600V, and 350-750V and for a capacity of 10 kW and over DC voltage can be between 200-500V, and 450-1000V [18].

For power system studies, a VSI system can be modeled by ignoring the switching transients phenomena, such as tailing current or reverse recovery current. This type of model is called a "switched" model. For faster simulations of a complex network, an average model is preferred for a VSI system in which no valves or switches are modeled; only the terminal current and voltage variables on both DC and AC side are used for this analysis [19]. For this thesis, the switched model is considered.

A VSI can be operated in either voltage control mode or current control mode. In voltage control mode, the output AC terminal voltage is controlled to become equal to a set reference value [19]. In current control mode, inverter output currents are measured and compared to the reference signals and control is performed so that actual output current agrees with the reference value. The voltage control scheme is suitable for standalone PV applications, whereas, the current control scheme is generally preferred in grid connected photovoltaic inverter applications due to its excellent dynamic characteristics, less susceptibility to grid voltage distortion, and inherent over-current limitation capabilities. Over-current limitation capability is particularly suitable during the fault scenarios, where a current controlled VSI type PV system can limit the fault current close to its rated value. Nearly 81% of grid connected PV inverters use current control schemes as per the survey made by IEA [18]-[19]. Hence, in this thesis, the current control scheme is employed.

1.2.3   Control Schemes for PV Inverter

The control scheme of the photovoltaic inverter is typically a combination of two control loops: the outer control loop and the inner control loop. The outer control loop can be of different types depending upon the operational objectives from the PV system [18], [19], [25]-[27]. These can be real or reactive power control loops, AC voltage control loop, etc. The outer control loop generates the reference currents to be tracked by the inner control loop. The inner control loop is essentially a current control loop which generates signals for the switching pulse generation module to generate firing pulses for the inverter switches.

1.2.4   Switching Pulse Generation Methods for PV Inverter

There are different switching methodologies adopted for firing pulse generation in photovoltaic inverters. The current control techniques which have performed effectively in different VSI inverter applications are the hysteresis current control and Pulse Width Modulated control techniques [28]-[29]. Hence, both Pulse Width Modulated (PWM) control and Hysteresis current control strategies are utilized in this thesis, and is discussed as follows.

1.2.4.1   *Hysteresis Current Control Technique*

The hysteresis current control method regulates the output current of a PV inverter by forcing it to follow a reference current signal. This is achieved by using a hysteresis band around the reference signal. The inverter output currents are sensed and compared with the respective reference currents using hysteresis comparators having a hysteresis band. Hysteresis comparators are used to impose a dead band around the reference current. As long as an error is within the hysteresis band, no switching action takes place [28]. Switching action takes place when an error hits the hysteresis band. Normally compensated current or voltage is compared to the reference current to produce an error signal to the hysteresis band comparator to determine gating signals for inverters. To obtain a compensating current with minimum switching ripples as small as possible, the hysteresis band has to be made small. However, doing so results in a higher switching frequency and hence increases system losses [28]-[31].

There are two types of hysteresis current controllers: fixed-band and sinusoidal band current controllers, shown in Figure 1.3.

(a) Sinusoidal Band   (a) Fixed Band
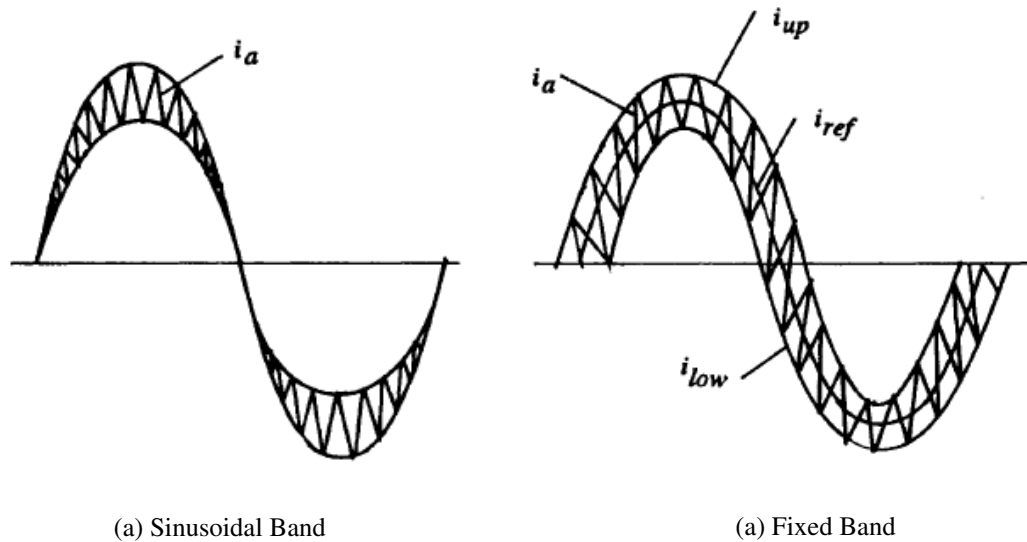
Figure 1.3 Hysteresis current controller (a) Sinusoidal band (b) Fixed band [28]

In fixed-band hysteresis control, the hysteresis band is fixed over the fundamental period, and in the case of a sinusoidal-band scheme, the hysteresis band varies sinusoidally over a period. The advantage of the hysteresis control method lies in the simplicity of its implementation and its excellent dynamic response. The main disadvantage of this scheme is that it generates low order harmonics and does not operate at a fixed switching frequency [29]-[30].

1.2.4.2   *PWM Control Technique*

PWM modulation is a voltage modulation technique. The most common methods for PWM modulation are carrier based PWM, space vector modulation (SVM), and random PWM. The fundamental differences between these methods are described in [23], [28], [31]. Among the above-mentioned PWM methods, the sinusoidal PWM method is the basic and most common technique to modulate the switching signals [23], [28].

Sinusoidal PWM voltage modulation of the power converter is done by comparing the modulating signal (sinusoidal signals) with the carrier signal. The sinusoidal signals representing the phase voltages are compared to a carrier signal of fixed frequency in order to generate switching signals for the power converter switches, so that current errors are reduced and PV inverter output current follows the reference current. The principle of the generation

of switch signals is shown in Figure 1.4, where triangular carrier signals are compared to sinusoidal signals. If the sinusoidal signal is larger than the carrier wave, the inverter switch is turned on, and if it is less, the switch is turned off [31].
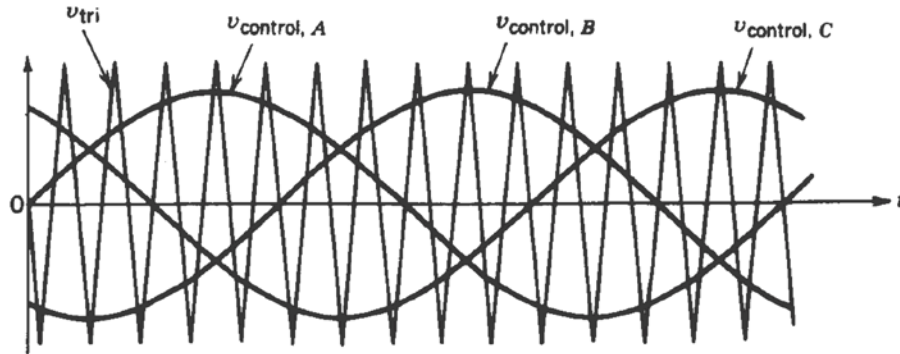
Figure 1.4 Generation of switching signal in PWM control method [23]

The main advantage of this control technique is the absence of low order harmonics at the output. As it operates at fixed switching frequency, voltage harmonics are generated around the switching frequency and multiples of switching frequency, which is much higher than the fundamental frequency. The main disadvantage of this scheme is the switching loss due to operation at higher switching frequency [23], [31].

1.3   STATCOM

A Static Synchronous Compensator (STATCOM) – a class of Voltage Source Converter based FACTS device is a controlled reactive power source consisting of a VSI that is connected to the network via a shunt transformer [32]-[33]. It is a shunt connected device used for voltage control, power factor correction, load balancing and harmonics compensation by providing reactive power using its underlying inverter technologies. The exchange of reactive power between the converter and the AC system can be controlled by varying the amplitude of the three-phase output voltage, E_s of the converter, as shown in Figure 1.5. If the amplitude of the output voltage is increased above that of the utility bus voltage, E_t, then the current flows from the converter to the AC system and the converter generates capacitive-reactive power for the AC system. Similarly, if the amplitude of the output voltage is decreased below the utility bus voltage, then the current flows from the AC system to the converter and the converter absorbs inductive-reactive power from the AC system [32]-[33].
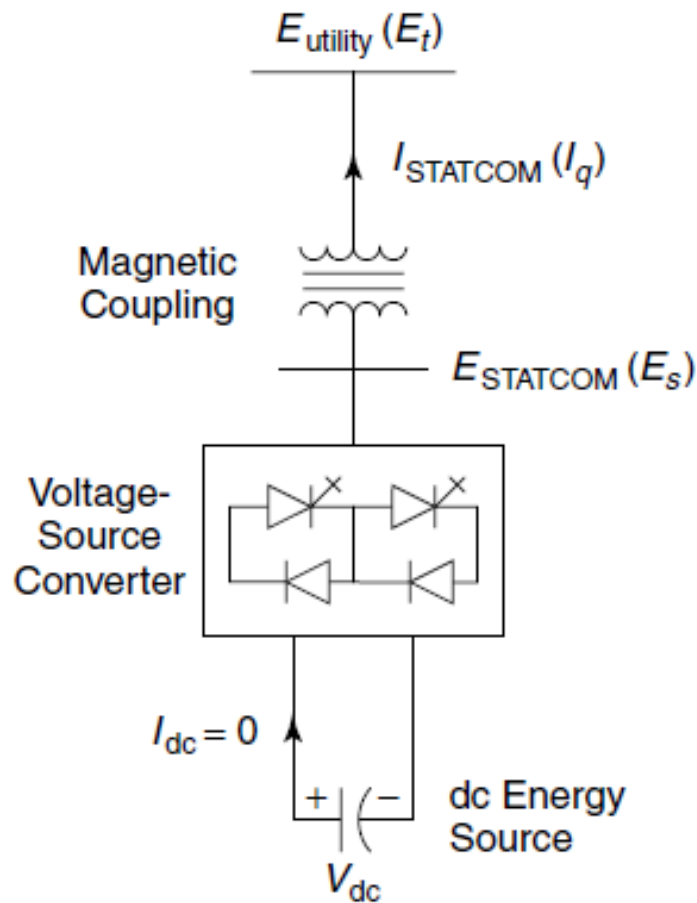
Figure 1.5 Basic Structure of a STATCOM [32]

If the output voltage equals the AC system voltage, the reactive-power exchange becomes zero, in which case the STATCOM is said to be in a floating state. STATCOM can supply real power to the AC system from its DC energy storage by adjusting the phase shift between the converter-output voltage and the AC system voltage. In this case, converter output voltage is made to lead AC system voltage. On the other hand, it can absorb real power from the AC system if its voltage lags behind the AC system voltage [32].

As shown in Figure 1.6, a STATCOM can supply both the capacitive and inductive reactive current over the rated maximum capacitive or inductive range irrespective of the system voltage. A STATCOM can provide full capacitive reactive power at a voltage of 0.15 pu. This characteristic of a STATCOM is particularly useful in situations where the STATCOM is required to support the grid voltage during and after the fault.
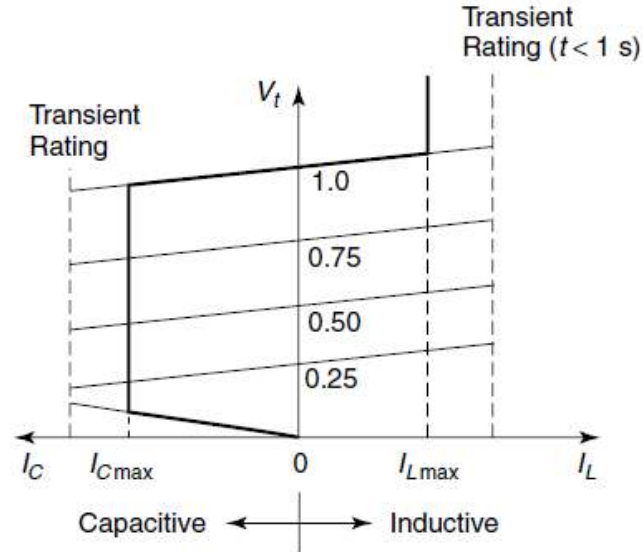
Figure 1.6 V-I characteristics of a STATCOM [32]

A STATCOM is used for providing voltage control, enabling grid integration of renewable energy [34]-[35], dynamic reactive power support, mitigating voltage flicker [36]-[38], power oscillation damping, mitigating sub-synchronous resonance [39]-[40], load balancing, and power factor correction [41]-[43].

1.4   NOVEL CONTROL OF PV SYSTEM AS PV-STATCOM

A STATCOM, as described in previous section, is based on a Voltage Source Converter (VSC), whereas a PV solar system is also built around a Voltage Source Inverter (VSI). A STATCOM is a controlled reactive power source that exchanges reactive power with a power system network, whereas a PV solar system is only an active power source. A new technology has been proposed for utilizing a PV solar system inverter as a STATCOM, the concept of which is described below [44].

Figure 1.7 depicts the variation in power output from a 10 kW PV system on a typical sunny day during the summer time. Conventionally, these PV inverters are designed to send active power based on the available DC power. However, over 80% of the time, PV inverters run below their rated output current, depicted in Figure 1.7. It is seen that the PV system starts producing real power P_{pv} around 6:30 AM, reaching its peak production around noon, and finally ceasing to generate by 8:00 PM. Thus, the entire 10 kVA inverter capacity is unused

during late evening and night hours, from 8:00 PM to 6:30 AM. In addition, the inverter capacity is only partially used during early morning and late evening hours.
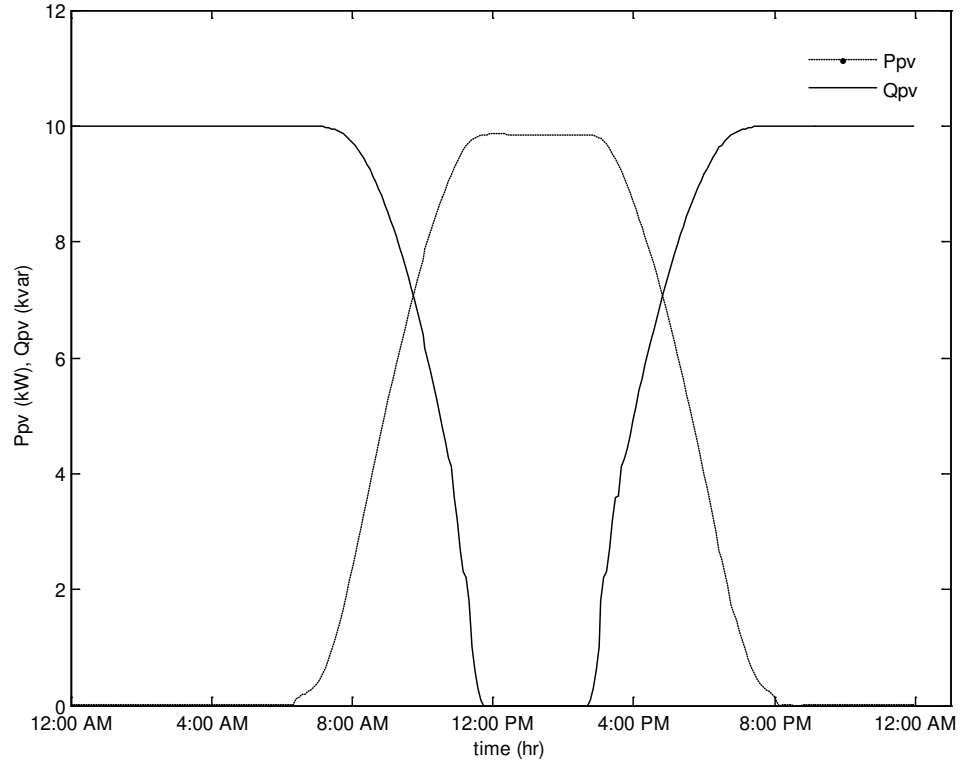
Figure 1.7 Power output of a 10 kW PV solar system on a sunny day during summer season

During the night, a PV system inverter can utilize inverter capacity S_{PV} to provide 10 kvar of support to the grid. Similarly, it can be seen that during the day, except around noon, a substantial amount of Q_{PV} from the PV solar system inverter is still available, $Q_{PV} = \sqrt{\left(S_{PV}^2 - P_{PV}^2\right)}$, which can be utilized for reactive power support to the grid. P_{PV} represents the real power from a PV system.

Thus, the unused capacity of the PV inverter can be put to use to generate reactive power by operating as a STATCOM to provide necessary reactive power support to the grid, depending on the availability of reactive power after real power generation. This allows full utilization of the expensive asset of the PV solar farm during an entire 24-hour period [44]-[49]. There is, therefore, an incentive to explore the utilization of a PV solar farm inverter as a STATCOM, for different objectives such as voltage control, and power factor correction, etc.

1.5   SIMULATION STUDIES

Modern power systems are currently undergoing a transformative change with market deregulation and with the addition of power electronics based renewable energy systems. These developments demand a more efficient use of power electronic technologies and a better control of power flow. Hence, a comprehensive analysis of these technologies is essential to understand their operating characteristics and their impact on the power systems. The design and development of these high power electronic systems needs considerable investment and time. The control system is an essential part of a power electronics system that needs to be evaluated thoroughly prior to installation in the network. To efficiently implement high power electronic control devices in power systems, a formal procedure is required to help transfer the design from the simulation model to the final hardware implementation. Usually this procedure includes: Electromagnetic Transients Software simulation, Real-time simulation, Hardware-in-the-Loop (HIL) simulation, and finally, the commissioning of these devices [50]-[53]. These different simulation techniques are described below.

1.5.1   Electromagnetic Transients Software Simulation Studies

Electromagnetic transient software simulation studies are the initial phase of designing a prototype hardware model. This is an efficient way for the designer to learn how a power electronic system and its controller work during the fault, or during any abnormal conditions, along with steady-state operation in a simulated power system environment. There are different commercially available software simulation tools used for the simulation of power electronic converters, such as MATLAB/SIMULINK [54], PSPICE [55] and PSCAD/EMTDC [56], etc. PSPICE is generally employed in the simulation of power electronics at low power levels, and MATLAB/SIMULNIK and PSCAD/EMTDC are used for low power and high power electronic applications [53]-[55].

1.5.2   Real-Time Digital Simulation Studies

Power system simulation softwares provide a wide range of power system block sets/models for different types of studies, but the main disadvantages of these power system tools are that they operate in non-real time. It means that the processing time required to compute the response of a network modeled in these software tools take more time to simulate than the

time taken by the phenomena in real time [57]-[58]. For example, a five-cycle fault may take several seconds or minutes depending upon the size of the system. Recent advances in digital signal processing, computing hardware, and sophisticated power system modeling techniques have significantly increased the application of real-time digital simulation in the power system industry [58]-[59].

The popular real-time digital simulation platforms available for the simulation of power system are RTDS and OPAL-RT [60]-[61]. The Real Time Digital Simulator (RTDS) from RTDS Technologies is a combination of specialized computer hardware and software designed specifically for the solution of power system electromagnetic transients. The power electronic converters with higher PWM carrier frequency in the range of 5-10 kHz require smaller time steps of less than 10 μs in order to validate the performance of the system. RTDS, with its small time step simulation feature, has the capability to simulate a FACTS based power electronics controller in less than 2 μs [60]. Besides this, RTDS provides facilities for Hardware-in-the-Loop simulations. RTDS is widely used by different power industry manufacturers and also in research centers for the testing and validation of different controllers used in power systems [62]-[65].

1.5.3 Hardware-in-the Loop Simulation Studies

A Hardware-in-the-Loop (HIL) simulation is an efficient method of comprehensive testing and verification of the performance of an actual hardware system. An HIL simulation is accomplished by isolating the control system from the real-time simulation environment using a real-time digital simulator (RTDS, eMEGASim, etc.), and replacing the simulated input/output signal for the control system with actual input/output signal. The RTDS simulation includes mathematical models, sensors, actuators, and various analog/digital channels to interact with the real hardware. It presents an actual environment to the control system running with real hardware, and exchanges signals in a realistic manner. The control system running on real hardware cannot differentiate between the real world and the simulated real-time environment in the HIL simulator [60]-[61]. Thus, the HIL simulator provides an array of testing features on the controller without any risk to the power system network or the test hardware. The HIL simulation is adopted in various industries and research centers for

testing control systems and protective relays [66]-[73]. The basic concepts of HIL simulation are demonstrated in Figure 1.8.
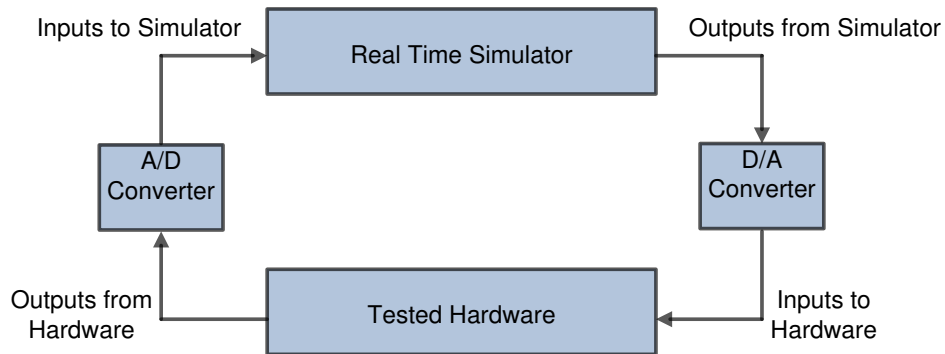
Figure 1.8 Basic concept of HIL Simulation

A motivation is therefore provided to design, develop, and test a PV-STATCOM controller through an electromagnetic transient simulation using PSCAD/EMTDC; and to subsequently validate its performance through real-time digital simulation and Hardware-In-the Loop simulation.

1.6 HARMONIC AND NETWORK RESONANCE IN THE PRESENCE OF PHOTOVOLTAIC SOLAR FARM

Power system harmonics are defined as currents or voltages with frequencies that are integral multiples of fundamental power frequency. Harmonics are classified as characteristics and non-characteristics [74]. Power electronic converters are the main source of characteristic harmonics (5th, 7th, 11th, and 13th) in the system. Even harmonics and non-characteristics harmonics (3rd, 9th, and 15th) are primarily caused by unbalanced supply voltage magnitude or phase asymmetry, even though some power electronic converters used in arc furnaces and railway traction systems which inject both even and non-characteristics harmonics [75]. Harmonics in a distribution network are due to the presence of different non-linear loads, demonstrated in [76]-[81]. A photovoltaic system is a prominent source of current harmonics. Some of the studies on commercial solar farms reveal that although the total current harmonic distortion from the PV solar farms is relatively high, the voltage harmonic distortion can be below the specified in standards such as IEEE 519 [82]-[84]. However, there is a technical concern of the amplification of harmonics from a PV solar farm due to resonances in the

network caused by bus capacitors in the network and other capacitive elements such as cables [84]-[88].

Network resonance can be classified into two types: series resonance, and parallel resonance. In the case of series resonance the impedance becomes low at resonant frequency, which causes the flow of large current in the network. At times this can also cause a high distortion in the voltage at the distant buses. However, parallel resonance is associated with high impedance at resonant frequencies that causes large distortion in the voltage and produces a large harmonics current [85]-[86]. A PV system is a source of harmonics current. If for any network condition(s), the network resonance frequency becomes aligned with the harmonics injected by the PV system, excessive voltage and current harmonics distortions may occur, and can cause damage to the customer and utility equipments. Network resonance frequency varies with the short circuit ratio (SCR) of the system. For a network, if the SCR increases, the resonance frequency shifts towards higher order frequencies and as SCR decreases, resonant frequency shifts toward lower order frequencies [88].

IEEE Standard 519-1992 specifies harmonic indices in order to quantify the limits for voltage and current harmonics in a network. These harmonic indices are Total Harmonic Distortion (THD), Total Demand Distortion (TDD) [84].

Total Harmonic Distortion of a voltage waveform (V_{THD}) is the square root of the ratio of sum of the squares of harmonic content of voltage waveform to the root mean square value of the fundamental voltage. Similarly, Total Harmonic Distortion of a current waveform (I_{THD}) is the square root of the ratio of sum of the squares of harmonic content of current waveform to the root mean square value of the fundamental current [84].

$$V_{THD} = \sqrt{\frac{\sum_{i=2}^{n} V_i^2}{V_1}} \qquad (1.1)$$

$$I_{THD} = \sqrt{\frac{\sum_{i=2}^{n} I_i^2}{I_1}} \qquad (1.2)$$

where, V_i and I_i represent the individual voltage and current harmonic component.

Total Demand Distortion of a voltage waveform is same as V_{THD}; however, Total Demand Distortion of a current waveform is different from I_{THD}. Total Demand Distortion of a current waveform (I_{TDD}) is defined as the square root of the ratio of sum of the squares harmonic content of current waveform to the root mean square value of the maximum rated load current[84].

$$I_{TDD} = \sqrt{\frac{\sum_{i=2}^{n} I_i^2}{I_{rated}}} \tag{1.3}$$

where, I_{rated} represent the maximum rated load current.

This standard identifies the network resonance condition as a key factor that impacts the harmonic level in a utility system. Table 10.2 in IEEE Standard 519 specifies permissible V_{THD} of 5% for any general system and 3% for a special system such as a hospital or airport. A harmonic current drawn through an impedance causes voltage distortion [84]. Hence, the level of V_{THD} on a network can be attributed to the impedance of the network at various harmonic frequencies. A thorough investigation is therefore needed to evaluate the impact of harmonics of both small scale and large scale PV solar farms, especially when network resonances are present.

1.7   OBJECTIVES AND SCOPE OF THE THESIS

The objectives and scope of the thesis are as follows:

1. To develop a novel controller of a PV solar farm inverter to perform as STATCOM for power factor correction along with generation of real power. Two utilities, Bluewater Power Distribution Corporation and London Hydro Inc., who are industry partners in the OCE project supporting this research, have offered to showcase this novel technology in their utility networks.

2. To perform a simulation case study using PSCAD/EMTDC with real-time measured data of the motor load and electrical system of the Bluewater Power headquarters building for application of a PV-STATCOM to correct power factor at the terminals of an induction motor in the office building.

3. To validate the performance of the developed PV-STATCOM controller on a Real-Time Digital Simulator (RTDS).

4. To develop the PV-STATCOM controller in a Digital Signal Processor (DSP) based dSPACE system, and test its performance in a Hardware-In-the Loop simulation environment.

5. To investigate the impact of harmonics emanation from both the largest 80MW solar farm in Canada, as well as a 10 kW PV solar system on the Bluewater Power utility system, and finally, to study the possible network resonance issues along with voltage harmonic distortion.

1.8   OUTLINE OF THESIS

A chapter-wise summary of this thesis is given below:

Chapter 2 demonstrates a simulation case study for a PV inverter as a STATCOM, termed as PV-STATCOM, for power factor correction of a motor load in the utility premises of Bluewater Power. Active power, reactive power, and power factor are measured at the terminal of motor load. A PSCAD/EMTDC model is developed with network data, motor load with field data, and with a PV system as a DC source for studying this novel application of a PV-STATCOM for power factor correction. Finally, the performance of a PV-STATCOM for power factor correction is demonstrated under various operating conditions during night and day.

Chapter 3 presents a real-time digital simulation of a PV-STATCOM for power factor correction of a motor load in RTDS. A system model is developed in RTDS comprised of the electrical network of the London Hydro headquarters building, motor load, and PV system. The controller is tested at different PV power outputs with different loading conditions during night, as well as during the day.

Chapter 4 deals with the Hardware-in-the Loop simulation of a PV-STATCOM controller. A PV-STATCOM control system is taken out from the RTDS simulation environment and implemented in a real hardware Digital Signal Processor based controller board. A network model, PV system with inverter switches, and motor load are modeled using the RTDS

simulation environment. Input/output signals for the control system running on hardware controller board are accessed through different input/output cards present in the RTDS hardware. A PV-STATCOM control system is tested and compared to the similar operating scenarios as that of RTDS simulation.

Chapter 5 presents a case study of harmonics impact analysis on the Bluewater Power distribution network that connects the largest solar farm in North America. This study is performed based on harmonics data from a PV solar farm and detailed network data available from Bluewater Power Corporation. The network is modeled using PSCAD/EMTDC and validated with load flow studies using CYME software and SCADA measurements. The validated network model is used for the network resonance study and harmonic analysis in the presence of a large solar 20 MW solar farm as well as a small 10 kW PV solar system for different loading conditions and short circuit levels.

Chapter 6 presents the conclusions and the main contributions of this thesis. Future research work on a PV-STATCOM is proposed.

Chapter 2

PSCAD/EMTDC SIMULATION OF PV-STATCOM FOR POWER FACTOR CORRECTION

2.1 INTRODUCTION

This chapter presents a new control of a Photovoltaic (PV) solar system inverter as STATCOM, termed PV-STATCOM, for power factor correction. A PV solar system typically generates real power during the day but the entire asset remains idle at night. Thus, this expensive system is only partially utilized. This novel concept of PV-STATCOM utilizes the entire rated inverter capacity during the night, and the remaining capacity of inverter after real power generation during the day to provide reactive power support for power factor correction. This new technology allows full utilization of the asset of the PV solar system during the entire 24-hr period. This concept of utilizing a PV system as STATCOM is being implemented at Bluewater Power Distribution Corporation, Sarnia, where a 10 kW small-scale photovoltaic solar system is installed on their office premises. This 10 kW PV inverter is planned to be operated as PV-STATCOM to correct the power factor of a heat pump used in the building for heating and cooling purposes. In this chapter, a model for the 10 kW PV-STATCOM and the Bluewater Power Distribution Corporation's main building is developed using the commercial grade electromagnetic transient simulation software PSCAD/EMTDC. The performance of a PV-STATCOM controller is demonstrated in both steady state and transient situation for power factor correction at the heat pump terminal.

2.2 SYSTEM DESCRIPTION

Bluewater Power Distribution Corporation is a utility company providing electrical power to over 35,000 customers in Southwestern Ontario, Canada. Figure 2.1 depicts the single line diagram of the Bluewater Power Distribution network office building.
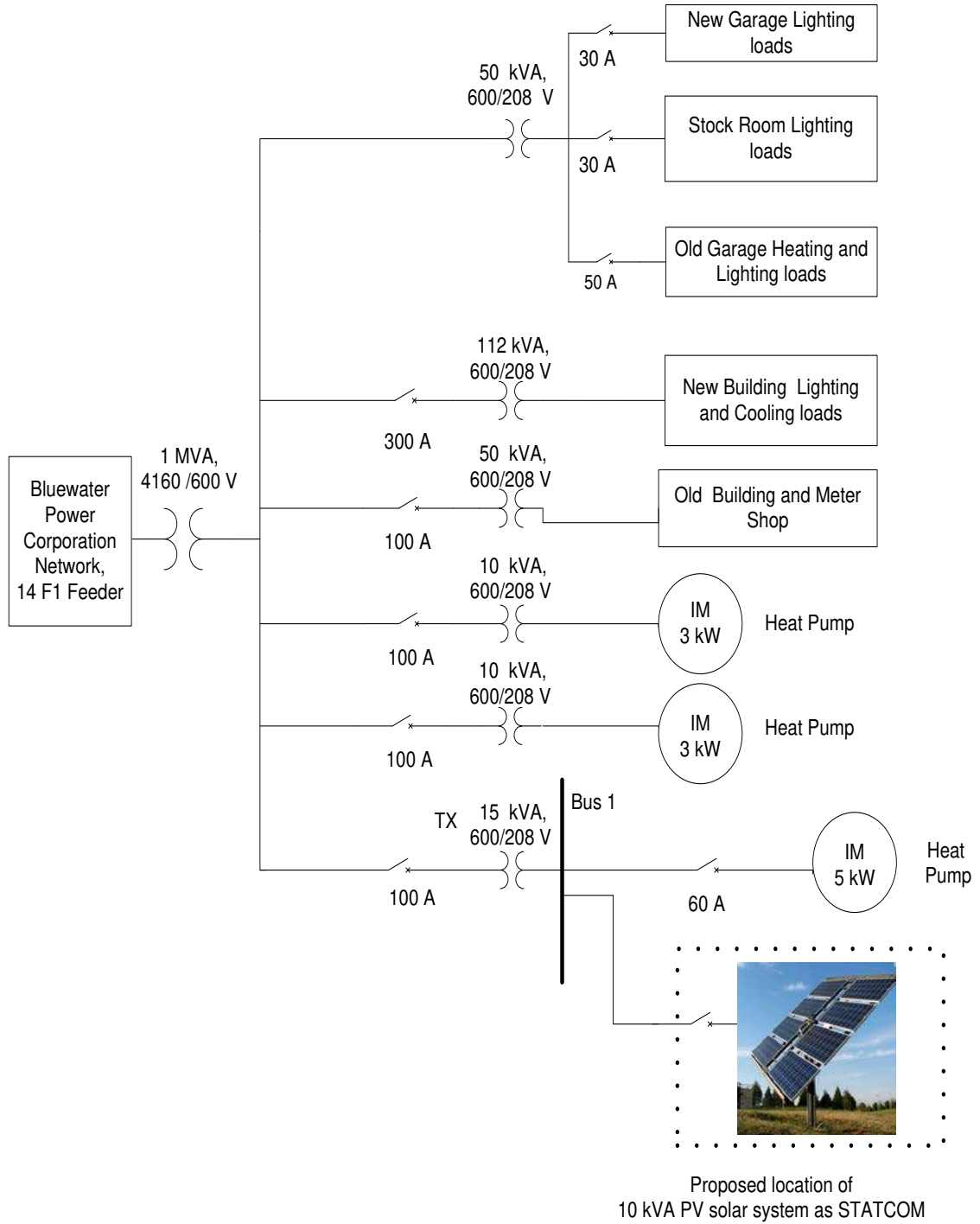
Figure 2.1 Electrical system diagram of Bluewater Power office building

The Bluewater Power office building is fed from a 14F1 feeder that is connected to the Hydro One network from the St. Andrew substation. The operating voltage of the 14F1 feeder is 4160V. The power supply to the main office building is provided through a step-

down transformer of rating 1 MVA, 4160/600V. The average load of the building is approximately 140 kW. The loads of the building are broadly categorized into two types: heating and lighting. Lighting loads are constant throughout the year, while the heating load varies over different seasons. As all of the loads inside the building operate at 208/120 V, separate smaller transformers are used to supply power to different types of loads in the building. There are three heat pumps inside the building for heating and cooling purposes. The largest one is a 5 kW heat pump that is fed from a 15 kVA transformer through a 60A breaker. The main components of a heat pump are the blower and the compressor, both of which are normally composed of squirrel cage induction motors. A 10 kW PV solar system is currently being installed in the main office building of Bluewater Power Distribution Corporation. In order to showcase the features of the new control, Bluewater Power has decided to connect the 10 kW PV solar system at Bus 1, as shown in Figure 2.1, to operate as PV-STATCOM to improve the power factor to unity.

2.3   MODELING OF STUDY SYSTEM

This section presents the models of the different components in the study system, shown in Figure 2.2, using PSCAD/EMTDC software. The Bluewater Power network is modeled as Thevenin's equivalent of the entire Bluewater Power network looking at the left of Bus 1, as demonstrated in Figure 2.1. $I_{i,a}$, $I_{i,b}$, $I_{i,c}$, represent the three-phase inverter output currents of a 10 kW inverter, whereas $I_{L,a}$, $I_{L,b}$, $I_{L,c}$ represent the 5 kW inductor motor terminal currents. $V_{s,a}$, $V_{s,b}$ and $V_{s,c}$ represent the three-phase source voltages at Bus 1 (Point of Common Coupling). V_{DC} represents the inverter DC link voltage that is provided by the 10 kW PV solar system. L_f and C_f represent the LC filter parameters, whereas C_{DC} represents the DC link capacitor.

2.3.1   Bluewater Power Network

The Bluewater Power network is modeled at Bus 1 as a voltage source behind a short circuit impedance, calculated from the values of short circuit level and X/R ratio, provided by Bluewater Power. Bluewater Power network parameters are given in Appendix A.1.

Bus 1

Bluewater Power Network

Induction Motor (5 kW)

IM

$I_{L,a}$

$I_{L,b}$

$I_{L,c}$

$V_{s,a}$

$V_{s,b}$

$V_{s,c}$

10 kW PV Solar System

LC Filter

C_f

L_f

$I_{i,c}$

$I_{i,b}$

$I_{i,a}$

C_{DC}

V_{DC}

VSI

Control Circuitry

$V_{s,a}$ $V_{s,b}$ $V_{s,c}$ V_{DC} $I_{i,a}$ $I_{i,b}$ $I_{i,c}$ $I_{L,a}$ $I_{L,b}$ $I_{L,c}$
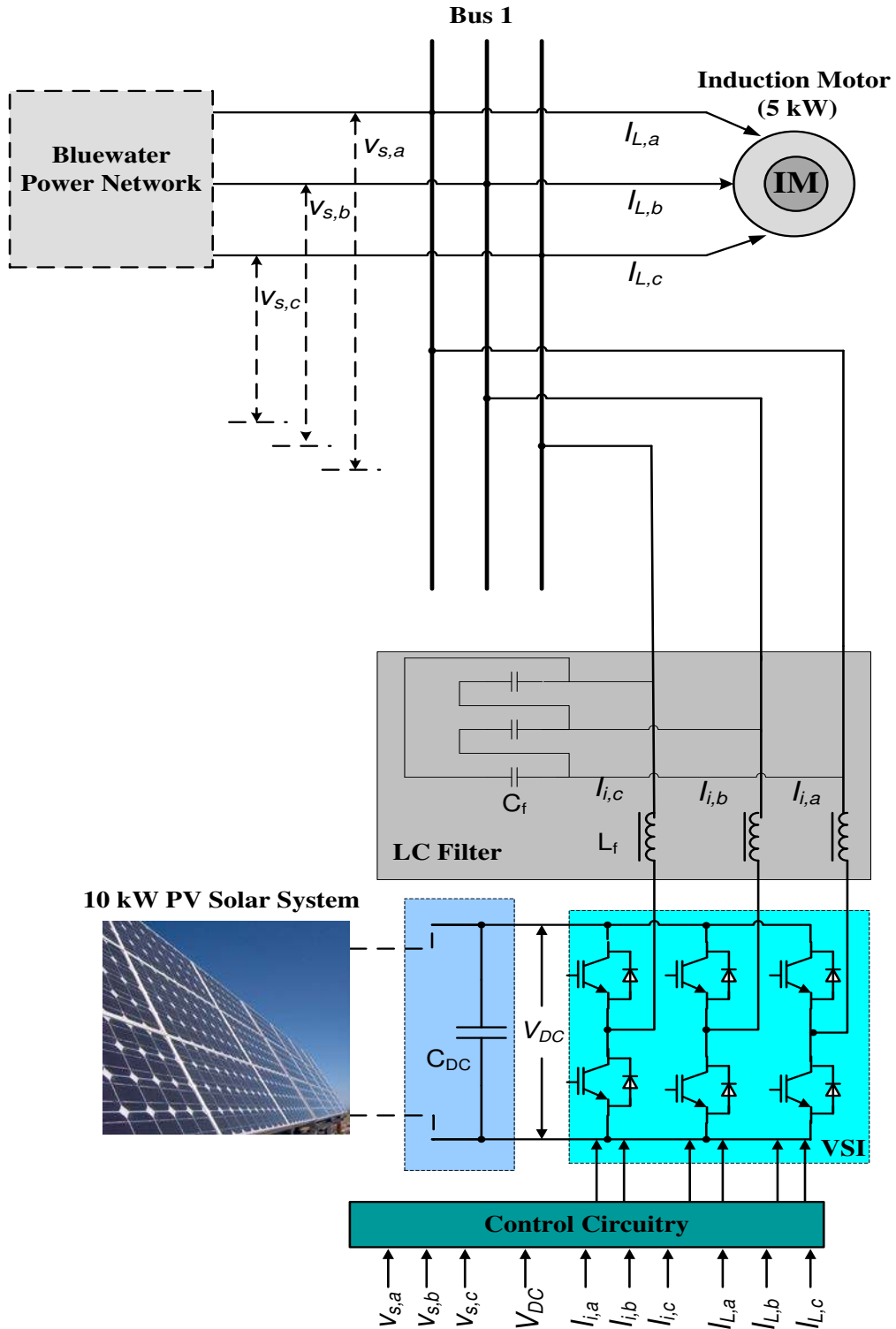
Figure 2.2 Study system for Bluewater Power Distribution System

2.3.2   Induction Motor

Figure 2.3 depicts the equivalent circuit of the induction motor [89]. R_1, jX_1, R_2' and jX_2' represent the stator resistance, stator reactance, equivalent rotor resistance, and equivalent rotor reactance per phase, respectively. R_c and jX_m represent core losses and magnetizing reactances, respectively. V_1 is the per phase supply voltage to the stator circuit and s represents slip of the induction motor. The electrical parameters of the induction motor are given in Appendix A.2.
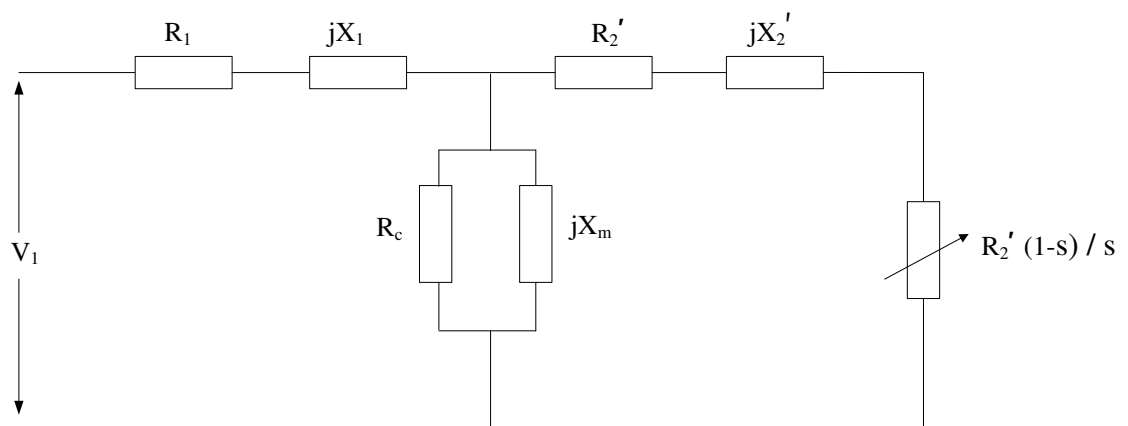
Figure 2.3 Equivalent circuit of an induction motor

2.3.3   Photovoltaic (PV) System

Figure 2.4 illustrates the PV system as modeled using a PSCAD/EMTDC software simulation. The PV solar system generates DC power at its output with an open circuit DC voltage. As a PV system model is not provided in the PSCAD library, for this study purpose all of the PV solar panels are lumped together and represented as a DC voltage source: V_{DC}. The DC voltage source model is implemented during the daytime when the PV solar system injects active power into the grid. As a constant DC source is used to model the PV solar system during the PV mode of operation, no MPPT algorithm is implemented. The DC source is able to maintain the desired DC link voltage. During the night, when the PV inverter is operated as STATCOM, the solar panels are disconnected, and consequently, the dc voltage source is disabled.
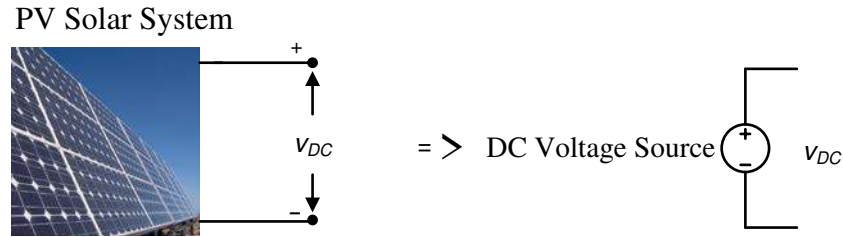
PV Solar System

Figure 2.4 PV solar system model

2.3.4   Photovoltaic Inverter

A photovoltaic inverter is modeled using a 2-level, 6-pulse VSI model utilizing IGBT switches [19]-[20]. The dc side capacitor C_{DC} serves two purposes: i) during the steady state it maintains the dc voltage constant at the DC link, and ii) during the transients, it serves as a mini energy storage unit, to temporarily supply real power. The DC link voltage and DC link capacitor values are determined as per the recommendations given in [23]. The minimum DC link voltage is calculated using the following equation:

$$V_{DC} \geq 1.633 \; V_{L\text{-}L} \tag{2.1}$$

where V_{DC} represents the dc link voltage and $V_{L\text{-}L}$ represents the line-line voltage at Bus 1. Similarly, C_{DC} is calculated as follows:

$$C_{DC} = \frac{2 \times P \times 16.7 \times 10^{-3}}{V_{DC}^{2} \times (1 - K^{2})} \quad F \tag{2.2}$$

where P represents the maximum real power handled by the capacitor, V_{DC} represents the DC link voltage, and K represents the ratio between the minimum DC link voltage to the maximum DC link voltage. 16.7×10^{-3} represents one cycle time at a power frequency of 60Hz.

2.3.5   PV-STATCOM Controller

Figure 2.5 presents the PV-STATCOM controller for power factor correction. The PV inverter is controlled in current-control mode, using the hysteresis band modulation technique described in [28]-[29]. The current injected by the inverter into the grid is split into two separately regulated components: active component (I_a), and reactive component (I_r).

During the daytime, when the PV system operates as PV-STATCOM, the DC source is used to regulate the DC link voltage and I_a is not regulated by the DC voltage control loop. During the night, when the PV system operates as a STATCOM, the DC source is disconnected and the DC voltage control loop is used to regulate the DC link of the inverter by controlling I_a. I_r is calculated based on the reference given to the power factor control loop during both day and night. The different subsystems used in the PV-STATCOM controller are described as follows.
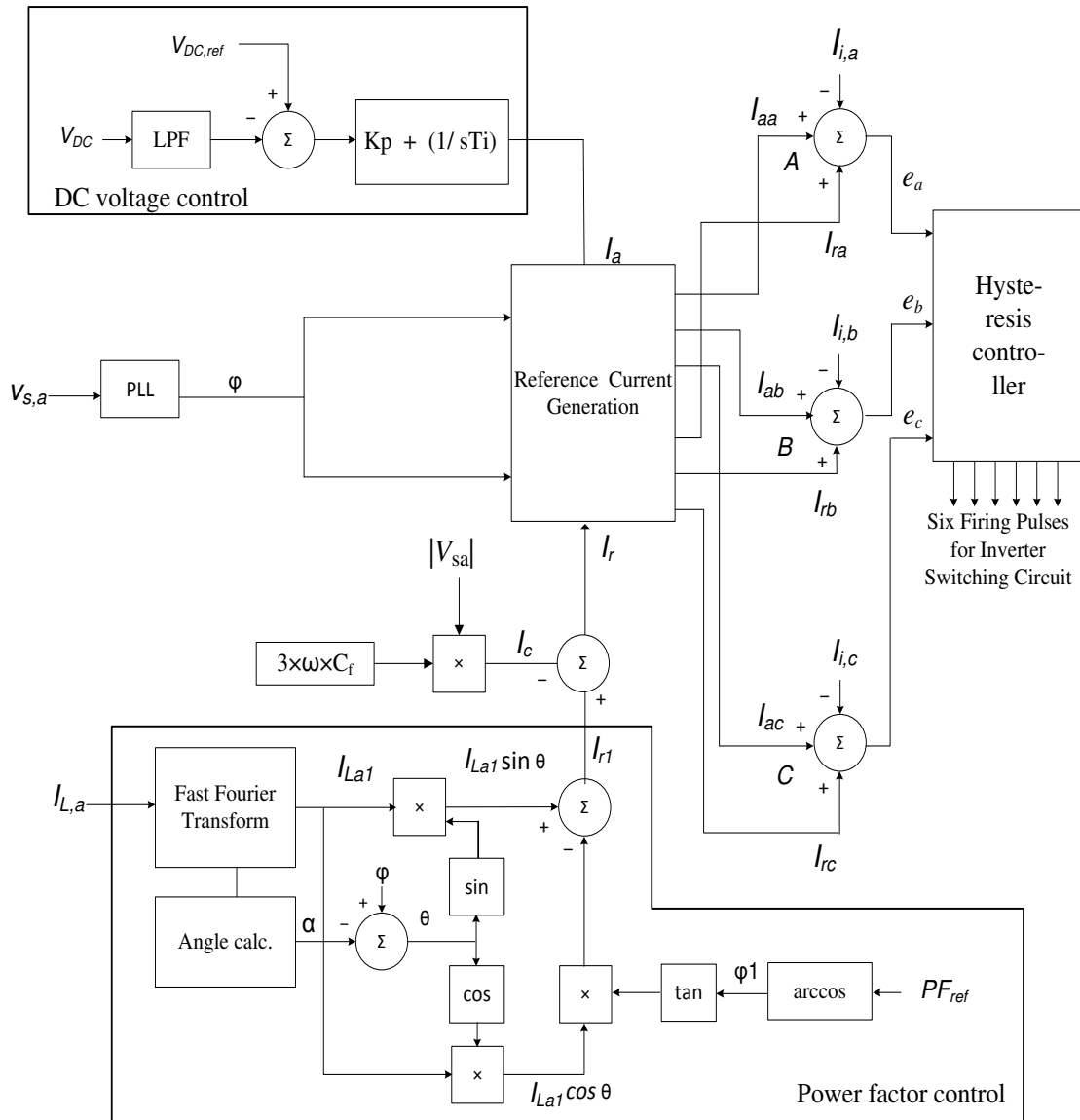
Figure 2.5 Control circuit of PV-STATCOM for power factor correction

2.3.5.1 *DC Voltage Control*

V_{DC} is measured at the dc link terminal of the inverter, and a low pass filter is used to remove any ripples. The filtered V_{DC} is compared to the reference value, $V_{DC, ref}$. The error is then fed to the PI controller to generate I_a, which helps to regulate the DC link voltage to $V_{DC,ref}$. The best parameters of the PI controller are chosen through step response studies of the controller by systematic trial and error [28]. A step input is given to $V_{DC,ref}$ and the response of V_{DC} is examined. Initially, K_p is kept constant and T_i is varied from 0.05 to 0.5. The best value of T_i is selected to be 0.02, which provides the fastest settling time and an overshoot of less than 10%. Keeping T_i fixed at 0.02, K_p is varied incrementally from 100 to 500, and the best gain is determined to be 200.

2.3.5.2 *Phase Locked Loop*

A Phase Locked Loop (PLL) produces an output signal which is synchronized in phase and frequency of the input signal [90]. The PLL generates the voltage angle φ at Bus 1 which is used to generate three sinusoidal active and reactive reference currents for the Hysteresis current controller.

2.3.5.3 *Power Factor Control*

Figure 2.6 presents the fundamental concept behind power factor controller operation. $V_{s,a}$ is the voltage phasor at Bus 1. The induction motor (heat pump) draws the lagging current $I_{L,a}$ at a power factor angle θ. The a-phase current, $I_{L,a}$, of the induction motor has two components: active component $I_{L,a} \cos(\theta)$, and reactive component $I_{L,a} \sin(\theta)$.
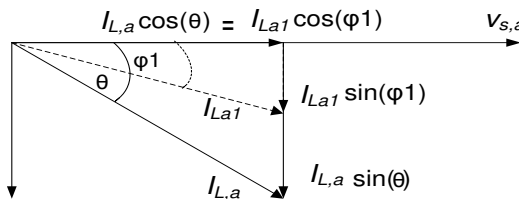
Figure 2.6 Phasor diagram for power factor correction

In order to improve power factor to the desired value, reactive component $I_{L,a} \sin(\theta)$ has to be decreased from the Bluewater Power supply system based on the desired amount of power

factor correction. PF_{ref} is the required power factor to be achieved at Bus 1. Based on this reference, a new power factor angle φ1 and tan (φ1) are calculated using:

$$\varphi1 = \cos^{-1}\left(PF_{ref}\right) \tag{2.3}$$

$$\tan(\varphi1) = \frac{I_{La1}\sin(\varphi1)}{I_{La1}\cos(\varphi1)} \tag{2.4}$$

Assuming the motor load is constant during the power factor correction mode, the active current before and after power factor correction are the same. Therefore, $I_{La1}\cos(\varphi1)$ is equal to $I_{L,a}\cos(\theta)$. Thus, the new reactive current $I_{La1}\sin(\varphi1)$ drawn from the supply system is:

$$I_{La1}\sin(\varphi1) = I_{L,a}\cos(\theta) \times \tan(\varphi1) \tag{2.5}$$

This concept is applied in the power factor controller implementation in PSCAD, as demonstrated below.

As illustrated in Figure 2.5, $I_{L,a}$ is the phase-a load current measured at the terminal of the induction motor and fed to a Fast Fourier Transformation block [67] in order to extract the fundamental current magnitude I_{La1} and the angle α. Voltage angle is calculated using PLL, as demonstrated in section 2.3.5.1. The power factor angle θ is then calculated based on the angle difference between the fundamental voltage $V_{s,a}$ and current $I_{L,a}$. $I_{La1}\cos\theta$ is the active current drawn by the induction motor and $I_{La1}\sin\theta$ is the reactive current drawn by the induction motor. $I_{La1}\cos\theta \times \tan(\varphi1)$ is the new reactive current to be drawn by the motor from the Bluewater Power supply system, based on PF_{ref}. Hence, the PV-STATCOM compensates for the reactive current from the supply by injecting Ir_1 into the network:

$$Ir_1 = (I_{La1}\sin\theta - I_{La1}\cos\theta \times \tan(\varphi1)) \tag{2.6}$$

where Ir_1 represents the peak magnitude of the reactive current.

A filter capacitor is provided at the terminal of the inverter to suppress the high frequency switching harmonics [20]-[23]. This filter capacitor also generates reactive power. Ic represents the total capacitive reactive current injected from the filter capacitor. Ic for all three phases is calculated as:

$$Ic = 3 \times \omega \times C_f \times V_{s,a} \qquad (2.7)$$

It is noted that the reactive power from the PV-STATCOM comes from two sources: the PV inverter and the filter capacitor.

Therefore, Ic is deducted from Ir_1 in order to generate the net magnitude of reactive current, Ir, to be injected from the PV-STATCOM.

$$Ir = Ir_1 - Ic \qquad (2.8)$$

2.3.5.4   Reference Current Generation

Hysteresis current controller adopted for this study uses instantaneous currents for control purposes [40], [42]. As such, instantaneous active current references I_{aa}, $I_{ab,}$ and I_{ac} are calculated for all three phases: a, b, and c using:

$$I_{aa} = I_a \cos(\varphi) \qquad (2.9)$$

$$I_{ab} = I_a \cos(\varphi - 120°) \qquad (2.10)$$

$$I_{ac} = I_a \cos(\varphi + 120°) \qquad (2.11)$$

Similarly, instantaneous reactive current references I_{ra}, $I_{rb,}$ and I_{rc} are calculated for all three phases: a, b, and c using:

$$I_{ra} = I_a \sin(\varphi) \qquad (2.12)$$

$$I_{rb} = I_a \sin(\varphi - 120°) \qquad (2.13)$$

$$I_{rc} = I_a \sin(\varphi + 120°) \qquad (2.14)$$

These currents I_{aa}, $I_{ab,}$ $I_{ac,}$ and I_{ra}, $I_{rb,}$ I_{rc} are computed in the Reference current generation block, in Figure 2.5.

2.3.5.5   Summation Blocks (A, B and C)

Three summation blocks A, B, and C, shown in Figure 2.5, are used for the three phases, a, b, and c, respectively. At summation block A, active current reference I_{aa} and reactive current

reference I_{ra} for phase-a are added to generate the total reference current for phase-a. $I_{i,a}$ represents the phase-a inverter output current which is compared to the reference current to generate the instantaneous current error e_a. The same procedure is followed for phase-b and phase-c to generate instantaneous current error signals e_b and e_c, which are then fed to the hysteresis current controller.

2.3.5.6 *Hysteresis Current Controller*

The hysteresis current controller uses three hysteresis blocks for each of the three phases. The hysteresis current controller is based on the fixed band hysteresis control method, with a hysteresis band of $\pm$ 1 A (3.24 % of the inverter output current) [27]-[30]. Three hysteresis blocks for the three phases keep the error signals e_a, e_b and e_c within the band of $\pm$ 1 A. As long as errors are within the hysteresis band, the inverter output current does not change. When the error reaches the upper or lower limit of the hysteresis band, the inverter switches are made to change their states to allow the inverter output current to bring the errors within the acceptable limit.

2.3.5.7 *LC Filter*

The hysteresis current controller is utilized in the PV-STATCOM controller which generates lower order harmonic components. Therefore, LC filter component parameters L_f and C_f are determined by analyzing the I_{THD} and I_{TDD} at different operating scenarios of the PV-STATCOM. L_f and C_f parameters are selected such that I_{THD} and I_{TDD} becomes less than 5% at the output of the PV-STATCOM, as per IEEE Standard 1547 [91] and IEEE Standard 519 [84]. The values of L_f, C_f, C_{DC}, and V_{DC} used for this simulation study are given in Appendix A.3.

2.3.6 Modeling of Real Time Loading Conditions

To demonstrate the proposed PV-STATCOM technology, different electrical parameters such as: active power, reactive power, and power factor are measured at the terminal of the 5 kW heat pump, using Fluke power quality analyzer for approximately 72 hrs. After analyzing the field test data using Fluke power quality analyzer software [92], it is observed that there is a substantial variation between the active and reactive power requirement of the   heat pump. Figure 2.7 (a) presents the measured real power at the load (heat pump) terminal for

24 hrs. To simulate the varying load behavior, the time period 8:00 AM to 10:00 PM is chosen. The simulation period of 8 seconds to 22 seconds in PSCAD corresponds to the 8:00 AM to 10:00 PM period in real time. It is seen that measured real power varies from 0.82 kW to 2.08 kW during the period chosen for analysis. The same behavior is simulated using PSCAD by varying the torque on the induction motor at a different simulation time with a 5 kW induction motor model, shown in Appendix A.2. It is noted that the increase and decrease in torque of the induction motor increases or decreases the motor power according to the toque speed characteristics of the motor [89]. It is shown in Figure 2.7 (b) that simulated real power follows the same pattern of measured real data. The variation of simulated real power is between 0.76 kW and 2.1 kW.

(a)   (b)
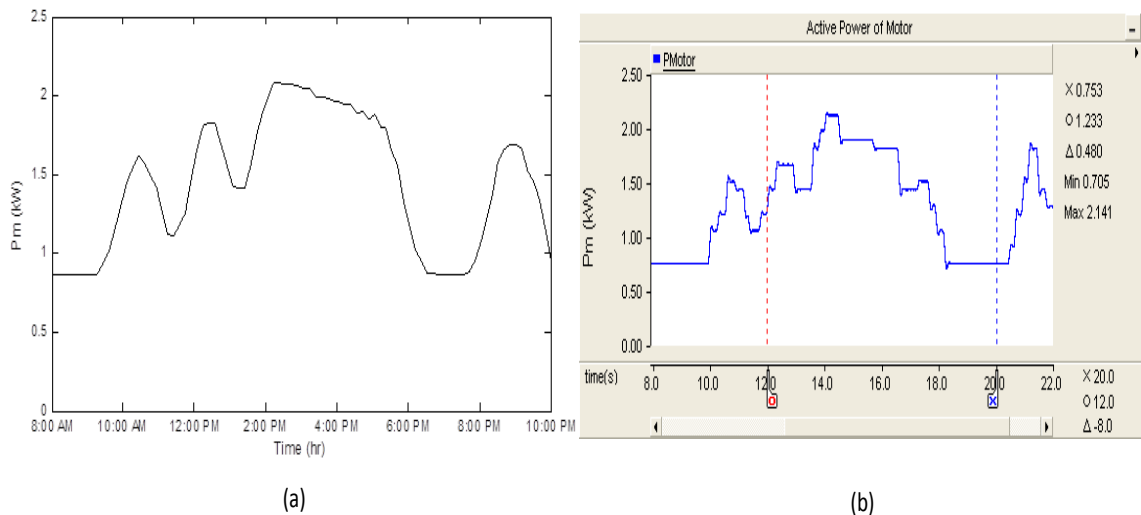
Figure 2.7 (a) Measured Active power and (b) Simulated Active power

Figure 2.8 (a) depicts the measured reactive power, which varies from 1.21 kvar to 1.42 kvar during the period chosen for analysis. The same behaviour is simulated using PSCAD by varying the torque on the induction motor at different simulation times, as shown in Figure 2.8 (b). It is demonstrated that the variation of simulated reactive power is between 1.23 kvar and 1.35 kvar. Figure 2.9 (a) shows the variation of measured power factor at the terminal of the induction motor. It is also shown that the measured power factor varies between 0.57 and 0.82. The same pattern of the measured data is achieved in PSCAD where the simulated power factor varies between 0.53 and 0.84, as illustrated in Figure 2.9 (b).
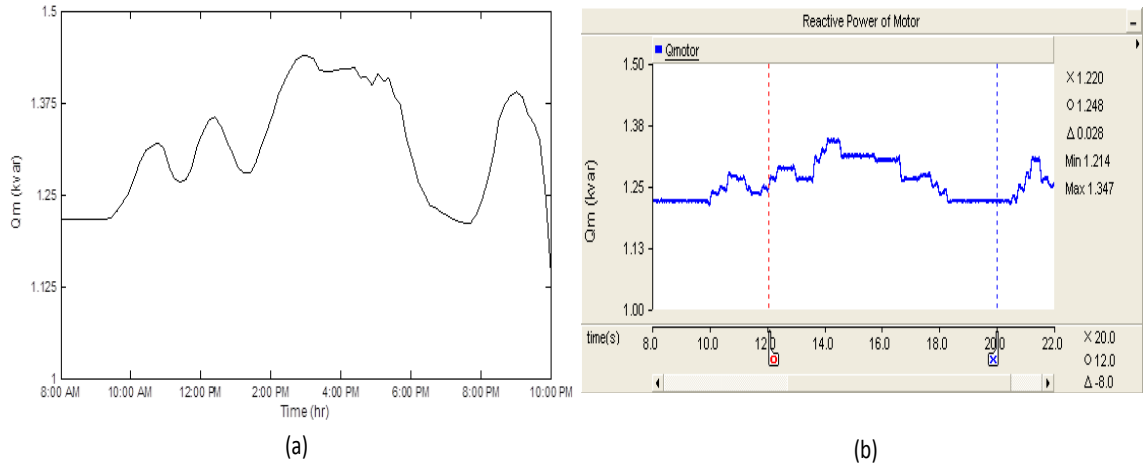
Figure 2.8 (a) Measured Reactive Power and (b) Simulated Reactive Power
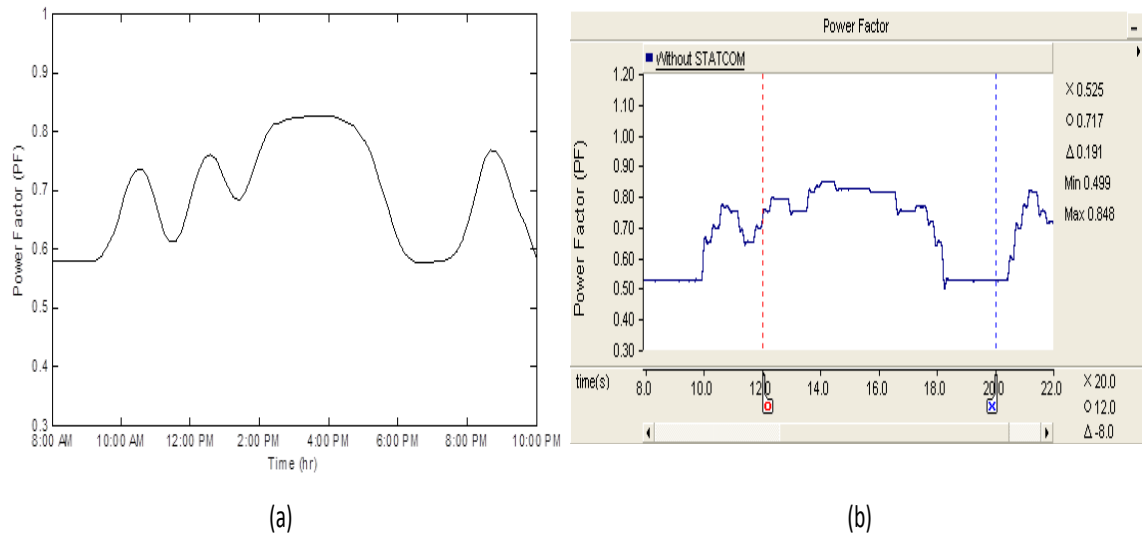
Figure 2.9 (a) Measured Power Factor and (b) Simulated Power Factor

2.4   SIMULATION RESULTS

The steady state and transient performance of a PV-STATCOM with power factor control mode is discussed in this section. The objective is to achieve a power factor of unity.

2.4.1   Steady state analysis

The steady-state performance of the PV-STATCOM controller for power factor correction is performed with the simulated real time data measured at the heat pump terminal. To

demonstrate the operation of the PV-STATCOM controller for power factor correction, the time period of 8:00 AM to 10:00 PM is considered.

It is noted that the only time the PV-STATCOM will not be able to inject the required reactive power, Q, to maintain unity power factor is at noon, around 12:00 PM, when the PV system generates its rated real power P of 10 kW. This is due to the unavailability of reactive power from PV inverter after rated power generation of 10 kW, since $Q = \sqrt{(S^2 - P^2)}$. S represents the total kVA of the PV inverter, which is 10 kVA.

Figure 2.10 demonstrates the power factor correction of the induction motor with and without PV-STATCOM for the study period. The motor runs at a power factor varying between 0.53 and 0.84 during this period, much below the utility recommended power factor of 0.9. It is observed that with the PV-STATCOM, power factor is improved to unity for the entire period by injecting the required amount of reactive power. This reactive power is contributed by both the PV-STATCOM and the filter capacitor. In this study, the filter capacitor of a 10 kVA PV-STATCOM generates 0.96 kvar continuously.
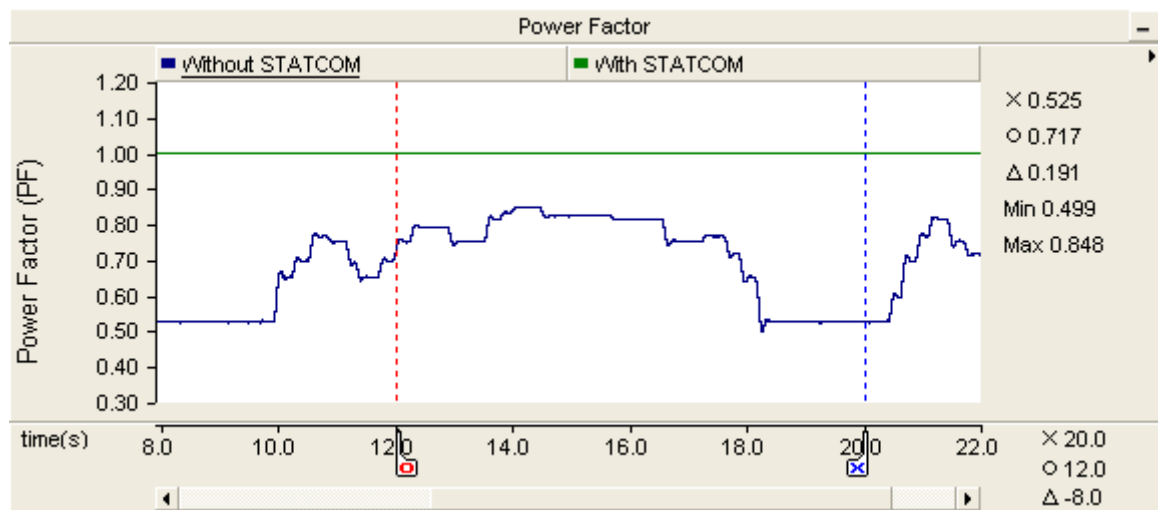
Figure 2.10 Power factor correction without and with PV-STATCOM

At noon, the active and reactive power requirement is 1.23 kW and 1.34 kvar. Also at noon, the PV system generates its rated real power of 10 kW and, therefore, cannot provide any reactive power support. However, the filter capacitor contributes a constant 0.96kvar during this time. The remainder of the reactive power, 0.38 kvar, is supplied by this source. During

this time, as there is high solar generation of 10 kW, there is also a real power flow of -8.77 kW to the source. Hence, source power factor becomes unity, according to the relation $\cos(\tan^{-1}(\frac{0.38}{-8.77}))$.

Table 2.1 presents a summary of the simulation results for steady-state power factor improvement at the PCC, at different times of the day. P_{Source} and Q_{Source} represent the power requirement from the source at Bus 1 (PCC). Similarly $P_{Statcom}$, $Q_{PV-Statcom}$, P_{Motor}, and Q_{Motor} represent the active power and the reactive power of the PV inverter and motor load respectively. PF_{Motor} and PF_{Source} represent the load and PCC power factor respectively.

Table 2.1 Steady-state power factor improvement

Time	$P_{Statcom}$ (kW)	$Q_{PV-Statcom}$ (kvar)	Q_{Cap} (kvar)	P_{Motor} (kW)	Q_{Motor} (kvar)	PF_{Motor}	P_{Source} (kW)	Q_{Source} (kvar)	PF_{Source}
8 am	1.68	9.85	0.96	0.86	1.22	0.57	-0.82	0.0	1
12 noon	10.0	0.0	0.96	1.23	1.34	0.70	-8.77	0.38	1
4 pm	8.0	5.23	0.96	2.0	1.46	0.80	-6.0	0.0	1
8 pm	0.1	9.99	0.96	1.22	1.22	0.70	1.12	0.0	1

It is seen that real power generation, $P_{Statcom}$, from the PV system varies throughout the day. $Q_{PV-Statcom}$ represents the capability of the PV inverter after real power generation. Q_{Cap} is a constant 0.96kvar throughout the day. As discussed in an earlier section, load on the motor varies throughout the day. The load power factor PF_{Motor} varies during the day corresponding to different active and reactive power requirements by the load. The PCC power factor, PF_{Source}, is made unity for a 24 hour period due to the PV inverter operating as STATCOM and injecting the necessary amount of reactive power, as required by the load.

For the considered loading condition of the heat pump, reactive power availability from the PV-STATCOM is enough to compensate the reactive power requirement of the load.

2.4.2   Transient Analysis

The transient performance of the PV-STATCOM is studied by giving a step input to the PV-STATCOM controller at time t = 0.5 seconds for power factor correction during both day and

night times. Transient performance is demonstrated with an assumed motor loading condition of close to 80% of its rating during the day, and 60% during the night.

2.4.2.1 *Daytime Performance*

At 4:00 PM, a loading condition is considered where real power, $P_{Load,}$ and reactive power, $Q_{\_Load,}$ of the load are 4 kW and 2.7 kvar, with a load power factor of 0.83.

Figure 2.11 depicts the source power at Bus 1 (PCC) and the PV solar system power output during the day. During the time period 0.4 to 0.5 seconds, the real power generation from the PV solar system, $P_{Statcom,}$ is 8 kW. $Q_{Statcom}$ represents the total reactive power from both the PV system and the filter capacitor. The filter capacitor provides 0.98 kvar. Thus, with the available 0.98 kvar, reactive power drawn from the source Q_{Source} becomes 1.72 kvar (Q_{Load} - $Q_{Statcom}$), to supply rest of the reactive power requirement of the load. As the motor real power requirement is 4 kW during this time, there is also a reverse power flow of -4 kW (P_{Load} - $P_{Statcom}$) to the Bluewater power network, and P_{Source} becomes -4 kW. At time t= 0.5 seconds, the PV system is made to operate as a PV-STATCOM in order to regulate the power factor to unity by giving a step input to the PV-STATCOM controller. It is seen that after t > 5 seconds, $Q_{Statcom}$ is 2.7 kvar. Accordingly, Q_{Source} becomes zero, thus making unity power factor at PCC.
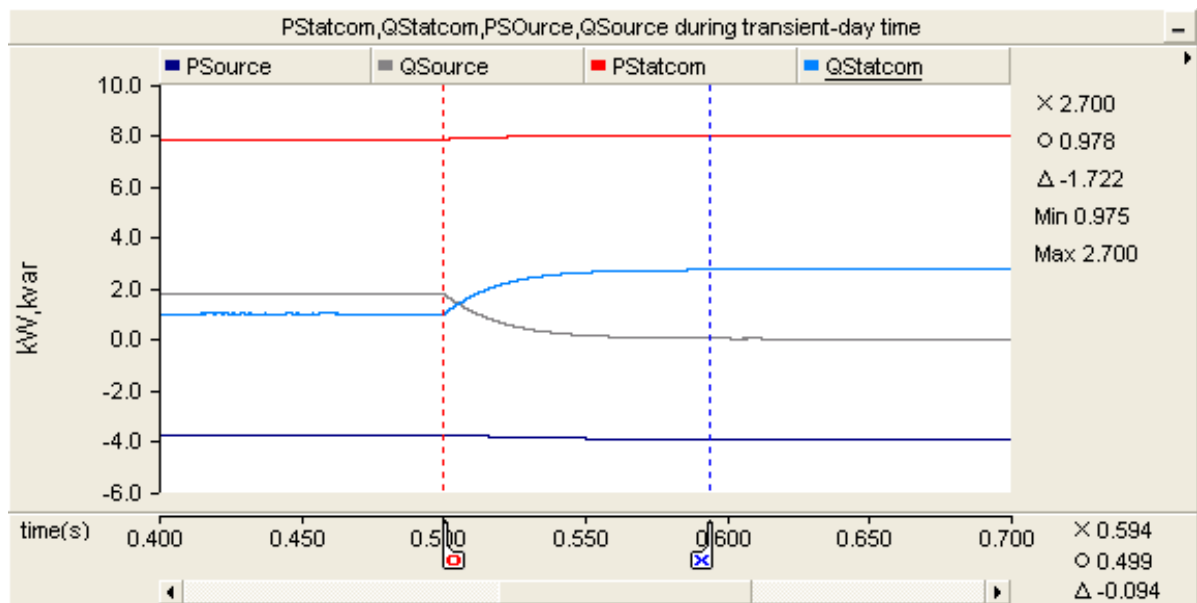
Figure 2.11 PV-STATCOM and source power during transient-daytime

Figure 2.12 demonstrates the power factor at Bus 1 with and without the PV-STATCOM. During the time period 0.4 to 0.5 seconds, the PCC power factor is 0.91 with P_{Source} of -4 kW and Q_{Source} of 1.72 kvar, according to the relation $\cos(\tan^{-1}(\frac{1.72}{-4}))$). At time t= 0.5 seconds, the PV system is made to operate as a PV-STATCOM to regulate the power factor to unity with a PF_{ref} =1 reference given to the PV-STATCOM controller. The PV-STATCOM controller responds within 2 to 3 cycles to regulate the power factor to unity by supplying 2.7 kvar to the network.
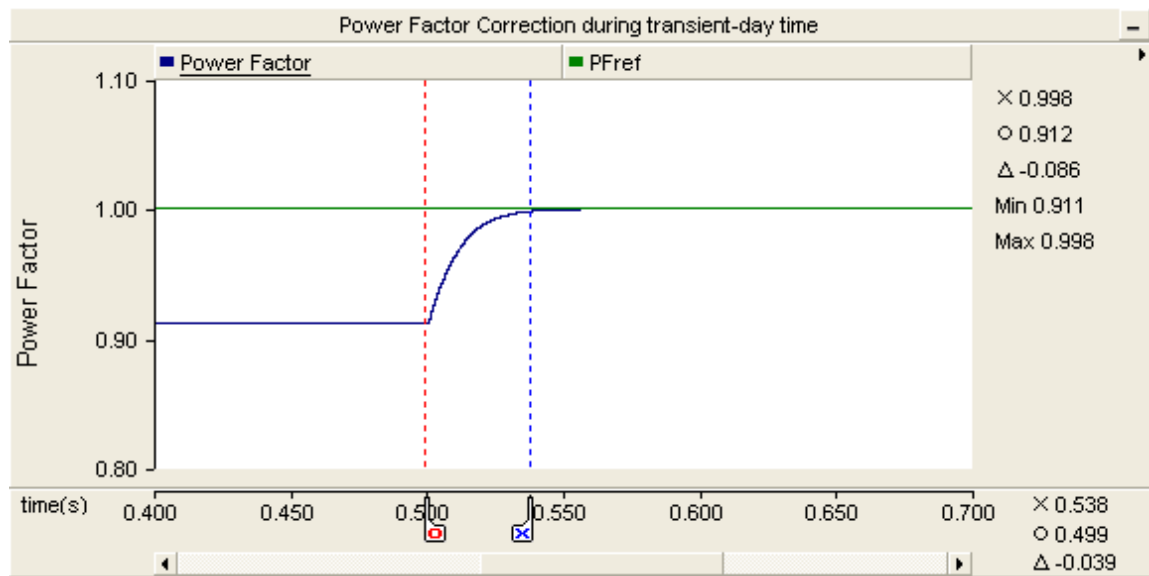
Figure 2.12 Power Factor Correction with PV-STATCOM

Figure 2.13 describes the voltage and current waveform in the transient state during the day. V_s, I_s, I_{gi}, and I_g represent the PCC voltage, PCC current, and PV-STATCOM current before filter and after filter, respectively. It is seen that the PCC voltage and current waveform are in phase during power factor correction mode due to unity power factor at PCC after time t > 0.5 seconds.
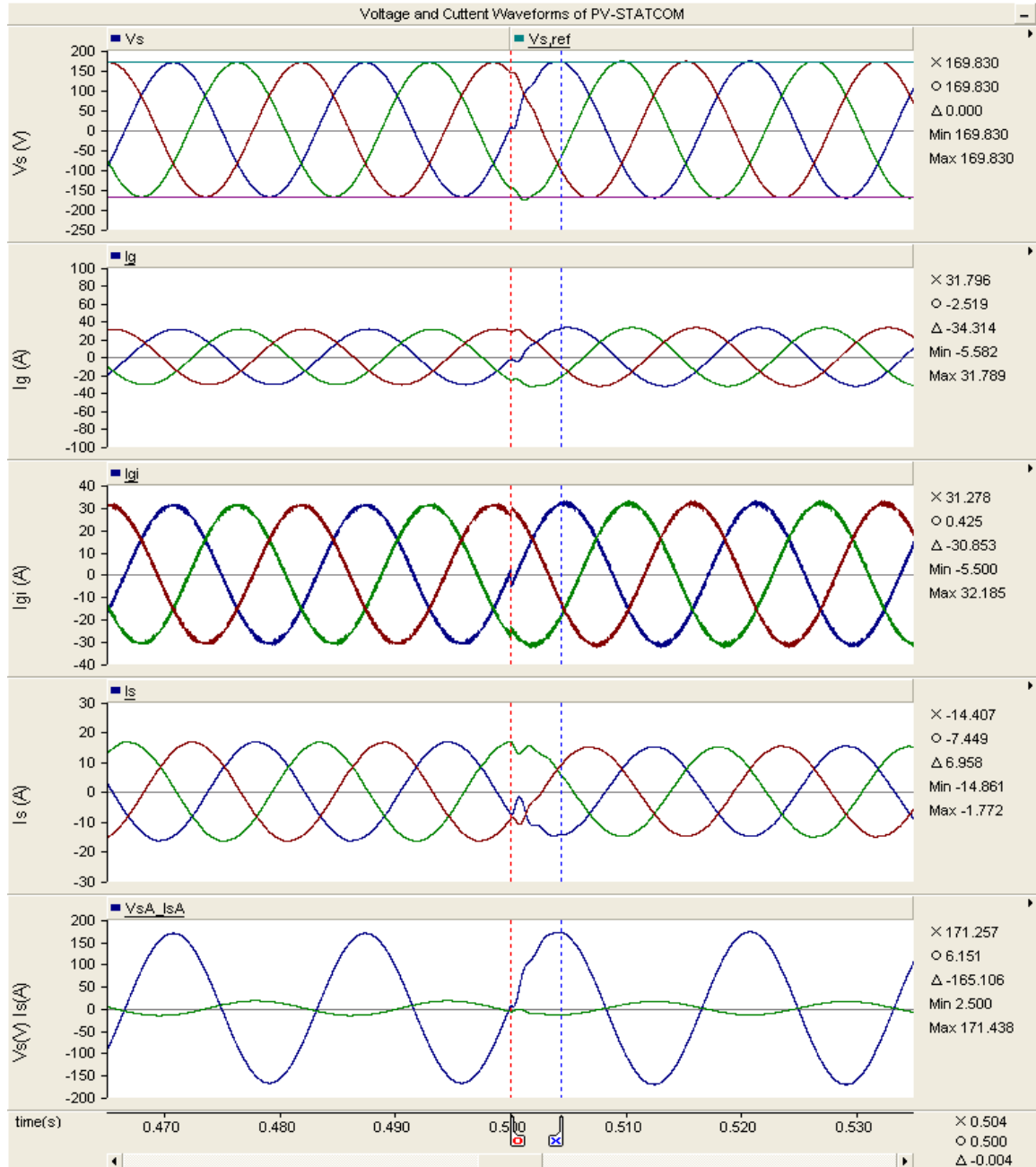
Figure 2.13 Transient response of PV-STATCOM at 4:00 PM

2.4.2.2   *Night time Performance*

The nighttime transient performance of the PV-STATCOM is demonstrated at 8:00 PM. The real power, $P_{Load,}$ and reactive power, $Q_{Load,}$ of the load are 3 kW and 2.4 kvar. The load operates at a power factor of 0.78.

Figure 2.14 depicts the source power at Bus 1 and the PV-STATCOM output power during the night. Between 0.4 and 0.5 seconds, the PV system draws only -50 W from the system to provide for the inverter losses. It is seen that $Q_{Statcom}$ is 0.93 due to reactive power from the filter capacitor. Q_{Source} (Q_{Load} - $Q_{Statcom}$) is 1.47 kvar to supply the rest of the reactive power to the load. As there is no real power generation from the PV system, the real power requirement of the load is supplied from the source. Thus, P_{Source} is 3.05 kW (P_{Load} + $P_{Statcom}$) and Q_{Source} is 1.47 kvar. At time t= 0.5 seconds, the PV system is made to operate as a PV-STATCOM in order to regulate the power factor to unity by providing a step input to the PV-STATCOM controller. It is seen that during the time t > 5 seconds, $Q_{Statcom}$ is 2.39 kvar. Accordingly, Q_{Source} becomes zero, making unity power factor operation at PCC.
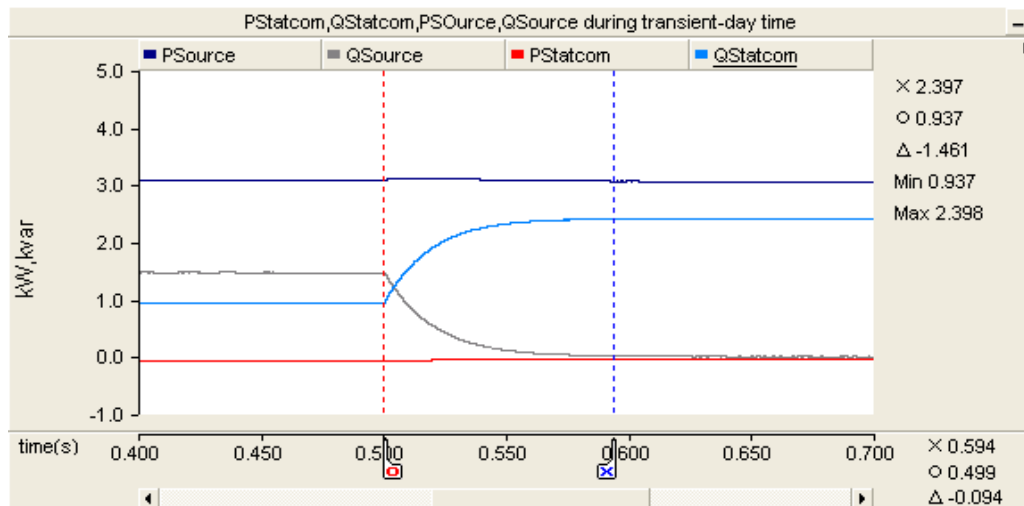
Figure 2.14 PV-STATCOM and source power during transient nighttime

Figure 2.15 demonstrates the power factor at Bus 1 with and without the PV-STATCOM. During the time period 0.4 to 0.5 seconds, PCC power factor is 0.91 due to P_{Source} of 3.05 kW and Q_{Source} of 1.47 kvar, respectively. At time t= 0.5 seconds, the PV-STATCOM controller is given a reference of PF_{ref}=1 to regulate the power factor to unity. The PV-STATCOM controller responds within 2 to 3 cycles to regulate the power factor to unity by injecting 2.39kvar to the network.

Figure 2.16 illustrates the voltage and current waveform in the transient state during the night. It is seen that PCC voltage and current waveform are in phase during power factor correction mode due to unity power factor at PCC after time t > 0.5 seconds.
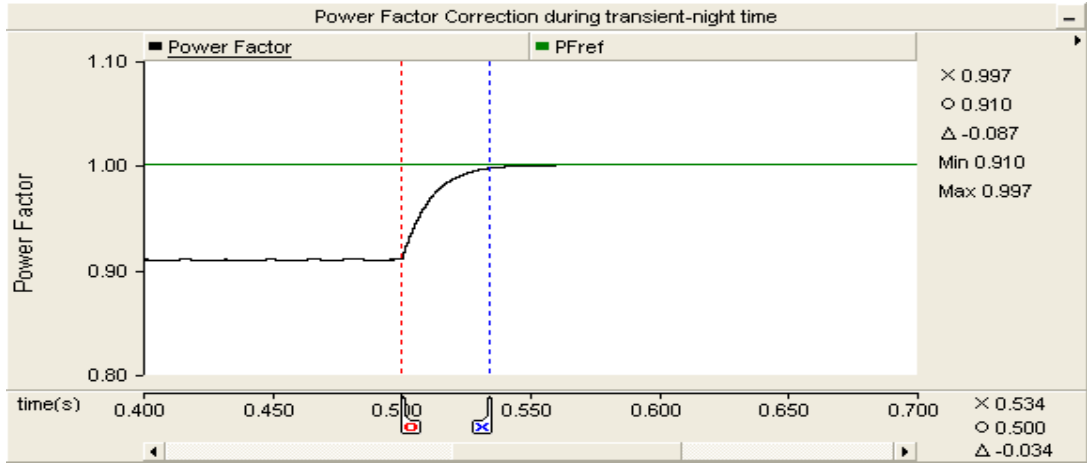
Figure 2.15 Power factor of PCC with and without PV-STATCOM
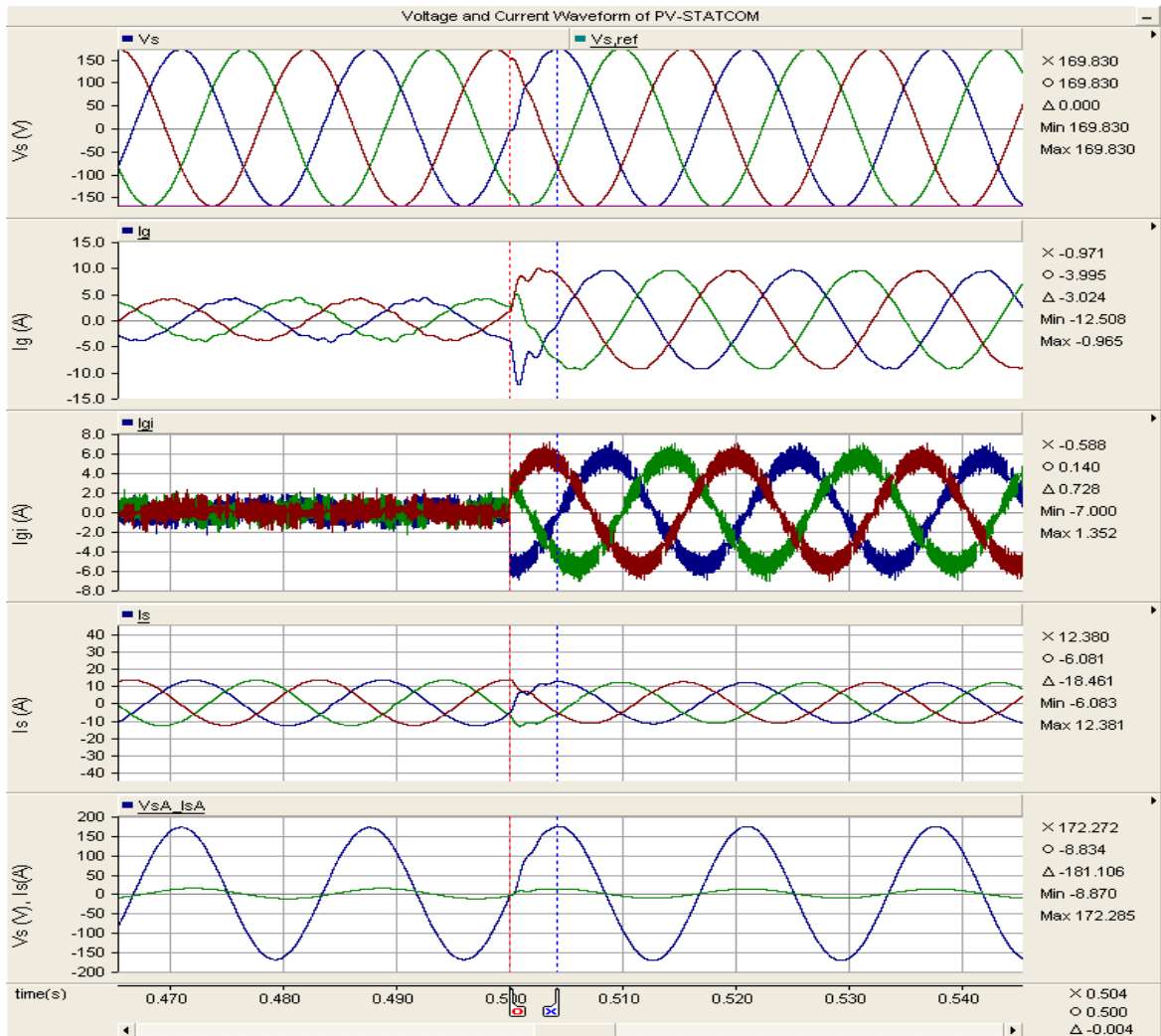
Figure 2.16 Transient response of PV-STATCOM at 8:00 PM

2.5 CONCLUSION

This chapter demonstrates a novel application of utilizing a 10 kW PV solar system as a STATCOM, termed PV-STATCOM, for power factor correction of a 5 kW induction motor in the Bluewater Power Distribution Network. The hysteresis current control scheme is employed for the PV-STATCOM controller. The steady-state and transient performance of the proposed controller for power factor correction are demonstrated through simulations carried out using electromagnetic transient PSCAD/EMTDC. A simulation model for the motor load is developed in accordance with the real time data measured at the motor terminal. The PV-STATCOM controller performance is illustrated for different loading conditions of the motor both during the day and night.

The following conclusions are made:

i)   The PV-STATCOM is able to regulate the PCC power factor to unity during the night, as well as during the day, with the available reactive power after real power generation from the PV solar system.

ii) The proposed hysteresis controller for the PV-STATCOM performs effectively both during the night and day times. The response of the PV-STATCOM controller for power factor correction during the transient is 2 to 3 cycles for both the cases.

With such novel functionality of a PV-STATCOM, a PV solar system can help a customer avoiding usage penalties while continuing to generate revenues from the sale of real power. Thus, such an expensive PV solar system can be entirely utilized for a full 24 hour period.

Chapter 3

REAL-TIME DIGITAL SIMULATION OF PV-STATCOM FOR POWER FACTOR CORRECTION

3.1 INTRODUCTION

This chapter presents the real-time digital simulation of a PV-STATCOM for power factor correction using a Real Time Digital Simulator (RTDS). RTDS is a digital power system simulator, widely used for real-time simulations and Hardware-in-the-loop (HIL) applications for different power systems control and protection equipment. The site for PV-STATCOM operation is chosen at the terminal of an induction motor load at the London Hydro headquarters building, the second location selected for demonstrating this technology, in addition to Bluewater Power, in Sarnia. A system model is developed using RTDS consisting of the electrical network of the London Hydro headquarters building, the PV-STATCOM, and the motor load. The PV inverter switching circuits are modeled in small time step environment and the control system is modeled in a large time step environment. The performance of the PV-STATCOM is evaluated for different loading conditions of the motor during the night, as well as during the day, at different PV power outputs.

3.2 OVERVIEW OF REAL-TIME DIGITAL SIMULATOR

The RTDS is a custom parallel-processing hardware architecture assembled in modular units called racks. A rack consists of high power processors capable of power system simulations in real-time, along with communication processors. Power system components, along with control systems, are modeled using these processors to solve mathematical equations for the power system and network models. The RTDS operates with real-time simulation software, RSCAD, which has a graphical user interface (GUI) and mathematical solution algorithms for network equations and component models. The GUI allows developers to build power system models using different power system blocks, and also provides a run time environment to analyze the simulation output. RTDS has different types of processor cards available in a rack such as: Three Processor Cards (3PC), Risc Processor Cards (RPC), and

Giga Processor Cards. RTDS also has various I/O cards such as Giga Transceiver cards, Analog I/O cards, and Digital I/O cards. The 3PC card contains three SHARC processors (ADSP21062), each operating at 80MHz. These 3PC cards are used to model power system components and control systems with a large time step of 50μs. RPCs contain two RISC processors (750CXe), each operating at 600MHz; whereas, the GPC contains two IBM PowerPC 750GX RISC processors, each operating at 1GHz. GPCs are typically used to model small time step simulations (< 2μs), such as voltage source converters with high switching frequency, as well as providing simulation for the standard power system components and network models [93]. The RTDS system used in this study has one rack with one GPC card, two 3PC cards, one GTDI card, and one DDAC card.

3.3   STUDY SYSTEM

London Hydro is a utility company in Southwestern Ontario, Canada. Figure 3.1 depicts the London Hydro office building with the induction motor load and the PV solar system indicated at the bottom right of the diagram. The power supply to the main building is through a 13.8kV feeder. This supply is stepped down through transformers in the basement of the building to 600/347 V to feed the 6 kW induction motor and other electrical loads in the building. Separate transformers provide a 208/120V supply for lighting and other small loads within the building.

For the real-time simulation studies of the PV-STATCOM in RTDS for power factor correction, a 6 kW induction motor in the office building of London Hydro, in the city of London, has been selected. The selected induction motor runs as a heat pump in the main building in order to provide for the heating and cooling requirements of the building. Due to its operation at a low power factor (typically 0.75), this motor load by itself will attract a penal tariff. With the objective of demonstrating the new STATCOM control technology on a PV solar system and solving a real-time industrial problem, the 5 kW PV solar system is connected at the terminals of the 6 kW induction motor to improve power factor to unity.
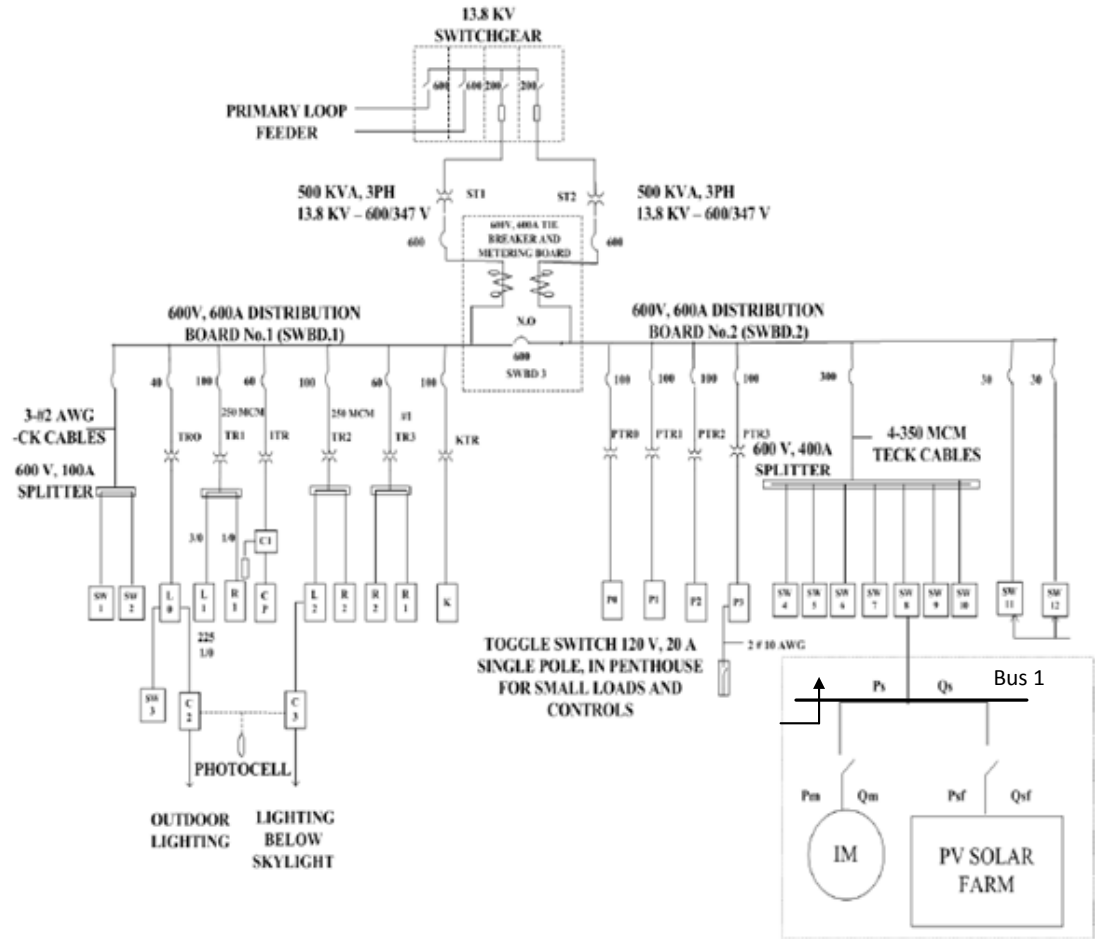
Figure 3.1 Electrical System diagram of London Hydro office building

3.4 MODELING OF THE STUDY SYSTEM

This section presents the models of different components of the study system shown in Figure 3.2. The London Hydro network is modeled as Thevenin's equivalent of the entire London Hydro network looking at the left of Bus 1, as demonstrated in Figure 3.1. I_{ga}, I_{gb}, and I_{gc} represent three phase inverter output currents of a 5 kW PV inverter; I_{La}, I_{Lb}, and I_{Lc} represent 6 kW inductor motor terminal currents. V_{sa}, V_{sb}, and V_{sc} represent three phase source voltages at Bus1 (Point of Common Coupling). V_{DC} represents the inverter DC link voltage which is provided by a 5 kW PV solar system. L_f and C_f both represent the LC filter components, whereas C_{DC} represents the DC link capacitor.
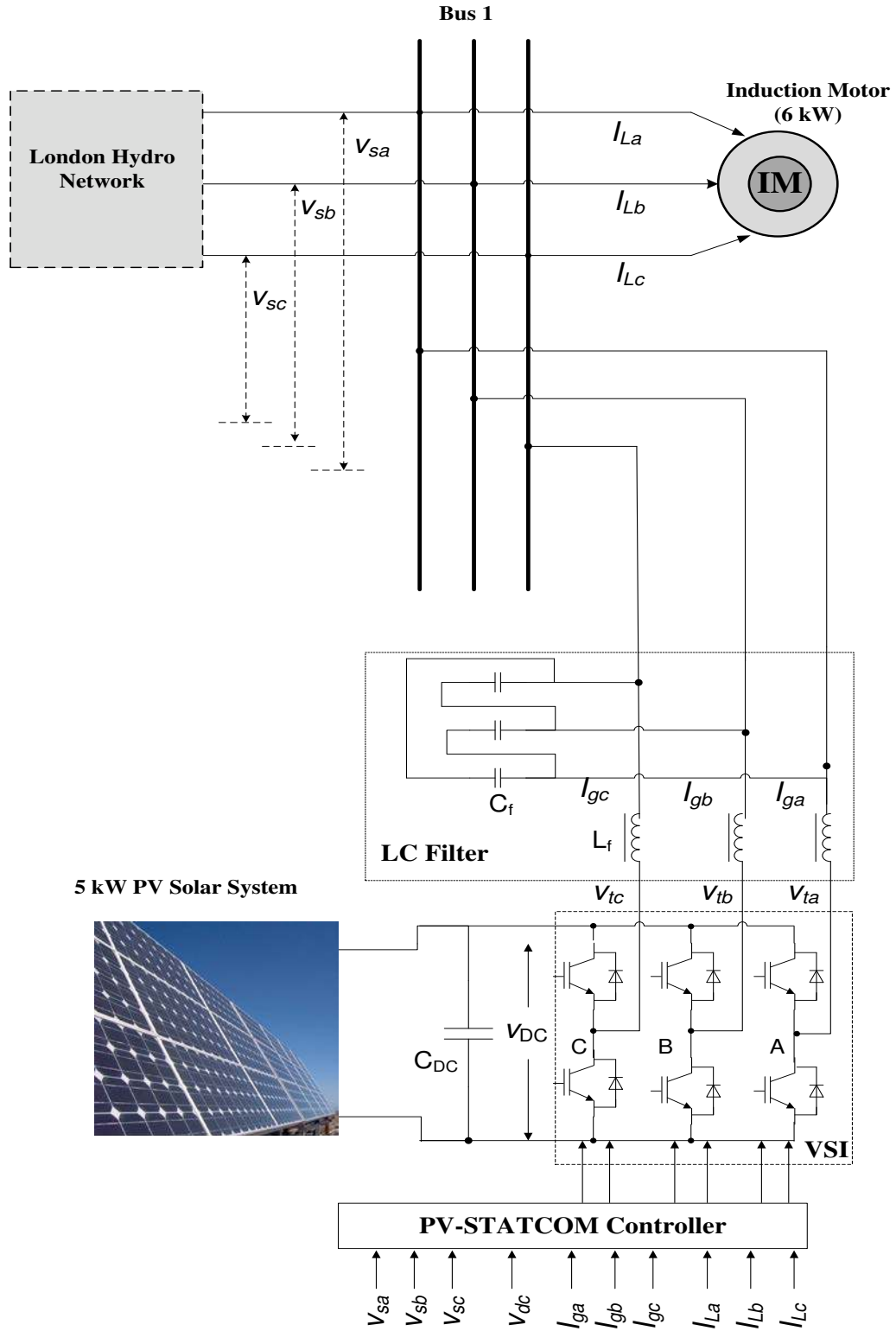
Figure 3.2 Study system in London Hydro headquarters building

3.5   SYSTEM MODELING

3.5.1   London Hydro Network

The London Hydro network is modeled as a Thevenin equivalent voltage source behind the short circuit impedance. The London Hydro network parameters include a short circuit level and X/R ratio, both given in Appendix B.1.

3.5.2   Induction Motor

The induction motor load model provided by the RSCAD system library is utilized for this analysis. For the simulation studies, a 6 kW induction motor is used [89]. The motor model demonstrated in Section 2.3.2 of Chapter 2 is used for the modeling of the induction motor using RTDS. The electrical parameters of the induction motor are given in Appendix B.2.

3.5.3   Photovoltaic System

3.5.3.1   *Photovoltaic Array*

The PV Array model is given in the RSCAD library. It has two power system nodes which allow it to be interfaced with other components in RTDS. Figure 3.3 demonstrates the output positive and negative terminals of the PV array, represented as Nodes P and N, respectively. The connections labeled as INSOLATION and TEMPERATURE are the control signal inputs of the PV model. Increase in the INSOLATION level increases the current output from the PV module, while an increase in TEMPERATURE decreases the voltage output of the PV module [93].
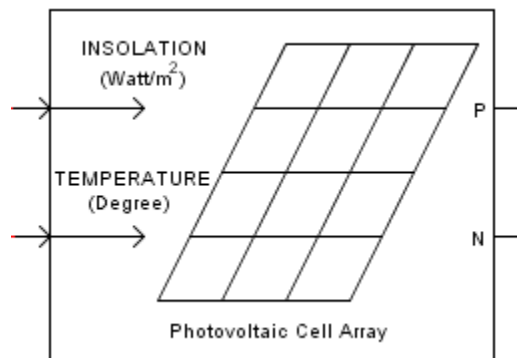
Figure 3.3 Photovoltaic Array model in RSCAD

RTDS has two different time step environments: a large simulation time step and a small simulation time step environment. PV arrays and the network model are modeled in a large time step environment, whereas the inverter is modeled in a small time step environment. In order to interface the small time step environment with the large time step environment, interface transformer components are used to transfer power system signals. As the output of a PV array is effectively DC signals, these interface transformers cannot be used for the PV array because DC signals cannot flow through the transformer. Hence, to construct an interface between two different simulation environments, voltage and current information are used between the two [93]. As demonstrated in Figure 3.4, the voltage signal, $V_{pv,}$ from the large time step side of the PV array simulation is transferred to the small time step side of the PV-STATCOM simulation. The current signal, I_{pv}, from the small time step side of PV-STATCOM simulation is brought to the large time step side of the PV-array. These voltage and current signals are interchanged between the large and small time step portions of the simulation in order to establish the interface between the PV array running in a large time step and the inverter circuit running in a small time step environment.
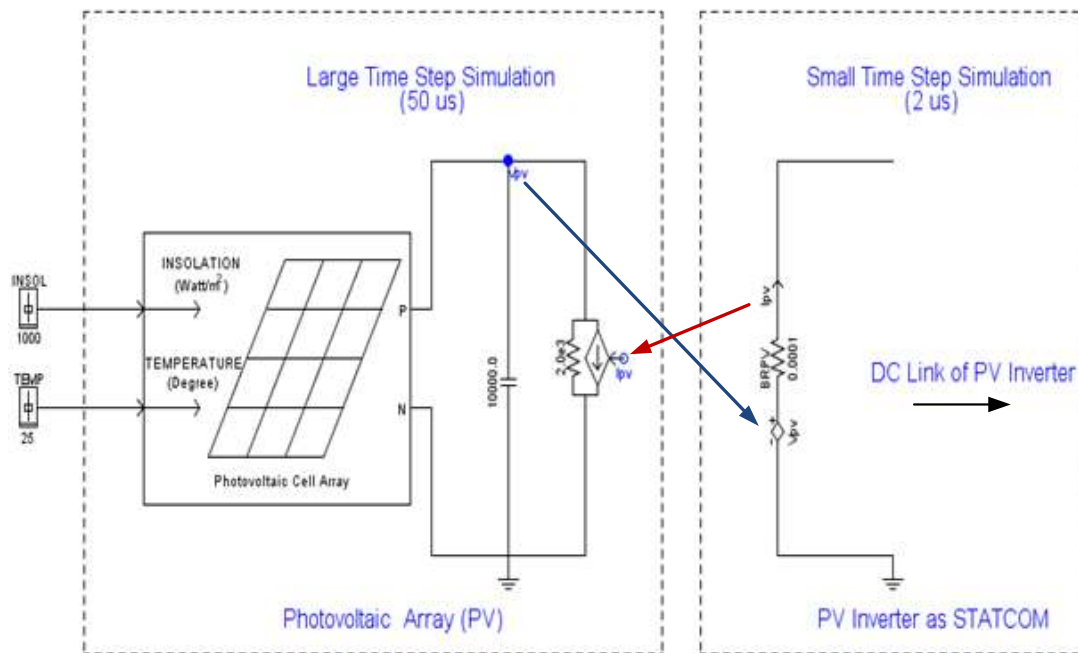
Figure 3.4 Large time step and small time step interaction in RSCAD

Due to the unavailability of adequate computing cards on the RTDS system in our lab, an MPPT algorithm is not implemented for this research work. Hence, all simulations are based on a PV system without MPPT algorithm. PV module parameters are given in Appendix B.3.

3.5.3.2 *Photovoltaic Inverter*

The photovoltaic inverter is modeled using a 2-level, 6-pulse voltage source inverter model, given in RSCAD library, with IGBT switches [93]. IGBT switch parameters, DC link voltage, and DC link capacitor values are taken from a commercial IGBT switching module and are shown in Appendix B.4 [94].   The criteria for designing the DC link voltage and DC link capacitor is presented in Section 2.3.4 of Chapter 2.

3.5.3.3 *LC Filter*

An LC filter is used to mitigate the harmonics generated by the switching events in the PV-STATCOM. The PV-STATCOM uses the Pulse Width Modulated (PWM) current control scheme, where the harmonics are generated around the switching frequency. A switching frequency of 6 kHz is considered for this study. Hence, the current and voltage harmonics are generated in the vicinity of the 6 kHz. Filter parameters L_f and C_f are chosen as per the recommendations given by IEEE benchmark system for power system studies for a PV system [9].

As per [9], [23], for a PWM current controlled inverter, L_f should be chosen between 0.1pu and 0.25pu in order to reduce the voltage drop across the inductor on the AC side, to provide better control of the AC output current of the PV-STATCOM, and to limit the harmonic current at the switching frequency to less than 0.3% [23],[84], [91]. C_f is calculated based on the percentage of reactive power supply from the filter capacitor, which is given as follows.

$$C_f = \frac{\propto \times P_{rated}}{3 \times \omega \times V_{pn}^{2}} \tag{2.1}$$

Where, $\propto$ represents the percentage of reactive power to be injected from the filter capacitor, P_{rated} is the rated power of the PV-STACOM. ω represents the system frequency in rad/sec. V_{pn} is the phase-to-neutral voltage of the network. Based on the value of L_f and C_f, the resonant frequency of the filter is calculated such that it is sufficiently larger than the grid

nominal frequency of 60Hz, but considerably smaller than the VSC switching frequency of 6kHz. The resonant frequency of the LC filter with grid inductance L_g is given as:

$$f_{res} = \frac{1}{2\pi} \times \sqrt{\frac{L_g + L_f}{L_g \times L_f \times C_f}} \tag{2.2}$$

$$10 \times f_g \leq f_{res} \leq 0.5 \times f_{sw} \tag{2.3}$$

Where f_g and f_{sw} represent the grid frequency and switching frequency of the PV-STATCOM. The LC filter is effective if proper damping is also provided. Hence, a damping resistor is used in conjunction with the capacitor. Resistor size is chosen as one third of the capacitor impedance at resonant frequency [9]. The calculated filter parameters L_f, C_f and R_d are refined through simulations in order to achieve I_{THD}, I_{TDD}, and V_{THD} below 5%, as recommended in [84], [91]. The Filter parameters used in the RTDS simulations are given in Appendix B.4. The complete system model in RSCAD is given in Appendix B.5.

3.6 PV-STATCOM CONTROLLER

The PV-STATCOM is essentially a VSC (Voltage Source Converter) system, in which the controller operates in two different modes: power factor correction mode and AC voltage regulation mode. Both of these modes are mutually exclusive, which means that the controller can operate in any one of the modes at a given time. During power factor correction mode and voltage regulation mode, the PV-STATCOM exchanges reactive power with the network along with injecting available active power from the PV system to the grid. The active power and reactive power are controlled through the phase angle and the amplitude of the VSC terminal voltage with respect to the PCC voltage. The proposed PV-STATCOM controller has one inner current control loop and multiple outer control loops, depending upon the application of the PV-STATCOM. The outer control loops can be DC voltage control loop, PV solar array output, AC voltage control loop, and power factor control loop. In this section, power factor control is discussed in detail as relevant to this thesis work, and the rest of the controller design has been taken from my colleague's work [95]. Figure 3.5 depicts the overall PV-STATCOM controller. The different subsystems of the PV-STATCOM are explained in next section.
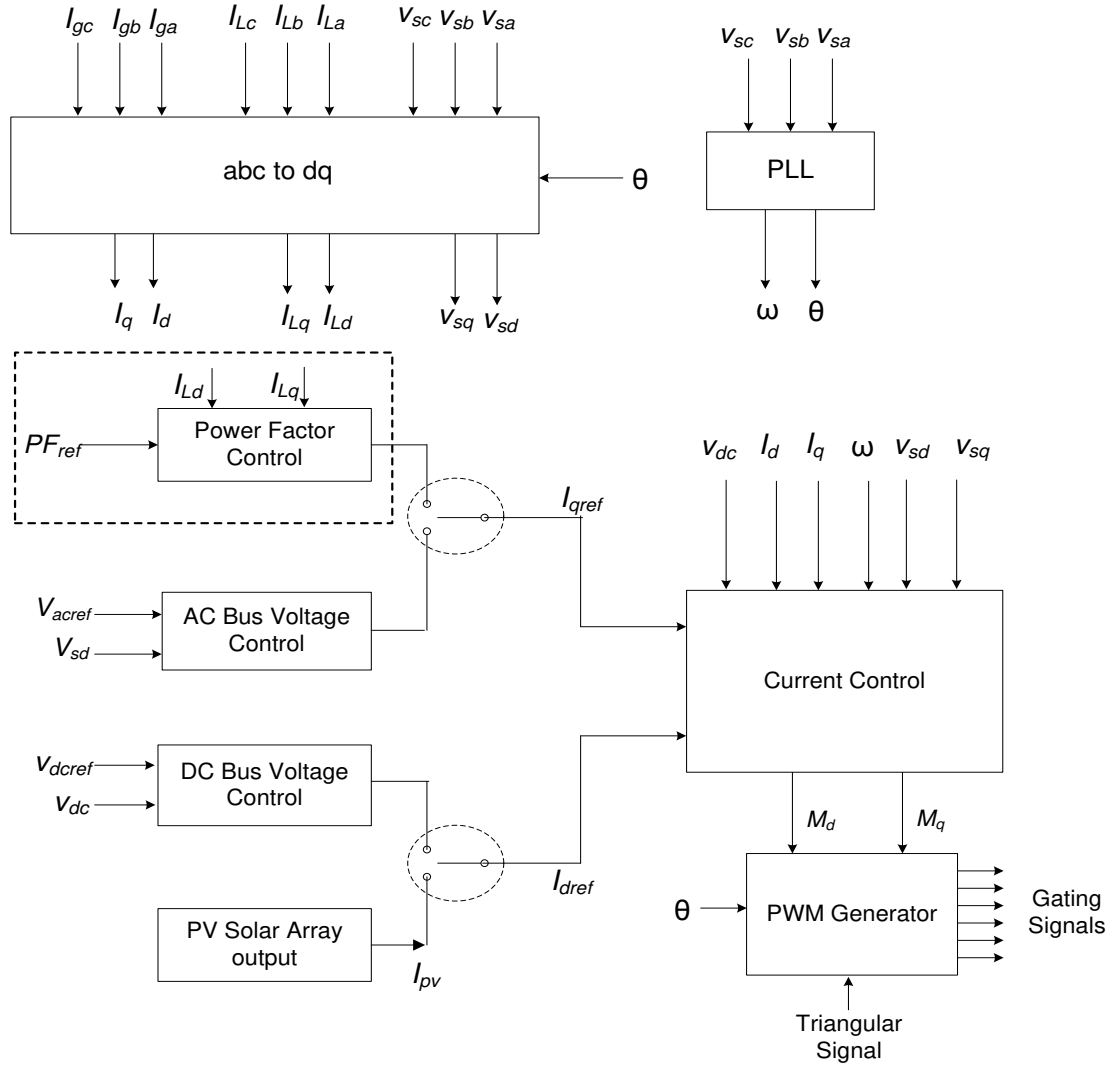
Figure 3.5 Control system of PV-STATCOM

3.6.1   abc to dq conversion

The PV-STATCOM controller is modeled in a synchronously rotating d-q reference frame, where d represents the direct axis component and q represents the quadrature axis component in the d-q reference frame. The abc to dq transformation enables the control system of a three-phase converter system to process DC signals rather than sinusoidal voltage and current signals, in a three-phase system. In a d-q frame the signals and variables are transformed to equivalent DC quantities, allowing the control system to be simple and easy to control [19].

$$\begin{bmatrix} V_d \\ V_q \\ V_0 \end{bmatrix} = \sqrt{\frac{2}{3}} \begin{bmatrix} \cos\theta & \cos(\theta - \frac{2\pi}{3}) & \cos(\theta + \frac{2\pi}{3}) \\ -\sin\theta & -\sin(\theta - \frac{2\pi}{3}) & -\sin(\theta + \frac{2\pi}{3}) \\ \frac{\sqrt{2}}{2} & \frac{\sqrt{2}}{2} & \frac{\sqrt{2}}{2} \end{bmatrix} \begin{bmatrix} V_a \\ V_b \\ V_c \end{bmatrix} \quad (3.1)$$

Where θ represents the voltage angle at the Point of common coupling.

If it is assumed that the three-phase quantities are symmetrical, then the zero sequence component becomes zero, and active and reactive power in the d-q reference frame is given by [19],

$$P = \frac{3}{2} (V_d I_d + V_q I_q) \quad (3.2)$$

$$Q = \frac{3}{2} (V_q I_d - V_d I_q) \quad (3.3)$$

Since the synchronization scheme ensures that the d axis of the d-q frame is aligned with the grid voltage reference phasor, that is $V_q = 0$, then P and Q can be controlled by I_d and I_q respectively [9]. For the PV-STATCOM controller, three phase voltages at PCC (V_{sa}, V_{sb}, $V_{sc)}$, three PV inverter output currents (I_{ga}, I_{gb}, $I_{gc)}$, and three load currents (I_{La}, I_{Lb}, $I_{Lc)}$ are transformed to their d-q equivalents using the abc-dq transformation method.

3.6.2   Phase Locked Loop (PLL)

A Phase Locked Loop (PLL) produces an output signal that is synchronized in phase and frequency of the input signal. A PV-STATCOM controller designed using a d-q reference frame requires a PLL in order to track the voltage angle of the AC system at the PCC (point of common coupling) to synchronize with the grid. As shown in Figure 3.5, PLL generates an angle, θ based on the input grid voltages. The PLL model given in the RSCAD library is used in the controller design [90].

3.6.3   Power Factor Control

Figure 3.6 depicts the power factor correction unit. This unit generates I_{qref} based on the reference power factor PF_{ref}. I_{Ld} and I_{Lq} represent the real and reactive currents drawn by the load. I_{Lqnew} represents the new reactive current to be drawn by the load from the London Hydro supply system, based on reference power factor PF_{ref} . I_{Lqnew} is calculated using:

$$I_{Lqnew} = I_{Ld} \times tan(\cos^{-1}(PF_{ref})) \qquad (3.8)$$

I_{Lqnew} is subtracted from I_{Lq} to generate I_{Sq}, which represents the required reference reactive current for the current control module in order to make the desired power factor PF_{ref} at the PCC. Q_c represents the three-phase reactive power generated by the filter capacitor. I_{Cq} represents the reactive current injected by the filter capacitor in d-q reference frame. As per (3.3) in Section 3.5.1, I_{Cq} is calculated as follows:

$$I_{Cq} = \frac{-2 \times Q_c}{3 \times V_{sd}} \qquad (3.9)$$

Now, I_{Cq} is subtracted from I_{Sq} in order to generate the required $I_{qref.}$ ω represents the system frequency in rad/s, and C_f represents the filter capacitance.
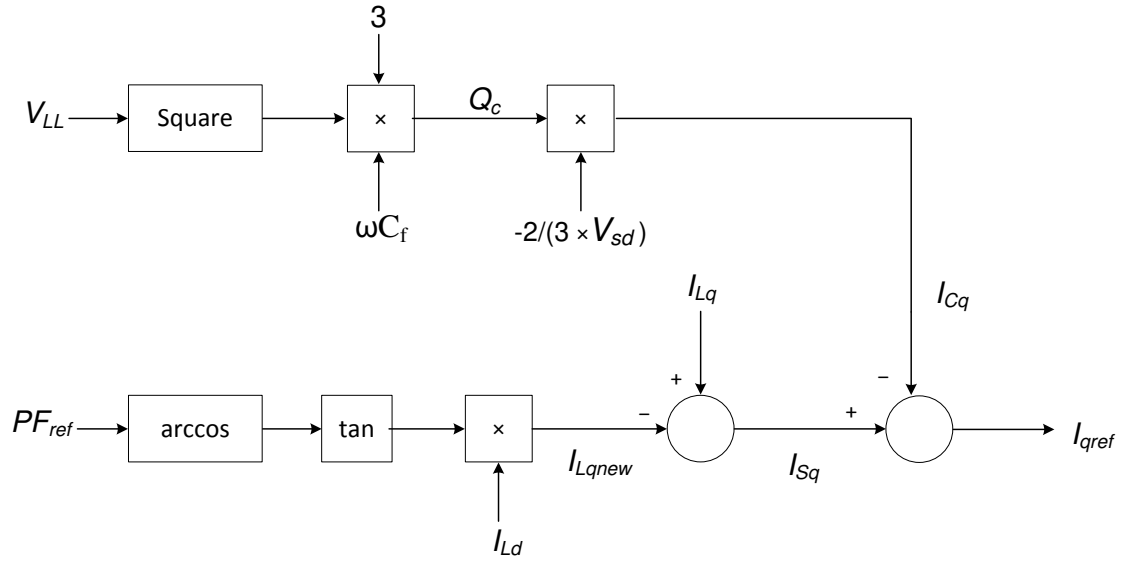
Figure 3.6 Power factor controller

3.6.4   AC Bus Voltage Control

Figure 3.7 describes the AC bus voltage controller. The AC bus voltage control compares the PCC bus voltage V_{sd} with the given reference value V_{acref}. The error is then fed to an integral controller in order to generate I_{qref} to achieve the desired PCC bus voltage. T_{iac} represents the integral controller time constant and its parameter, given in Appendix B.6.
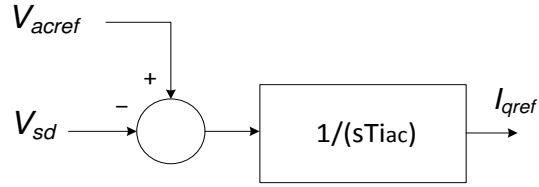
Figure 3.7 AC Bus voltage controller

3.6.5 DC Bus Voltage Control

The DC bus voltage control shown in Figure 3.8 uses a lead-lag compensator in order to generate the reference current, $I_{dref,}$ to control the DC link voltage to a desired value. For this study, the desired value of the DC link of the PV inverter is chosen as 400V DC. The DC Bus voltage controller parameters G, T_{dc}, $T_{Ld,}$ and T_{Lg} parameters are given in Appendix B.6.
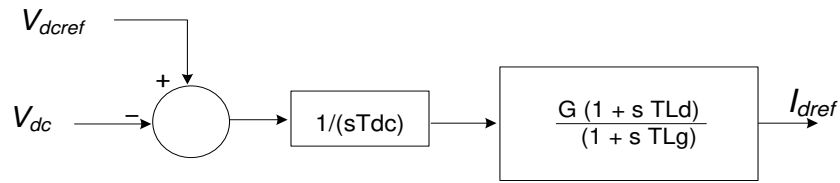
Figure 3.8 DC Bus voltage controller

3.6.6 PV Solar Output

The PV solar output module represents the 5 kW PV solar array model given in the RSCAD/RTDS library. As an MPPT controller is not implemented in this study, this module generates I_{pv} based on the available solar insolation for the current control unit.

3.6.7 Current Control

Figure 3.9 depicts the current control unit for the PV-STATCOM controller. The current control unit is the core element of the PV-STATCOM controller. It has two control loops that independently control the direct axis and quadrature axis components of the VSC currents I_d and I_q in the d-q reference frame, to generate the direct axis and quadrature axis voltage components (V_{sd}, V_{sq}) of the VSC terminal voltage. In each control loop, the inverter output current signals, I_d and $I_{q,}$ are taken and fed back to the controller. This is compared to the reference values I_{dref} and I_{qref}, generated from the outer control loops as described above. The

error signals are then fed to the PI controllers. These PI controllers with identical gains, generate output voltage signals in both direct and quadrature axes, which are added with respective direct and quadrature axis components of the grid voltage (V_{sd}, V_{sq}) and coupling elements $\omega L_f I_q$ and $\omega L_f I_d$ in order to generate inverter terminal voltages (V_{td}, V_{tq}) respectively. V_{td} and V_{tq} represent the inverter terminal voltage in the d-q reference frame. The current controller, shown in Figure 3.9, is taken from page 126 of [19].
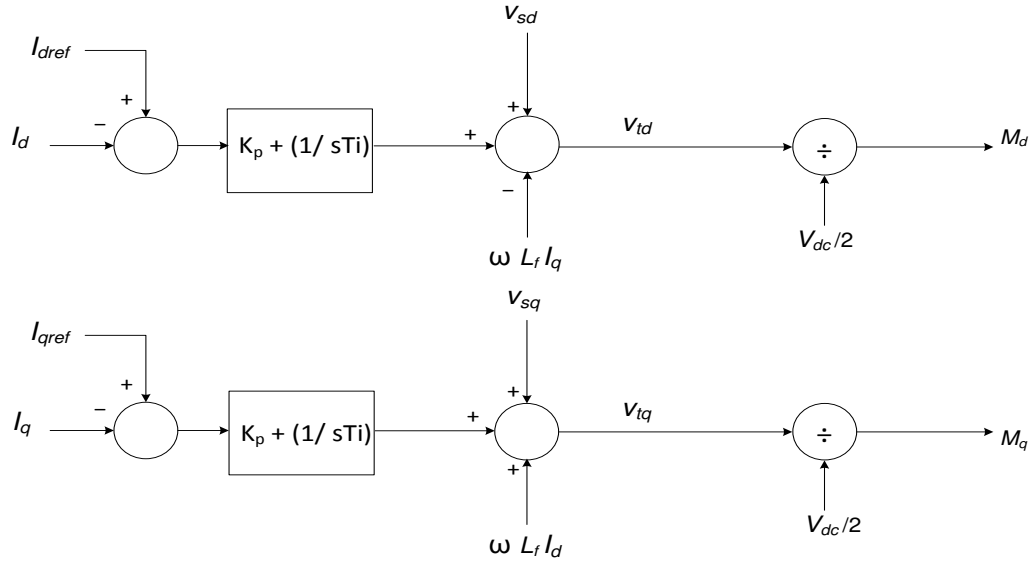
Figure 3.9 Current controller for PV-STATCOM

The d-axis and q-axis components of the VSC AC side terminal voltages V_{td} and V_{tq} are linearly proportional to the corresponding components of the modulating signals, with a proportionality constant of $V_{dc}/2$, as given by the following equations [19]:

$$M_d = \frac{V_{td}}{V_{dc/2}} \tag{3.6}$$

$$M_q = \frac{V_{tq}}{V_{dc/2}} \tag{3.7}$$

These inverter terminal voltages are divided by $V_{dc}/2$ in order to generate modulating signals (M_d, M_q) in the d-q reference frame. The controller parameters K_p and T_i are given in Appendix B.6.

3.6.8   Pulse Width Modulation Generator

A pulse width modulation (PWM) generator uses PLL output θ to convert modulating signals (M_d, M_q) in the d-q reference frame into three sinusoidal modulating signals that are 120^0 apart from one another using dq to abc transformation. These modulating signals are fed to the RSCAD firing pulse generation module. This module compares the modulating signals with triangular waves at 6 kHz to generate the gating signals for the VSC switches modeled in small signal time step environment [93].   Sinusoidal PWM voltage modulation is employed for the RTDS simulation due wide range of application of this control method in various commercial PV inverters [20]-[22].

3.7   SELECTION OF CONTROLLER PARAMETERS

The best choices of the gain K_p and T_i for the current controller are chosen by studying the controller performance for different K_P and T_i values during both night and day. Initially, K_P = 0.5 and T_i = 2 ms are chosen for the simulation. Then, K_P is varied over a wide range keeping $T_{i\ =}$ 2 ms fixed and the PV-STATCOM response is obtained for the different gains. The K_P value giving the fastest response time is selected for the study system. With this best K_P value, the controller response is obtained for varying T_i. This process is followed for both night and day. The specific T_i value which gives the fastest response is then selected for the controller. A similar procedure is followed to find the best gains for the DC voltage control loop, K_{pd} and T_{id}.   Time constant (T_{iac}) for the AC Bus voltage control unit and controller parameters (G, T_{dc}, $T_{Ld,}$ and T_{Lg}) are taken from my colleague's work [95].

Figure 3.10 (a)-(e) depict the PV-STATCOM controller response for K_p = 0.5, 2, 10, 18, and 20, respectively, during the day, at 4 kW PV generation with 50% loading condition of the motor. It is shown that the best response is achieved with a K_P = 2. With this K_P and T_i = 2 ms, the controller responds in 10ms. With high K_P values, the response of the controller becomes slower and the controller finally becomes unstable at a K_P = 19. Figure 3.11 (a)-(d) depict the PV-STATCOM controller response during the day, at 4 kW PV generation with a 50% loading condition of the motor. It is shown that best response of 17 ms is achieved at K_P = 2 and Ti = 2 ms.
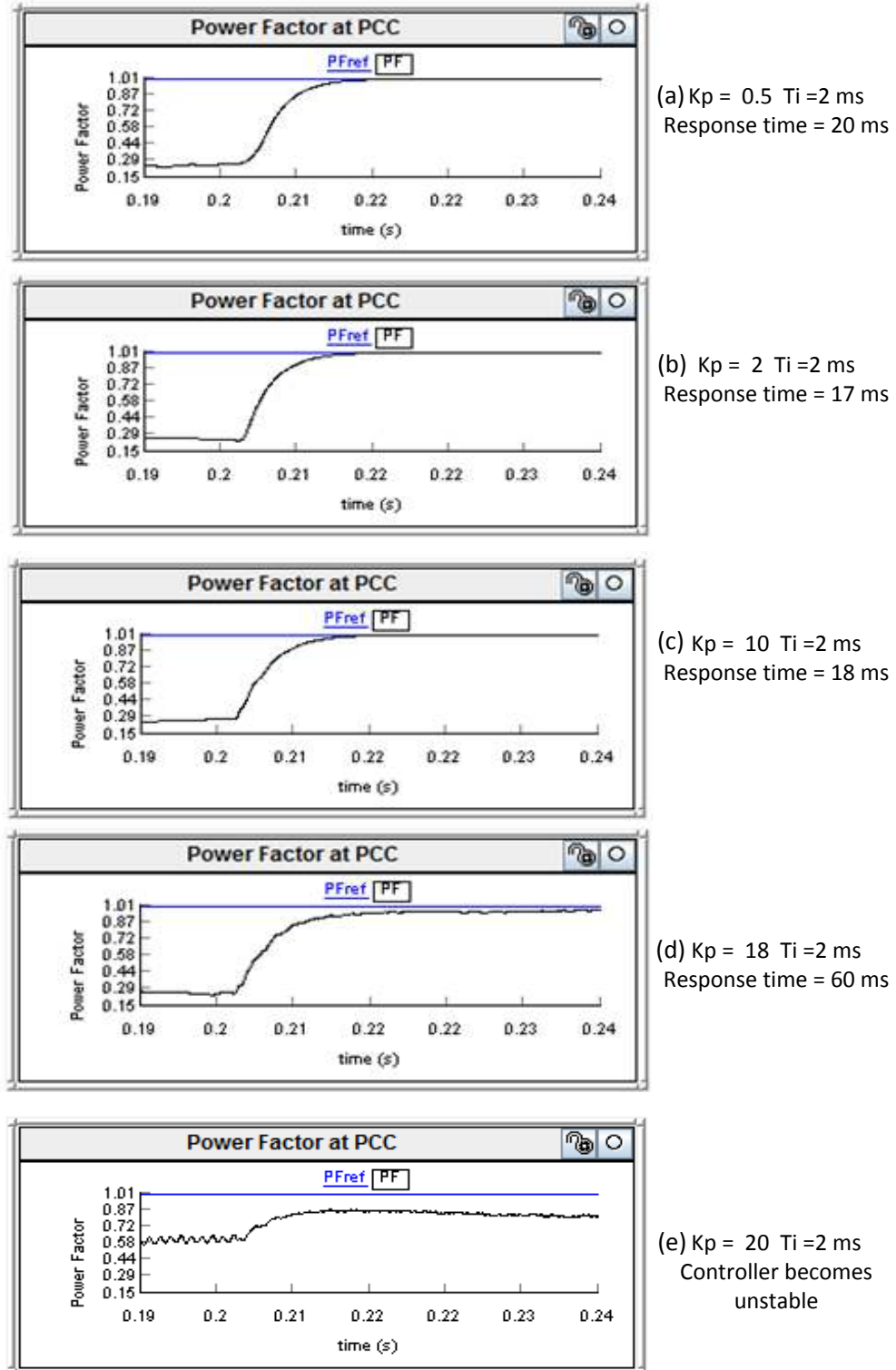
Figure 3.10 PV-STATCOM controller response with varying K_p during the light load condition with 4 kW PV generation
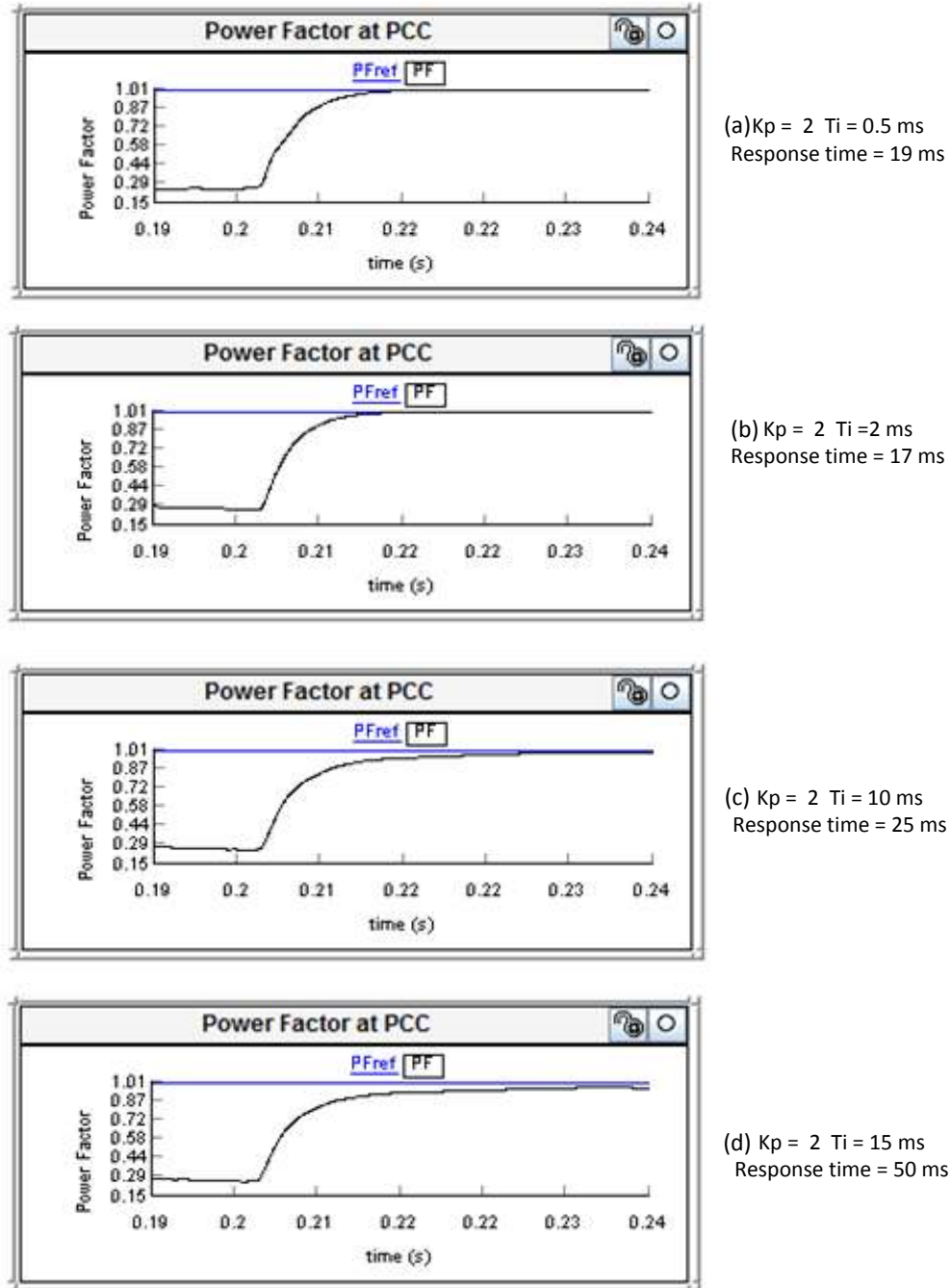
Figure 3.11 PV-STATCOM controller response with varying T_i during the light load condition with 4 kW PV generation

Figure 3.12 and Figure 3.13 represent current controller response for a wide range of K_P and T_i during the day, for both light load and peak load conditions with a PV generation of 4 kW. It is depicted that during day, for both loading conditions, the best gains are found to be $K_P = 2$ and $T_i = 2$ ms, respectively. With these parameters, the response of the controller is 10ms

for the light load condition and 17ms for the peak load condition. Figure 3.14 and Figure 3.15 demonstrate the response of the current controller during the night when the PV-STATCOM operates in STATCOM mode. It is seen that during the night, for both loading conditions, the best parameters are found to be $K_P = 2$ and $T_i = 2$ms. With these parameters, the best response of the controller is 9.8ms for a light load condition and 10.2ms for a peak load condition.
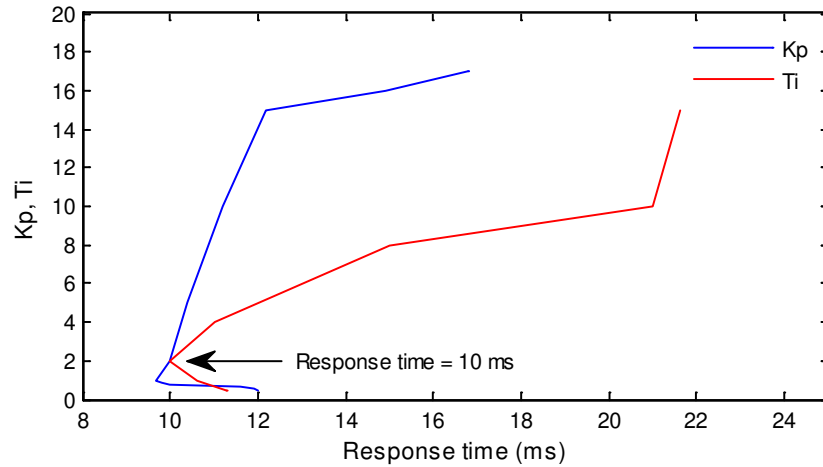
Figure 3.12 Controller parameters with varying K_p and T_i Day time with PV solar generation = 4 kW and motor operating at light load
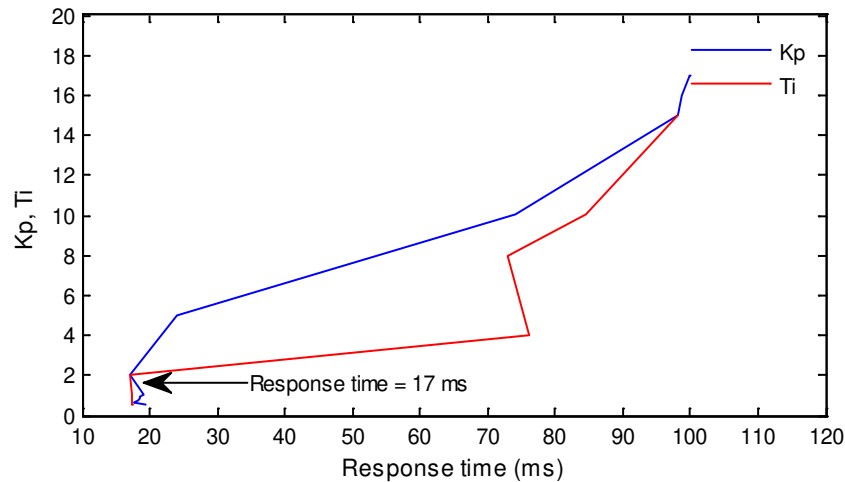
Figure 3.13 Controller parameters with varying K_p and T_i Day time with PV solar generation = 4 kW and motor operating at peak load
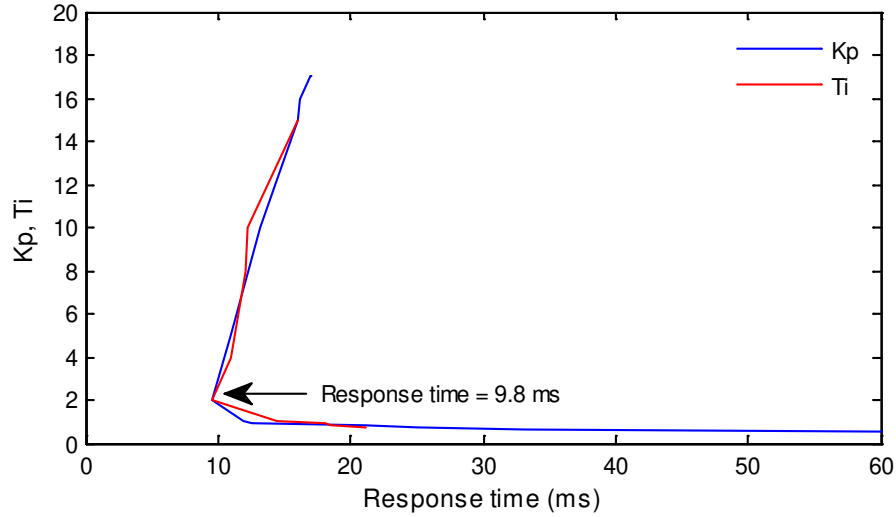
Figure 3.14 Controller parameters with varying K_p and T_i nighttime with STATCOM mode and motor operating at light load
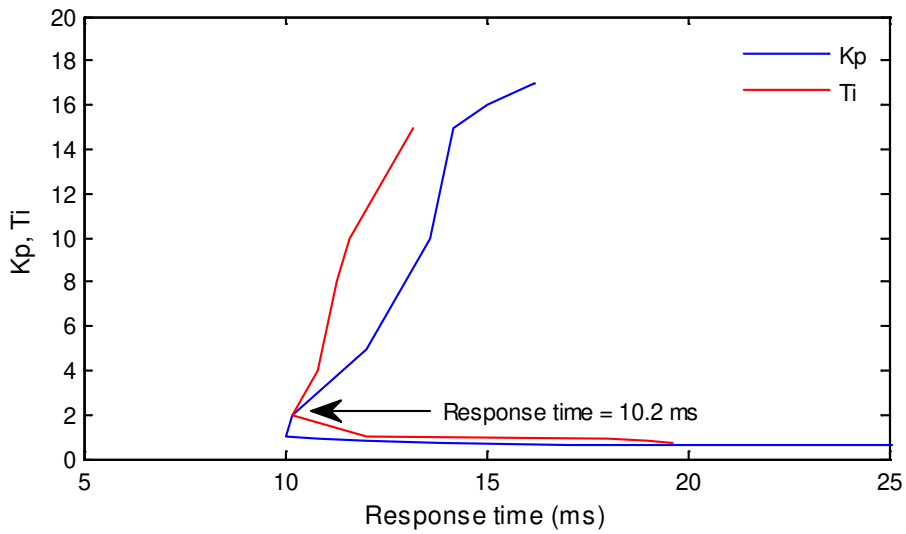
Figure 3.15 Controller parameters with varying K_p and T_i nighttime with STATCOM mode and motor operating at peak load

From the above studies, it is found that the best parameters for the current controller, K_P and T_i do not change for different operating scenarios of the PV-STATCOM. Hence, $K_P = 2$ and $T_i = 2ms$ are chosen for the PV-STATCOM current controller.

3.8   PV-STATCOM PERFORMANCE FOR POWER FACTOR CORRECTION

The performance of the PV-STATCOM controller developed using RTDS is demonstrated both during night and day; with different PV power outputs of 2 kW and 4 kW during 80% and 50% loading scenarios. The PV-STATCOM controller operation is presented for a time interval from 0.15 seconds to 0.3 seconds for all of the test scenarios during the night and day. During the time $0.15 \leq t \leq 0.2$, the controller operates in voltage regulation mode (this work is done by my colleague which is presented in [95]). At t=0.2 seconds, the PV-STATCOM controller is given a step input to operate in power factor correction mode.

3.8.1   Nighttime operation

Two different loading scenarios are considered for analysis to verify the controller performance during the nighttime; one at 80% loading condition and another at 50% loading condition. It is noted that the PV-STATCOM operates as STATCOM during the night and it draws a small amount of real power from the source to compensate for inverter losses.

3.8.1.1   *Case 1 (80% loading)*

Figure 3.16 depicts power drawn by the motor during a peak load (80%) condition. At 80% loading condition, the real power and reactive power drawn by the motor are 5 kW and 3.4 kvar, respectively. It is seen that real and reactive power of the motor is increased to 5.08 kW and 3.5 during the power factor correction mode. This is due to the increase in motor terminal voltage from 123.2V (1.026pu) to 125.4V (1.045pu) during power factor correction.
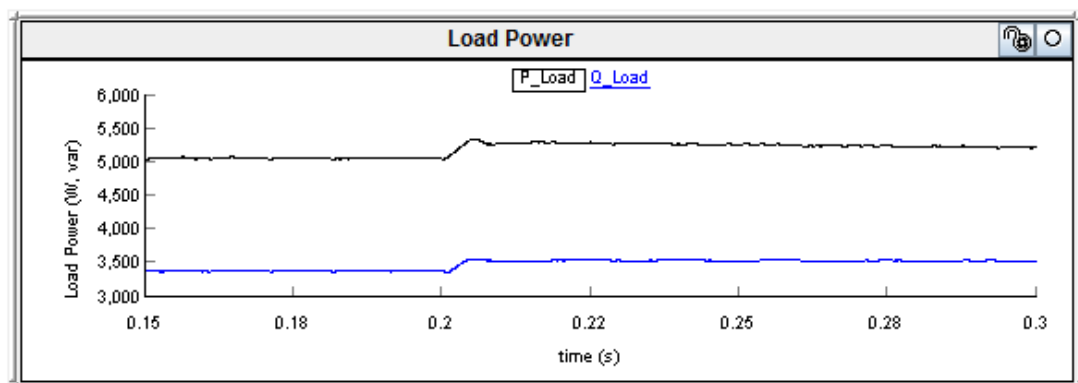
Figure 3.16 Motor power during peak load

Figure 3.17 depicts RMS voltage at the PCC before and after power factor correction.
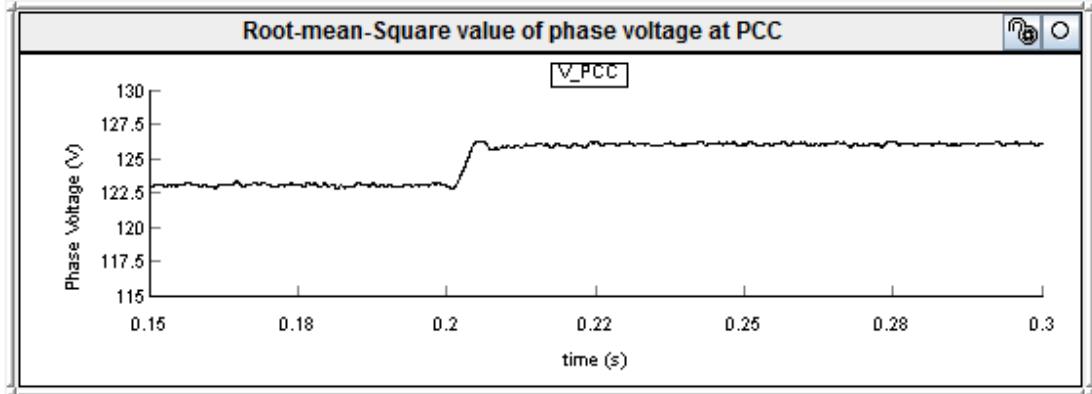
Figure 3.17 PCC voltage before and after power factor correction

Figure 3.18 shows the PV-STATCOM output power during voltage regulation mode and power factor correction mode. As the PV solar system operates as STATCOM during the night, it draws only a small amount of real power from the grid to regulate the DC link voltage to 400V. Hence, during the time $0.15 \leq t \leq 0.2$, the real power from PV system P_Statcom is -60 W and the reactive power from the PV inverter Q_Statcom is 250var, to regulate PCC voltage. At time $t \geq 0.2$ seconds, the controller injects 3.51kvar to entirely compensate the load reactive power requirement operating in power factor correction mode. At time $t \geq 0.2$ seconds, when the transient period dies out, P_Statcom and Q_Statcom are -80 kW and 3.51 kvar, respectively. The requirement of P_Statcom increases in power factor correction mode to compensate for the PV inverter losses.
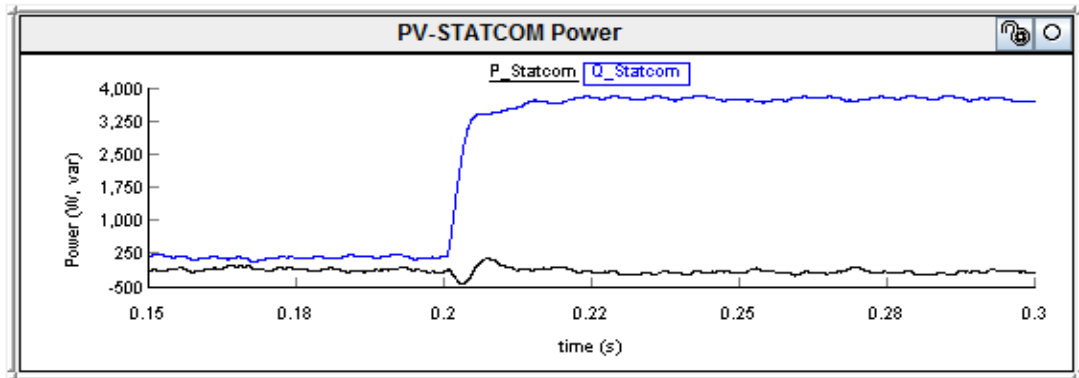
Figure 3.18 PV-STATCOM power at 80% loading condition during the night

Figure 3.19 depicts the source power at PCC. During the time $0.15 \leq t \leq 0.2$, P_Source (P_Load + P_Statcom) and Q_Source (Q_Load - Q_Statcom) are 5.06 kW and 3.15 kvar, respectively as the real and reactive power requirement of the load is 5 kW and 3.4 kvar, respectively. At time $t \geq 0.2$ seconds, P_Load and Q_Load are increased to 5.08 kW and 3.5 kvar. Hence, P_Source supplies 5.16 kW to the load and to compensate for additional losses of the PV-STATCOM. Similarly, Q_Source becomes -10 var due to a 3.51 kvar injection from the PV-STATCOM. Figure 3.20 depicts the DC link voltage of the PV inverter, maintained at 400V DC during both modes of operation.
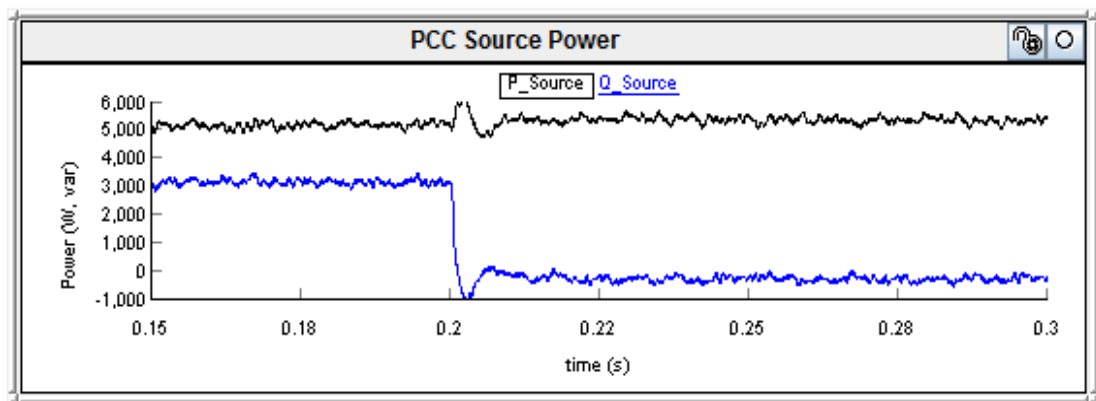
Figure 3.19 Source power at PCC at 80% loading condition during the night
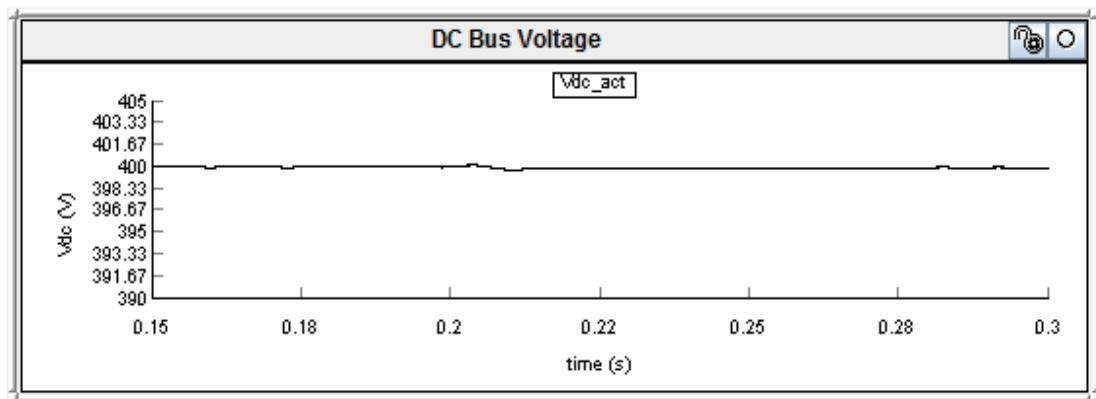
Figure 3.20 DC link voltage of PV Inverter at 80% loading condition during the night

Figure 3.21 depicts the grid PCC power factor during voltage regulation mode and power factor correction mode. During the night, there is no PV power and the PV-STATCOM works in STATCOM mode to regulate the grid voltage to operate within ± 6%, as per the utility requirement. Load power factor at this loading condition is 0.82 ($\cos(\tan^{-1}(\frac{Q\_Load}{P\_Load})$)).

However, PCC power factor improves to 0.85 due to a small amount of reactive power injection from the PV-STATCOM during voltage regulation mode. At t=0.2 seconds, the PV-STATCOM controller is given a reference of PF_{ref}=1 to regulate the power factor to unity. It is seen that at time t ≥ 0.2 seconds, the controller injects 3.51 kvar within 10.2ms to entirely compensate the load reactive power requirement. Thus, PCC power factor improves to unity.

Figure 3.22 demonstrates the PCC voltage and current waveform during both modes of operation. It is observed that during the power factor correction mode at time t ≥ 0.2 seconds, PCC voltage and current are in phase, thus confirming the unity power factor at PCC.
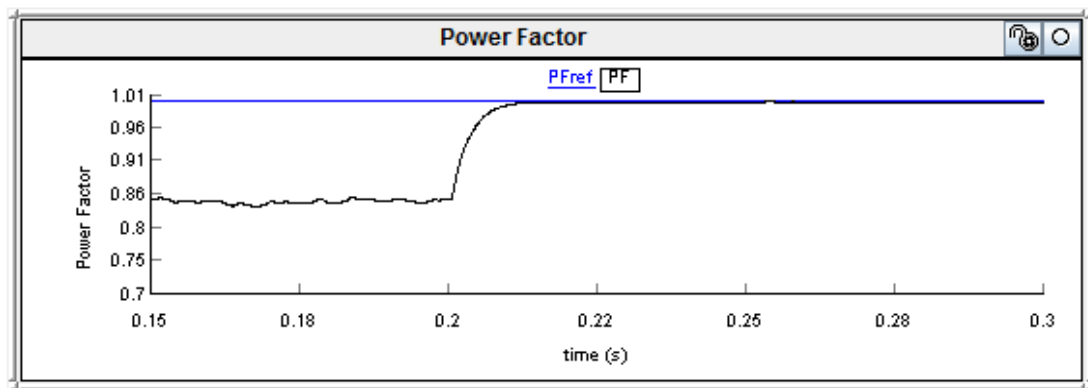
Figure 3.21 PCC Power factor correction at 80% loading condition during the night
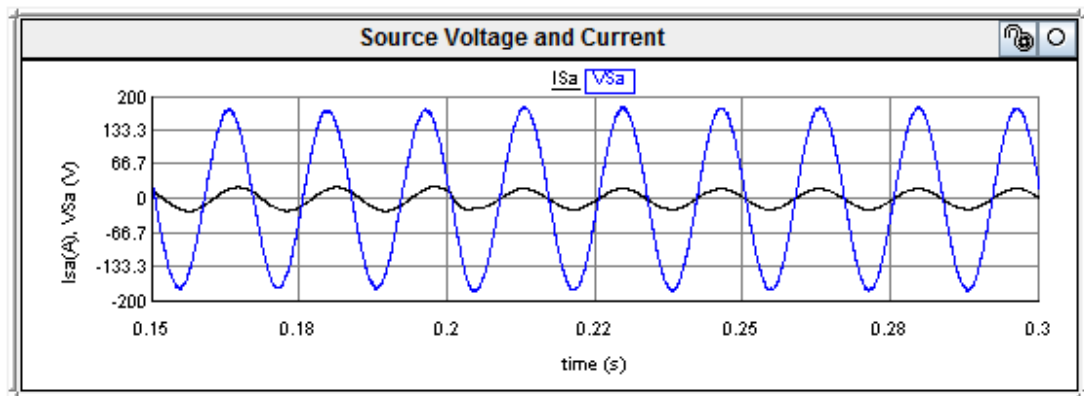
Figure 3.22 PCC voltage and current waveform at 80% loading condition during the night

Figure 3.23 demonstrates the PV-STATCOM output current; which is sinusoidal in nature. To verify the harmonics output from the PV-STATCOM output current, the total voltage harmonics distortion and the total current demand distortion are calculated at PCC, and are

found to be 1.9% and 5.8% respectively which are within the specified limits of IEEE 519 [84] .
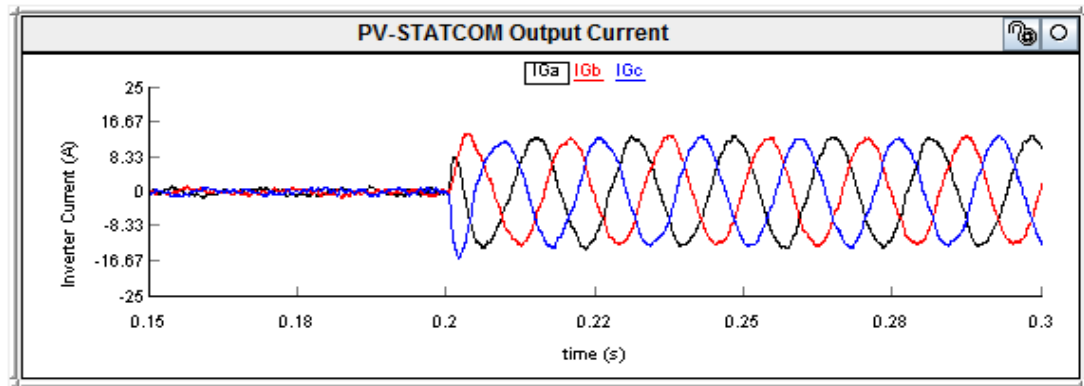
Figure 3.23 PV-STATCOM output current at 80% loading condition during the night

3.8.1.2   *Case 2 (50% loading)*

Figure 3.24 shows the real and reactive power drawn by the motor at a 50% loading condition with a load power factor of 0.69. The real and reactive power values at a 50% loading condition are 3 kW and 3.1 kvar, respectively. It is seen that real and reactive power drawn by the motor increases to 3.16 kW and 3.26 kvar, respectively, during the power factor correction mode. This is due to the increase in motor terminal voltage from 124V (1.031pu) to 126.6V (1.055pu) during power factor correction. Figure 3.25 depicts the RMS voltage at the PCC before and after power factor correction.

Figure 3.26 demonstrates the PV-STATCOM output power during voltage regulation mode and power factor correction mode. During the voltage regulation mode, it injects Q_Statcom of 180var to the grid in order to regulate the grid voltage. During power factor correction mode, it injects 3.27 kvar to compensate for the load reactive power to make PCC power factor unity. P_Statcom is -80W during voltage regulation mode and becomes -100W in power factor correction mode, to compensate for the PV inverter losses.

Figure 3.27 depicts the source power at PCC at a 50 % loading condition. During the time $0.15 \leq t \leq 0.2$, P_Source (P_Load + P_Statcom) and Q_Source (Q_Load - Q_Statcom) are 3.08 kW and 2.92 kvar, respectively, as the real and reactive power requirement of the load is 3 kW and 3.1 kvar, respectively. At time $t \geq 0.2$ seconds, P_Load and Q_Load are increased

to 3.16 kW and 3.26 kvar. Hence, P_Source supplies 3.26 kW to the load, and to compensate for additional losses of the PV-STATCOM. Similarly, Q_Source becomes -10 var due to a 3.27 kvar reactive power injection from the PV-STATCOM.
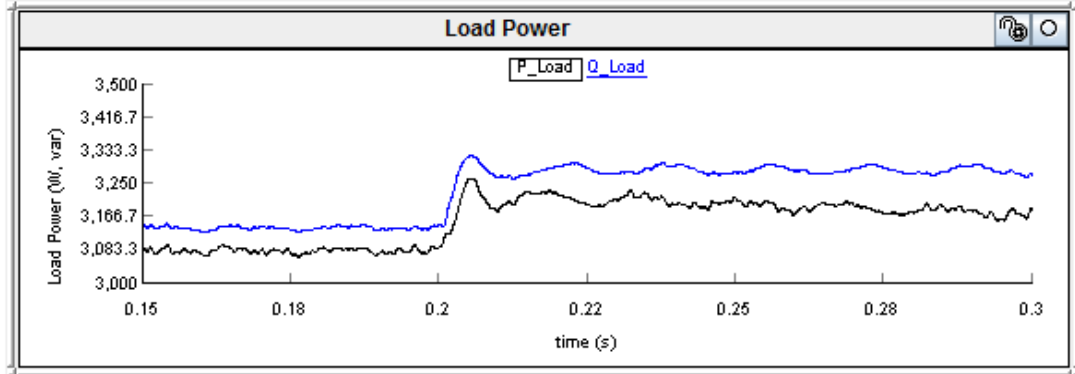
Figure 3.24 Motor power during light load

Figure 3.25 PCC voltage before and after power factor correction
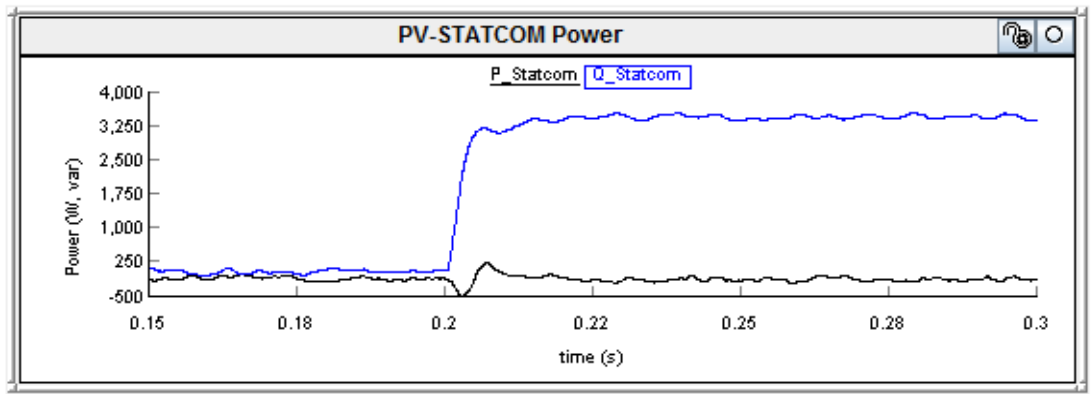
Figure 3.26 PV-STATCOM output power at 50% loading condition during the night
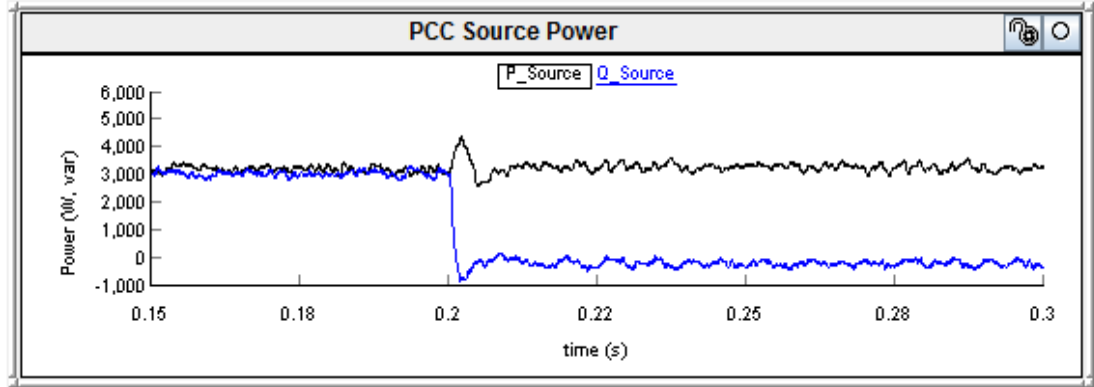
Figure 3.27 Source power at PCC at 50% loading condition during the night

Figure 3.28 depicts the DC link voltage of PV inverter, maintained at 400V DC during both modes of operation.

Figure 3.29 describes the PCC power factor during voltage regulation mode and power factor correction mode. During $0.15 \leq t \leq 0.2$, the controller is in voltage regulation mode, and the grid power factor improves to 0.72 due to a small reactive power injection from the PV inverter. At t=0.2 seconds, the PV-STATCOM controller is given a reference $PF_{ref} = 1$ to regulate the power factor to unity. It is shown that controller responds within 9.8ms to regulate the power to unity by injecting 3.27 kvar to the load.
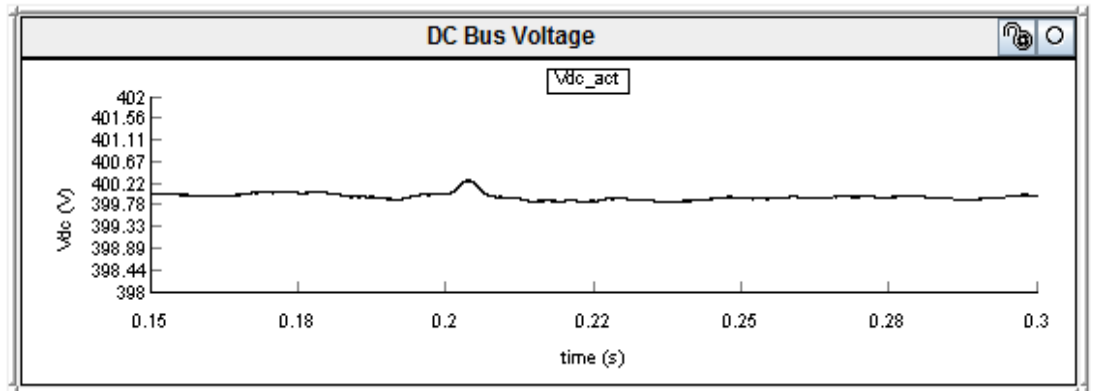
Figure 3.28 DC link voltage of PV Inverter at 50% loading condition during the night
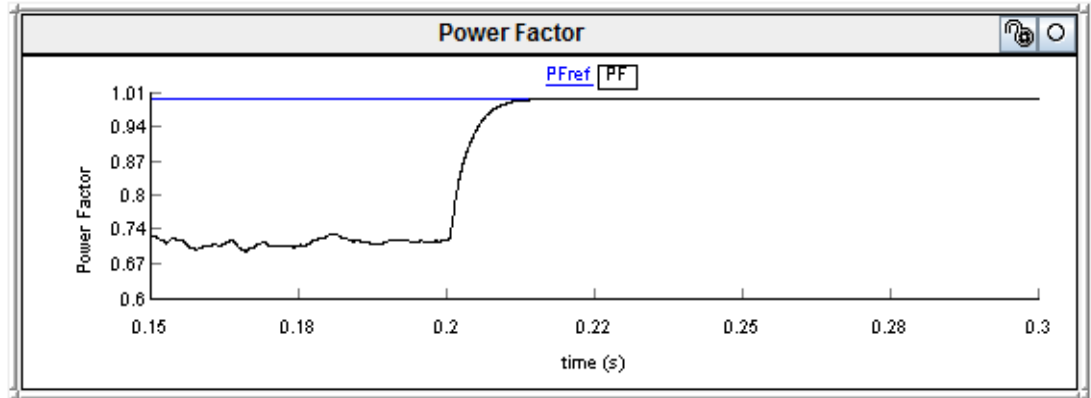
Figure 3.29 PCC Power factor correction at 50% loading condition during the night

Figure 3.30 demonstrates the PCC voltage and line current. It is observed that during the power factor correction mode, at time t ≥ 0.2 seconds, PCC voltage and current are in phase, thus confirming the unity power factor at PCC. Figure 3.31 demonstrates the PV-STATCOM output current, which is sinusoidal in nature.

Figure 3.30 PCC voltage and current at 50% loading condition during the night
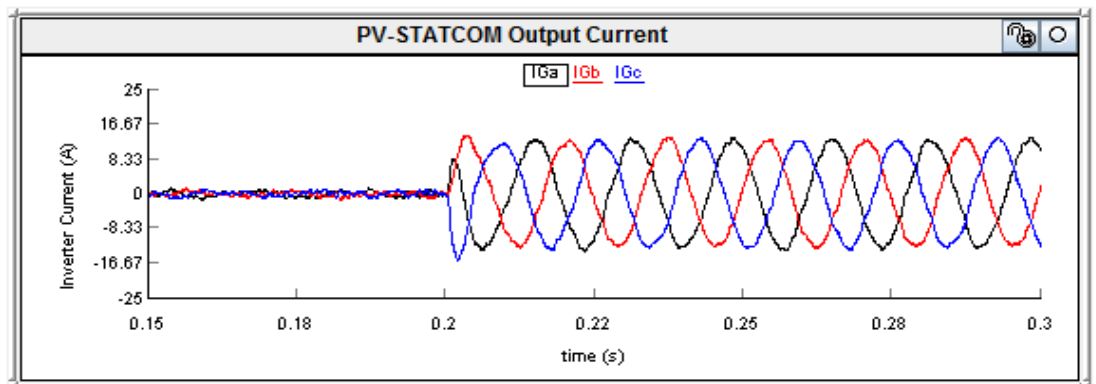
Figure 3.31 PV-STATCOM output current at 50% loading condition during the night

To verify the harmonics output from the PV-STATCOM output current, the total voltage harmonics distortion and the total current demand distortion are calculated at PCC and are found to be 2% and 5.98% respectively, during this 50% loading condition which are considered acceptable as per IEEE 519 [84].

3.8.2   Day time operation

The PV-STATCOM controller performance is demonstrated with two different PV power outputs of 2 kW and 4 kW for 80% and 50% loading scenarios respectively. It is noted that the PV system used for this study does not have an MPPT controller due to the unavailability of computing cards in RTDS. As such, the DC link voltage of the PV inverter is not maintained to the reference value of 400V DC. It is noted that during the day, the PV system generates real power, so that the real power requirement of the motor load is fulfilled by both the PV system and the source.

3.8.2.1   *2 kW PV power output*

During the day, the PV-STATCOM controller injects real power from the PV array to the grid, while also operating in either voltage regulation mode or power factor correction mode, utilizing the remaining reactive power capacity after real power generation. At 2 kW PV power output from a 5 kVA PV inverter, the reactive power availability is 4.58kvar based, on the relation $Q = \sqrt{(S^2 - P^2)}$.

Case 1: 80% Loading

Figure 3.32 demonstrates the 80% loading condition of the motor, where the real and reactive powers drawn by the motor are 5 kW and 3.4kvar, respectively, with motor load operating at a power factor of 0.82. It is shown that power drawn by the motor increases to 5.1 kW and 3.52kvar during the power factor correction mode. This is due to the improvement in the motor terminal voltage from 123.4V (1.027 pu) to 126.1V (1.05 pu) after t > 0.2 seconds during power factor correction. Figure 3.33 illustrates the RMS voltage at the PCC before and after power factor correction.

Figure 3.34 demonstrates the PV-STATCOM output power during the day at an 80% loading condition. During the time $0.15 \leq t \leq 0.2$, the real power from the PV system P_Statcom is 2

kW, and the reactive power Q_Statcom from the PV inverter is 150 var to regulate PCC voltage. At time t ≥ 0.2 seconds, the PV-STATCOM controller operates in power factor correction mode and Q_Statcom becomes 3.58 kvar. At time t ≥ 0.2 seconds, when the transient period dies out, P_Statcom and Q_Statcom are 1.9 kW and 3.58 kvar, respectively. The decrease in P_Statcom is attributed to the PV inverter losses of 100 W, due to the high injection of reactive power during power factor correction mode. It is also observed that the response of real power P_Statcom is slow compared to the response of the reactive power during the transient period, due to slow response of the DC link voltage of the PV-STATCOM.

Figure 3.35 demonstrates DC link voltage of PV-STATCOM during the day, at 2 kW PV. It is seen that after the PV-STATCOM controller is given a step input to change to power factor correction mode, the DC link voltage takes around 0.1 second to stabilize to 386 V DC, from 363 V DC in voltage regulation mode. It is shown that there is a variation in the DC link voltage from 363 V DC to 386 V DC due to the absence of an MPPT controller, which affects the response of the real power P_Statcom. As the DC link voltage takes longer to stabilize due to the unavailability of an MPPT controller, the DC link voltage is simulated from 0.15 seconds to 0.45 seconds.

Figure 3.36 depicts the power requirement from the source during this interval. During the time 0.15 ≤ t ≤ 0.2, P_Source (P_Load - P_Statcom) and Q_Source (Q_Load - Q_Statcom) are 3 kW and 3.25 kvar respectively, as the real and reactive power requirements of the load are 5 kW and 3.52kvar. At time t ≥ 0.2 seconds, the motor's real and reactive power are increased to 5.1 kW and 3.52 kvar, respectively. Hence, source power P_Source and Q_Source become 3.2 kW and -60 var due to 3.58 kvar from the PV-STATCOM. As P_Statcom is decreased to 1.9 kW due to more losses in the PV inverter, P_Source compensates for the additional losses of 100 W. It is noted that, when the PV-STATCOM injects more reactive power, extra real power is needed from the source to compensate for the PV inverter losses.
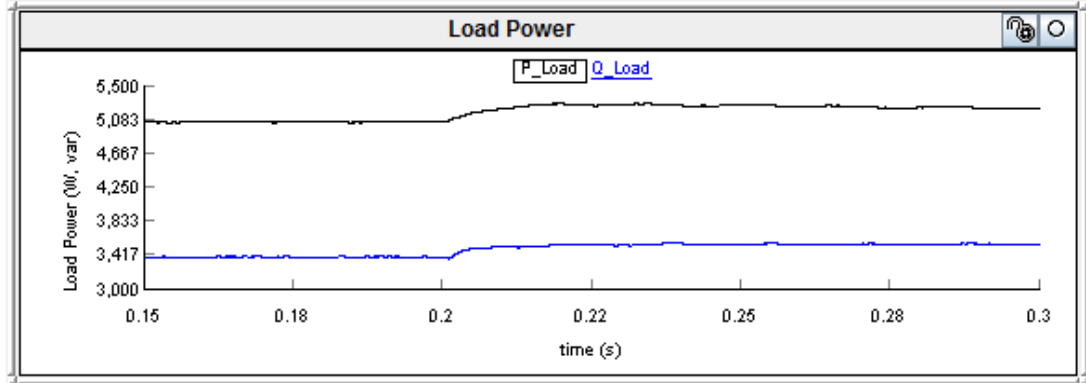
Figure 3.32 Motor power during the day time at 80 % load with 2 kW PV generation
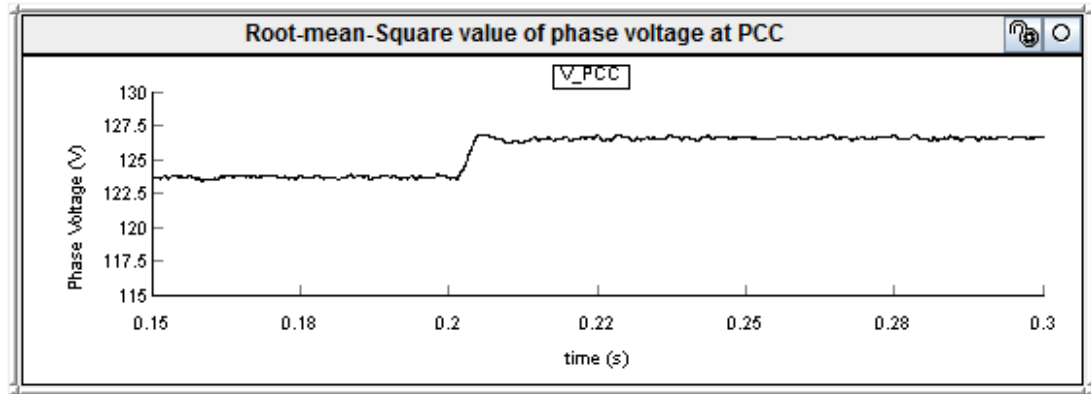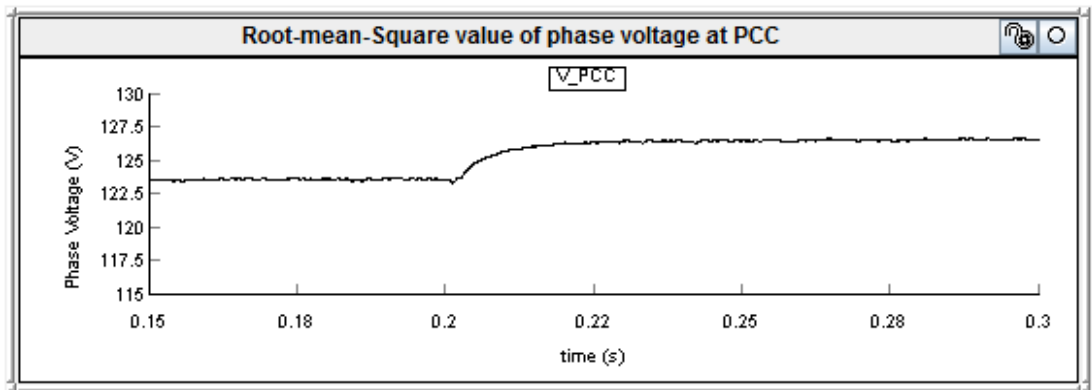

**Figure 3.33** PCC voltage before and after power factor correction during the day
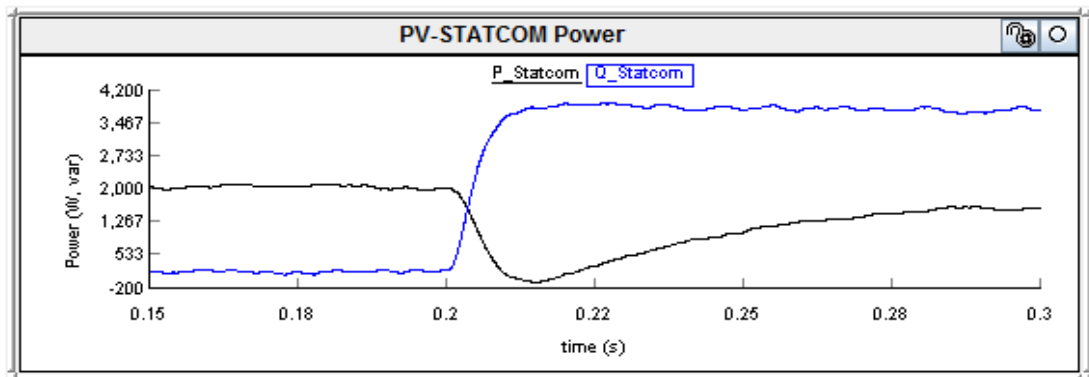
Figure 3.34 PV-STATCOM output power at 2 kW PV and 80% loading condition
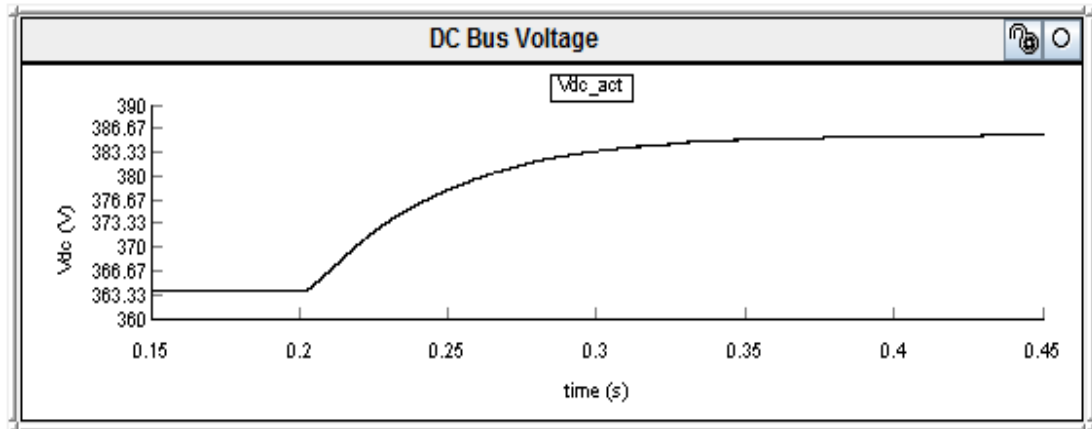
Figure 3.35 DC link voltage at 2 kW PV and 80% loading condition
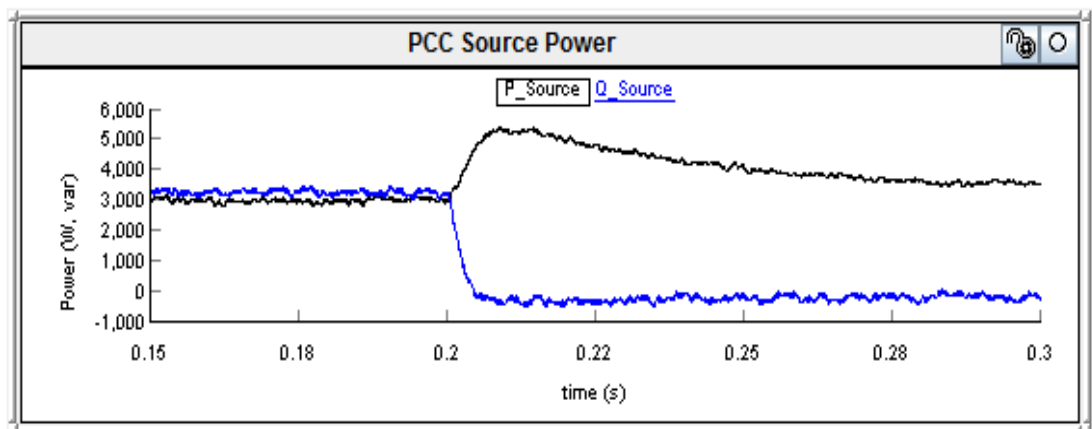
Figure 3.36 Source power at PCC at 2 kW PV and 80% loading condition

Figure 3.37 presents the PCC power factor during both voltage regulation mode and power factor correction mode. During the time $0.15 \leq t \leq 0.2$, power factor at PCC becomes 0.67 according to the relation $\cos(\tan^{-1}(\frac{Q\_Source}{P\_Source})$). At t=0.2 seconds, the PV-STATCOM controller is given a reference PF_{ref}=1 to regulate the power factor to unity. It is seen that controller responds within 9.8ms to regulate the power factor to unity by injecting 3.58 kvar to system. It is clarified that the reactive power from the PV-STACOM system is a combination of reactive power from the PV-STATCOM and the filter. Figure 3.38 shows the reactive power Q_Filter of 1.46kvar from the filter capacitor.
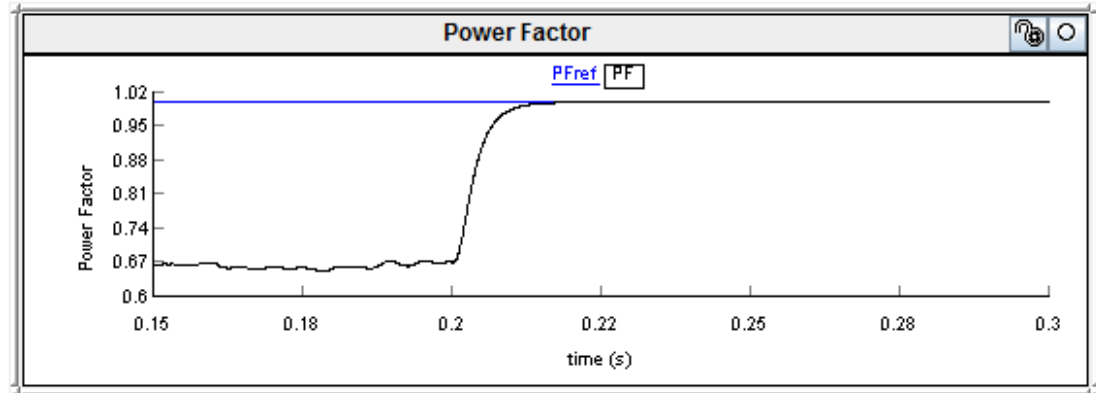
Figure 3.37 PCC power factor at 2 kW PV and 80% loading condition
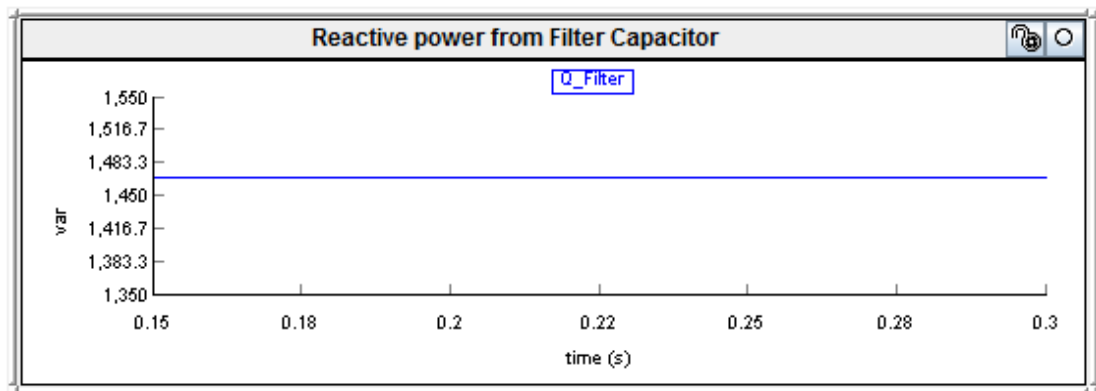
Figure 3.38 Reactive power output from filter capacitor
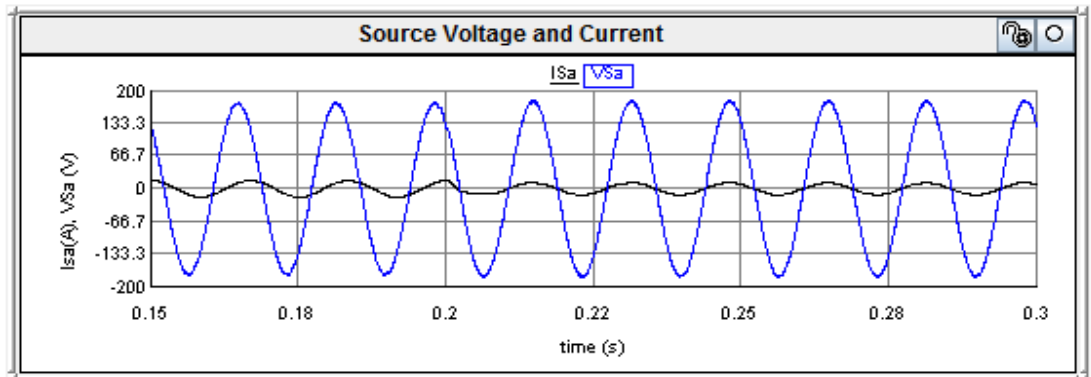
Figure 3.39 depicts the PCC voltage and current waveform during both modes of operation. It is observed that during the power factor correction mode at time $t \geq 0.2$ seconds, PCC voltage and current are in phase, thus confirming the unity power factor at PCC. Figure 3.40 demonstrates the PV-STATCOM output current. An increase in the PV-STATCOM output current is noted during power factor correction mode, compared to during voltage regulation mode. This is attributed to high reactive current injection from the PV-STATCOM during power factor correction mode, at time $t \geq 0.2$ seconds. To check the harmonics content from the PV-STATCOM output current, total voltage harmonics distortion and total current demand distortion at PCC are calculated and found to be 1.9% and 4.9% respectively, which is within the specified limit, as per IEEE 519 [84].
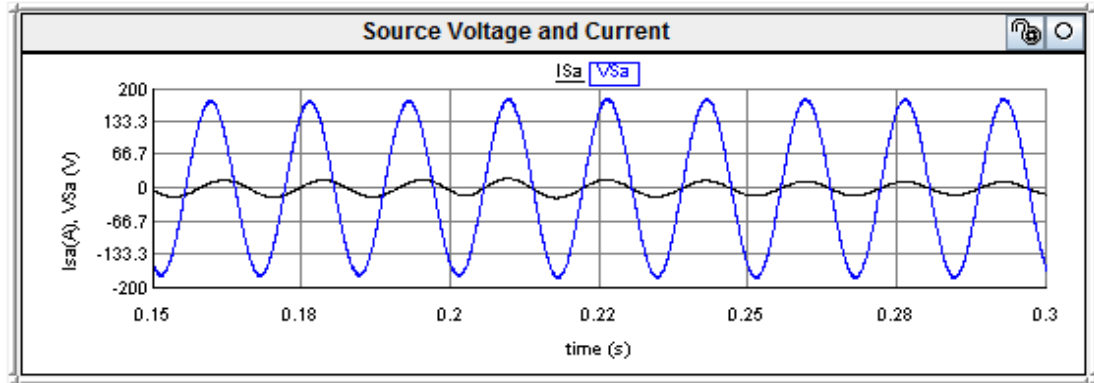
Figure 3.39 PCC voltage and current waveform at 2 kW PV and 80% loading condition
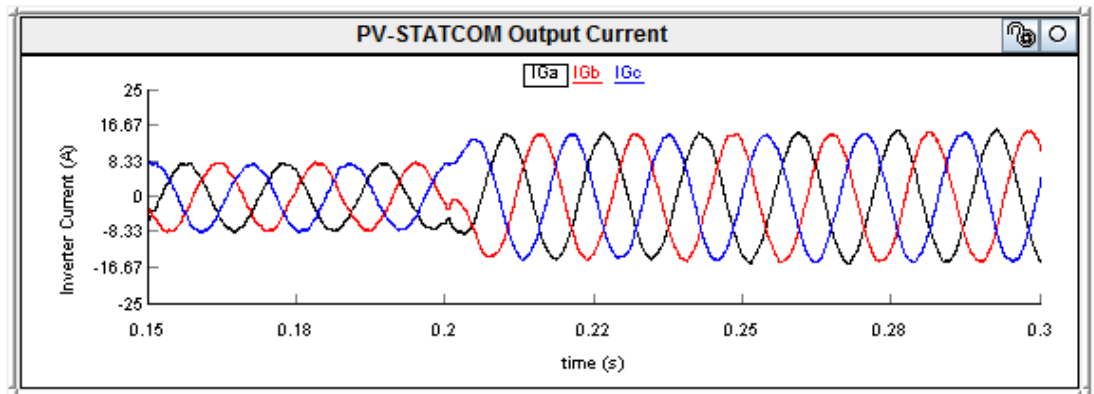
Figure 3.40 PV-STATCOM output current at 2 kW PV and 80% loading condition

Case II: 50% Loading

Figure 3.41 depicts the 50% loading condition where the real and reactive powers drawn by the motor are 3 kW and 3.1 kvar, respectively. In this loading scenario, the load operates at a power factor of 0.69. It is shown that real and reactive power drawn by the motor increases to 3.16 kW and 3.25 kvar, respectively, due to the increase in motor terminal voltage from 124.3 V (1.027pu) to 126.7 V (1.05pu) during the power factor correction mode. Figure 3.42 depicts the RMS value of the PCC voltage. Figure 3.43 presents the PV-STATCOM output power during the day, when the motor operates at a 50% loading condition. During the time $0.15 \leq t \leq 0.2$, P_Statcom is 2 kW and Q_Statcom is 50 var. Similarly, at $t \geq 0.2$ seconds, P_Statcom is 1.9 kW due to a 100 W loss in the PV inverter, and Q_Statcom is 3.4 kvar as the PV-STATCOM operates in power factor correction mode.
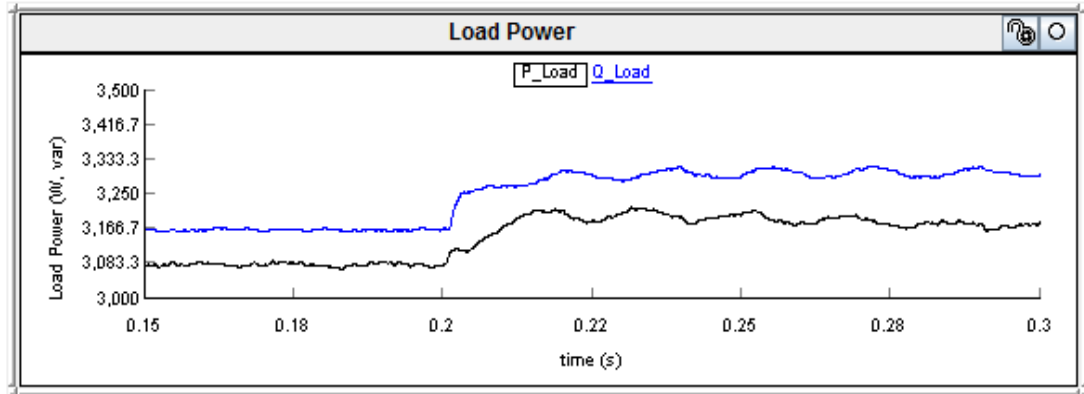
Figure 3.41 Motor power during the day at 2 kW PV and 50% loading condition
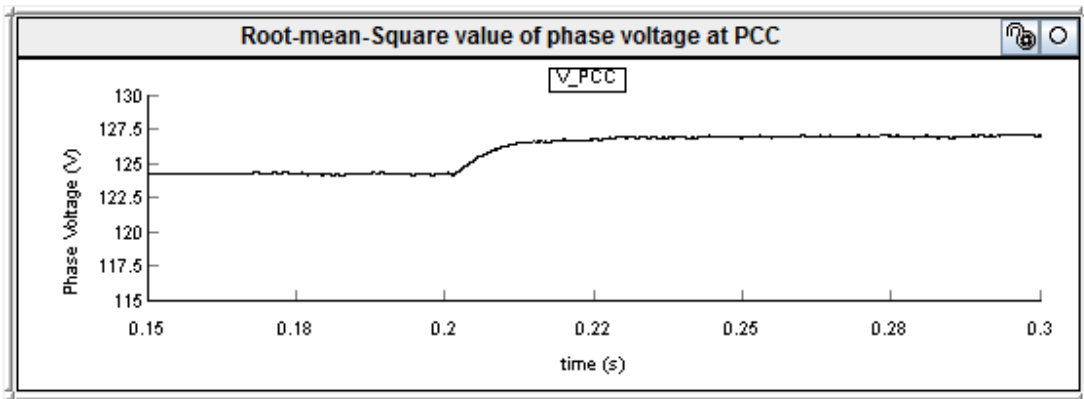
Figure 3.42 PCC voltage before and after power factor correction at 50% loading condition
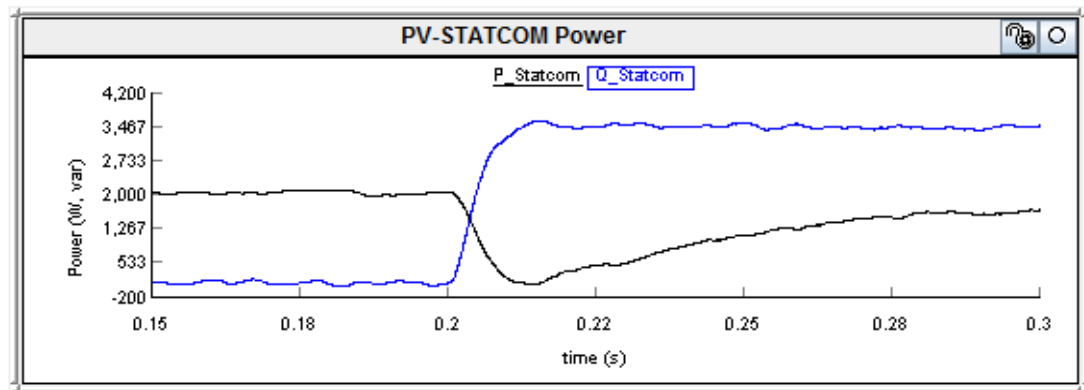
Figure 3.43 PV-STATCOM output power at 2 kW PV and 50% loading condition

Figure 3.44 depicts the power requirement from the source at a 50% loading condition. It is seen that P_Source (P_Load - P_Statcom) and Q_Source (Q_Load - Q_Statcom) are 1 kW and 3.05 kvar respectively, at PCC during voltage regulation mode due to a 50var injection from the PV-STATCOM. At time t ≥ 0.2 seconds, P_Load and Q_Load are increased to 3.16

and 3.25 kvar, respectively. Hence, P_Source becomes 1.26 kW to supply an additional load power requirement and Q_Source becomes -150 var due to the reactive power injection of 3.4 kvar from the PV-STATCOM.

Figure 3.45 demonstrates the PCC power factor during both voltage regulation mode and power factor correction mode. During the time $0.15 \leq t \leq 0.2$, PCC power factor becomes $0.32 \cos(\tan^{-1}(\frac{Q\_Source}{P\_Source}))$. At t=0.2 seconds, the PV-STATCOM controller is given a reference *PFref*=1 to regulate the power factor to unity. It is seen that controller responds within 9.6 ms to regulate the power to unity due to full reactive power support of 3.4 kvar from both the PV inverter and the filter capacitor. The variations of power output of the PV-STATCOM and source power at PCC during the transient follow the same pattern due to the absence of an MPPT controller as in the 80% loading condition.
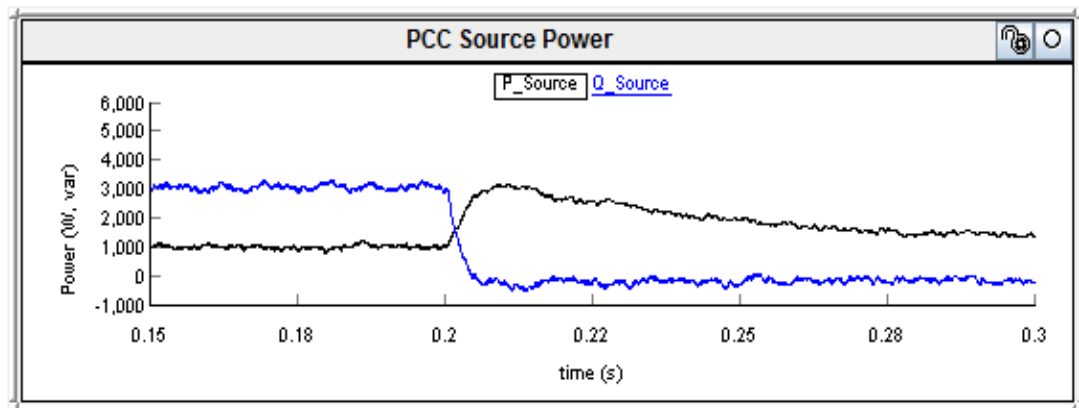
Figure 3.44 Source Power at PCC with 2 kW PV and 50% loading condition
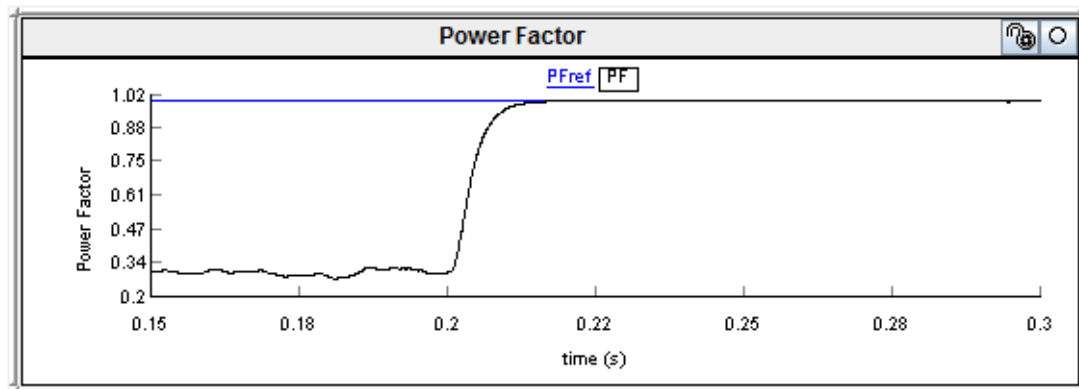
Figure 3.45 PCC Power factor at 2 kW PV and 50% loading condition

Figure 3.46 depicts the PCC voltage and line current that confirms the unity power factor at PCC. DC link voltage and PV-STATCOM output currents are similar in both cases of 80% and 50% loading. Total voltage harmonics distortion and total current demand distortion are calculated at PCC and found to be 1.8% and 4.5%, respectively, both of which are considered acceptable as per IEEE 519 [84].
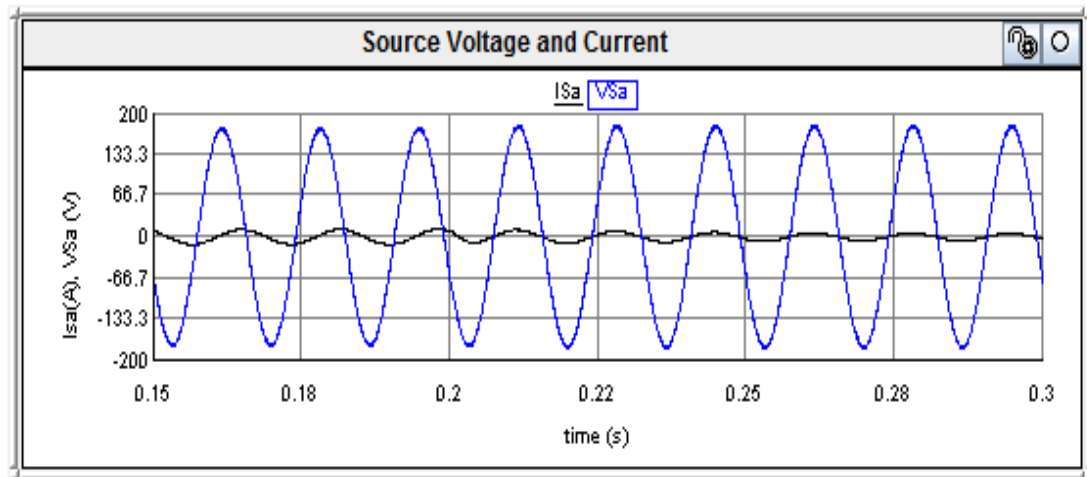
Figure 3.46 PCC voltage and current waveform at 2 kW PV and 50% loading condition

3.8.2.2   *4 kW PV power output*

At 4 kW PV power output from a 5kVA PV inverter, the reactive power availability is 3kvar based on the relation $Q = \sqrt{(S^2 - P^2)}$. the PV-STATCOM controller is tested with 80% and 50% loading conditions at 4 kW PV output.

Case 1: 80% Loading

Figure 3.47 demonstrates the 80% loading condition of the motor; where the real and reactive powers drawn by the motor are 5 kW and 3.4 kvar respectively, with the load operating at a power factor of 0.82. It is shown that power drawn by the motor increases to 5.2 kW and 3.58 kvar during the power factor correction mode, due to the increase in motor terminal voltage as demonstrated in previous cases.
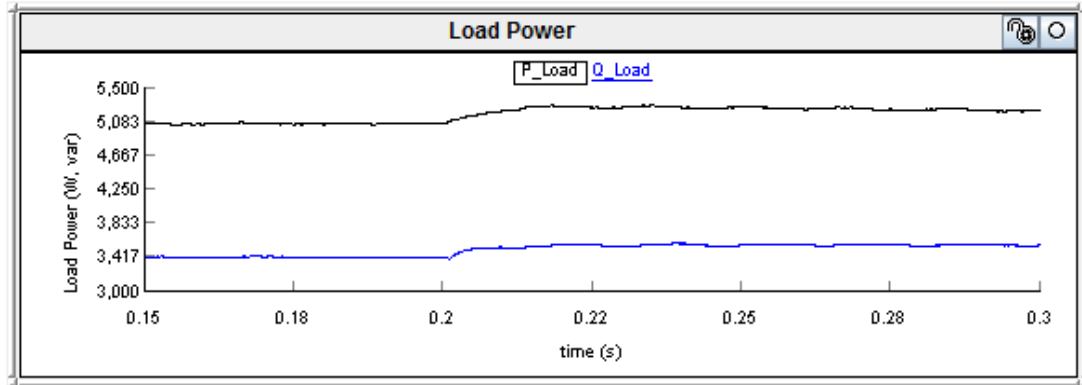
Figure 3.47 Motor power during the day at peak load

Figure 3.48 depicts the PV-STATCOM output power during the day at 4 kW PV with 80% loading condition of the motor. During the time $0.15 \leq t \leq 0.2$, P_Statcom is 4 kW and Q_Statcom is 150 var. At time $t \geq 0.2$ seconds, during power factor correction mode, Q_Statcom is 3.6 kvar, to compensate for the reactive power requirement of the load. P_Statcom is decreased to 3.8 kW due to inverter losses. The decrease in P_Statcom is related to the losses of the PV inverter. It is seen that response of real power P_Statcom is slow, due to the variation in the DC link voltage. Figure 3.49 depicts the DC link voltage Vdc at 4 kW PV. During the voltage regulation mode, Vdc is 385V and it increases to 403V DC during power factor correction mode due to the unavailability of an MPPT controller.

Figure 3.50 depicts the power requirement from the source during a 4 kW PV generation at 80% loading condition of the motor. It is seen that P_Source (5 kW - 4 kW) and Q_Source (3.4 kvar – 0.15 kvar) are 1 kW and 3.25 kvar, respectively, at PCC during the time $0.15 \leq t \leq 0.2$. At time $t \geq 0.2$ seconds, P_Load and Q_Load both are increased to 5.2 kW and 3.58 kvar, respectively. Hence, P_Source becomes (5.2 kW - 3.8 kW) 1.4 kW and Q_Source becomes (3.58 kvar- 3.6 kvar) -20 var.

Figure 3.51 demonstrates the PCC power factor during both voltage regulation and power factor correction mode. During the time, $0.15 \leq t \leq 0.2$, power factor at PCC is 0.29 $(\cos(\tan^{-1}(\frac{3.25}{1}))$). At t=0.2 seconds, the PV-STATCOM controller is given a reference *PF*$_{ref}$=1 to regulate the power factor to unity, operating in power factor correction mode. The PV inverter and filter capacitor both contribute 3.6kvar to compensate for the load reactive

power requirement. Variation of power output of the PV-STATCOM and source power at PCC during the transient follows the same pattern due to the absence of an MPPT controller.
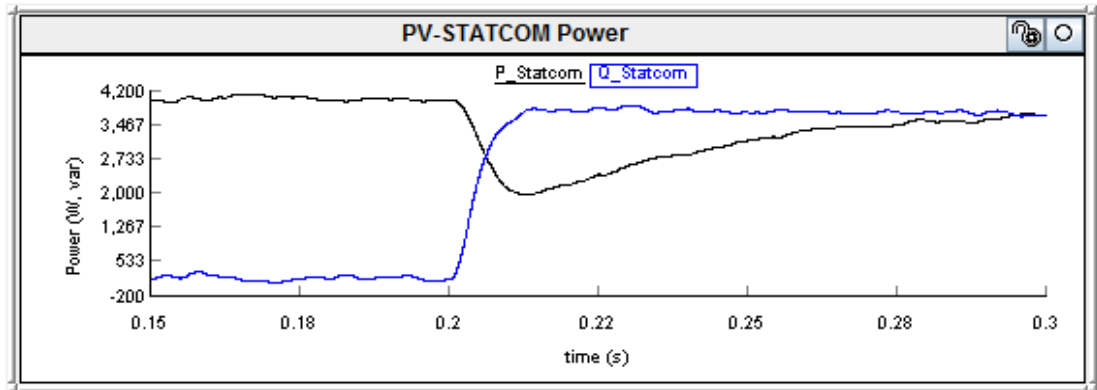
Figure 3.48 PV-STATCOM output power at 4 kW PV and 80% loading condition
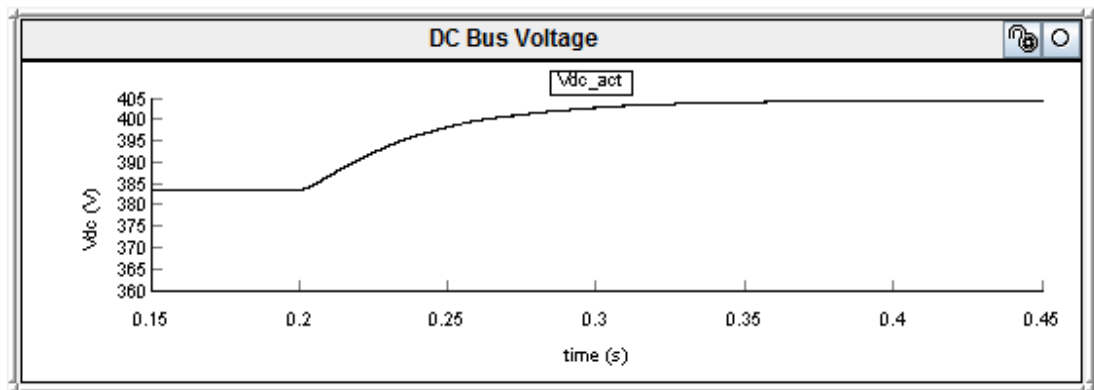
**Figure 3.49** PV-STATCOM DC link voltage at 4 kW PV and 80% loading condition
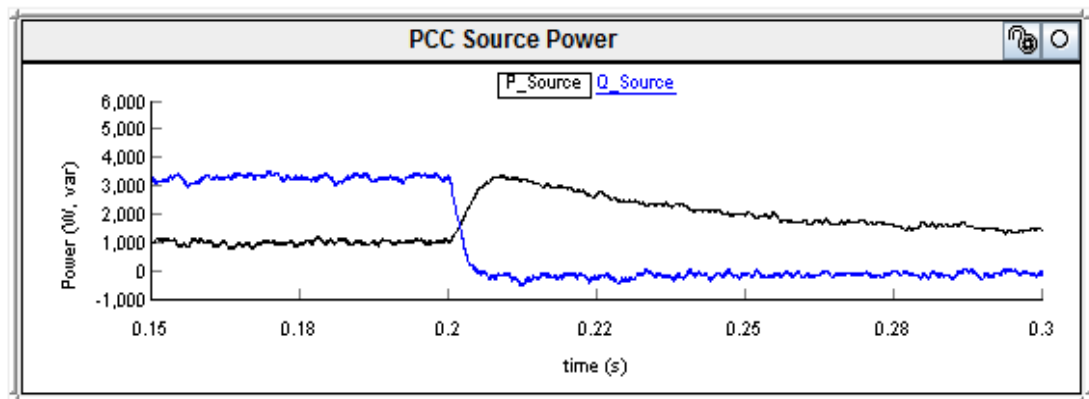
Figure 3.50 Source power at PCC during 80% loading condition at 4 kW PV
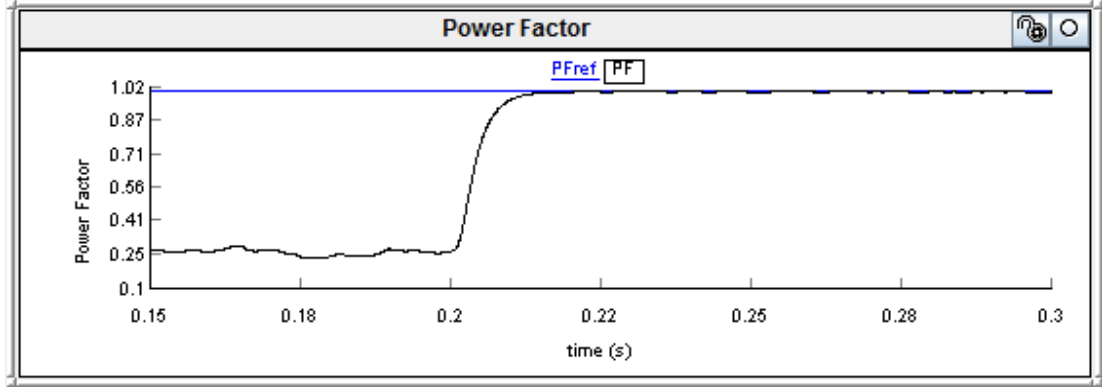
Figure 3.51 Power factor at PCC during 80% loading condition at 4 kW PV

Figure 3.52 depicts the PCC voltage and line current, which are in phase, thus confirming unity power factor mode of operation at time t ≥ 0.2 seconds. Figure 3.53 demonstrates the PV-STATCOM output current. Total voltage harmonics distortion and total current demand distortion at the PCC are calculated and are found to be 2.1% and 4.5% respectively which are considered acceptable as per IEEE 519 [84].
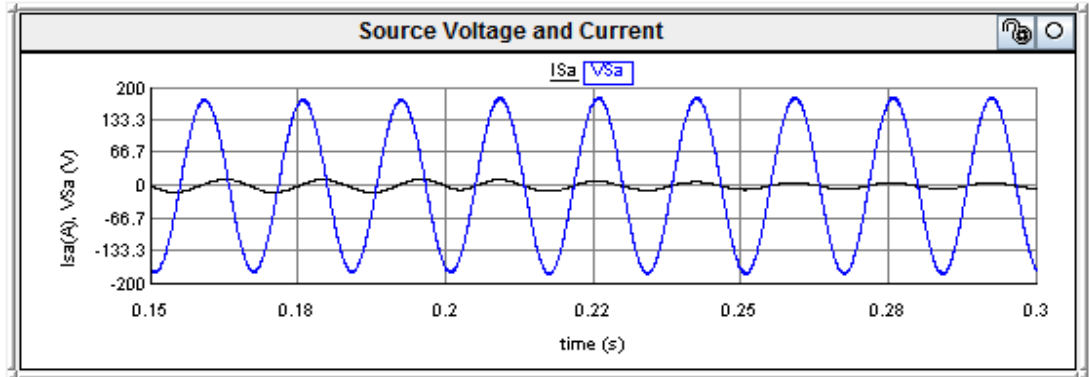
Figure 3.52 PCC voltage and current waveform at 4 kW PV and 80% loading condition
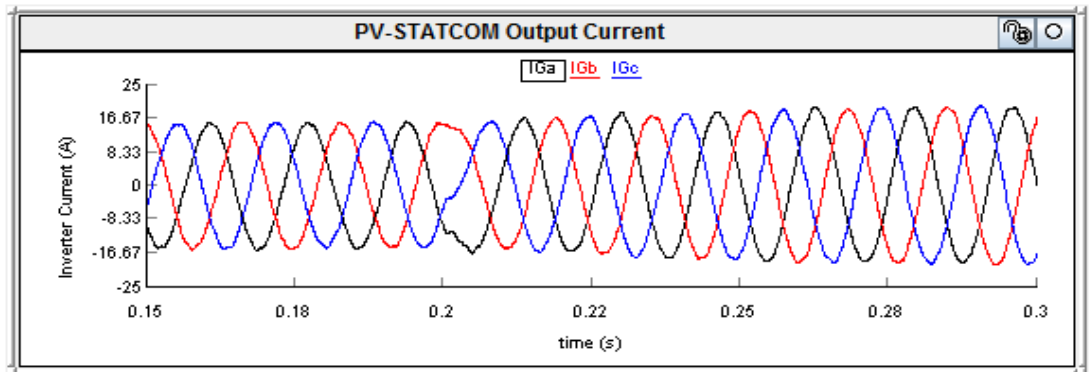

Figure 3.53 PV-STATCOM output current at 4 kW PV power and 80% loading condition

Case II: 50% Loading

Figure 3.54 depicts a 50% loading condition where the real and reactive powers drawn by the motor are 3 kW and 3.1 kvar respectively, and the load operates at a power factor of 0.69 ($\cos(\tan^{-1}(\frac{3.1}{3})$)). It is seen that the real and reactive power values are increased to 3.16 and 3.28 kvar, respectively.

Figure 3.55 demonstrates the PV-STATCOM real and reactive power at 4 kW PV power output and a 50% loading condition. During the time $0.15 \leq t \leq 0.2$, P_Statcom is 4 kW and Q_Statcom is 100 var. At time $t \geq 0.2$, the PV-STATCOM operates in power factor mode. At steady state, P_Statcom is 3.85 kW and Q_Statcom is 3.3 kvar to compensate for the load reactive power requirement.

Figure 3.56 depicts the power requirement from the source at a 50% loading condition. During the time $0.15 \leq t \leq 0.2$, PV power output is 4 kW, and the load power requirement is 3 kW, hence there is a reverse power flow of -1 kW to the source. Thus, P_Source is -1 kW (3 kW- 4 kW). As Q_Statcom is 100var and Q_Load is 3.1kvar, Q_Source is 3 kvar (3.1 kvar - .1 kvar). At time $t \geq 0.2$, P_Load and Q_Load are 3.16 kW and 3.28 kvar, respectively. P_Source is -690 W (3.16 kW – 3.85 kW) during the steady state and Q_Source becomes -20 var (3.28 kvar - 3.3 kvar) due to the reactive power support from the PV inverter and filter capacitor.
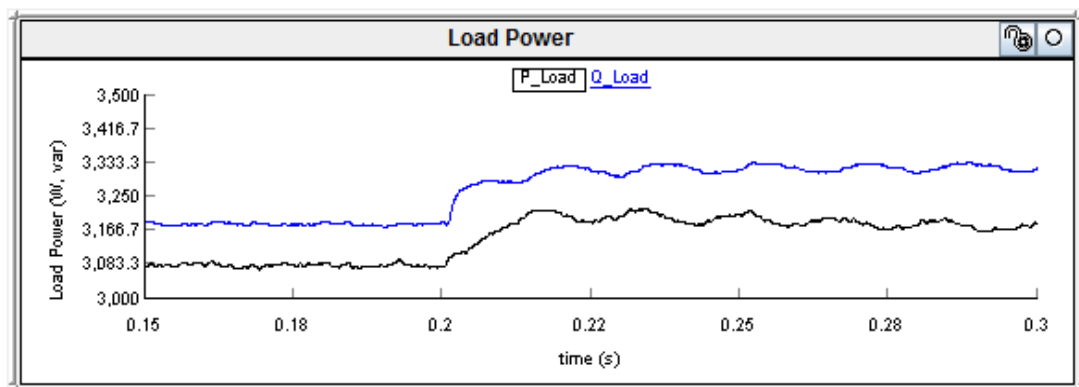
Figure 3.54 Load power during 4 kW PV and 50% loading condition
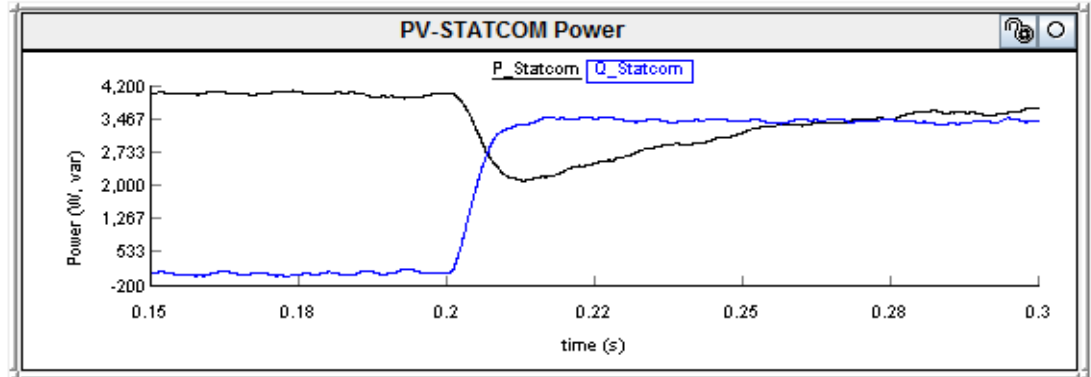
Figure 3.55 PV-STATCOM output power at 4 kW PV and 50% loading condition
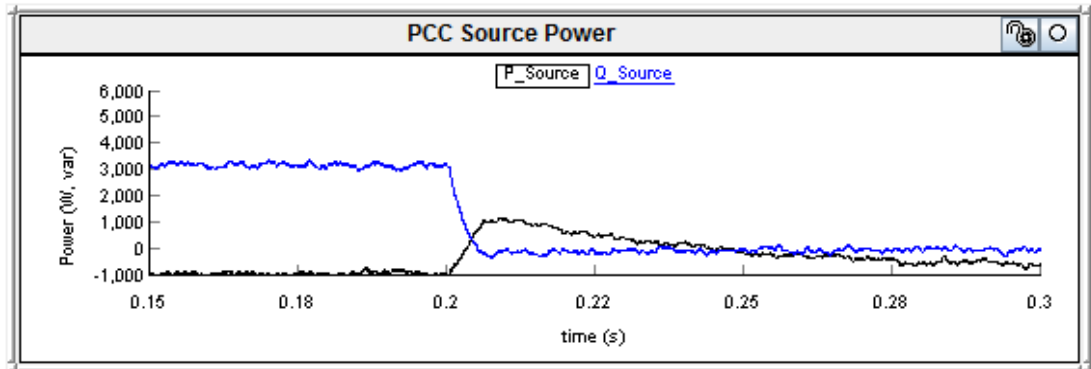
Figure 3.56 PCC power at 4 kW PV and 50% loading condition

Figure 3.57 depicts the power factor at PCC during the day at 4 kW and a 50% loading condition. It is seen that during the time, $0.15 \leq t \leq 0.2$, the PCC power factor is 0.32 according to this relation $(\cos(\tan^{-1}(\frac{3}{1}))$. At time $t \geq 0.2$, the PV-STATCOM controller operates in power factor correction mode. It is seen that controller responds within 10ms by supplying 3.3 kvar to the network, thus regulating the power to unity. From Figure 3.57, it is also seen that power factor becomes zero at two instances; one at 0.205 seconds, and the other at 0.248 seconds. This is due to zero crossing of P_Source during the transient state, which is explained below. During the time $0.15 \leq t \leq 0.2$, P_Source is -1 kW. At time t = 0.2 seconds, the controller changes its state from voltage regulation mode to power factor correction mode. During the transient, P_Statcom drops from 4 kW to 2 kW and again comes back to 3.8 kW in steady state. It is seen from Figure 3.56 that P_Source changes from -1 kW to 1 kW; making a zero crossing at t=0.205 seconds, to supply the load power of 3 kW.
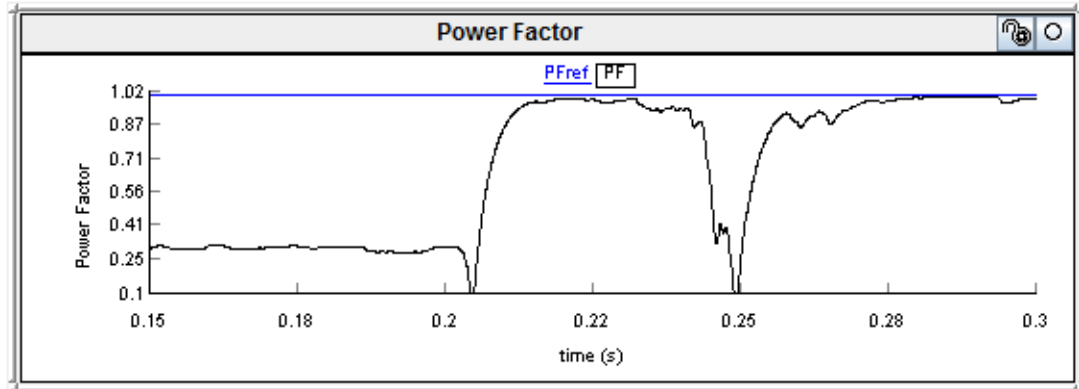
Figure 3.57 Power factor at PCC at 4 kW PV and 50% loading condition

Another instance at t=0.248 seconds, when P_Statcom stabilizes to 3.8 kW, there is a zero crossing of P_Source from a positive value to -690 W, making the power factor zero again due to the relationship $(\cos(\tan^{-1}(\frac{3.4}{0})$). These two scenarios of change of P_Source makes P_Source become zero; thus making the power factor zero momentarily, according to the relation $(\cos(\tan^{-1}(\frac{Q\_Source}{P\_Source})$).

The DC link voltage and PV inverter output current are similar in both cases of 80% and 50% loading. Total voltage harmonics distortion and total current demand distortion are calculated at PCC and found to be 2% and 4.2% respectively, during the 50% loading condition at 4 kW PV output which are within the limits specified in IEEE 519 [84].

3.9 CONCLUSIONS

A real-time digital simulation in RTDS of the PV-STATCOM controller for power factor correction for both night and day is presented. A system model of the London Hydro network, 5 kVA PV-STATCOM, and 6 kW motor load is developed using RTDS. The Pulse Width Modulated control method is employed for the PV-STATCOM controller. Due to the hardware limitation of RTDS in our laboratory, an MPPT could not be modeled. The PV system without the MPPT controller is considered for this study. The PV-STATCOM controller for power factor correction is demonstrated for both 80% and 50% loading conditions during the night, and at two different PV power outputs of 4 kW and 2 kW during the day. The following conclusions are made:

i) The PV-STATCOM controller responds in approximately one cycle during both night and day, for different loading conditions at different PV power outputs of 2 kW and 4 kW.

ii) When the PV-STATCOM injects both real power and reactive power during the day, the inverter losses are seen to increase.

iii) During the night, when the PV-STATCOM operates as STATCOM, the response of both real and reactive power during switching to power factor correction mode is exactly the same. However, during the day, the response of reactive power and real power are less than one cycle and 6 cycles, respectively. The slow response of real power is due to the absence of an MPPT controller to stabilize the DC link voltage.

From the studies, it is confirmed that the developed PV-STATCOM controller works effectively for different PV outputs and during different loading conditions.

Chapter 4

HARDWARE IN THE LOOP SIMULATION OF PV-STATCOM CONTROLLER FOR POWER FACTOR CORRECTION

4.1 INTRODUCTION

This chapter presents a Hardware-in-the-Loop (HIL) simulation of the PV-STATCOM controller developed using the Real Time Digital Simulator (RTDS), as discussed in Chapter 3. The objective of the HIL simulation is to verify the performance of the PV-STATCOM controller in a real hardware system. The PV system, London Hydro network, induction motor load, and the PV Inverter are all modeled internally using RTDS. The PV-STATCOM controller is implemented external to RTDS using a digital signal processor based dSPACE controller [73]. The dSPACE system is interfaced to RTDS through interface circuits. The performance of the PV-STATCOM controller is evaluated for power factor correction during both day and night, for different loading conditions. A comparison of the real time software simulation and hardware simulation of the PV-STATCOM controller is also presented.

4.2 HIL SIMULATION ENVIRONMENT FOR PV-STATCOM CONTROLLER IN RTDS AND dSPACE

Figure 4.1 depicts the HIL simulation environment of the PV-STATCOM controller. The interfacing of the external controller with the RTDS is illustrated in Figure 4.1. Ten input signals for the controller are sent from the RSCAD run time simulation environment through the Digital-Digital Analog Converter (DDAC) card present in RTDS. dSPACE reads these signals and performs appropriate control actions to generate six output signals for the PV-STATCOM IGBT switches modeled in the RSCAD run time environment. These signals are brought into the RTDS simulation environment using a Giga Transceiver Digital Interface (GTDI) card. The dSPACE controller board and RTDS used in the laboratory for HIL simulation are shown in Appendix C.1 and C.2 respectively.
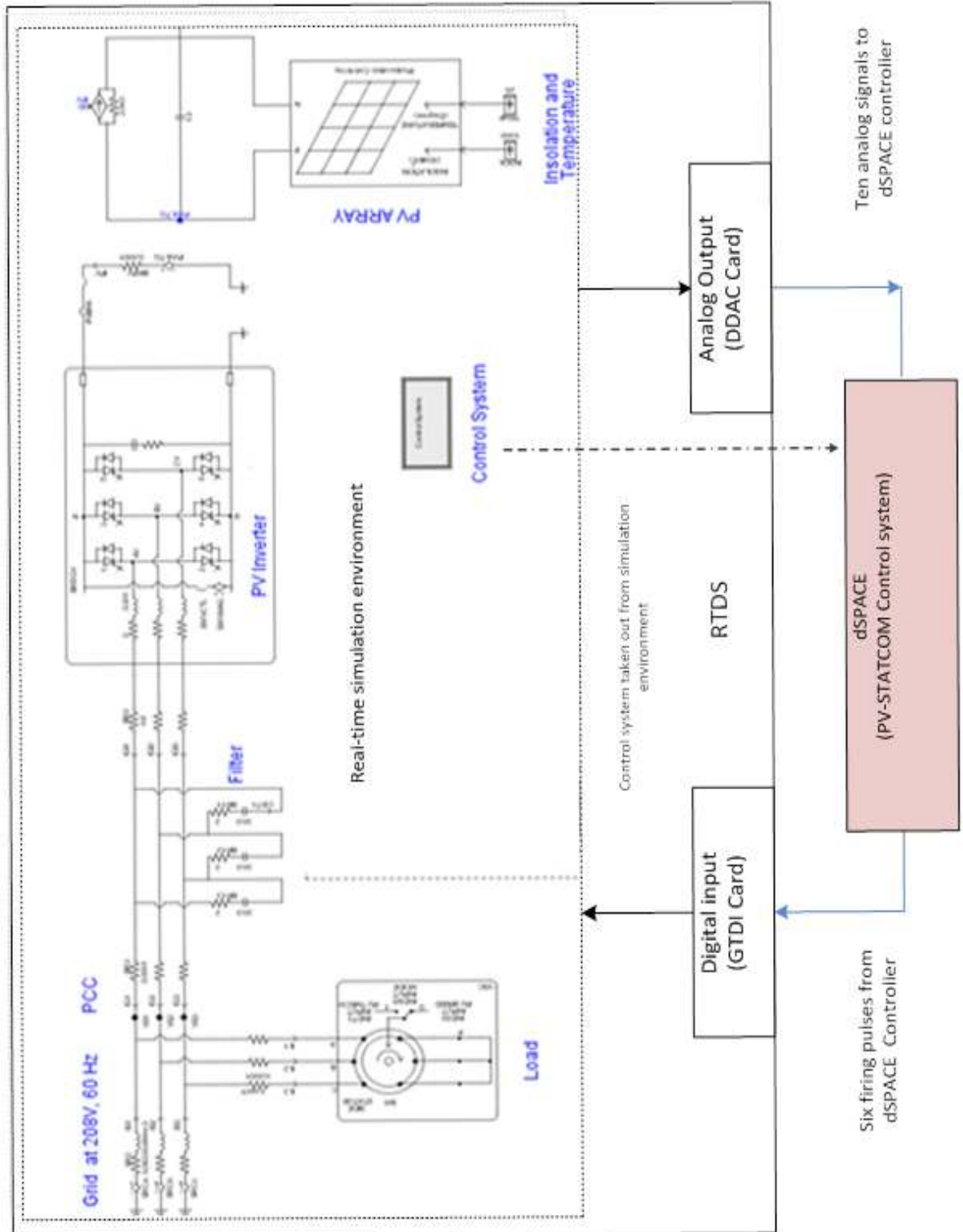
Figure 4.1 HIL simulation of PV-STATCOM controller using dSPACE and RTDS

4.3   dSPACE PLATFORM

4.3.1   Overview of dSPACE Software

Different types of real time controller platforms are used in the Controller-Hardware-In-Loop (CHIL) simulation, such as dSPACE [73], xPC targets [96], and National Instruments [97], for rapid prototype developments. dSPACE is one of the popular platforms used in various industrial applications because of its several advantages such as: extensive array of software, visualization tools, and different hardware options. Hence, the dSPACE hardware platform is chosen for the implementation of the PV-STATCOM controller.
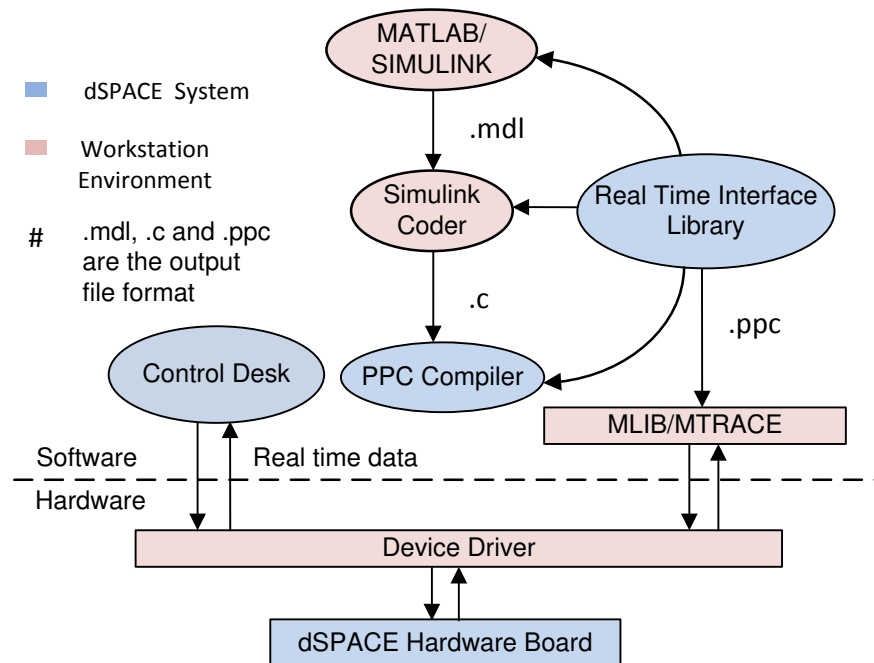
Figure 4.2 Block Diagram of dSPACE software system

Figure 4.2 demonstrates the dSPACE software system. MATLAB/Simulink provides different block sets to create a model for the PV-STATCOM controller. Simulink Coder then translates the model into custom C code specific to the dSPACE controller board. PPC Compiler combines the C code with RTI libraries information in order to execute the developed model on the dSPACE controller board using the MATLAB library functions MLIB/MTRACE. To enable a model to run in a specific dSPACE hardware platform, RTI libraries provide Simulink/dSPACE blocks as well as an input/output interface between Simulink and the dSPACE controller. Similarly, Control Desk is a GUI (Graphical User

Interface) used to monitor the program variables during the run time of the simulation. Device Driver provides an interface to access the dSPACE controller board from the MATLAB/Simulink environment, or from the Control Desk software, running on the workstation PC. The detailed software architecture is provided in the dSPACE software manual [73].

4.3.2   Overview of dSPACE Controller Board

Figure 4.3 demonstrates the dSPACE Controller hardware subsystems. The dSPACE controller board is comprised of a DS1103 controller card, link boards (DS817 and DS814) to communicate between host PC and the PX4 expansion box, and a connector panel (CLP1103). The detailed hardware architecture is outlined in the dSPACE hardware manual [73]. Ethernet crossover cable is used to connect the host PC to the dSPACE system. Similarly, different adapter cables are used to connect the DS1103 controller board to the CLP1103.

4.3.2.1   *PX4 Expansion Box*

A PX4 expansion box houses the power supply units, the DS1103 controller card, and the DS814 link board.

4.3.2.2   *DS1103 controller card*

The DS1103 controller card is the main controller card where PV-STATCOM controller runs. It is comprised of two controllers: the master controller, and a slave Digital Signal Processor (DSP) subsystem. The master controller is a Motorola Power PC (PPC) processor running at a clock rate of 333MHz. The slave DSP is a Texas Instrument based DSP microcontroller (TMS320F240) which operates at 20MHz.

4.3.2.3   *DS817 Link Board*

The DS817 is a PCI interface card installed in the PC. It is used to communicate between the PC and the DS814 link board installed in the PX4 expansion box, housing the DS1103 controller card.
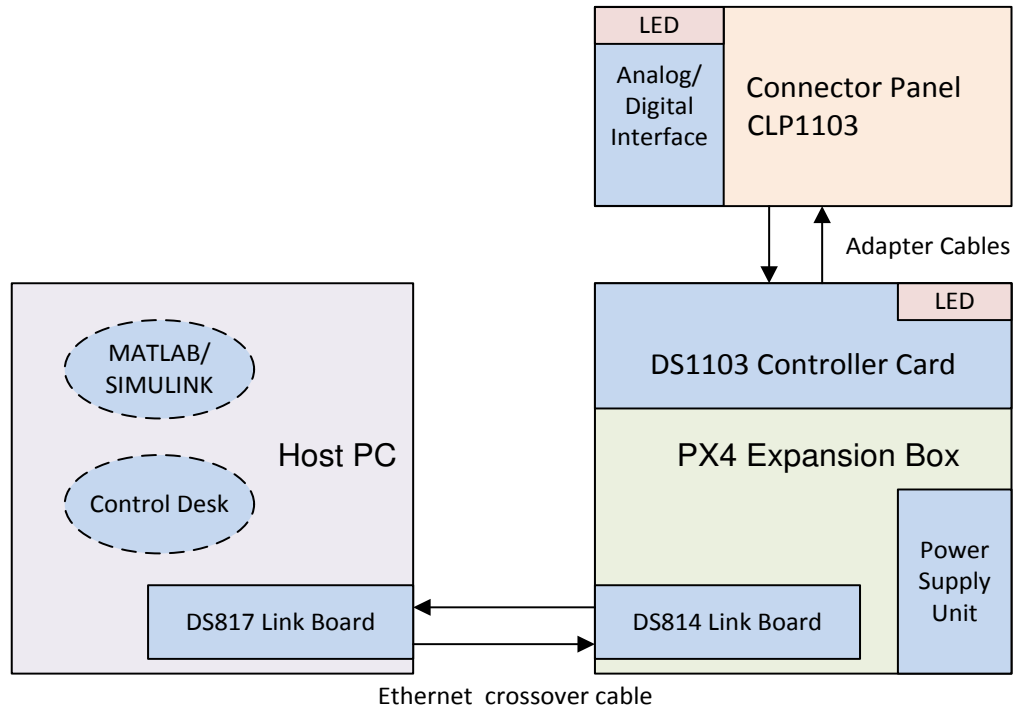
Figure 4.3 Block Diagram of dSPACE hardware system

4.3.2.4 *DS814 Link Board*

The DS814 is an ISA bus interface card installed in the expansion box [73]. It is used to communicate between the DS1103 located in PX4, and the DS817 card installed in the PC.

4.3.2.5 *CLP1103 Connector Panel*

The CLP1103 provides analog and digital input and output signals to access I/O units of the DS1103 controller board. The connector panel is equipped with BNC connectors to provide connections for the analog signals. Similarly, digital signals and serial interface signals are accessed by Sub-D connectors.

4.4 SIMULINK MODEL OF PV-STATCOM CONTROLLER

The PV-STATCOM controller is developed using the Simulink software environment, with MATLAB-dSPACE block sets. These block sets are available from RTI1103 and from MATLAB libraries. These libraries are initialized in the MATLAB/Simulink environment once MATLAB starts running [54].

Figure 4.4 depicts the Simulink model of the PV-STATCOM controller. This model is developed with Simulink block sets along with dSPACE real time interface library block sets. Simulink block sets are used for the PLL module and for three abc to dq conversion modules such as: Vs, and abc2dq to calculate bus voltages, Iinv abc2dq to calculate inverter currents, and ILoad abc2dq to calculate load currents in the d-q reference frame, for control purposes. Similarly, current control, power factor control, DC bus voltage controllers, and voltage regulation modules are developed using Simulink block sets. These modules and their operations are discussed in Chapter 3 (Sec. 3.5). The components related to Simulink and dSPACE block sets are discussed in this section.

Analog to Digital Converter (ADC) blocks are used to read analog signals from RTDS to dSPACE hardware. "MUXADC" is used to read up to four channels of one of the 4 parallel A/D converters. Input voltage ranges of these blocks are between ±10V, and output signals are between ±1V. Hence, appropriate scaling factors are used to obtain the required values at the output of the ADC block in the Simulink model of the controller. In this study, ADC blocks are used to read three Point of Common Coupling (PCC) bus voltages and one DC link voltage from RTDS. Similarly, MUXADC blocks are used to read three load currents and inverter output currents. As such, ten voltage sensors are connected to different ADC channels of the connector panels (CLP1103) to forward these signals from RTDS into the DS1103 controller hardware.

Configuration parameters for the Simulink model are chosen as per the dSPACE user manual [73]. The controller developed using RTDS operates at a fixed time step of 50µs, hence a 50µs time step is used in the Simulink model, to validate the controller performance. A DS1103_DSP_PWM2 block is used to generate three phase pulse width modulated (PWM) signals for the IGBT switches in RTDS. 6kHz of PWM frequency is chosen for this simulation. This block generates 6PWM signals with original and inverted outputs, which are then sent through the Sub-D type connector on the slave I/O to the RTDS simulation environment.
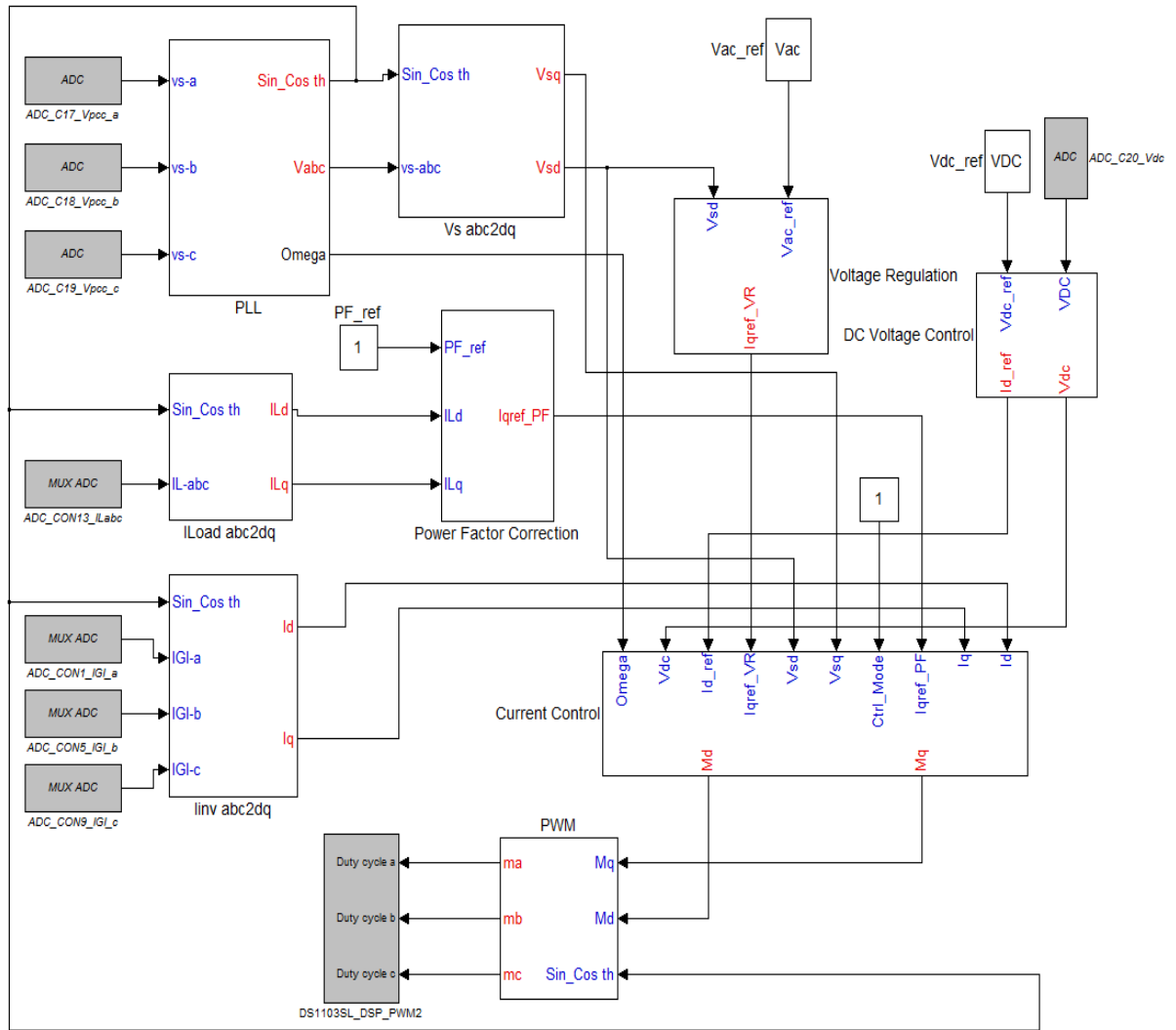
Figure 4.4 Simulink model of PV-STATCOM controller

4.5 HIL TEST SET UP

In the HIL test setup, the network, the photovoltaic system, and the inverter with IGBT switches are all implemented in RTDS and the PV-STATCOM controller is implemented in the dSPACE controller board. As described in the previous section, the PV-STATCOM controller requires ten input signals to generate PWM firing pulses for the IGBT switches of the PV-STATCOM.

Figure 4.5 presents the DDAC card, a 12-channel output block in RTDS, which is used to send ten analog signals out from the RTDS simulation environment to the dSPACE controller board.
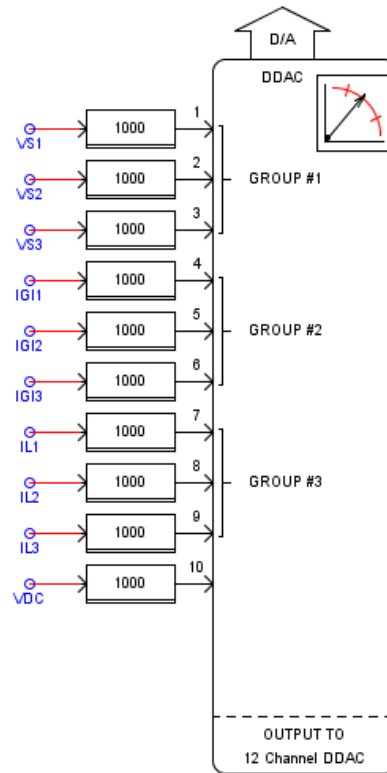
Figure 4.5 DDAC card used to send signals from RTDS to dSPACE Controller

It is noted that the DDAC channel output gives the peak values of all of the voltage and current signals sent from the RTDS simulation environment. The voltage ranges of DDAC analog channels are ±10V. These ten signals are divided into four different groups: GROUP #1, GROUP #2, GROUP #3, and VDC, due to the different amplitude of the signals. GROUP #1 represents three PCC bus voltages. GROUP #2 represents three inverter output currents. GROUP #3 represents three load currents, and finally, VDC represents the PV inverter DC link voltage. Each group is applied with a different scaling factor to match the ±10V voltage level of the DDAC output channels.

Figure 4.6 illustrates the scaling factors used for the grid voltage. A scaling factor of 100 is applied to GROUP #1 to match the grid voltage of 169.831V (peak value of grid phase voltage) to the ±10 V range of the DDAC analog channel. From Figure 4.6, it is shown that a value of 100V in the RTDS simulation environment corresponds to 5V at the output of the DDAC channel. Thus, 169.831V corresponds to 8.49V at the output of the DDAC channel. Similarly, a scaling factor of 20 is applied to both GROUP #2 and GROUP #3 signals, which

represent a PV inverter output current (19.62A) and the induction motor current (23.55A), respectively. A factor of 225 is applied for the DC link voltage (400V).

rtds_sharc_ctl_DDAC

Name	Description	Value	Unit	Min	Max
scl1	Peak value for 5 Volts D/A out Group#1:	100	units	0.01	1e6
invad1	Initial Output Advance Group#1(1.0=nominal)	1.0	steps	0.0	5.0

GROUP #2 SCALING & ADVANCE | GROUP #3 SCALING & ADVANCE | BASIC SCALING
CONFIGURATION | GROUP DATA | GROUP #1 SCALING & ADVANCE

Update | Cancel | Cancel All

Figure 4.6 Scaling factors used for grid voltage

Figure 4.7 depicts the HIL simulation set up. The output of the DDAC channels are connected to the analog channels of the connector panel (CLP1103) of the dSPACE controller board. These DDAC analog channels are used to bring ten analog signals from RTDS to the dSPACE hardware. Control software running on the DS1103 controller card reads these signals from CLP1103 and internally processes these signals based on different modes of operation (either power factor correction mode or voltage control mode) of the controller and finally, generates six firing pulses.

These firing pulses are sent to RTDS through a Sub-D type connector. To transfer six PWM pulses from the dSPACE controller board to the RTDS environment, a Giga Transceiver Digital Input (GTDI) card on RTDS is used. The GTDI card provides 64 optically isolated digital input channels that operate at 5V. The GTDI card is connected to the Giga Processor Card (GPC) on the RTDS. GPC is responsible for small time step simulation where the PV-STATCOM switches (IGBTs) are modeled. Figure 4.7 shows the GTDI card on the rear end of RTDS, used to retrieve PWM pulses from dSPACE board into the GPC card of RTDS. The control compiler running on RTDS software reads these signals from GPC and generates the proper firing sequence for the PV-STATCOM IGBT switches.
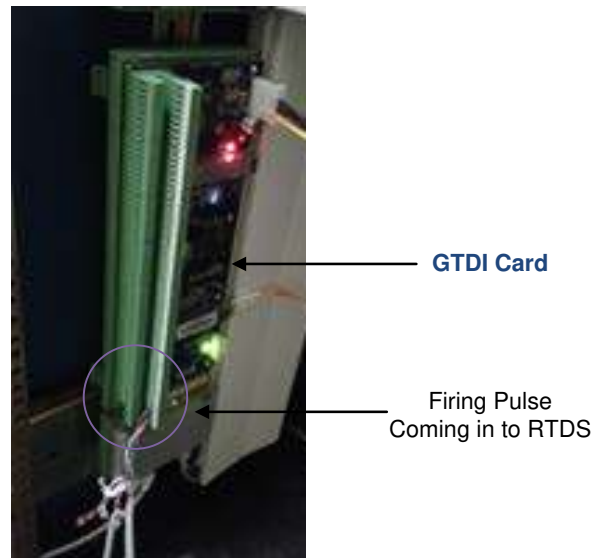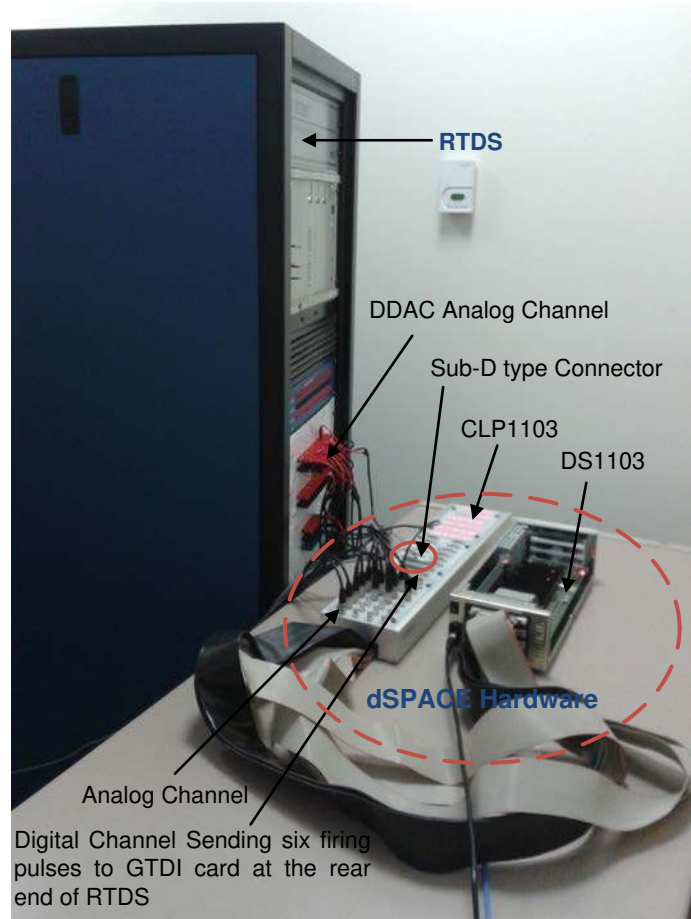
Figure 4.7 HIL simulation environment

4.6   HIL TEST RESULTS

This section presents the results from the HIL simulation of the PV-STATCOM controller during the day with PV power output of 2 kW, as well as during the night, with 80% and 50% loading conditions. As described in Sections 4.4 and 4.5, the PV-STATCOM controller needs ten input signals for power factor control and generates six firing pulses for the IGBT switches modeled in RTDS. Hence, these input/output signals, along with the results from the RTDS real time environments, are presented in this section.

4.6.1   Daytime operation

4.6.1.1   *Case 1: 80% loading*

The measurements have been performed using a Tektronix oscilloscope (TDS2024). The number of Volts/div, A/div, and time/div are specified below each photograph. Figure 4.8 demonstrates the experimental results for the PV-STATCOM controller during a 2 kW power output from the PV system at an 80% loading condition of the induction motor.

Figure 4.8 (a), (b), (c) and (d) present three phase PCC bus voltages, three phase inverter output currents, three phase load currents, and DC link voltages, respectively. These 10 analog signals are sent through the DDAC card of RTDS to the PV-STATCOM controller, running on the dSPACE board. Three phase bus voltages (125.86V rms phase to ground) at the PCC are applied with a scaling factor of 100. These voltage signals are sent to the DDAC output channel. The measured values at the DDAC channels for three phase voltages are 8.9V. Three phase inverter output currents of 13A rms values are applied with a scaling factor 20. These signals are sent to the DDAC output channel and the measured values at the DDAC channels for three phase currents are 4.6V. Three phase motor load currents of magnitude 16.97A rms values are applied with a scaling factor of 20. The measured values for motor load currents at the DDAC channel are found to be 6V. Similarly, a DC bus voltage of 400V DC is applied with a scaling factor of 225. The corresponding value measured at the DDAC output channel is found to be 8.8V. The PV-STATCOM controller, running in the dSPACE controller board to generate six firing pulses, processes these ten signals from the DDAC card of RTDS. Figure 4.8 (e) demonstrates the inverter output current before and after filter, which demonstrates the effectiveness of the filter. Figure 4.8 (f) depicts that the PCC voltage and current are in phase, thus, confirming the unity power factor operation at PCC. Figure 4.8 (g), (h), and (i) present the firing pulses coming out

from the PV-STATCOM controller to the GTDI card on RTDS. These firing pulses are 5V signals that come to the input of the GTDI card. The control compiler running in RTDS reads these signals and generates proper firing sequences for the PV-STATCOM IGBT switches.

(a) Three Phase Voltage at PCC

(b) Three Phase Inverter output current

(c) Three Phase Load current

(d) DC link Voltage

(e) Inverter current before and after filter

(f) Voltage and Current at PCC

(g) Firing Pulses for Leg A

(h) Firing Pulses for Leg B

(i) Firing Pulses for Leg C
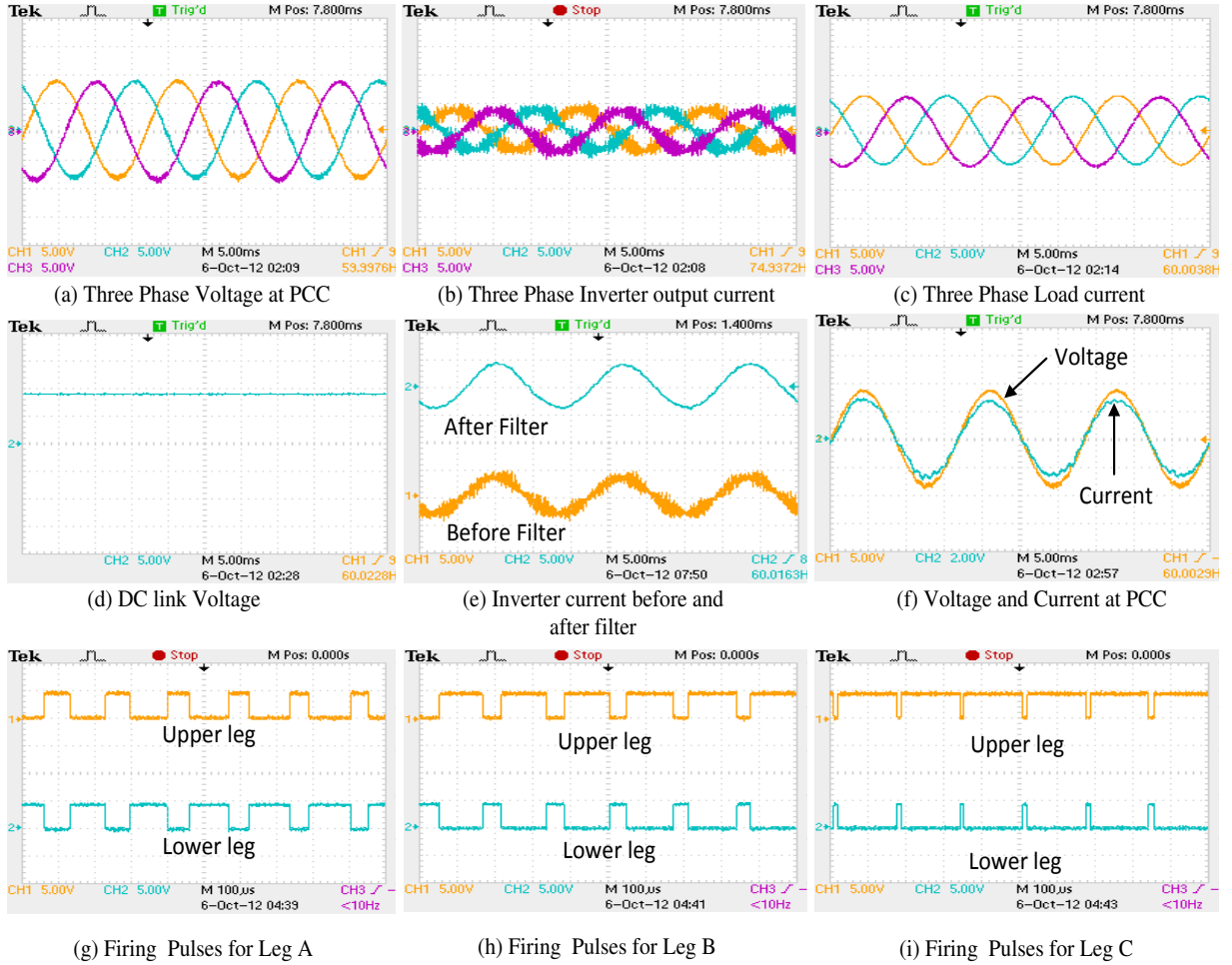
Figure 4.8 HIL Experimental results at 80% loading during PV- STATCOM mode
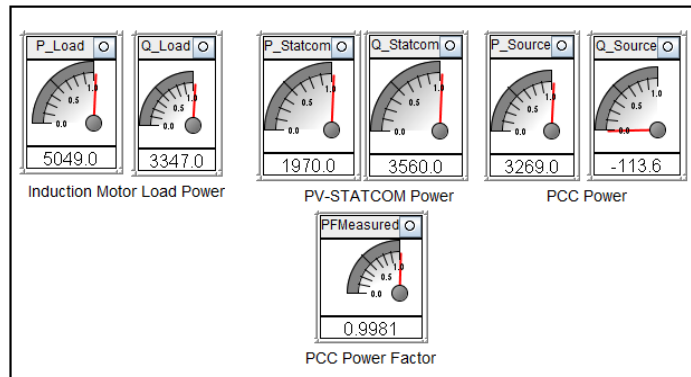
Figure 4.9 RTDS Measurements during PV-STATCOM mode at 80% loading condition

Figure 4.9 demonstrates the meter readings of motor load, PCC, and PV-STATCOM output power, along with PCC power factor in RTDS simulation environment in watts and vars, respectively. These values are then compared with the RTDS simulation result in Section 3.7.2.1 of Chapter 3, during the power factor correction mode described below.

The real and reactive power values of the motor load were 5100 watt and 3520 var, respectively, in the RTDS software simulation and are shown to be 5049 watt and 3347 var in the HIL simulation, respectively. The real and reactive power values from the PV inverter were 1900 watt and 3580 var, respectively, in the RTDS software simulation, and are demonstrated to be 1970 watt and 3560 var in the HIL simulation. The real and reactive power values of the source were found to be 3200 watt and -60 var in the RTDS software simulation and are shown to be 3269 watt and -113var in the HIL simulation, respectively. The power factor is demonstrated to be unity. It is thus seen from the meter reading that the steady-state performance of the PV-STATCOM controller is similar in both the RTDS simulation and the HIL simulation.

4.6.1.2 *Case 2: 50% loading*

Figure 4.10 (a), (b), (c), and (d) demonstrate ten signals sent from RTDS to the dSPACE controller board. These are three phase PCC bus voltages, three phase inverter output currents, three phase load currents, and the DC link voltage. Three phase bus voltages (127V rms phase to ground) at PCC are applied with a scaling factor of 100, and are sent to the DDAC output channel. The measured value at the DDAC channels for three phase voltages are 8.98V. Three phase inverter output currents of 12.4A rms values are applied with a scaling factor 20 and sent to the DDAC output channel. The values measured at the DDAC channels for three phase voltages are 4.4V. Three phase motor load currents of magnitude 13A rms values are applied with a scaling factor of 20, and the measured values for the motor load currents at the DDAC channel are 4.6V. Similarly, a DC bus voltage of 396V DC is applied with a scaling factor of 225, and the measured value for the DC bus voltage at the DDAC output channel is 8.8V. An increase in PCC voltage is noted, caused by the light load condition of motor load. Figure 4.10 (e) demonstrates the inverter output current. Figure 4.10 (f) demonstrates the PCC voltage and current waveform. It is seen that both PCC voltage and current are in phase, which ensures unity power factor operation.   Similarly, Figure 4.10 (g), (h), and (i) represent the firing pulses coming out from the PV-STATCOM controller to the GTDI card on RTDS. The control compiler

generates proper firing sequences for the PV-STATCOM IGBT switches, based on the firing pulses received at the GTDI input.

(a) Three Phase Voltage at PCC (b) Three Phase Inverter output current (c) Three Phase Load current

(d) DC link Voltage (e) Inverter current before and after filter (f) Voltage and Current at PCC

(g) Firing Pulses for Leg A (h) Firing Pulses for Leg B (i) Firing Pulses for Leg C

Figure 4.10 HIL Experimental results at 50% loading during PV- STATCOM mode
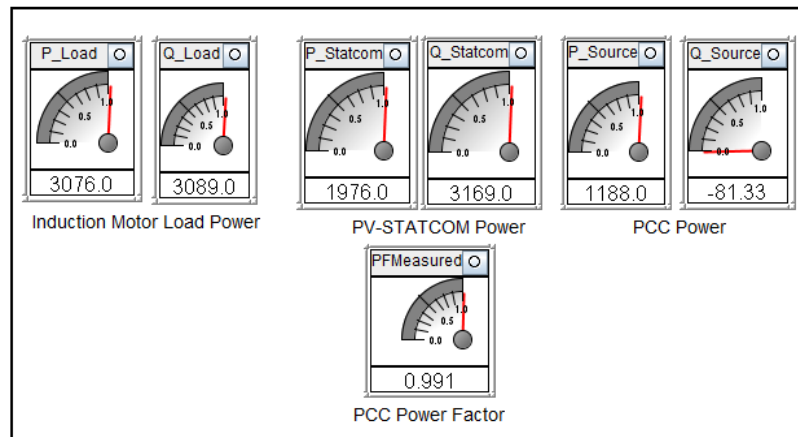
Figure 4.11 RTDS Measurements during PV-STATCOM mode at 50% loading condition

Figure 4.11 demonstrates the meter reading of load, PCC, and PV-STATCOM output power, along with the PCC power factor in RTDS simulation environment. These values are compared to the RTDS simulation results in Section 3.7.2.1 of Chapter 3 during the power factor correction mode, described below.

The real and reactive power of the motor load were 3160 watt and 3250 var, respectively, in the RTDS software simulation and are shown to be 3076 watt and 3089 var in the HIL simulation, respectively. The real and reactive power from the PV inverter were 1900 watt and 3400 var, respectively, in the RTDS software simulation and are demonstrated to be 1976 watt and 3169 var in the HIL simulation, respectively. The real and reactive power of the source were 1260 watt and -150 var, respectively, in the RTDS software simulation, and are shown to be 1188 watt and -81 var in the HIL simulation. The power factor is demonstrated to be unity. It is thus seen from the meter reading that the steady-state performance of the PV-STATCOM controller is similar in both the RTDS simulation and the HIL simulation.

4.6.2   Nighttime operation

4.6.2.1   *Case 1: 80% loading*

Figure 4.12 (a), (b), (c), and (d) present three phase bus voltages at PCC, three phase inverter output currents, three phase load currents, and DC link voltages, respectively. Three phase bus voltages (125.8V rms phase to ground) at PCC are applied with a scaling factor of 100. The measured values at the DDAC channels for three phase voltages are 8.9V. Three phase inverter output currents of 11.8A rms values are applied with a scaling factor 20 and sent to the DDAC output channel. The values measured at the DDAC channels for three phase voltages are 4.2V. Three phase motor load currents of magnitude 16.97A rms values are applied with a scaling factor of 20, and the measured values for motor load currents at the DDAC channel are found to be 6V. Similarly, a DC bus voltage of 400.5V DC is applied with a scaling factor of 225, and the measured value for the DC bus voltage at the DDAC output channel is 8.9V. These ten signals from the DDAC card in RTDS are processed by the PV-STATCOM controller running on the dSPACE controller board, to generate six firing pulses. Firing pulses during the STATCOM mode are found to be similar to those produced during the day. Figure 4.12 (e) demonstrates the inverter output current before and after the filter, demonstrating the satisfactory performance of

the filter. Figure 4.12 (f) shows that PCC voltage and current are in phase, thus confirming the unity power factor operation at PCC. Figure 4.13 demonstrates the meter reading of the load, PCC, and PV-STATCOM output power, along with PCC power factor in the RTDS simulation environment. These values are compared with the RTDS simulation results in Section 3.7.1.1 of Chapter 3, during power factor correction mode, described below.

| (a) Three Phase Voltage at PCC | (b) Three Phase Inverter output current | (c) Three Phase Load current |

| (d) DC link Voltage | (e) Inverter current before and after filter | (f) Voltage and Current at PCC |

Figure 4.12 HIL Experimental results at 80% loading during STATCOM mode
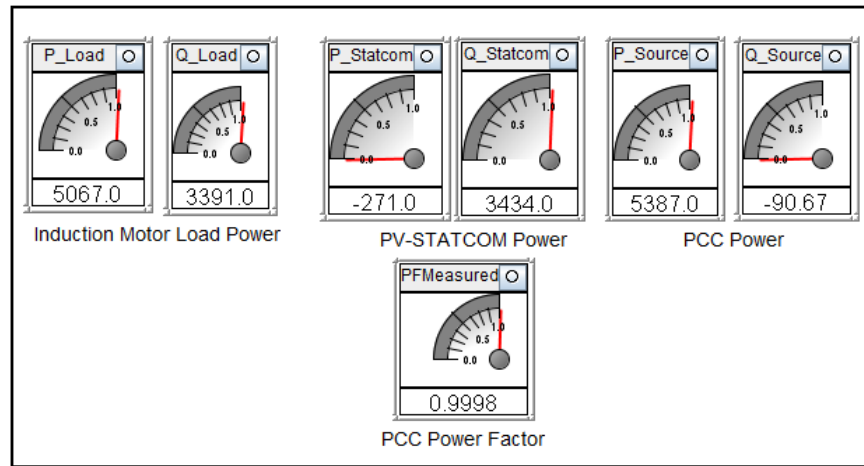
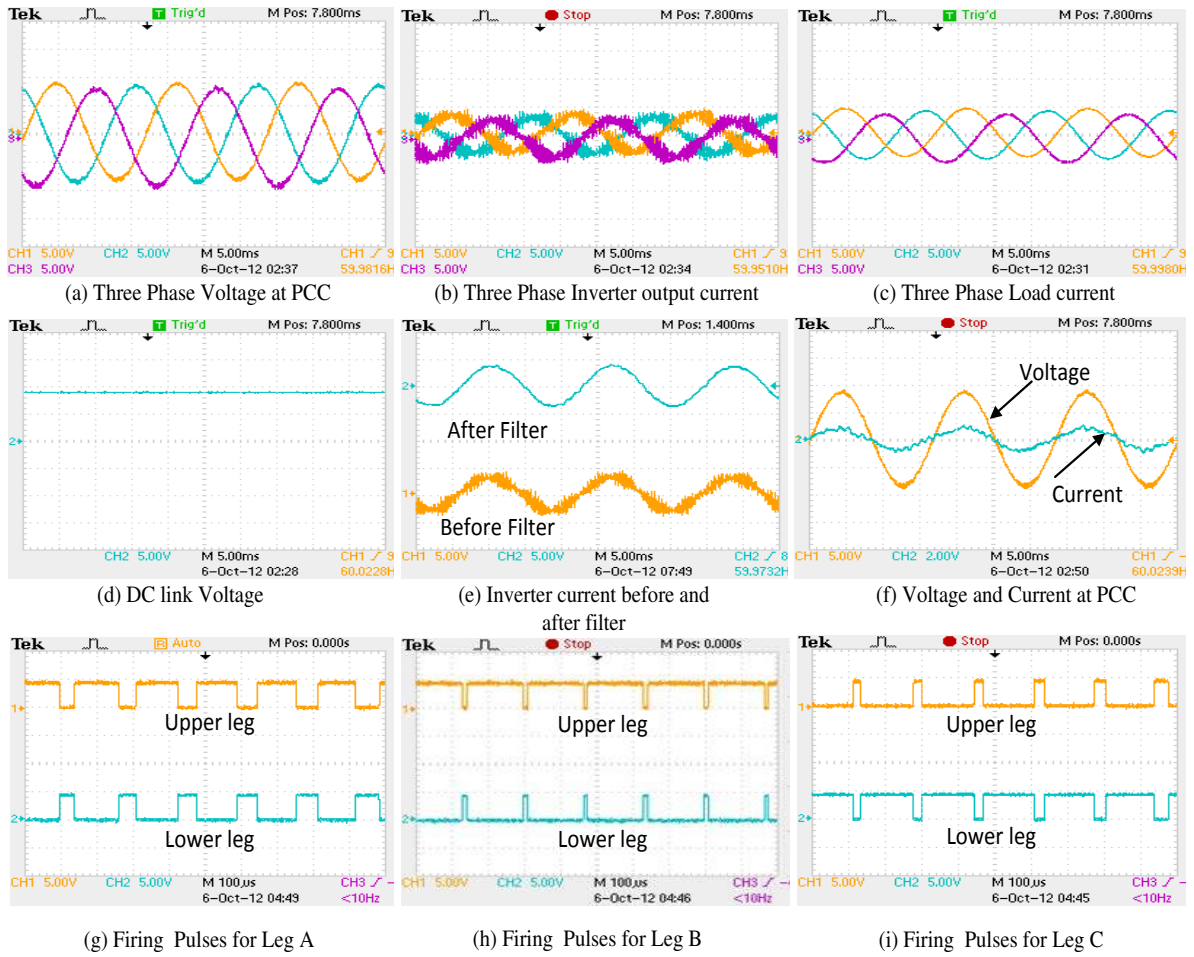**Figure 4.13** RTDS Measurements during STATCOM mode at 80% loading condition

The real and reactive power values of the motor load were 5080 watt and 3500 var, respectively, in the RTDS software simulation, and are shown to be 5067 watt and 3391 var in the HIL simulation. The real and reactive power values from the PV inverter were -80 watt and 3510 var, respectively, in the RTDS software simulation, and are demonstrated to be -271 watt and 3434 var in the HIL simulation. The values of real and reactive power of the source were 5160 watt and -10 var, respectively, in the RTDS software simulation, and are shown to be 5387 watt and -90 var in the HIL simulation. The power factor is demonstrated to be unity. It is thus seen from the meter reading that the steady-state performance of the PV-STATCOM controller is similar in both the RTDS simulation and the HIL simulation.

4.6.2.2   *Case 2: 50% loading*

Figure 4.14 (a), (b), (c), and (d) demonstrate ten signals sent from RTDS to the dSPACE controller board: three phase PCC bus voltages, three phase inverter output currents, three phase load currents, and the DC link voltage. Three phase bus voltages (127.2V rms phase to ground) at PCC are applied with a scaling factor of 100 and are sent to the DDAC output channel. The measured values at the DDAC channels for three phase voltages are found to be 9V. Three phase inverter output currents of 11.8A rms values are applied with a scaling factor 20 and sent to the DDAC output channel. The values measured at the DDAC channels for the three phase voltages are 4.2V. Three phase motor load currents of magnitude 13A rms values are applied with a scaling factor of 20. The measured values for motor load currents at the DDAC channel are 4.6V. Similarly, a DC bus voltage of 400.5V DC is applied with a scaling factor of 225, and the measured value for the DC bus voltage at the DDAC output channel is 8.9V. Firing pulses going into RTDS from dSPACE are similar to those seen during the day. The control compiler generates proper firing sequences for the PV-STATCOM IGBT switches based on the firing pulses received at the GTDI input. Figure 4.14 (e) and (f) demonstrate the inverter output current and unity power factor operation at PCC. Figure 4.15 demonstrates the steady state meter reading of the load, PCC, and PV-STATCOM output power, along with PCC power factor in the RTDS simulation environment. These values are compared to the RTDS simulation results in Section 3.7.1.2 of Chapter 3, during power factor correction mode as discussed below.
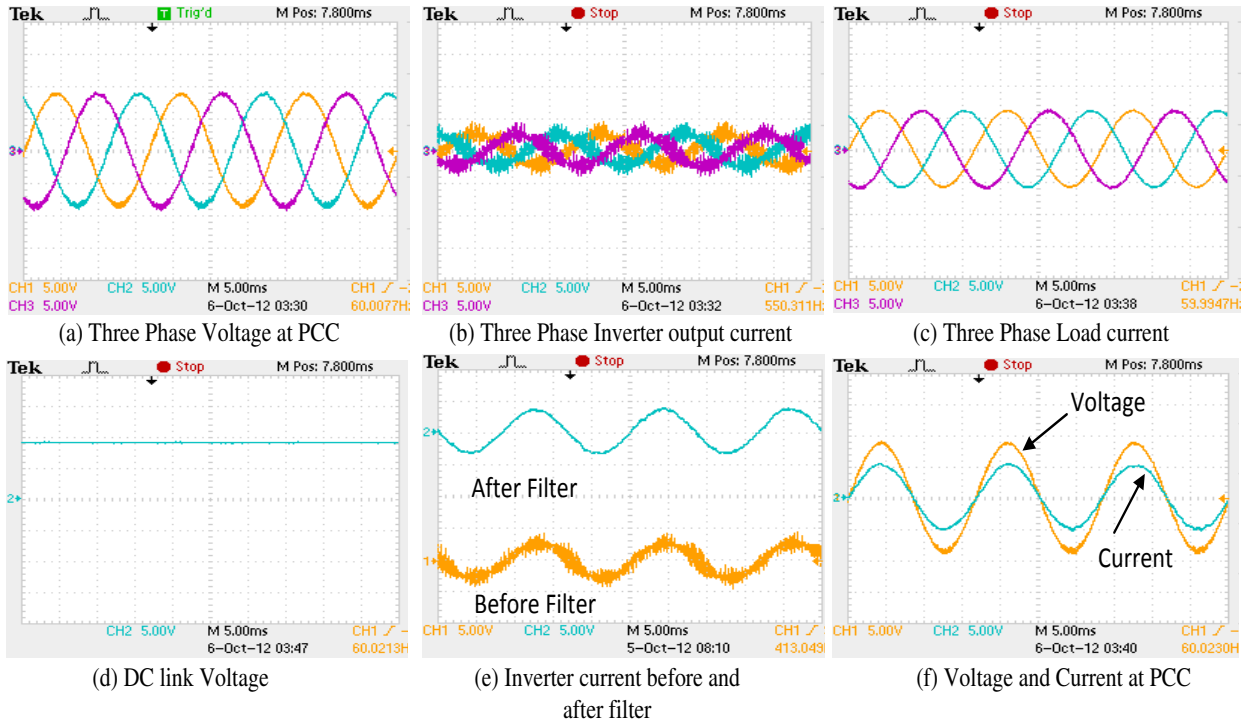
The real and reactive power of the motor load were 3166 watt and 3260 var, respectively, in the RTDS software simulation, and are shown to be 3051 watt and 3081 var in the HIL

simulation. The real and reactive power from the PV inverter were -100 watt and 3270 var, respectively, in the RTDS software simulation, and are demonstrated to be -180 watt and 3178 var in the HIL simulation. The real and reactive power of the source were 3266 watt and -10 var, respectively, in the RTDS software simulation, and are shown to be 3299 watt and -120 var in the HIL simulation. The power factor is demonstrated to be unity. It is thus seen from the meter reading that the steady-state performance of the PV-STATCOM controller is similar in both the RTDS simulation and the HIL simulation.

(a) Three Phase Voltage at PCC

(b) Three Phase Inverter output current

(c) Three Phase Load current

(d) DC link Voltage

(e) Inverter current before and after filter

(f) Voltage and Current at PCC
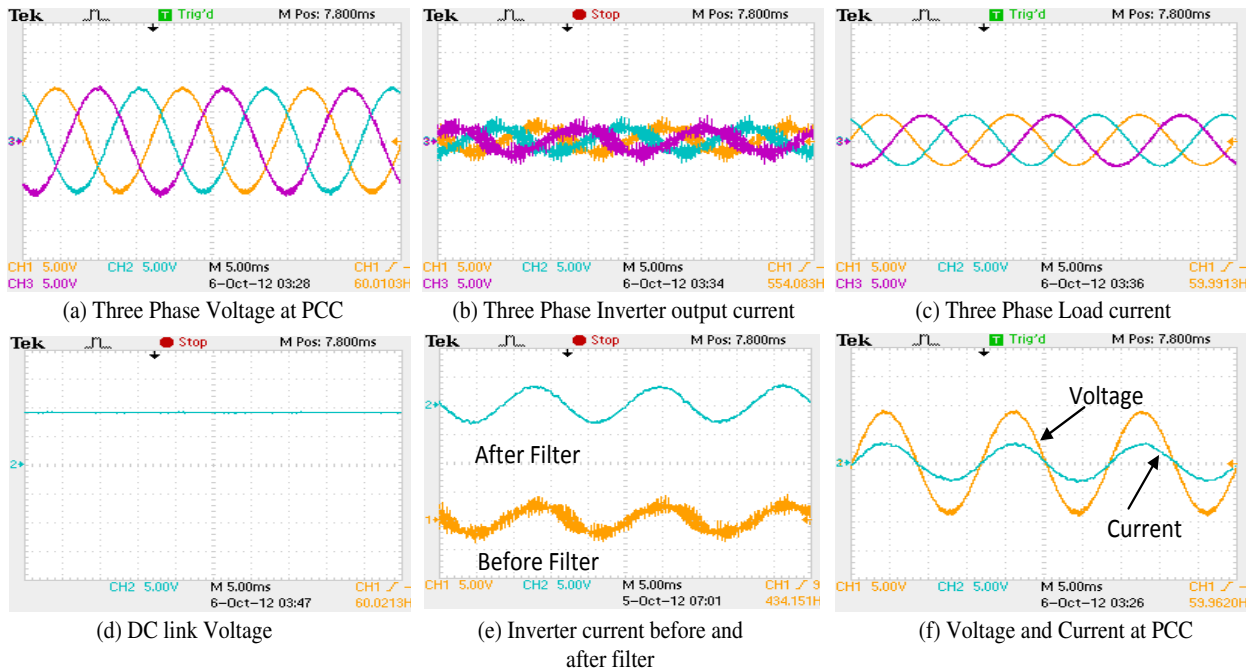
Figure 4.14 HIL Experimental results at 50% loading during STATCOM mode
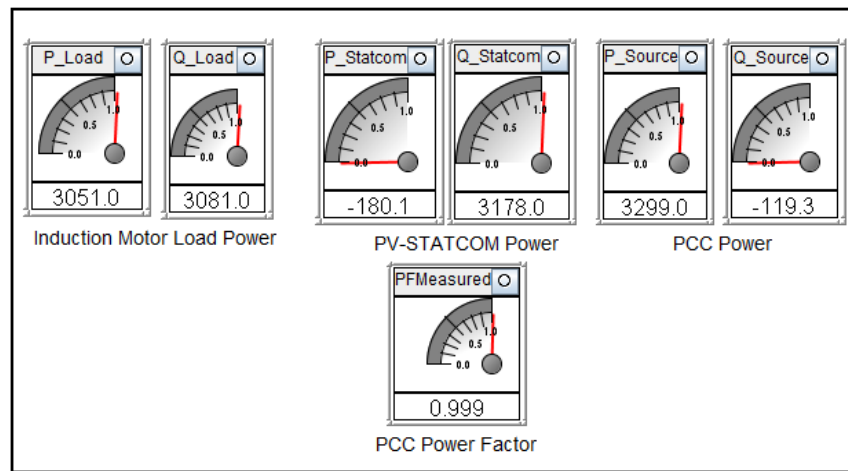
Figure 4.15 RTDS simulation during STATCOM mode results at 50% loading condition

4.7 CONCLUSION

This Chapter presents a Hardware-in-the Loop simulation of the PV-STATCOM controller, developed in dSPACE, to test the controller performance for power factor correction. dSPACE has two main controllers: a master controller and a slave DSP controller. The PV-STATCOM controller developed in the RTDS simulation environment is taken out and implemented in dSPACE hardware, while the London Hydro network, 5 kW PV panel with a PV Inverter and motor load are simulated in the RTDS environment. Ten input signals for the controller are sent from the RSCAD run time simulation environment through the Digital-Digital Analog Converter (DDAC) card present in RTDS. dSPACE reads these signals and performs appropriate control actions to generate six output signals for the PV inverter, modeled in RSCAD run time environment. The real-time simulation in RTDS and the experimental HIL simulation are both carried out during the time when PV is generating 2 kW and also during the night, at 80% and 50% loading conditions of the motor. The power factor correction performance of the PV-STATCOM controller designed in the RTDS environment is validated by the dSPACE-based PV-STATCOM controller developed in the HIL simulation.

From the HIL simulation, it is confirmed that the PV-STATCOM controller works effectively during different operating scenarios. The performance of the PV-STATCOM controller for power factor correction is demonstrated by the PV-STATCOM generating active power during the day, and acting as a STATCOM during the night.

Chapter 5

HARMONIC IMPACT STUDIES OF LARGE SCALE SOLAR FARM

5.1 INTRODUCTION

This chapter presents a unique case study of harmonics impact and network resonance in the Bluewater Power distribution network which connects the largest solar farm in North America of 80 MW. IEEE 519 recommends a power quality analysis for the system as it has a large number of dispersed generators that inject harmonics to the network. Large scale PV solar farms use a substantial number of power electronic converters. Therefore, a detailed harmonic analysis is performed on the Bluewater Power network in order to study the impact of this large scale solar farm on its distribution system. In addition to this analysis, the impact of harmonics from a 10 kW PV solar system is also presented. This study is performed based on the detailed network data, central Geographical Information System (GIS) database, and Supervisory Control and Data Acquisition (SCADA) infrastructure made available by Bluewater Power Corporation. The network is modeled in detail using PSCAD/EMTDC, which is validated with load flow studies using the CYME software and SCADA measurements. The validated network model is used for the network resonance study and harmonic analysis in the presence of a large solar farm for different operating scenarios of the network. This study is conducted for the steady state operating conditions neglecting any presence of ambient harmonics in the network.

5.2 SYSTEM DESCRIPTION

5.2.1 Sarnia Solar Farm

The Sarnia solar farm is the largest solar farm in Canada, with a total size of 80 MW. This solar farm is connected to the Bluewater Power (BWP) distribution network at a 27.6 kV voltage level. There are four different feeders: 96M23, 96M27, 96M28, and 18M14 that are connected to the solar farm; each feeder being fed with 20 MW solar generation. Feeders 96M23, 96M27, and 96M28 are connected to the Modeland station and feeder 18M14 is connected to the St. Andrews substation. Both substations are connected to the Hydro One

network. For this harmonic impact study requiring two feeders connected to the Modeland substation, 96M23 and 96M27 are chosen.

5.2.2   Modeland Substation

The Modeland substation is connected to the Hydro One Inc. network at a 230 kV voltage level through two 125 MVA tap changer transformers. The nominal voltage at the low voltage side of the BWP network is 27.6 kV. Although the nominal voltage is 27.6 kV, the operating voltage at the Modeland station varies throughout the day from 28 kV to 29 kV, depending on the loading conditions on the feeder. This substation does not have an installed feeder capacitor.

5.2.3   Feeders

5.2.3.1   *Feeder 96M23*

Figure 5.1 depicts the geographical illustration of feeder 96M23, with BWS-1 and BWS-2 solar farms of 10 MW each; as per the GIS (Geographical Information System) software used in the Bluewater Power (BWP) network. Hence, the maximum generation on this feeder is 20MW. The longest distance on the feeder is from the Modeland station to the BWS-2 location, which is approximately 7.5 km. This feeder mostly feeds residential and commercial consumers, such as shopping malls, through both overhead lines and underground cables. There are no industrial customers on the M23 feeder. The total number of distribution transformers connected with a 27.6 kV system on this feeder are 239, feeding both residential and commercial customers. Overhead lines and underground cables are used to connect these distribution transformers to the main feeder operating at 27.6 kV. There is no power factor correction capacitor installed on this feeder.

5.2.3.2   *Feeder 96M27*

Figure 5.2 depicts the geographical illustration of feeder 96M27 with Solar 3 and Solar 6 solar farms, each 10 MW, as per the GIS data. Therefore, the maximum generation on this feeder is 20 MW. The longest distance on the feeder is between the Modeland station and the Solar 6 location, approximately 6.5 km. The total number of distribution transformers connected with a 27.6 kV system on this feeder are 165, feeding both residential and commercial customers. There are no industrial customers on the M27 feeder. Underground

cables are mainly used to connect these distribution transformers to the main feeder operating at a 27.6 kV voltage level. There is no power factor correction capacitor installed on this feeder.
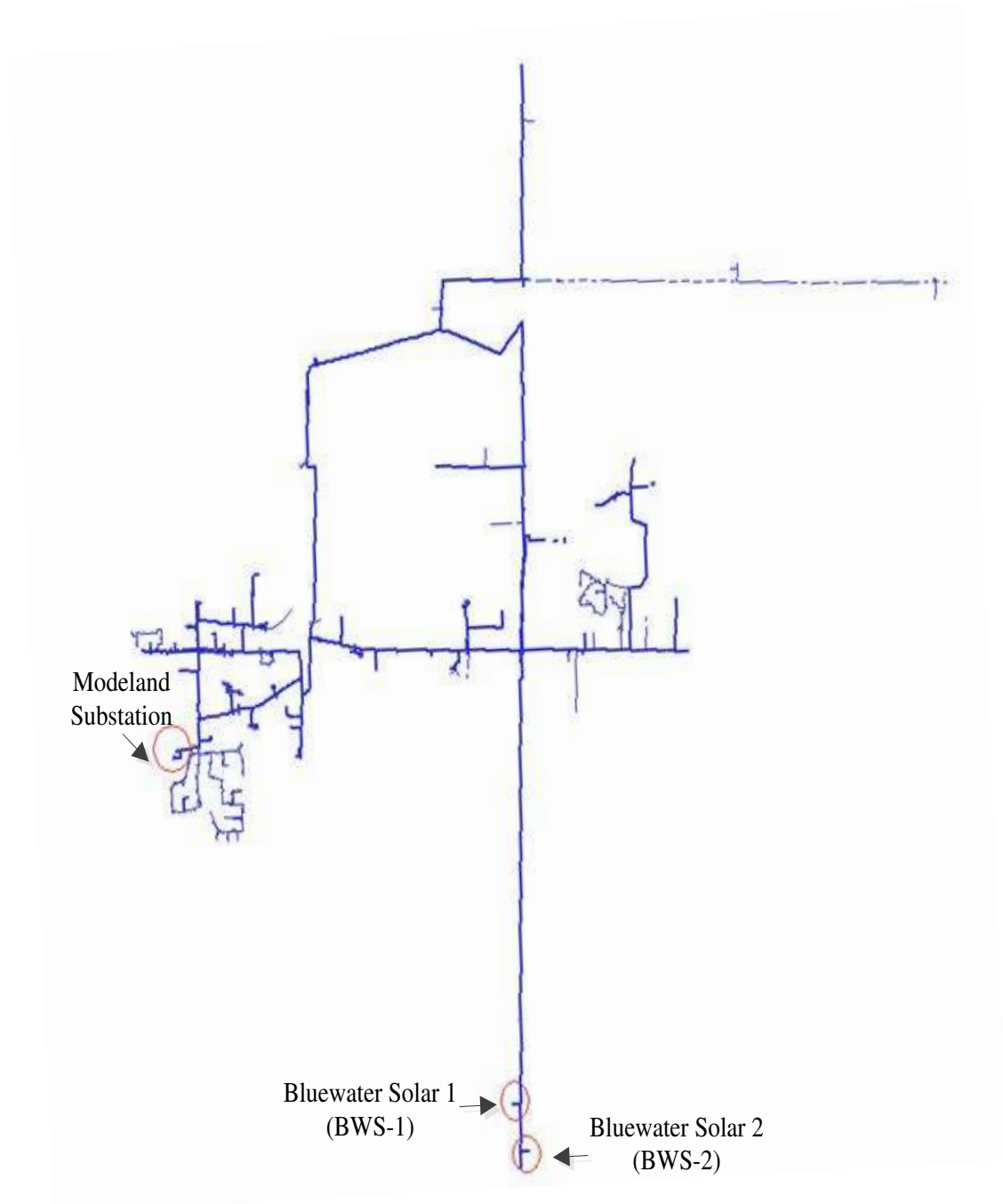
Figure 5.1 Feeder 96M23 model in GIS software
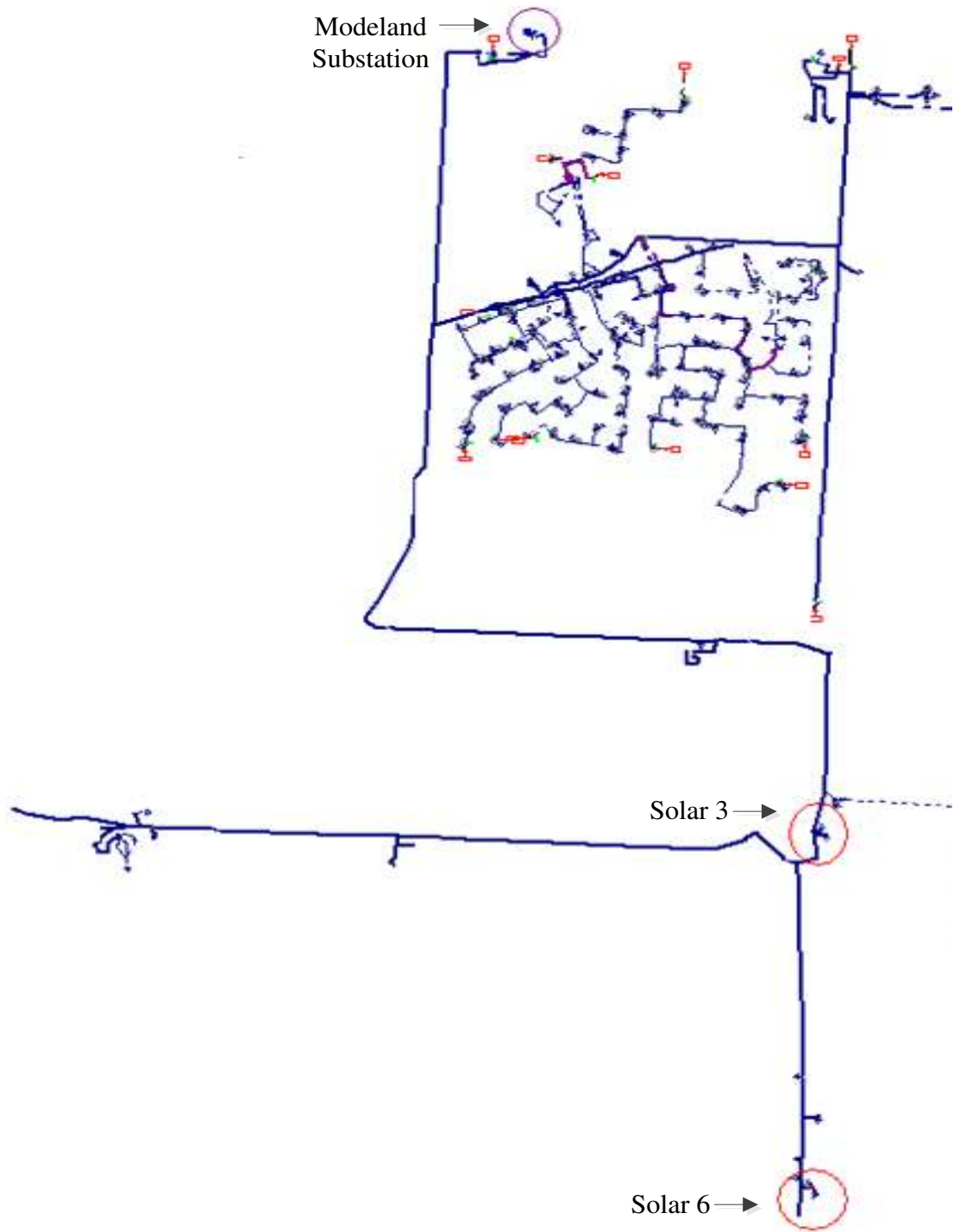
Figure 5.2 Feeder 96M27 model in GIS software

5.3   NETWORK DATA ACQUISITION SYSTEM

Network data such as feeder information, data related to solar farms, and substations are obtained from Supervisory Control and Data Acquisition System (SCADA), installed at the BWP office, GIS, central database, and the BWP control room personnel.

5.3.1   SCADA system

The SCADA system is a centralized monitoring and control system. It gathers data from the monitoring equipment, or from the sensors on the network, and controls the system based on the sensor data. Bluewater Power uses the SCADA system to monitor online power flow, voltages, currents, power factor, and the status of switches at different substations, solar farm locations, and other critical locations in its network [98].

5.3.2   GIS system

The GIS system is used to capture, store, and manage all types of geographical data. It stores the technical parameters of an electrical network, such as the location of loads, line lengths, and transformers (underground or overhead), switches, and breakers, along with their specifications laid out on a geographical map [99].

5.4   SYSTEM MODELING

The CYMDIST and PSCAD/EMTDC software applications are used for this research work. The CYMDIST software is used at BWP for the load flow, voltage profile, and short circuit studies of BWP [100]. CYMDIST is used to construct the network model from the GIS data and SCADA information in order to simulate the steady state load flow study. As CYMDIST does not have the capability to perform harmonic resonance studies, the network is modeled using PSCAD/EMTDC, which has this capability. Hence, CYMDIST is used to validate the steady state load flow results of the PSCAD/EMTDC model. After the steady state load flow is validated using PSCAD/EMTDC, a network model developed in PSCAD/EMTDC and is used for the network resonance harmonic impact studies.

5.4.1   Grid/Source Model

5.4.1.1   *CYME Model*

In CYMDIST, the Modeland substation is modeled as a voltage source behind the short circuit impedance according to the short circuit data available from BWP on the low voltage side of the substation transformer, given in Table 5.1. Based on this data, CYMDIST calculates the equivalent short circuit impedance.

Table 5.1 Short Circuit Data at Low Voltage side of Modeland Station

Substation	3-ph Fault MVA	3-ph Fault kA	3-ph X/R
Modeland	633.7	13.25	35.5

5.4.1.2   *PSCAD/EMTDC Model*

In PSCAD/EMTDC, the grid is modeled as per the short circuit data given in Table 5.1 and depicted in Figure 5.3.
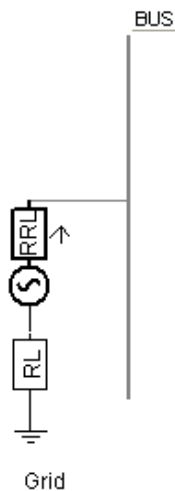
Figure 5.3 Grid model in PSCAD/EMTDC software

5.4.2   Feeder Model

5.4.2.1   *CYME Model*

Each overhead line and cable are modeled based on the data collected from these sources:

a. Bluewater Power material list document for underground cables and overhead line conductors.

b. Conductor manufacturer's datasheet

c. Engineering design team information

d. BWP stock room and control room personnel

Based on the above information, resistance (R), inductive reactance (X_L), and capacitive reactance (X_C), for both positive and zero sequence networks, are calculated and used for the modeling of each segment on the network. Cables and overhead conductor lengths are taken from the GIS system used in BWP.

5.4.2.2 *PSCAD Model*

Figure 5.4 depicts the model of overhead lines and underground cables in PSCAD/EMTDC. The R, X_L, and X_C parameters used in the CYMDIST model for both positive and zero sequence are used in PSCAD/EMTDC to model the entire feeder. In PSCAD/EMTDC, each cable and overhead conductor is modeled as a nominal PI section. Cables and overhead conductor lengths are used as per the GIS data.
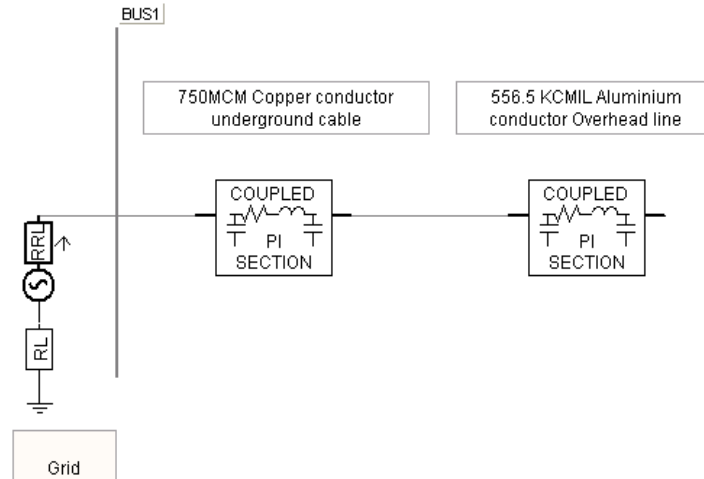
Figure 5.4 Overhead line and underground cable model of the feeder in PSCAD/EMTDC software

5.4.3 Load Model

The distribution system analysis software uses different types of load models such as constant power, constant impedance, and constant current load models [112]. In a distribution system, incandescent lighting, cooking stoves, and water heaters are classified as

constant impedance loads; electric motors and switched mode power supplies (SMPS) are classified as constant power loads. Whereas, welding units and smelters used in industries are considered as constant current loads. Figure 5.5 shows the variation of demand on different types of loads with voltage profiles of the system [101]. For this study, as both feeders supply mainly residential and commercial loads, the loads are modeled as an aggregation of both constant impedance and constant power loads. Different load allocation methods are employed for the analysis of a distribution system such as daily consumption (kWh) data [101]-[103], monthly consumption (kWh) data, transformer kVA rating (connected kVA) [103], and the REA (Rural Electrification Allocation) [103] method. For this study, the transformer kVA rating load allocation method is chosen for load allocation for both feeders, as transformer loading information is readily available from the BWP metering units, SCADA data, and BWP control room personnel. The connected kVA method assigns the metered load demand defined at the substation among the different loads, in proportion to the distribution transformer capacity [101]-[104].
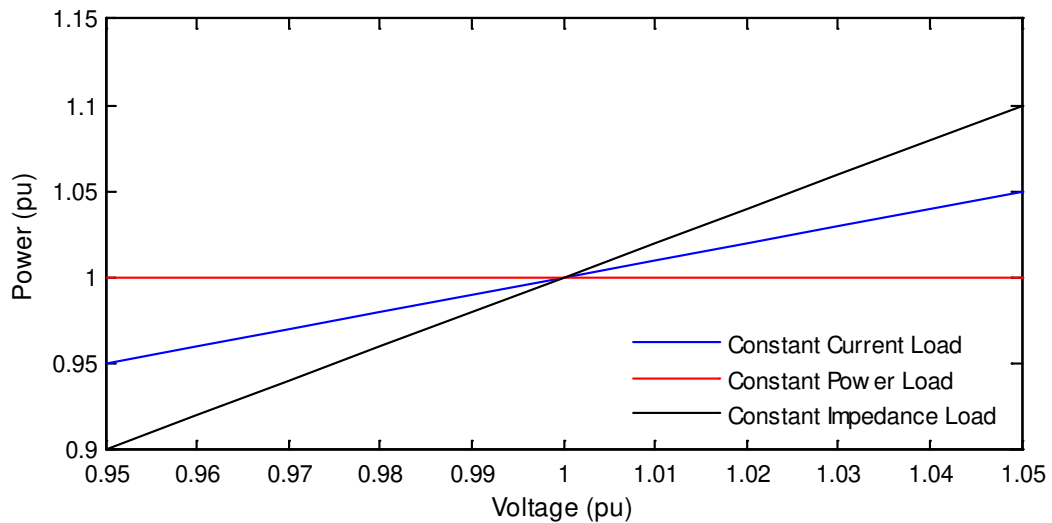
Figure 5.5 Variation of load demand with system voltage for different types of load

5.4.3.1 *CYME Model*

In CYMDIST, all transformers in Feeder 1 and Feeder 2 are considered to be spot loads and are modeled as an aggregation of both constant impedance and constant power loads. For the allocation of kW and kvar on the transformers, a power factor of 0.92 is chosen for Feeder 1

and a power factor of 0.94 is chosen for the Feeder 2, as per the SCADA (Supervisory Control and Data Acquisition System) system and BWP control room personnel.

5.4.3.2 *PSCAD Model*

Figure 5.6 shows the modeling of three-phase and single-phase loads using PSCAD/EMTDC. In PSCAD/EMTDC, the loads in Feeder 1 and Feeder 2 are considered to be spot loads and are modeled as an aggregation of both constant impedance and constant power loads in order to validate the steady state load flow model in both software applications. The power factor for both models are chosen as per the CYMDIST model of 0.92 for Feeder 1 and 0.94 for Feeder 2.
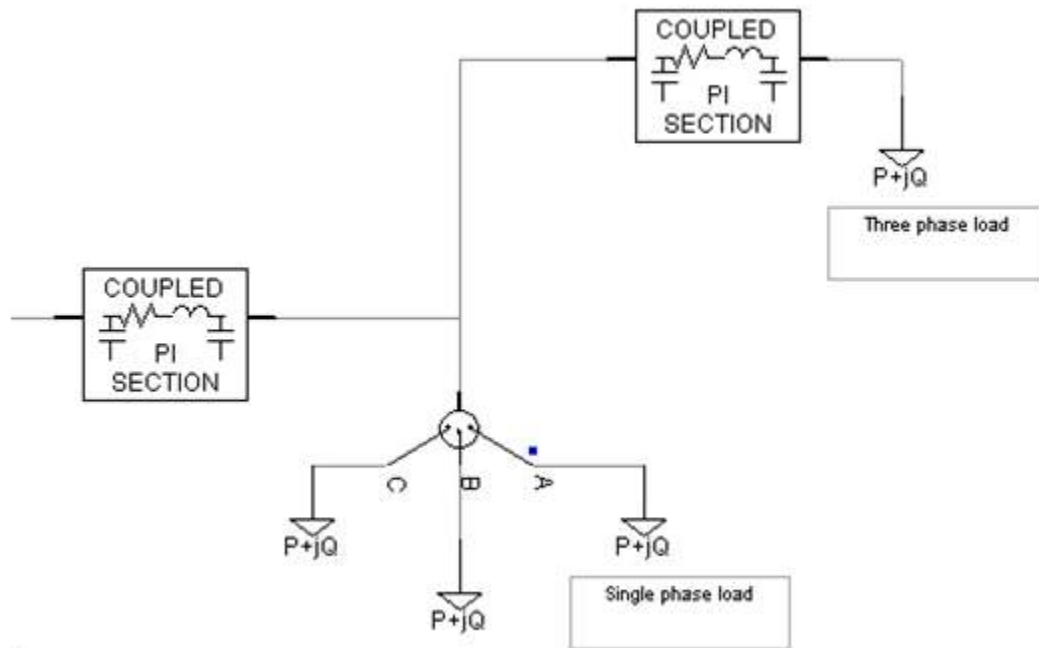
Figure 5.6 Load Model in PSCAD/EMTDC

5.4.4   PV Model

Distributed generators are not allowed to control the voltage at the point of common coupling and usually control the output current in order to operate at unity power factor, as per IEEE 1547 [91],[105]. Hence, for this study purpose, these PV inverters are modeled as an equivalent P-Q bus for load flow validation purposes only. However, for a detailed harmonics analysis, the inverter based DGs are represented as current sources with an

aggregation of multiple harmonic current sources [105]. For load flow studies and for harmonic analysis, each of the 10 MW PV systems is modeled as a single aggregated source, both in CYMDIST and PSCAD/EMTDC software applications.

5.4.4.1 *CYME Model*

The PV system is modeled as an electronic coupled generator, as provided in the CYME library.

5.4.4.2 *PSCAD Model*

Figure 5.7 demonstrates the current source model to represent the PV system. This PV model represents the PV system as a P-Q bus by injecting active power in to the grid at unity power factor. ANG is the voltage angle at the PCC in order to control both active and reactive power injection to the grid, to operate the PV system at unity power factor.
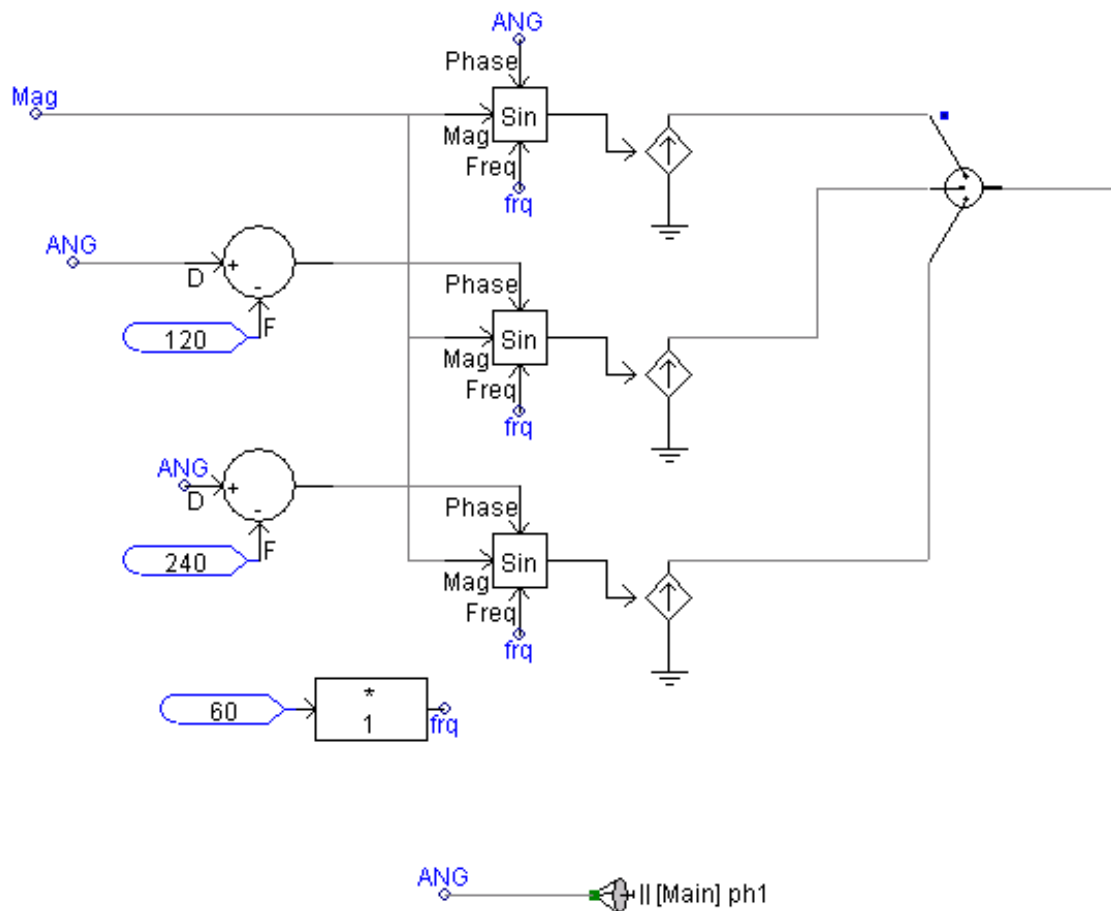
Figure 5.7 PV modeled as a current source

PV inverters are a source of different harmonics. Hence, for the harmonic resonance studies, the PV system is modeled as an aggregation of harmonic current sources at different frequencies. Figure 5.8 illustrates different harmonics injections from a typical PV system. The line impedance between the PCCs of the two 10 MW PV systems is very small and therefore does not create any significant phase differences between the current sources of the same order of two 10 MW PV units.
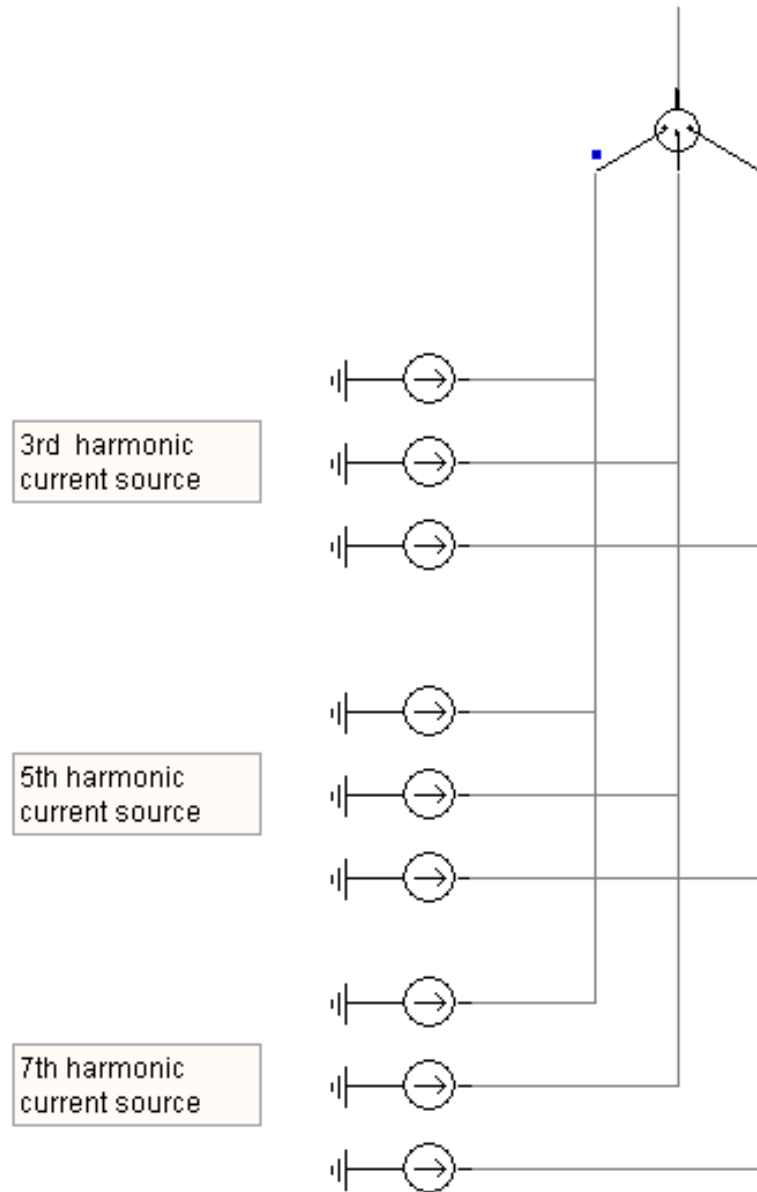
Figure 5.8 PV system as harmonic current source

5.4.5   Complete System Modeling

A complete system model for both Feeders 96M23 and Feeder 96M27 using PSCAD/EMTDC are given in Appendix D.1, D.2 and D.3, respectively.

5.5   STEADY STATE LOAD FLOW VALIDATION

Steady state load flow results for both feeders are verified using PSCAD/EMTDC and CYME, with real time SCADA data for one peak load and light load condition. Although PSCAD/EMTDC is electromagnetic transient simulation software, the load flow results can be validated with its steady state simulation output. This validation is performed in terms of voltages at different points on the feeder, with corresponding power flow.

5.5.1   Feeder 96M23

Figure 5.9 presents the load pattern of feeder 96M23 for two days. It is seen that the peak load occurs during the day, from 9:00 AM until 8:00 PM in the evening, with a peak load of approximately 12 MW to 16 MW. Similarly, light load occurs during the night, from 8:00 PM until 9:00 AM, with a load of approximately 6 MW to 9 MW. For load flow validation, one peak load scenario is chosen during the daytime, at 4:06 PM, and one light condition is chosen during the night, at 11:00 PM. Load flow results for active power, reactive power, and rms line to line voltages are verified at the Modeland station and at the solar farm (Bluewater Solar 1 and Bluewater Solar 2) locations. As SCADA data is available only at the Modeland station and at two solar farm locations (Bluewater Solar 1 and Bluewater Solar 2), these locations are taken into account to match the steady state load flow. Table 5.2 and Table 5.3 depict the load flow results on feeder 96M23 for both peak load and light load conditions respectively. It is observed from both tables that load flow results from CYMDIST closely match with the real time SCADA data, with an error rate of less than 0.6%. The close correlation of load flow results confirms the accuracy of the feeder model built in CYMDIST. It is further seen that the load flow results of PSCAD/EMTDC matches very well with that of the CYMDIST model, with an error rate of less than 0.6%, thus, validating the PSCAD/EMTDC model of feeder 96M23 for both peak load and light load conditions.
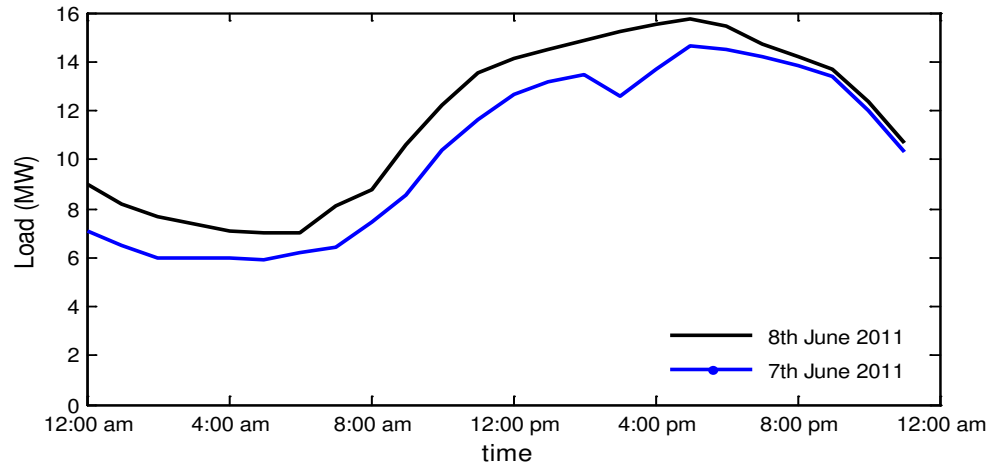
Figure 5.9 Load profile of 96M23

Table 5.2 Load flow validation during peak load

Location	Real Time SCADA data	CYME	PSCAD	Deviations (%) SCADA vs. CYME	Deviations (%) CYME vs. PSCAD
Voltage (kV)					
Modeland Substation	28.71	28.71	28.71	0	0
Bluewater Solar 1	28.92	28.82	28.84	0.34	0.06
Bluewater Solar 2	28.98	28.83	28.85	0.51	0.07
Active Power (MW)					
Modeland Substation	-1.70	-1.71	-1.70	0.58	0.58
Bluewater Solar 1	8.15	8.14	8.14	0.12	0
Bluewater Solar 2	8.01	8.01	8.00	0	0.12
Reactive Power (MVAR)					
Modeland Substation	7.71	7.70	7.69	0.12	0.12
Bluewater Solar 1	0.02	-0.05	-0.0004	-	-
Bluewater Solar 2	0.01	-0.08	-0.0003	-	-

Table 5.3 Load flow validation during light load

Location	Real time SCADA data	CYME	PSCAD	Deviations (%) SCADA vs. CYME	Deviations (%) CYME vs. PSCAD
Voltage (kV)					
Modeland Substation	28.57	28.57	28.57	0	0
Bluewater Solar 1	28.40	28.44	28.43	0.14	0.03
Bluewater Solar 2	28.52	28.44	28.43	0.28	0.03
Active Power (MW)					
Modeland Substation	9.20	9.21	9.21	0.10	0
Bluewater Solar 1	0.00	0.00	0.00	-	-
Bluewater Solar 2	0.00	0.00	0.00	-	-
Reactive Power (MVAR)					
Modeland Substation	3.90	3.89	3.91	0.25	0.51
Bluewater Solar 1	0.00	0.00	0.00	-	-
Bluewater Solar 2	0.00	0.00	0.00	-	-

5.5.2   Feeder 96M27

Figure 5.10 demonstrates the load pattern of feeder 96M27 for two days.
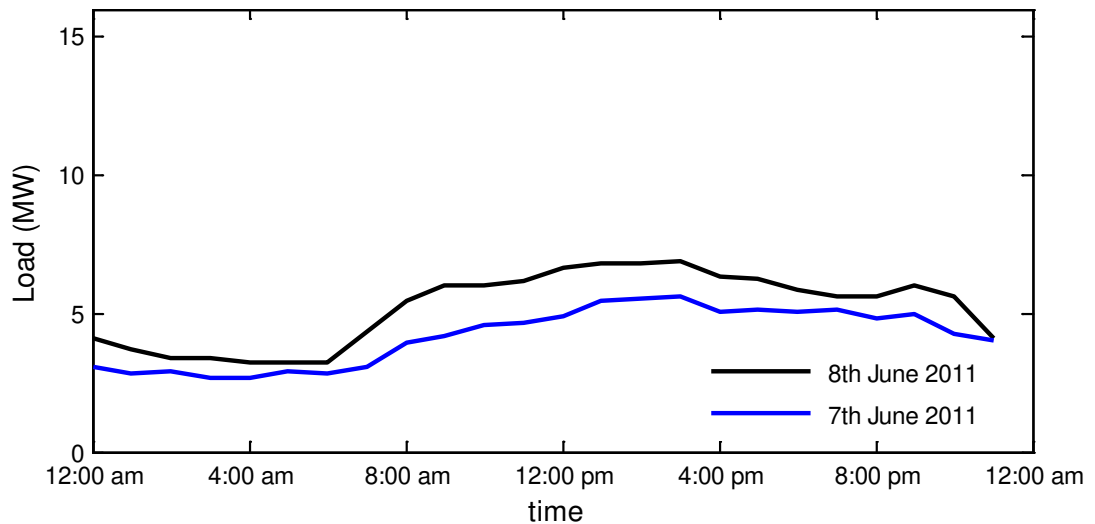
Figure 5.10 Load profile of 96M27

It is observed that the peak load occurs during the day, from 10:00 AM until 8:00 PM at night, with a peak load of approximately 6 MW to 7 MW. Similarly, light load occurs during the night until 8:00 AM, with a load between 3 MW to 5 MW. To validate the load flow, one peak load scenario is chosen during the day, at 5:00 PM, and one light condition is chosen during the night, at 12:00 AM. Table 5.4 and Table 5.5 depict the load flow results on feeder 96M27 for both peak load and light load conditions respectively. Load flow results for active power, reactive power, and rms line-to-line voltages are verified at the Modeland station and at the solar farm (Solar 3 and Solar 6) locations. It is observed from both tables that load flow results from CYMDIST closely match with the real time SCADA data, with an error rate of less than 0.8%. The close correlation of load flow results confirms the accuracy of the feeder model built in CYMDIST. It is further seen that the load flow results of PSCAD/EMTDC match very well with that of the CYMDIST model, with an error rate of less than 0.6%, thus validating the PSCAD/EMTDC model of feeder 96M27 for both peak load and light load conditions.

Table 5.4 Load flow validation during peak load

Location	Real Time SCADA data	CYME	PSCAD	Deviations (%) SCADA vs. CYME	Deviations (%) CYME vs. PSCAD
Voltage (kV)					
Modeland Substation	28.17	28.28	28.20	0.39	0.28
Solar 3	28.35	28.37	28.37	0.07	0
Solar 6	28.38	28.40	28.40	0.07	0
Active Power (MW)					
Modeland Substation	-6.10	-6.10	-6.07	0	0.49
Solar 3	6.07	6.07	6.06	0	0.16
Solar 6	6.25	6.29	6.24	0.64	0.79
Reactive Power (MVAR)					
Modeland Substation	2.70	2.68	2.69	0.74	0.37
Solar 3	0.03	-0.04	-0.0003	-	-
Solar 6	0.01	-0.07	-0.0004	-	-

Table 5.5 Load flow validation during light load

Location	Real Time SCADA data	CYME	PSCAD	Deviations (%) SCADA vs. CYME	Deviations (%) CYME vs. PSCAD
Voltage (kV)					
Modeland Substation	29.02	28.96	28.92	0.20	0.13
Solar 3	29.01	28.91	28.85	0.34	0.20
Solar 6	29.01	28.91	28.85	0.34	0.20
Active Power (MW)					
Modeland Substation	4.00	3.98	3.99	0.5	0.25
Solar 3	0.00	0.00	0.00	-	-
Solar 6	0.00	0.00	0.00	-	-
Reactive Power (MVAR)					
Modeland Substation	1.40	1.37	1.39	2.14	1.45
Solar 3	0.00	0.00	0.00	-	-
Solar 6	0.00	0.00	0.00	-	-

5.6 NETWORK IMPEDANCE AND RESONANCE ANALYSIS

Every electrical network exhibits resonance at certain frequencies due to the presence of inductive and capacitive elements in the system. This resonance behavior of the network varies with different loading conditions, short circuit level, and line outages. The frequency scan technique is adopted in PSCAD/EMTDC models for feeders, 96M23 and 96M27, to analyze the network resonance in the presence of PV. The frequency scan technique [106] calculates the Thevenin equivalent network impedance as a function of frequency, as observed from a particular bus/location on the system. By plotting the impedance magnitude versus frequency obtained from the frequency scan, the network resonance frequency can be identified where the impedance is maximum.

5.6.1   Feeder 96M23

Network resonance analysis is performed on feeder 96M23 for different operating conditions at different buses in the network. Three major locations are chosen: the Modeland substation (Station) and two solar farm locations - Bluewater Solar 1 (BWS-1) and Bluewater Solar 2 (BWS-2), as SCADA sensors are connected at these locations. The results of the network impedance analysis at different operating conditions of the network are presented below.

5.6.1.1   *Base Case at actual Short Circuit Level (633.7 MVA)*

Figure 5.11 depicts the frequency scan for the actual short circuit level (SCL) at the Modeland substation for different loading conditions, taken as a base case scenario. It is observed that network resonance occurs above the 33rd harmonics at three locations for both peak load and light load conditions. The peak magnitude of impedance varies for different loading conditions.
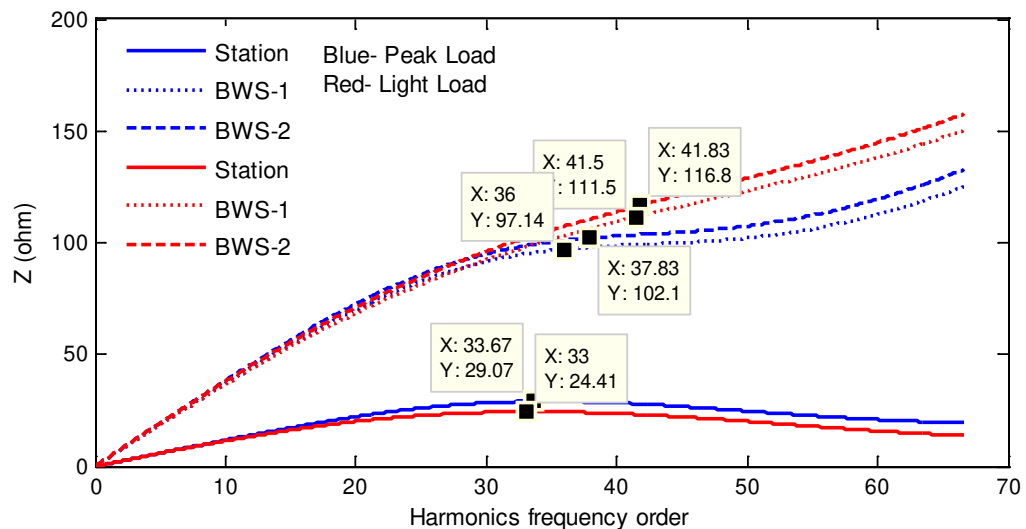
Figure 5.11 Network impedance vs harmonics frequency for 96M23 at SCL

5.6.1.2   *Variation of Short Circuit Level and loading condition*

As network resonance varies with different SCLs of the source, the SCL of the source is varied and the frequency scan of the network is conducted for three different short circuit levels. A strong system with two times SCL is selected. Further, two weak systems, with half and one fifth SCL, are selected for the study.

Figure 5.12 demonstrates the network impedance at 2×SCL. It is observed that resonant frequency occurs above the 41st harmonic for both the loading conditions at three different locations for 2×SCL. Similarly, Figure 5.13 and Figure 5.14 depict the network resonance at 1/2×SCL and 1/5×SCL respectively. It is seen that at 1/2×SCL, resonance occurs around the 25th harmonic for different loading conditions. It is also observed that resonance occurs at the 17th harmonic for a short circuit level of 1/5×SCL. As such, it is thus confirmed that, when the SCL decreases, the system becomes weak and the resonant frequency shifts toward lower frequencies. Similarly when SCL increases, the resonant frequency shifts towards higher order frequency. Although not presented here, the effects of line outages and their associated impacts on the system's harmonic performance are evaluated at different arbitrary locations on the M23 feeder. It is observed that resonant frequency occurs around the 31st and 41st harmonics for different outage conditions. Based on this analysis, it is evident that resonant frequency on 96M23 lies between the 17th harmonic and the 41st harmonic, for different SCLs at different loading conditions. It is also observed that peak impedance is lower during peak loading condition compared to during a light load condition.
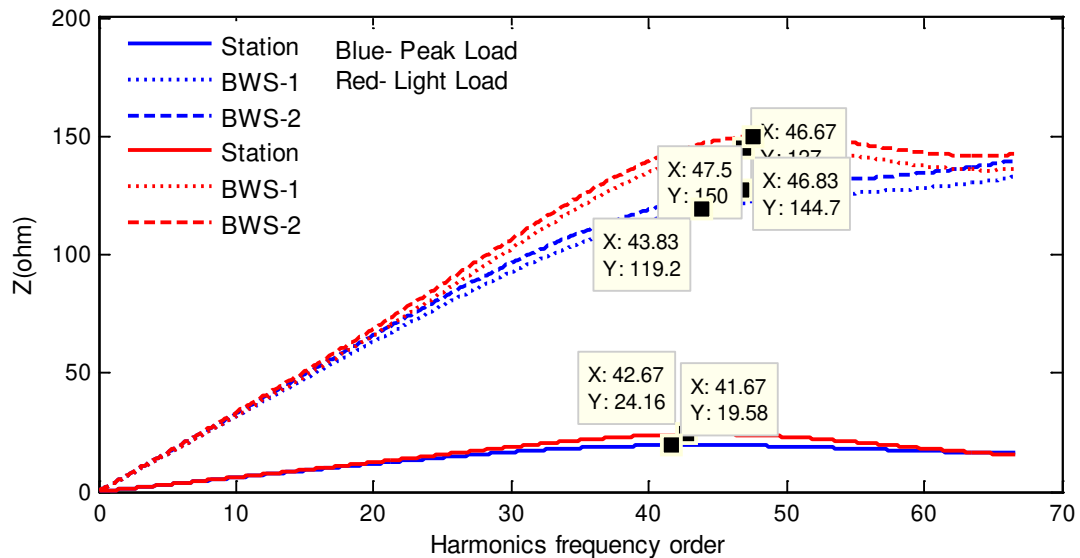
Figure 5.12 Network impedance vs harmonics frequency for 96M23 at 2×SCL
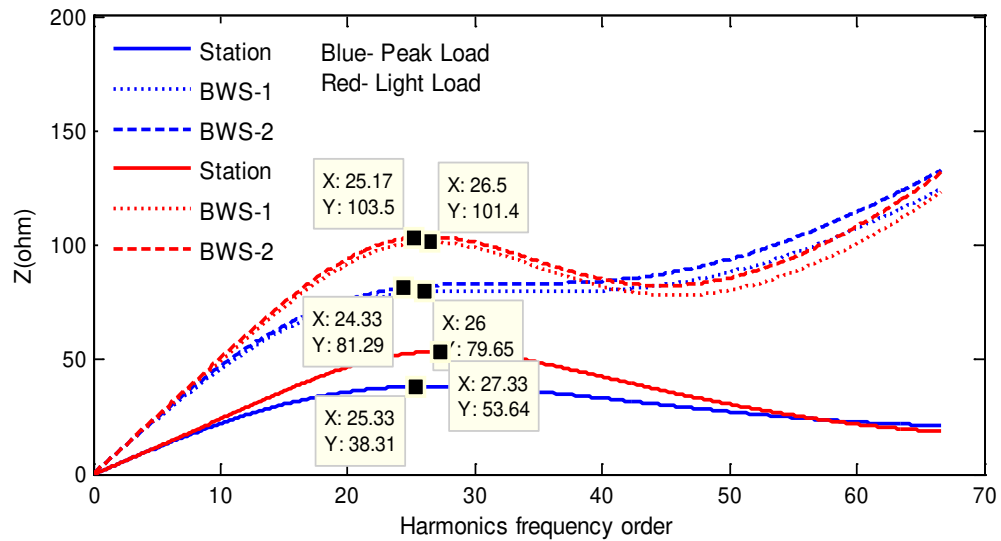
Figure 5.13 Network impedance vs harmonics frequency for 96M23 at 1/2×SCL
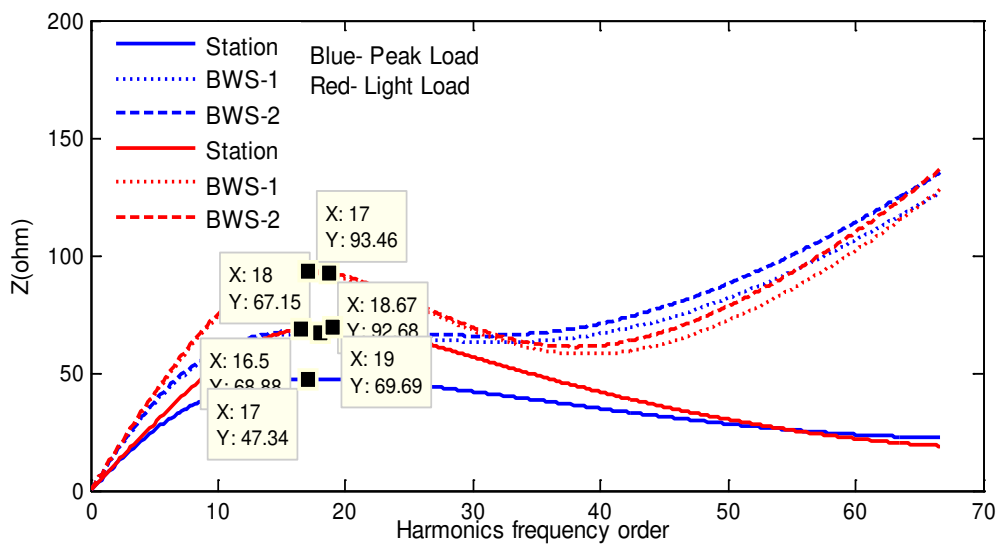
Figure 5.14 Network impedance vs harmonics frequency for 96M23 at 1/5×SCL

5.6.2   Feeder 96M27

Network impedance analysis is performed on the 96M27 feeder for different operating conditions at different buses in the network. The Modeland substation (Station), two solar farm locations (Solar 3 and Solar 6) are chosen for this network resonance analysis. The different studies performed are discussed below.

5.6.2.1 *Base Case at actual Short Circuit Level (633.7 MVA)*

Figure 5.15 depicts the frequency scan at the actual short circuit level (SCL) at the low voltage side of the Modeland substation for different loading conditions.
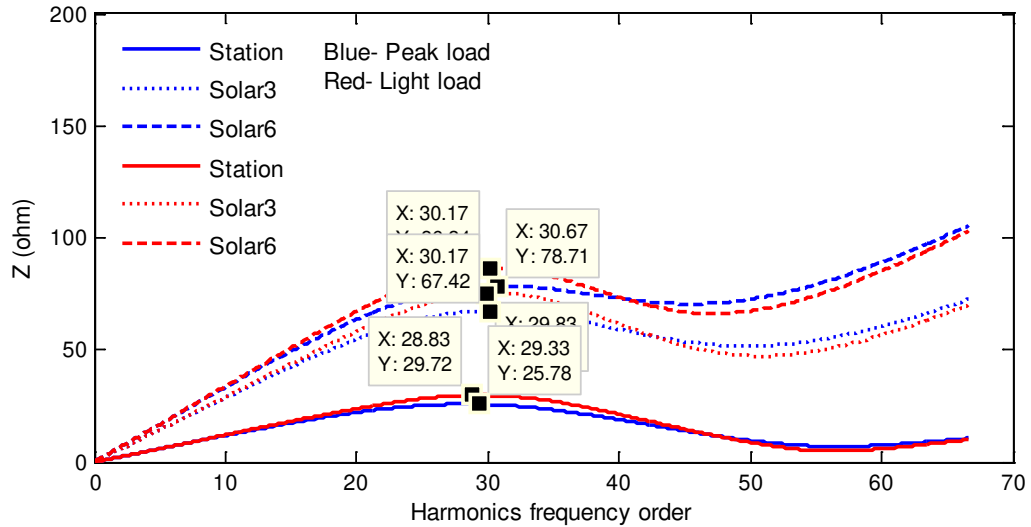
Figure 5.15 Network impedance vs harmonics frequency for 96M27 at SCL

This condition is taken as a base case scenario. It is observed that network resonance occurs above the 28th harmonic at three locations for both loading conditions. The peak impedance magnitude varies for different loading conditions.

5.6.2.2 *Variation of Short Circuit Level and different loading condition*

Figure 5.16, Figure 5.17, and Figure 5.18 present the frequency scan at 2×SCL, 1/2×SCL, and 1/5×SCL respectively. It is seen that resonance occurs around the 35th harmonic for 2×SCL, around the 23rd harmonic for 1/2×SCL, and around the 15th harmonic for 1/5×SCL. Thus, it is concluded that resonant frequency on 96M27 lies between the 15th harmonic and the 36th harmonic for this feeder, for various operating scenarios of the network. It is also observed that peak impedance is lower during a peak loading condition as compared to light load condition.
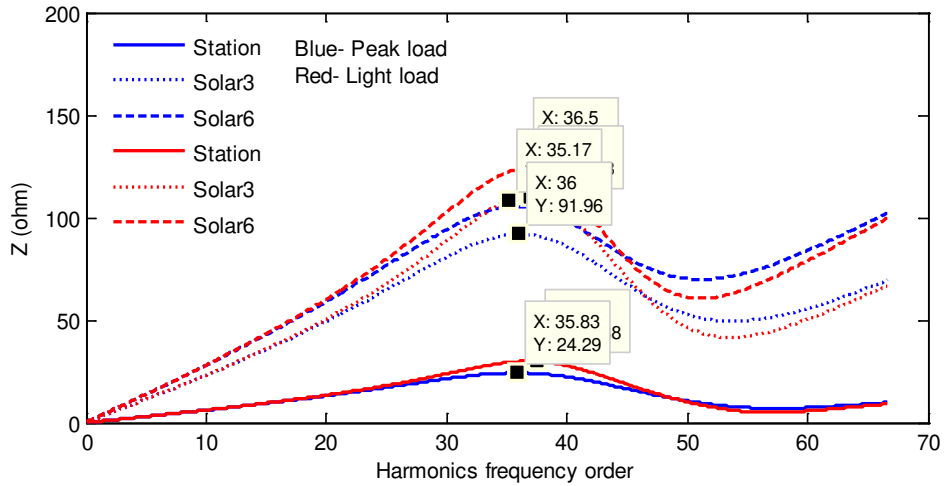
Figure 5.16 Network impedance vs harmonics frequency for 96M27 at 2×SCL
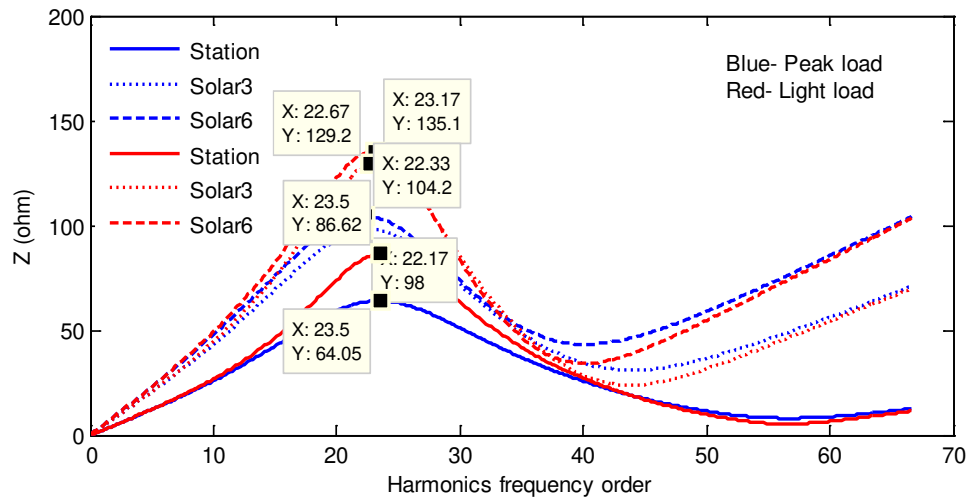
Figure 5.17 Network impedance vs harmonics frequency for 96M27 at 1/2×SCL
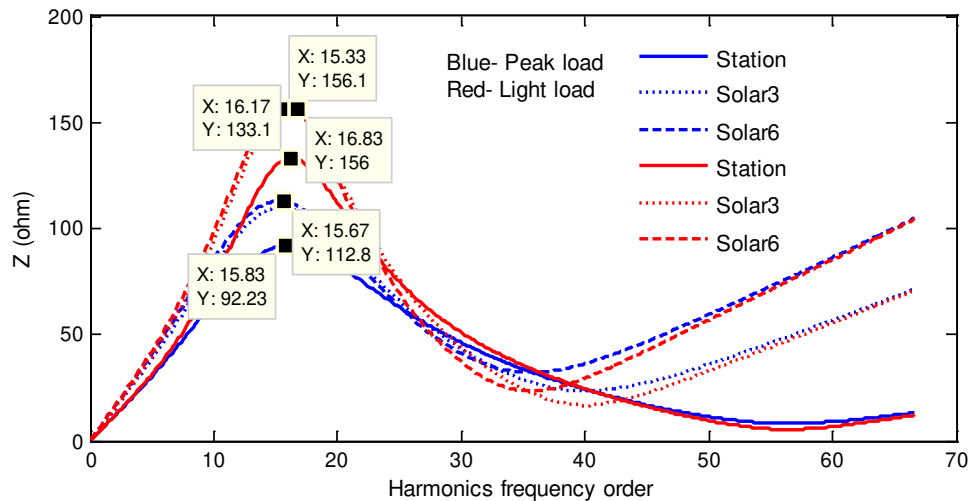
Figure 5.18 Network impedance vs harmonics frequency for 96M27 at 1/5×SCL

5.7   HARMONICS INJECTIONS FROM A 10MW PV SOLAR FARM

The harmonics injection from a 10 MW solar farm is recorded for the month of June, 2012 and analyzed at different power outputs from the PV inverters. Figure 5.19, Figure 5.20, Figure 5.21, and Figure 5.22 depict the harmonics injection at 9.98 MW, 5.33 MW, 2.71 MW, and 0.65MW power output from a 10MW PV system, respectively. As the harmonics datasets are available up to the 25th order, only this range of harmonics is chosen for the analysis. It is observed that the 5th, 7th, 11th, 13th, 17th, and 19th harmonics are the dominant harmonics and maximum individual harmonic distortion occurs at 2.71 MW power output. Similarly, the minimum individual harmonics occur at a power level of 0.65 MW. It is also noticed that individual harmonics distortion at a rated power output of 9.98 MW is less than that at 5.33 MW and 2.71 MW power output, but more than at 0.65 MW.
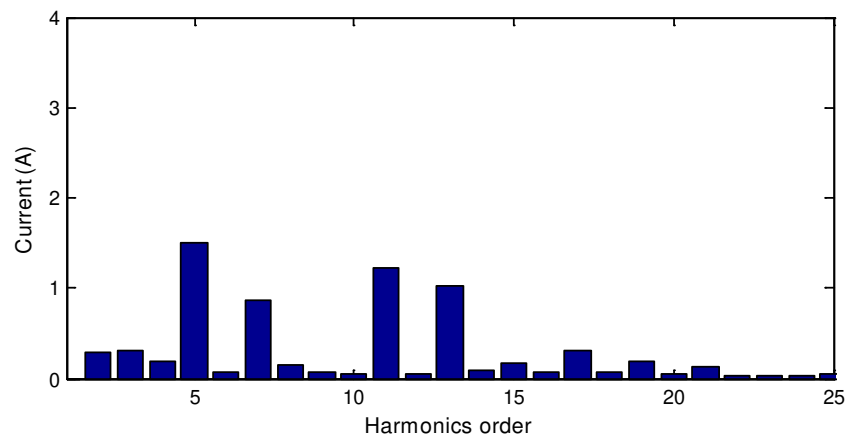
Figure 5.19 Harmonics injection at 9.98 MW power level from a 10 MW PV solar farm
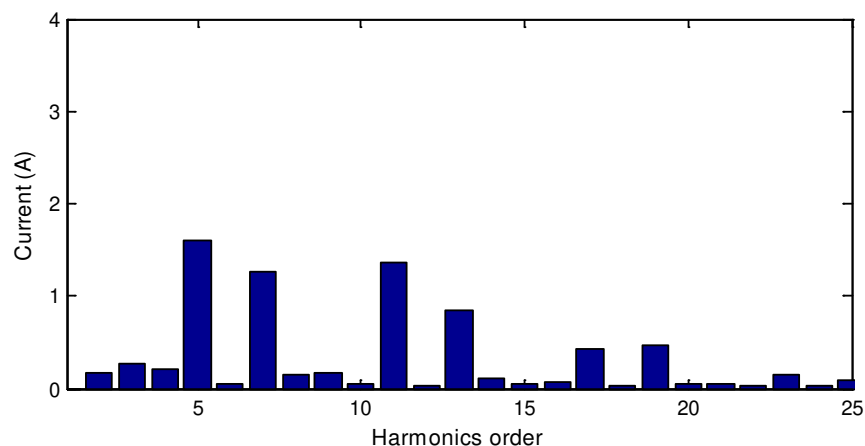
Figure 5.20 Harmonics injection at 5.33 MW power level from a 10 MW PV solar farm
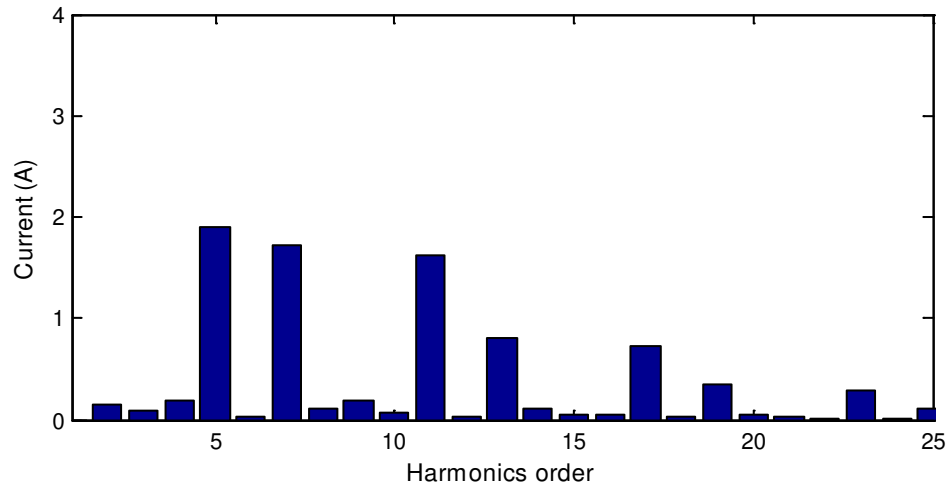
Figure 5.21 Harmonics injection at 2.71 MW power level from a 10 MW PV solar farm
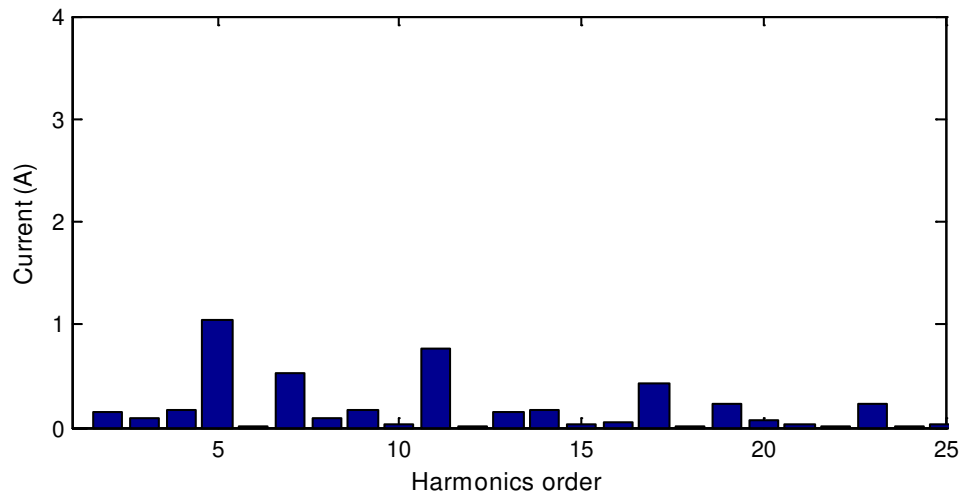
Figure 5.22 Harmonics injection at 0.65 MW power level from a 10 MW PV solar farm

Figure 5.23 shows the calculated Total Demand Distortion (TDD) for the output current harmonics (I_{TDD}) at different power levels from a 10MW PV system. The variation in individual harmonics distortions at different power levels is attributed to the design of the PV inverter, and for this 10MW solar farm, maximum distortion occurs at approximately 25-30% of power output. It is observed that I_{TDD} satisfies the IEEE standard 519 and remains within the specified limits for a wide range of power generation [84].
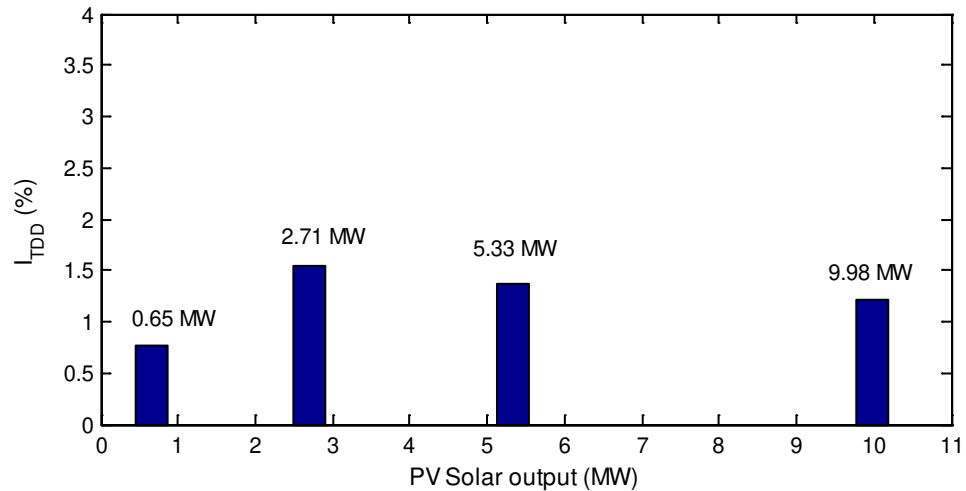
Figure 5.23 Total Current Demand Distortion at different power level

5.8   IMPACT OF 20MW PV SOLAR FARM HARMONICS ON THE NETWORK

This section presents the voltage harmonic distortion studies for the two feeders, for both peak load and light load conditions with the presence of 20MW solar farms.

5.8.1   Feeder 96M23

5.8.1.1   *Peak load Condition*

Peak load normally occurs between 10:00 AM and 8:00 PM, as demonstrated in Section 5.5. As such, noon is considered for this analysis, where the load is 14 + j7.7MVA. During this time, the PV solar farm generates different power depending upon the availability of the sun. On a full sunny day, it generates rated power of 10MW; whereas, on a cloudy day, power output from a solar farm varies depending upon the availability of the solar insolation. Hence, to study the voltage distortion at different location in the network, three different possible power outputs during peak load condition are examined.

Figure 5.24, Figure 5.25, and Figure 5.26 demonstrate the V_{THD} at three locations in the feeder with a short circuit level varying between 127 MVA (1/5 × nominal SCL) and 3168 MVA (5×nominal SCL) for different PV power outputs of 9.98 MW, 5.33 MW, and 2.71 MW, respectively.
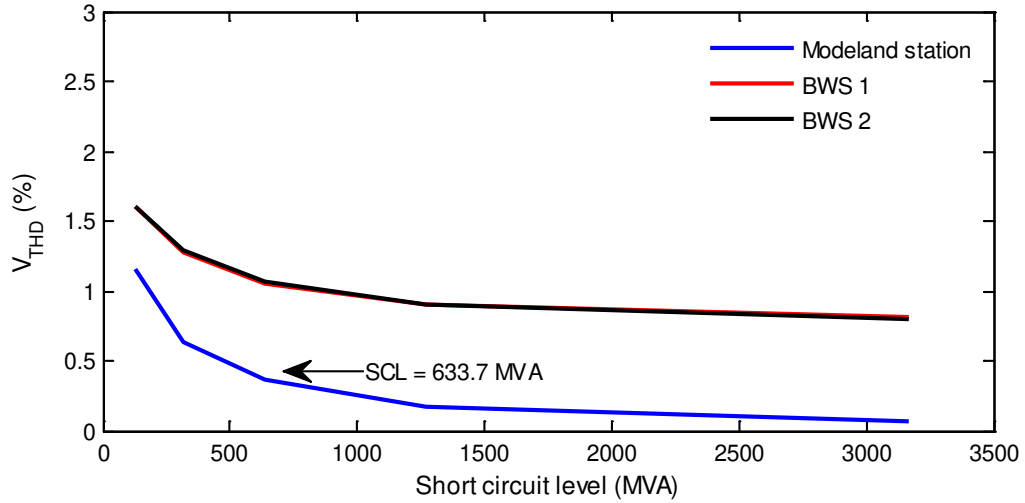
Figure 5.24 V_{THD} at different locations at PV Solar output = 9.98 MW
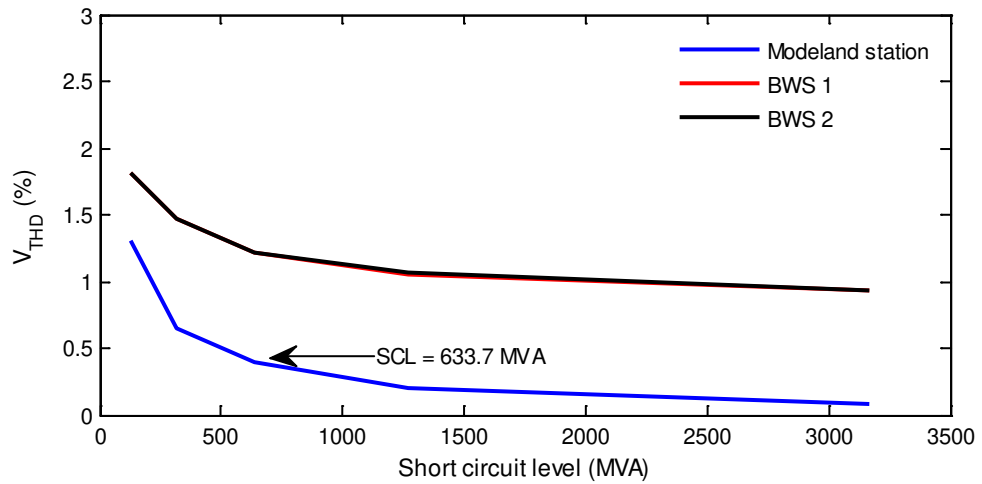
Figure 5.25 V_{THD} at different locations at PV Solar output = 5.33 MW
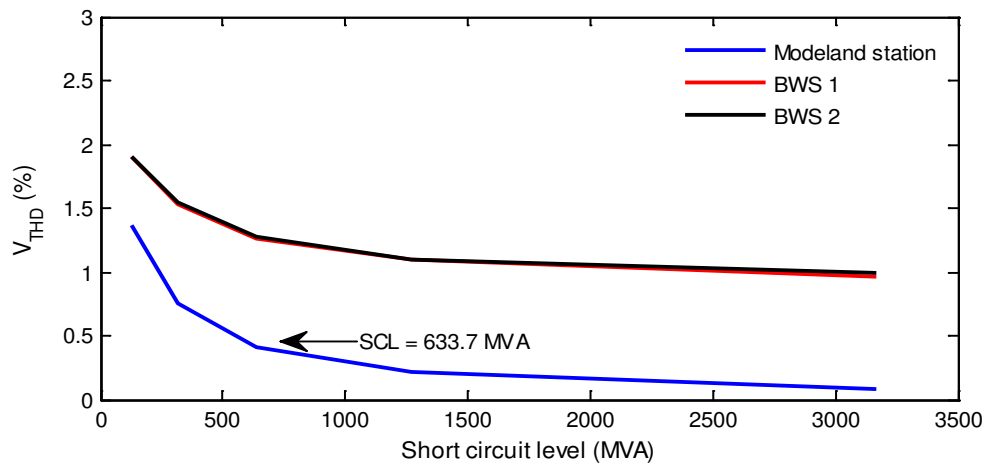
Figure 5.26 V_{THD} at different locations at PV Solar output = 2.71 MW

In each of these cases, it is observed that V_{THD} is less than 2% at all locations for three different PV power outputs; which is well below the acceptable voltage distortion rate of 5%, as per IEEE standard 519 [84]. Maximum voltage distortion V_{THD} occurs at 1/5 of the nominal short circuit level of 127MVA, whereas V_{THD} is minimal when the short circuit level is 5 times that of the nominal value of 633.7MVA. It is further noted that the voltage harmonic distortion is highest at the terminals of solar farms, and is much lower at the Modeland substation.

5.8.1.2   *Light load condition*

Light load normally occurs between 8:00 PM and 9:00 AM, as demonstrated in Section 5.5. Hence, 8:00 AM is chosen for this study, where the load is 8.7 + j3.8 MVA. At this time, the PV solar farm can only generate 20-30% of its rated power, as demonstrated in Section 2.2.1 in Chapter 2. Hence, to investigate the V_{THD}, a power output of 2.71 MW is considered.

Figure 5.27 demonstrates V_{THD} at three locations in the feeder with the short circuit level varying between 127 MVA and 3168 MVA for a PV power output of 2.71 MW. It is observed that V_{THD} is less than 2.5% at all three locations for a PV power output of 2.71 MW, which satisfies IEEE standard 519 [84].
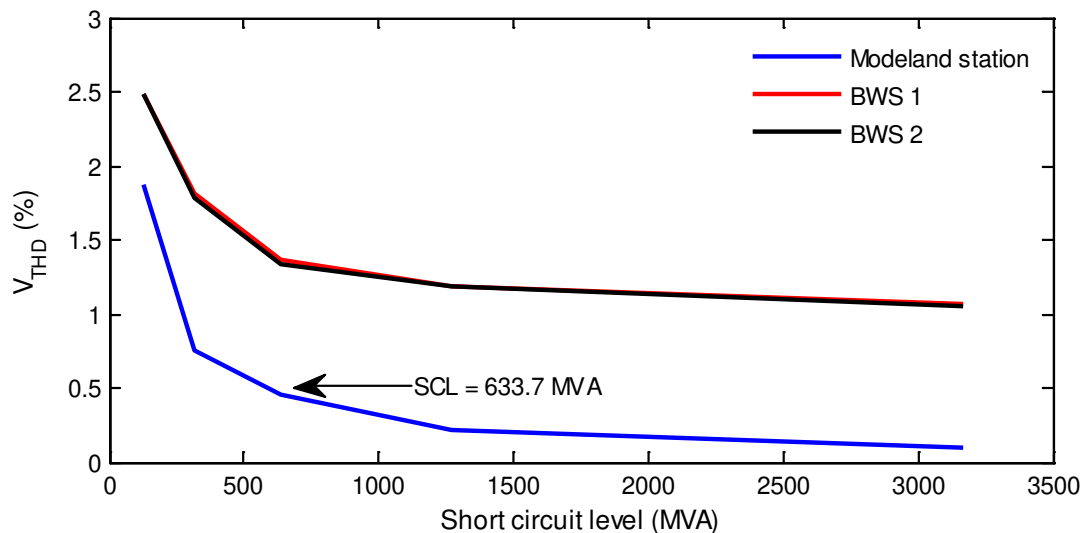
Figure 5.27 V_{THD} at different location at PV Solar output = 2.71 MW

5.8.2   Feeder 96M27

5.8.2.1   *Peak load condition*

Peak load for 96M27 is chosen at noon, or 12:00 PM. During this time, the load on the feeder is 6 + j2.7 MVA. To verify the voltage distortion at a different location in the network, three different possible power outputs from the PV solar farm are chosen during the peak load condition, as in the study of feeder 96M23.

Figure 5.28, Figure 5.29, and Figure 5.30 demonstrate the V_{THD} at three locations in the feeder with a short circuit level for different PV power outputs. In all cases, the V_{THD} is about 2.5%, which is within 5%, as specified in IEEE 519 [84].
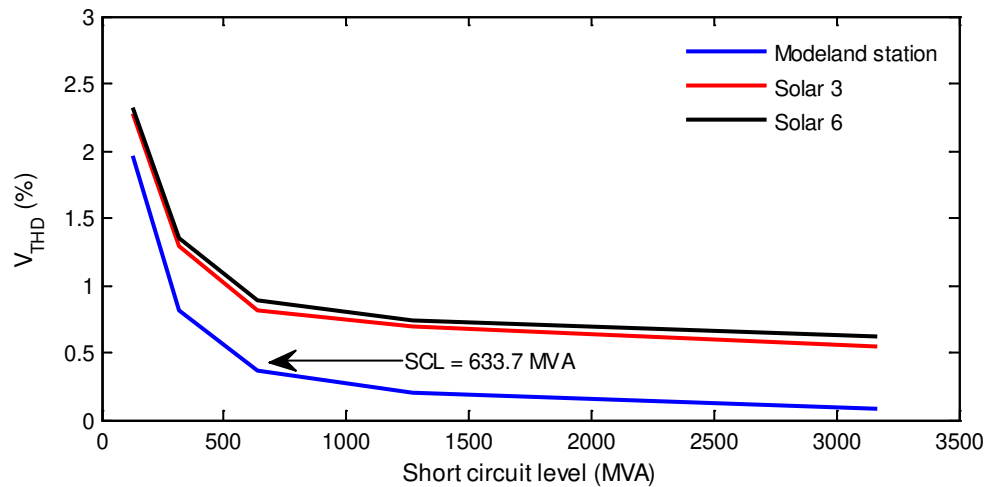
Figure 5.28 V_{THD} at different location at PV Solar output = 9.98 MW
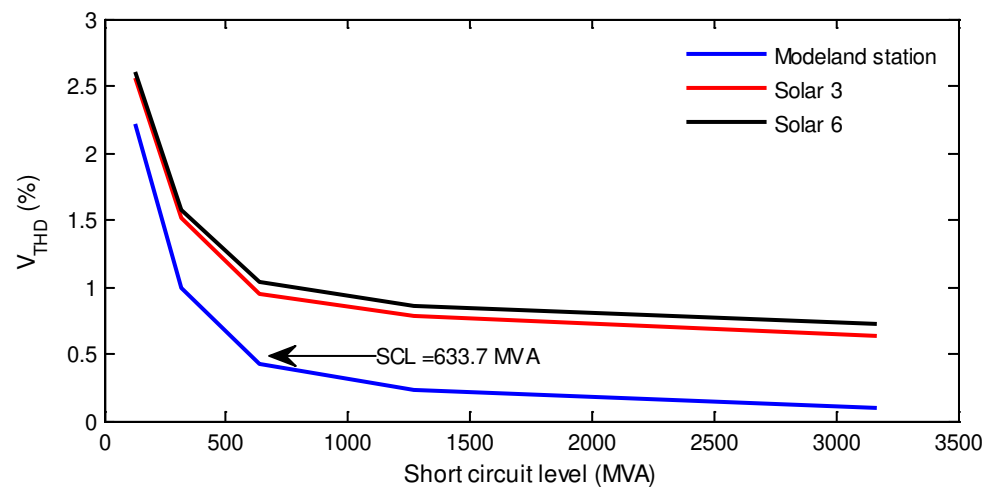
Figure 5.29 V_{THD} at different location at PV Solar output = 5.33 MW
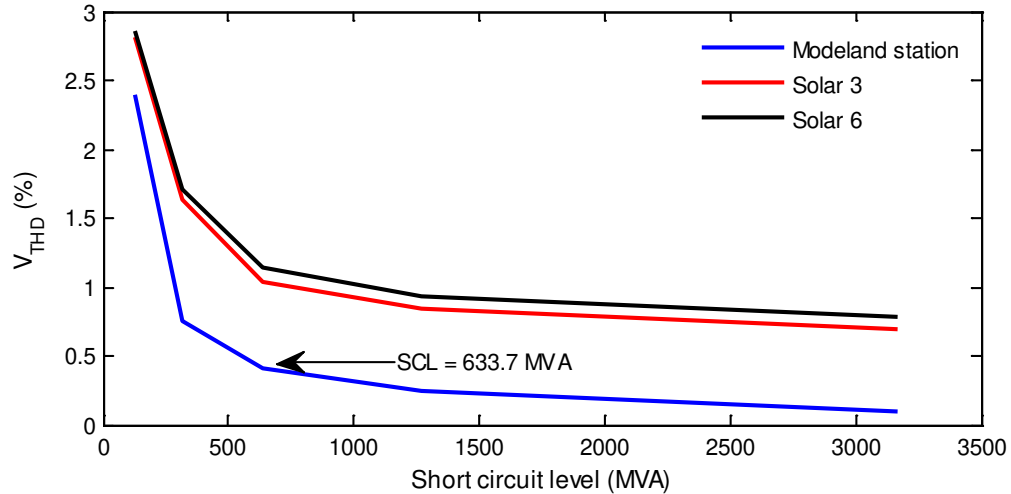
Figure 5.30 V_{THD} at different location at PV Solar output = 2.71 MW

It is also found that maximum V_{THD} occurs at a short circuit level of 127 MVA, where the minimum V_{THD} occurs at a short circuit level of 3168 MVA, as demonstrated in the previous case. It is further noted that the voltage harmonic distortion is highest at the terminals of solar farms, and is much lower at the Modeland substation.

5.8.2.2 Light load condition

A light load condition of 4 + j1.7 MVA is chosen during the morning at 8:00 AM, the same as that of feeder 96M23. This loading condition is considered with a PV power output of 2.71 MW for voltage harmonic distortion study at three different locations. It is observed that the V_{THD} is less than 3% at all three locations for a PV power output of 2.71 MW, which is within 5%, as specified in IEEE standard 519 [84].
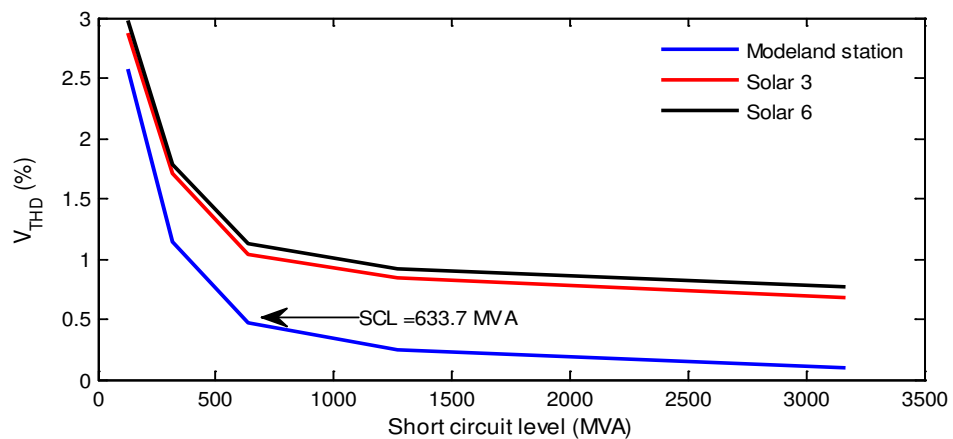
Figure 5.31 V_{THD} at different location at PV Solar output = 2.71MW

5.9   IMPACT OF A 10 KW PV SOLAR SYSTEM HARMONICS ON NETWORK RESONANCE

This section presents the harmonic impact of a small scale 10 kW PV solar farm on the BWP network. Figure 5.32 depicts a 10 kW PV solar system connected to a commercial shopping complex on Feeder 96M23. This 10 kW PV system is considered to be connected to a 600V bus and is connected to 96M23 through a step-up transformer operating at a voltage level of 600/27600V. A 20 MW PV solar farm is also connected on the feeder.
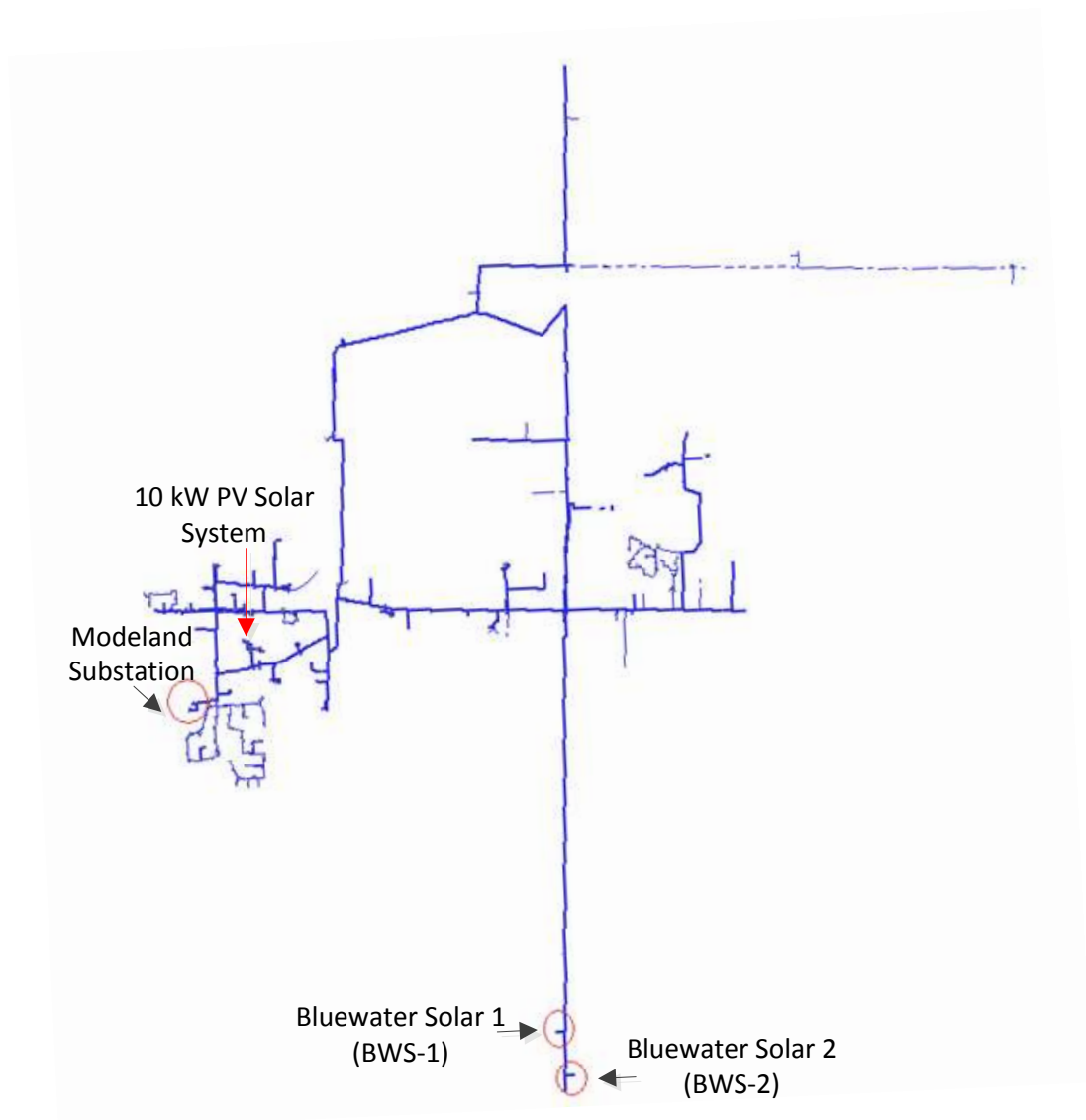
Figure 5.32 Feeder 96M23 with a 10 kW PV Solar System

Figure 5.33 demonstrates the worst case harmonics output from the commercial 10 kW PV solar system. It is observed that the worst case harmonics occurs at a power level of 4 kW. For this case, I_{TDD} is found to be 5.1%. The prominent harmonics generated from this PV system are the 3rd, 5th, 7th, 9th, 11th, 13th, 17th, and 19th harmonics. The magnitude of individual harmonics is shown in Figure 5.33.

Figure 5.34 demonstrates the V_{THD} at the Modeland station and at the location where the 10kW PV system is connected with a varying short circuit level. It is seen that the maximum V_{THD} occurs at a SCL level of 127 MVA. Even at this SCL, the V_{THD} is much below 5%.
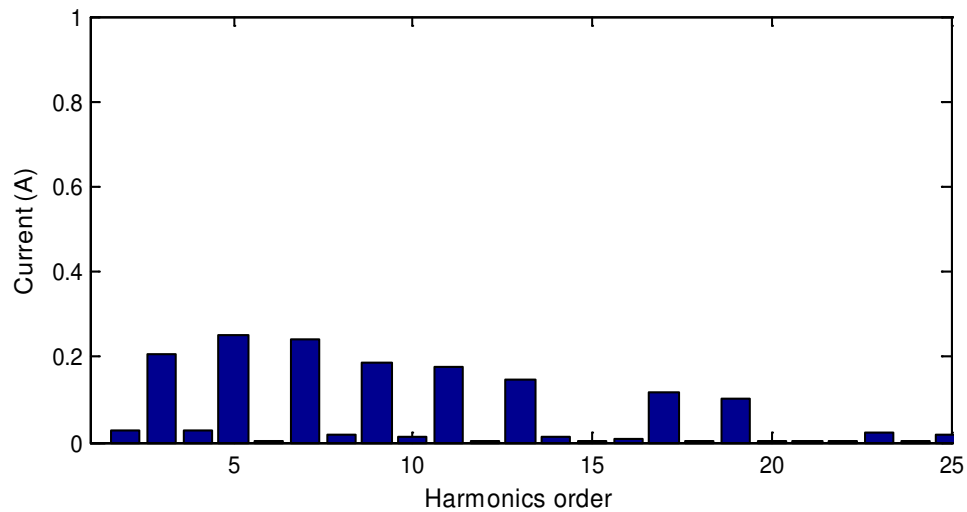
Figure 5.33 Harmonics output from a 10kW PV Solar System
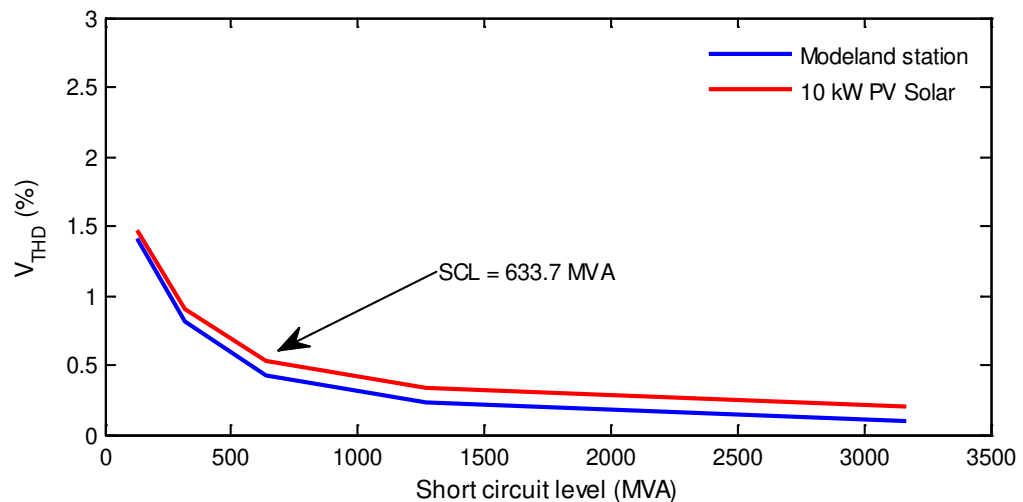
Figure 5.34 V_{THD} at different location with worst-case harmonic injection

Table 5.6 describes the increase in V_{THD} at the Modeland substation with the addition of a 10kW PV system to the feeder, with a 20 MW PV Solar System. It is seen that maximum increase in V_{THD} is 0.1 for the weak system, and 0.03 at a nominal short circuit level of 633.7 MVA at the Modeland substation with the addition of a 10 kW PV Solar system.

Table 5.6 V_{THD} with and without 10 kW PV Solar System

Short Circuit Level (MVA)	V_{THD} at Modeland Station without 10kW PV system (%)	V_{THD} at Modeland Station with 10 kW PV system (%)	Increase in V_{THD}
126.7	1.31	1.41	0.10
316.8	0.65	0.81	0.16
633.7	0.40	0.43	0.03
1267.4	0.20	0.23	0.03
3168.5	0.08	0.09	0.01

5.10 CONCLUSIONS

In this chapter, a detailed system model using PSCAD/EMTDC software is developed for the two feeders of the Bluewater Power network connected to the 20 MW solar farm in Sarnia, for the harmonics impact studies. The model is developed with extensive Bluewater Power network data and actual harmonics injections from the 10 MW solar farm, provided by Hydro One. This network model is validated with the load flow studies conducted using CYMDIST load flow software and real time SCADA data. The resonance behavior of the Bluewater Power network is analyzed using frequency-scanning studies with the developed model in PSCAD/EMTDC for feeders 96M23 and 96M27, with different loading conditions and varying short circuit levels. The measured harmonics data at a different power level from a 10MW solar farm is analyzed. Three different harmonics datasets corresponding to three different power levels are chosen for the harmonics impact studies in the presence of a large scale solar farm. These individual harmonics are injected from the solar farm model developed using the PSCAD/EMTDC model and voltage THDs are calculated at solar farm locations and the Modeland substation feeding these two feeders. The impact of a small scale 10kW PV system is also investigated.

The following conclusions are made:

i) Both feeders connected to solar farms exhibit parallel resonance caused by cable capacitance. Network resonance occurs above the 25th harmonic for the nominal short circuit level for both feeders. When the short circuit capacity decreases, the resonant frequency shifts toward lower order frequencies. However, when the short circuit capacity increases, resonant frequency shifts towards higher order frequencies.

ii) The highest voltage distortion is observed for the case with high harmonics injection from the solar farm, where V_{THD} is found to be less than 3% for both feeders, for different loading conditions. This is within the 5% V_{THD} limit specified by IEEE Standard 519.

iii) Based on this study, it can be concluded that the 20 MW large scale solar farm may not cause significant voltage distortion on feeders 96M23 and 96M27 during steady state operating conditions.

Chapter 6

CONCLUSIONS AND FUTURE WORK

6.1   INTRODUCTION

This thesis presents a novel utilization of a PV inverter as a STATCOM, termed PV-STATCOM for power factor correction of an induction motor load in two utility premises and harmonic impact studies on a utility distribution network in the presence of the largest solar farm and 10 kW PV system in Canada. The PV-STATCOM controller is designed and tested on the networks for Bluewater Power, Sarnia and London Hydro, who have kindly offered to showcase this novel technology in their power systems.

The main conclusions of the thesis are summarized below and also further studies on this research work are also proposed.

6.2   PSCAD/EMTDC SIMULATION OF PV-STATCOM FOR POWER FACTOR CORRECTION

In Chapter 2, a novel application for utilizing a 10 kW PV-STATCOM for power factor correction of a 5 kW induction motor in Bluewater Power Distribution network is demonstrated. The Bluewater power network, the motor load, hysteresis based PV-STATCOM controller and 10 kW PV system are developed using PSCAD/EMTDC software.

A simulation model for the motor load is developed in accordance with the real time data measured at the motor terminal. The steady-state and transient performance of the proposed PV-STATCOM controller for power factor correction is demonstrated with different loading conditions of the motor both during the day time and night time. The PV-STATCOM is able to regulate the PCC power factor to unity during the night time as well as during the day time with the available reactive power after real power generation. The proposed Hysteresis controller for the PV-STATCOM performs effectively both during night time and the day

time. The response time of the PV-STATCOM controller during the transient is 2 to 3 cycles in both the cases.

6.3   REAL-TIME DIGITAL SIMULATION OF PV-STATCOM FOR POWER FACTOR CORRECTION

In Chapter 3, a real-time simulation of a PV-STATCOM controller for power factor correction during both night time and day time on the Real Time Digital Simulator (RTDS) is presented. This study is conducted on the network of London Hydro. The London Hydro network, 5 kVA PV inverter as STATCOM and a 6 kW motor load are modeled in RTDS.

The PV-STATCOM controller operation for power factor correction is demonstrated for both 80% and 50% loading conditions during the night time as well as during the day time at 2 kW and 4 kW PV power outputs. The PV-STATCOM controller uses PWM control method to generate firing pulses for the inverter and operates at a switching frequency of 6 kHz.

When the PV-STATCOM injects both real power and reactive power during the day time, the inverter losses are seen to increase. During the night time, when PV-STATCOM operates as STATCOM, the response of both real and reactive power is exactly the same. However during the day time, response of reactive power and real power are less than one cycle and 6 cycles, respectively. The slow response of active power is due to the absence of an MPPT controller for stabilizing the DC link voltage. From the RTDS studies, it is confirmed that the developed PV-STATCOM controller works effectively for different PV outputs and at different loading conditions, both during night time and day time.

6.4   HARDWARE IN THE LOOP SIMULATION OF PV-STATCOM CONTROLLER FOR POWER FACTOR CORRCETION

Chapter 4 presents the Hardware-In-the Loop (HIL) simulation of the developed PV-STATCOM controller for London Hydro system. The London Hydro network, the 5 kW PV Inverter and the motor load are modeled in RTDS and the PV-STATCOM controller is implemented on a Digital Signal Processor (DSP) based dSPACE platform. The dSPACE platform is comprised of two controllers: Master controller and a Slave DSP controller. The

HIL simulation of PV-STATCOM controller is performed for the day time at 2 kW PV power output and at night time for 80% and 50% loading conditions of the motor.

Ten analog signals for the PV-STATCOM controller are taken out from run time simulation environment in RTDS with a DDAC card and fed into the dSPACE controller. The PV-STATCOM controller running in dSPACE performs appropriate control actions to generate six firing pulses. These firing pulses generated by the PV-STATCOM controller are sent to the run time simulation environment through GTDI card present on RTDS. The same time-step, switching frequency, and the controller parameters for the PV-STATCOM controller used in the RTDS simulation are utilized in the HIL simulation.

The power factor correction performance of the PV-STATCOM controller designed in RTDS environment is validated by the dSPACE based PV-STATCOM controller developed in the HIL simulation. From the HIL simulation, it is confirmed that the PV-STATCOM controller works effectively during different operating scenarios. The performance of PV-STATCOM controller for power factor correction is demonstrated with PV-STATCOM generating active power during the day time and acting as a STATCOM during the night time.

6.5 HARMONIC IMPACT STUDIES OF LARGE SCALE SOLAR FARM

Chapter 5 presents a novel study of the impact of harmonics on two distribution feeders in the Bluewater power network in the presence of a large scale solar farm in Canada of 80 MW and also of a 10 kW PV solar system. Two feeder models are developed with extensive Bluewater Power network data and actual harmonics injections from two 10 MW solar farms and a 10 kW PV system using PSCAD/EMTDC. This network model is validated with the load flow studies conducted with CYMDIST load flow software and real time (Supervisory Control and Data Acquisition System) SCADA data.

Frequency scan studies with the developed model in PSCAD/EMTDC are conducted to analyze the resonance behavior of both the feeders 96M23 and 96M27 with different loading conditions and varying short circuit levels. It is observed that when the short circuit capacity decreases, the resonant frequency shifts toward lower order frequencies. Similarly when short circuit capacity increases, the resonant frequency shifts towards higher order

frequencies. It is found that both the feeders 96M23 and 96M27 connected to the solar farm exhibit parallel resonance. Network resonance occurs above the 25th harmonic for the nominal short circuit level for both the feeders.

To study the impact of harmonics from the PV solar farm on these two feeders, harmonics data at different power level from a 10 MW solar farm at different power outputs are analyzed. Three different worst case harmonics datasets corresponding to three different power levels are chosen for the harmonics impact studies. These individual harmonics are injected from the solar farm model developed in the PSCAD/EMTDC model and voltage THDs are calculated at solar farm locations and the Modeland substation feeding these two feeders. The highest voltage distortion is observed for one of the above mentioned three cases with high harmonics injection from the solar farm where V_{THD} is found to be less than 3% for both the feeders for different loading conditions. This is within the 5% V_{THD} limit specified by IEEE Standard 519. Based on this study, it is concluded that the 20 MW large scale solar farm and the 10 kW PV system may not cause significant voltage distortion on the feeders during steady state operating conditions. The impact of a small scale 10 kW PV system is also investigated with real-time measurements data. The highest voltage distortion is observed at different locations and found to be within the 5% V_{THD} limit specified by IEEE Standard 519.

6.6 CONTRIBUTIONS

The main contributions of this thesis are the following:

i) This study presents a novel application of a PV inverter as STATCOM during the night and day. PSCAD/EMTDC simulation of PV inverter as STATCOM is presented for power factor correction of an induction motor in a utility premise with real time data measured data.

ii) The performance of the developed PV-STATCOM controller is demonstrated on a Real Time Digital Simulator both during night and day.

iii) The RTDS developed PV-STATCOM controller is physically implemented in DSP based dSPACE platform and its performance is validated in a Hardware-In-the Loop

simulation The controller will be implemented in the utility network of London Hydro.

iv)   Harmonic impact studies of a large scale 20 MW solar farm on a distribution network is presented. Such a study has been performed for the first time in the world on any large scale PV solar farm.

6.7 FUTURE WORK

Further research works on PV-STATCOM may be performed as follows:

- Implementation of an MPPT along with validation of the PV-STATCOM controller performance for all of the cases demonstrated in this thesis

- Implementation of the prototype controller developed in dSPACE hardware with a DSP based Texas Instrument controller board TMS320F28335 and Interfacing the controller with the inverter of the 10 kW PV solar system to make it a complete PV-STATCOM.

- Field installation and testing of PV-STATCOM in the network of Bluewater Power Corporation and London Hydro.

REFERENCES

[1]   European Photovoltaic Industry Association. [Online] http://www.epia.org

[2]   Canada Solar Industry Association. [Online] http://www.cansia.ca

[3]   Ontario Green Energy Act (Province of Ontario, Canada). [Online] http://ontariogreenenergyact.ca

[4]   The California Solar Initiative program (California, USA). [Online] http://www.gosolarcalifornia.org/

[5]   Solar Energy USA. [Online] http://solarenergy-usa.com

[6]   National Solar Mission (Government of India). [Online] http://www.mnre.gov.in/

[7]   www.powerauthority.on.ca, accessed in Aug, 2012.

[8]   http://en.wikipedia.org/wiki/List_of_photovoltaic_power_stations, accessed in Sept,2012.

[9]   A. Yazdani, A.R. Di Fazio, H. Ghoddami, M. Russo, M. Kazerani, J. Jatskevich, K. Strunz, S. Leva and J.A. Martinez, "Modeling Guidelines and a Benchmark for Power System Simulation Studies of Three-Phase Single-Stage Photovoltaic Systems," *IEEE Trans. on Power Delivery*, vol.26, no.2, pp.1247-1264, April 2011.

[10]   Hydro One Network Inc, "Distributed Generation Technical Interconnection Requirements; Interconnection at Voltages 50 kV and Below," June 2011.

[11]   Solectria Renewables LLC, "PVI 10kW, 13 kW and 15 kW Installation and Operation Manual," April 2012.

[12]   M.G. Villalva, J.R. Gazoli and E.R. Filho, "Comprehensive Approach to Modeling and Simulation of Photovoltaic Arrays," *IEEE Trans. on Power Electronics*, vol. 24, no. 5, pp. 1198-1208, 2009.

[13]   D. Sera, R. Teodorescu and P. Rodriguez, "PV panel model based on datasheet values," in *Proc. 2007 IEEE International Symposium on Industrial Electronics*, pp. 2392-2396.

[14]   J. A. Gow and C. D. Manning, "Development of a photovoltaic array model for use in power electronics simulation studies," in *Proc. 2009 IEE on Electric Power Applications*, vol. 146, no. 2, pp. 193-200.

[15]   G. R. Walker, "Evaluating MPPT Converter Topologies Using a MATLAB PV Model", *Journal of Electrical & Electronics Engineering, Australia*, vol. 21, no. 1, pp. 49-55. 2001.

[16]   P.P. Dash and M. Kazerani, "Dynamic Modeling and Performance Analysis of a Grid-Connected Current-Source Inverter-Based Photovoltaic System," *IEEE Trans. on Sustainable Energy*, vol.2, no.4, pp.443-450, Oct. 2011.

[17]   A.Yazdani and P.P. Dash, "A control methodology and characterization of dynamics for a photovoltaic (PV) system interfaced with a distribution network," *IEEE Trans. on Power Delivery*, vol.24, no.3, pp.1538-1555, Jul. 2009.

[18]   International Energy Agency (IEA) Task Force on Photovoltaic Power Systems, "Grid-connected photovoltaic power systems: Survey of inverter and related protection equipments," Dec, 2002.

[19]   A.Yazdani and R. Iravani, *Voltage-Sourced Converters: Modeling, Control, and Applications*. Hoboken, NJ: Wiley, 2010.

[20]   http://www.solren.com/, accessed in Oct, 2012.

[21]   http://www.xantrex.com/, accessed in Oct, 2012.

[22]   http://www.sma-canada.ca/, accessed in Oct, 2012.

[23]   N. Mohan, T.M. Undeland and W.P. Robbins, *Power Electronics: Converters, Applications, and Design*, 3rd ed. Hoboken, NJ: Wiley, 2003.

[24]   F. Delfino, R. Procopio, M. Rossi and G. Ronda, "Integration of large-size photovoltaic systems into the distribution grids: a p-q chart approach to assess reactive support capability," *IET Renewable Power Generation*, vol.4, no.4, pp.329-340, July 2010.

[25]   E. Demirok, P.C. González, K.H.B. Frederiksen, D. Sera, P. Rodriguez and R. Teodorescu, "Local Reactive Power Control Methods for Overvoltage Prevention of Distributed Solar Inverters in Low-Voltage Grids," *IEEE Journal of Photovoltaics*, vol.1, no.2, pp.174-182, Oct. 2011.

[26]   P. Sanchis, J. Lopez, A. Ursua and L. Marroyo, "Electronic controlled device for the analysis and design of photovoltaic systems," *IEEE Power Electronics Letters*, vol.3, no.2, pp. 57- 62, June 2005.

[27]   M.A. Rahman, T.S. Radwan, A.M. Osheiba and A.E. Lashine, "Analysis of current controllers for voltage-source inverter," *IEEE Trans. on Industrial Electronics,* vol.44, no.4, pp.477-485, Aug 1997.

[28]   M.P. Kazmierkowski, R. Krishnan, F. Blaabjerg, *Control in Power Electronics Selected Problems*, USA: Academic Press, 2002.

[29]   N.A. Rahim, J. Selvaraj and Krismadinata, "Hysteresis Current Control and Sensorless MPPT for Grid-Connected Photovoltaic Systems," in *Proc. 2007 IEEE International Symposium on Industrial Electronics*, pp.572-577.

[30]   A. Tripathi and P.C. Sen, "Comparative analysis of fixed and sinusoidal band hysteresis current controllers for voltage source inverters," *IEEE Trans. on Industrial Electronics*, vol.39, no.1, pp.63-73, Feb 1992.

[31]   J. Holtz, "Pulsewidth modulation-a survey," *IEEE Trans. on Industrial Electronic*, vol.39, no.5, pp.410-420, Oct 1992.

[32]   R.M. Mathur and R.K. Varma, *Thyristor-Based FACTS Controllers for Electrical Transmission Systems*, New York: IEEE Press-Wiley, 2002.

[33]   Narain G. Hingorani and Laszlo Gyugyi, *Understanding FACTS: Concepts and Technology of Flexible AC Transmission Systems*, New York: IEEE-Wiley, 1999.

[34]   B. Ronner, P. Maibach and T. Thurnherr, "Operational experiences of STATCOMs for wind parks," *IET Renewable Power Generation*, vol.3, no.3, pp.349-357, Sept. 2009.

[35]   M.K. Mishra, A. Ghosh and A. Joshi, ''Operation of a STATCOM in Voltage Control Mode,'' *IEEE Trans. on Power Delivery*, vol.18, No.1 , pp. 258-264, July 2003.

[36]   K. Anuradha, B. P. Muni and A. D. R. Kumar, "Modeling of electric arc furnace control algorithms for voltage flicker mitigation using DSTATCOM, " in *Proc.2009 IEEE Conference on Power Electronics and Motion Control*, pp. 1123-1129.

[37]   A. K. Goswami, C. P. Gupta and G. K. Singh, "Minimization of financial losses due to voltage sag in an Indian distribution system using D-STATCOM, " *International Journal of Emerging Electric Power Systems*, vol. 10, no.3, 2009.

[38]   M. Joorabian, D. Mirabbasi and A. Sina, "Voltage flicker compensation using STATCOM," in *Proc. 2009 IEEE Conference on Industrial Electronics and Applications*, pp.2273-2278.

[39]   M. S. El-Moursi, B. Bak-Jensen, and M. H. Abdel-Rahman, "Novel STATCOM controller for mitigating SSR and damping power system oscillations in a series compensated wind park," *IEEE Trans. on Power Electronics*, vol. 25, no. 2, pp. 429-441, Feb. 2010.

[40]   K. V. Patil, J. Senthil, J. Jiang and R. M. Mathur, "Application of STATCOM for damping torsional oscillations in series compensated AC systems," *IEEE Trans. on Energy Conversion*, vol. 13, no. 3, pp. 237-243, Sep. 1998.

[41]   A. Ghosh and A. Joshi, "A new approach to load balancing and power factor correction in power distribution system," *IEEE Trans. on Power Delivery*, vol.15, no.1, pp.417-422, Jan 2000.

[42]   B. Blazic and I. Papic, "Improved D-StatCom control for operation with unbalanced currents and voltages," *IEEE Trans. on Power Delivery*, vol.21, no.1, pp. 225- 233, Jan. 2006.

[43]   C.K. Sao, P.W. Lehn, M.R. Iravani and J.A. Martinez, "A benchmark system for digital time-domain simulation of a pulse-width-modulated D-STATCOM," *IEEE Trans. on Power Delivery,* vol.17, no.4, pp. 1113- 1120, Oct 2002.

[44]   Rajiv K. Varma, Vinod Khadkikar and Shah Arifur Rahman, "Utilization of Distributed Generator Inverters as STATCOM" PCT Patent application PCT/CA2010/001419 filed on 15 September, 2010. This PCT patent application is for worldwide coverage (covering 142 countries)

[45]   R.K. Varma, V. Khadkikar and R. Seethapathy, "Nighttime Application of PV Solar Farm as STATCOM to Regulate Grid Voltage," *IEEE Trans. on Energy Conversion*, vol.24, no.4, pp.983-985, Dec. 2009.

[46]   R.K. Varma, B. Das, I. Axente and T. Vanderheide, "Optimal 24-hr utilization of a PV solar system as STATCOM (PV-STATCOM) in a distribution network," in *Proc. 2011 IEEE Power and Energy Society General Meeting,* pp.1-8.

[47]   R.K. Varma, E.M. Siavashi, B. Das and V. Sharma, "Novel application of a PV solar plant as STATCOM (PV-STATCOM) during night and day in a distribution utility network: Part 2," in *Proc. 2012 IEEE Transmission and Distribution Conference and Exposition (T&D),* pp.1-8.

[48]   R.K. Varma, S.S. Rangarajan, I. Axente and V. Sharma, "Novel application of a PV solar plant as STATCOM during night and day in a distribution utility network," in *Proc. 2011 IEEE Power Systems Conference and Exposition (PSCE),* pp.1-8.

[49]   R. K. Varma, S. A. Rahman, V. Sharma and T. Vanderheide, "Novel control of a PV solar system as STATCOM (PV-STATCOM) for preventing instability of induction motor load," in *Proc. 2012 IEEE Canadian Conference on Electrical & Computer Engineering,* pp.1-5.

[50]   N. Mohan, W.P. Robbins, T.M. Undeland, R. Nilssen and O. Mo, "Simulation of power electronic and motion control systems-an overview," in *Proc. 1994 IEEE Conference*, vol.82, no.8, pp.1287-1302.

[51]   V.R. Dinavahi, "Real-time Digital Simulation of Switching Power Circuits", PhD Thesis, University of Toronto, Toronto, Ontario, 2000.

[52]   C. Yong, W. Jian and H.L. Ginn, "Active compensator prototyping tools for electric ship applications," in *Proc. 2005 IEEE Electric Ship Technologies Symposium*, pp. 268- 273.

[53]   G. K. Venayagamoorthy, "Comparison of power system simulation studies on different platforms – RSCAD, PSCAD/EMTDC, and SIMULINK SimPowerSystems", in Proc. *2005 International Conference on Power System Operations and Planning*, pp-1-4.

[54]   MATLAB, http://www.mathworks.com/products/matlab/, accessed in Oct, 2012.

[55]   PSPICE,http://www.cadence.com/products/orcad/pspice_simulation/Pages/default.as px, accessed in Oct, 2012.

[56]   PSCAD, https://pscad.com/, accessed in Oct, 2012.

[57]   G.G. Parma and V. Dinavahi, "Real-Time Digital Hardware Simulation of Power Electronics and Drives," *IEEE Trans. on Power Delivery*, vol.22, no.2, pp.1235-1246, April 2007.

[58]   W. Ren, M. Sloderbeck, M. Steurer, V. Dinavahi, T. Noda, S. Filizadeh, A.R. Chevrefils, M. Matar, R. Iravani, C. Dufour, J. Belanger, M.O. Faruque, K. Strunz and J.A. Martinez, "Interfacing Issues in Real-Time Digital Simulators," *IEEE Trans. on Power Delivery*, vol.26, no.2, pp.1221-1230, April 2011.

[59]   S. Suryanarayanan, W. Ren, M. Steurer, F. Ribeiro and G.T. Heydt, "A real-time controller concept demonstration for distributed generation interconnection," in *Proc. 2006 IEEE Power Engineering Society General Meeting,* pp.3.

[60]   RTDS, http://www.rtds.com, accessed in Oct, 2012.

[61]   eMEGAsim, http://www.opal-rt.com, accessed in Oct, 2012.

[62]   A. Edris, L. Kirschner, R. Escher, D. Durbak, G. Zhou, R. Derra, M. Fritzsche, A. Engelmann, D. Schooley, D. Torgerson, G. Irwin and A. Flueck, "ComEd's Elmhurst SVCs: Challenges and opportunities," in *Proc. 2010 IEEE Transmission and Distribution Conference and Exposition*, pp.1-6.

[63]   Z. Gajic, "Use of Standard 87T Differential Protection for Special Three-Phase Power Transformers—Part II: Application and Testing," *IEEE Trans. on Power Delivery*, vol.27, no.3, pp.1041-1046, July 2012.

[64]   P. Mitra, K. Vinothkumar and Z. Lidong, "Dynamic performance study of a HVDC grid using real-time digital simulator," in *Proc. 2012 IEEE Complexity in Engineering*, vol., no., pp.1-6, 11-13 June 2012.

[65]   P.R. Bishop, Z.Q. Bo, , X.F. Shen, L. Denning and, M. O'Keeffe, "Implementation of dynamic distance relay scheme evaluation testing guidelines using analogue and real time digital simulators," in *Proc. 2001 IEE International Conf. on Developments in Power System Protection*, vol., no., pp.213-217.

[66]   M. Andrus, M. Steurer, C. Edrington, F. Bogdan, H. Ginn, R. Dougal, E. Santi and A. Monti, "Real-time simulation-based design of a power-hardware-in-the-loop setup to support studies of shipboard MVDC issues," in *Proc. 2009 IEEE Electric Ship Technologies Symposium*, pp.142-151.

[67]   L. Gregoire, K. Al-Haddad and G. Nanjundaiah, "Hardware-in-the-Loop (HIL) to reduce the development cost of power electronic converters," in *Proc. 2011 IEEE International Conf. on Power Electronics (IICPE)*, pp.1-6.

[68]   S. Hyo-Ryong, M. Park, Y. In-Keun and S. Byeong-Mun, "Performance analysis and evaluation of a multifunctional grid-connected PV system using power hardware-in-the-loop simulation," in *Proc. 2011 IEEE Applied Power Electronics Conference and Exposition (APEC)*, pp.1945-1948.

[69]   J. Jin-Hong, K. Jong-Yul, K. Hak-Man, K. Seul-Ki, C. Changhee, K. Jang-Mok, A. Jong-Bo and N. Kee-Young, "Development of Hardware In-the-Loop Simulation

System for Testing Operation and Control Functions of Microgrid," *IEEE Trans. on Power Electronics,* vol.25, no.12, pp.2919-2929, Dec. 2010.

[70] M. Steurer, S. Woodruff, T. Baldwin, H. Boenig, F. Bogdan, T. Fikse, M. Sloderbeck and G. Snitchler, "Hardware-in-the-Loop Investigation of Rotor Heating in a 5 MW HTS Propulsion Motor," *IEEE Trans. on Applied Superconductivity*, vol.17, no.2, pp.1595-1598, June 2007.

[71] M. Steurer, "PEBB based high-power hardware-in-loop simulation facility for electric power systems," in *Proc. 2006 IEEE Power Engineering Society General Meeting*, pp.3.

[72] H.Z. De La Parra, G. Demetriades, H. Olsson and I. Bird-Radolovic, "Evaluation of ripple compensation algorithm for PM motors," in *Proc. 2008 IEEE Power Electronics Specialists Conference, 2008,* pp.2018-2022.

[73] dSPACE Hardware, http://www.dspace.com, accessed in Oct, 2012.

[74] J. Arrillaga, D.A. Bradley and P.S. Bodger, *Power System Harmonics*: John Wiley and Sons, New York, 1985.

[75] J.A. Pomilio, and S.M. Deckmann, "Characterization and Compensation of Harmonics and Reactive Power of Residential and Commercial Loads," *IEEE Trans. On Power Delivery*, vol.22, no.2, pp.1049-1055, April 2007.

[76] N.R. Watson, T.L. Scott, and S. Hirsch, "Implications for Distribution Networks of High Penetration of Compact Fluorescent Lamps," *IEEE Trans. On Power Delivery*, vol.24, no.3, pp.1521-1528, July 2009.

[77] D. Essah, E. Feiste, R. O'Connell, R.G. Hoft and G. Brownfield, "Harmonic effects of variable speed air conditioners on a single-phase lateral and on the distribution feeders in a typical residential power system. I," in *Proc. 1994 IEEE Applied Power Electronics Conference and Exposition*, pp.622-627.

[78] A.B. Nassif, and X. Winsun, "Characterizing the Harmonic Attenuation Effect of Compact Fluorescent Lamps," *IEEE Trans. On Power Delivery*, vol.24, no.3, pp.1748-1749, July 2009.

[79] Y. Zhou, "Harmonic sources in the city distribution system," in *Proc. 1997 IEEE Fourth International Conference on Advances in Power System Control, Operation and Management*, vol.2, pp.549-551.

[80] H.O. Aintablian, and H.W. Jr. Hills, "Harmonic currents generated by personal computers and their effects on the distribution system neutral current," in *Proc. 1993 IEEE Industry Applications Society Annual Meeting*, pp. 1483-1489.

[81] T.C. Shuter, H.T. Jr. Vollkommer and T.L. Kirkpatrick, "Survey of harmonic levels on the American Electric Power distribution system," *IEEE Trans. On Power Delivery*, vol.4, no.4, pp.2204-2213, Oct 1989.

[82] R.K. Varma, J. Berge, I. Axente, V. Sharma and K. Walsh, "Determination of maximum PV solar system connectivity in a utility distribution feeder," in *Proc. 2012 IEEE Transmission and Distribution Conference and Exposition (T&D)*, pp.1-8.

[83] C. D. Crites, R. K. Varma, V. Sharma and B. Milroy, "Characterization of Harmonics in a Utility Feeder with PV Distributed Generation," in *Proc. 2012 IEEE Electrical Power and Energy Conference,* pp. 1-6.

[84] IEEE Recommended Practices and Requirements for Harmonic Control in Electrical Power Systems, IEEE Standard 519-1992, 1993.

[85] G. Lemieux, "Power system harmonic resonance-a documented case," *IEEE Trans. on Industry Applications*, vol. 26, no. 3, pp. 483-488, May/Jun. 1990.

[86] W. Xu, Z. Huang, Y. Cui and H. Wang, "Harmonic resonance mode analysis," *IEEE Trans. on Power Delivery*, vol. 20, no. 2, pp. 1182- 1190, Apr. 2005.

[87] P. C. Buddingh, "Even harmonic resonance-an unusual problem," *IEEE Trans. on Industry Applications*, vol. 39, no. 4, pp. 1181- 1186, Jul.-Aug. 2003.

[88] M. Contreras, H. Calleja and V. Cardenas, "Study of Harmonic Propagation in Ring Bus Distribution System," in *Proc. 2005 IEEE Power Electronics Specialists Conference*, pp.1901-1907.

[89] S. J. Chapman, *Electric machinery fundamentals*, 4th Edition, Toronto: McGRAW-HILL, 2005.

[90] S.-K. Chung, "Phase-locked loop for grid-connected three-phase power conversion systems," in *Proc.2000 IEE Electric Power Applications*, vol.147, no.3, pp.213-219.

[91] IEEE Standard for Interconnection Distributed Resources with Electric Power System, IEEE Std 1547-2003.

[92] Fluke 1750 Three-Phase Power Quality Recorder, http://www.fluke.com, accessed in Oct 2012.

[93]   RSCAD Software Suite, http://www.rtds.com, accessed in Oct 2012.

[94]   PP100T060, IGBT power module, http://www.pwrx.com/pwrx, accessed in Oct, 2012.

[95]   R. K. Varma, E. M. Siavashi**,** B. Das and V. Sharma, "Real-Time Digital Simulation of PV Solar system as STATCOM (PV-STATCOM) for voltage regulation and power factor correction", Accepted for publication *in IEEE EPEC Conference* 10-12 Oct 2012.

[96]   xPC Targets, http://www.mathworks.com, accessed in Oct, 2012.

[97]   CompactRIO system, http://www.ni.com, accessed in Oct,2012.

[98]   Survalent SCADA system, http://www.survalent.com, accessed in Oct,2012.

[99]   GIS software, http://www.esri.com, accessed in Oct,2012.

[100]   CYME Power Engineering Software, http://www.cyme.com, accessed in Oct,2012.

[101]   William H. Kersting, *Distribution System Modeling and Analysis*: CRC Press 2012.

[102]   W.H. Kersting and W.H. Phillips, "Load allocation based upon automatic meter readings," in *Proc. 2008 IEEE T&D Conference and Exposition,* vol., no., pp.1-7.

[103]   I. Roytelman and V. Landenberger, "Real-time Distribution System Analysis - integral part of DMS," in *Proc. 2009 IEEE Power Systems Conference and Exposition*, vol., no., pp.1-6, 15-18.

[104]   W.H. Kersting and W.H. Phillips, "Modeling and analysis of rural electric distribution feeders," *IEEE Trans. on Industry Applications*, vol.28, no.4, pp.767-773, Jul/Aug 1992.

[105]   M. Liserre, R. Teodorescu and F. Blaabjerg, "Stability of grid-connected PV inverters with large grid impedance variation," in *Proc. 2004 IEEE Power Electronics Specialists Conference,* vol.6, no., pp. 4773- 4779.

[106]   M. El-Marsafawy, "Use of frequency-scan techniques for subsynchronous-resonance analysis of a practical series-capacitor compensated AC network," in *Proc. 1983 IEE Proceedings on Generation, Transmission and Distribution,* , vol.130, no.1, pp.28-40.

APPENDIX A

A.1 Bluewater Power Headquarters Building Network Parameter

AC Source Voltage	$V_{L-L} = 208$ V
AC Source Thevenin Impedance	$R = 0.15\ \Omega$, $L = 1.2$ mH
System X/R Parameters	$X/R = 4$

A.2 Heat Pump Electrical (Induction Motor) parameters

Rated Stator Voltage	$V_{L-L} = 208$ V
Rated kVA	$S = 5$ kVA
Rated Frequency	$f = 60$ Hz
Stator Resistance	$R_S = 0.02$ pu
Stator Leakage Reactance	$X_S = 0.08$ pu
Magnetizing Reactance	$X_m = 4$ pu
First Cage Rotor Resistance	$R_r = 0.025$ pu
First Cage Rotor Reactance	$X_r = 0.08$ pu

A.3 PV Inverter Parameters

IGBT ON State Resistance	$R_{ON} = 0.01\ \Omega$
IGBT Off State Resistance	$R_{OFF} = 1e6\ \Omega$
IGBT Forward Voltage Drop	$V_D = 0$ V
Snubber Resistance	$R_{Snubber} = 5000\ \Omega$
Snubber Capacitance	$C_{Snubber} = 0.05\ \mu F$
DC link Capacitor	$C_{DC} = 2000\ \mu F$
DC link Voltage	$V_{DC} = 400V$ DC
Filter Parameters	$L_f = 1.5$ mH, $C_f = 30\ \mu F$

APPENDIX B

B.1 London Hydro System Parameters

AC Source Voltage	$V_{L-L} = 208$ V
AC Source Thevenin Impedance	$R = 0.083\Omega$, $L = 0.88$ mH
System Parameters	$X/R = 4$

B.2 Induction Motor Parameters

Rated Stator Voltage	$V_{L-L} = 208$ V
Rated kVA	$S = 6$ kVA
Rated Frequency	$f = 60$ Hz
Stator Resistance	$R_S = 0.02$ pu
Stator Leakage Reactance	$X_S = 0.08$ pu
Magnetizing Reactance	$X_m = 2$ pu
First Cage Rotor Resistance	$R_r = 1$ pu
First Cage Rotor Reactance	$X_r = 0.05$ pu

B.3 PV Module Parameters

Open Circuit Voltage	$V_{OC} = 21.7$ V
Short Circuit Current	$I_{SC} = 3.35$ A
Voltage at Maximum Power	$V_{MPP} = 17.4$ V
Current at Maximum Power	$I_{MPP} = 3.05$ A
PV Modules in Series	$N_S = 23$
PV Modules in Parallel	$N_P = 8$

B.4 PV Inverter Parameters

|	
IGBT ON State Resistance	$R_{ON} = 0.05\ \Omega$
IGBT Off State Resistance	$R_{OFF} = 1e5\ \Omega$
IGBT Forward Voltage Drop	$V_D = 0$ V
Snubber Resistance	$R_{Snubber} = 1000\ \Omega$
Snubber Capacitance	$C_{Snubber} = 0.002\ \mu F$
DC link Capacitor	$C_{DC} = 14000\ \mu F$
DC link Voltage	$V_{DC} = 400V$ DC
Filter Parameters	$L_f = 1$ mH, $C_f = 20\ \mu F$, $R_{damping} = 2\ \Omega$
Switch rating	$V_{rating} = 600$ V, $I_{rating} = 100$ A

B.5 Complete System Model in RSCAD Software
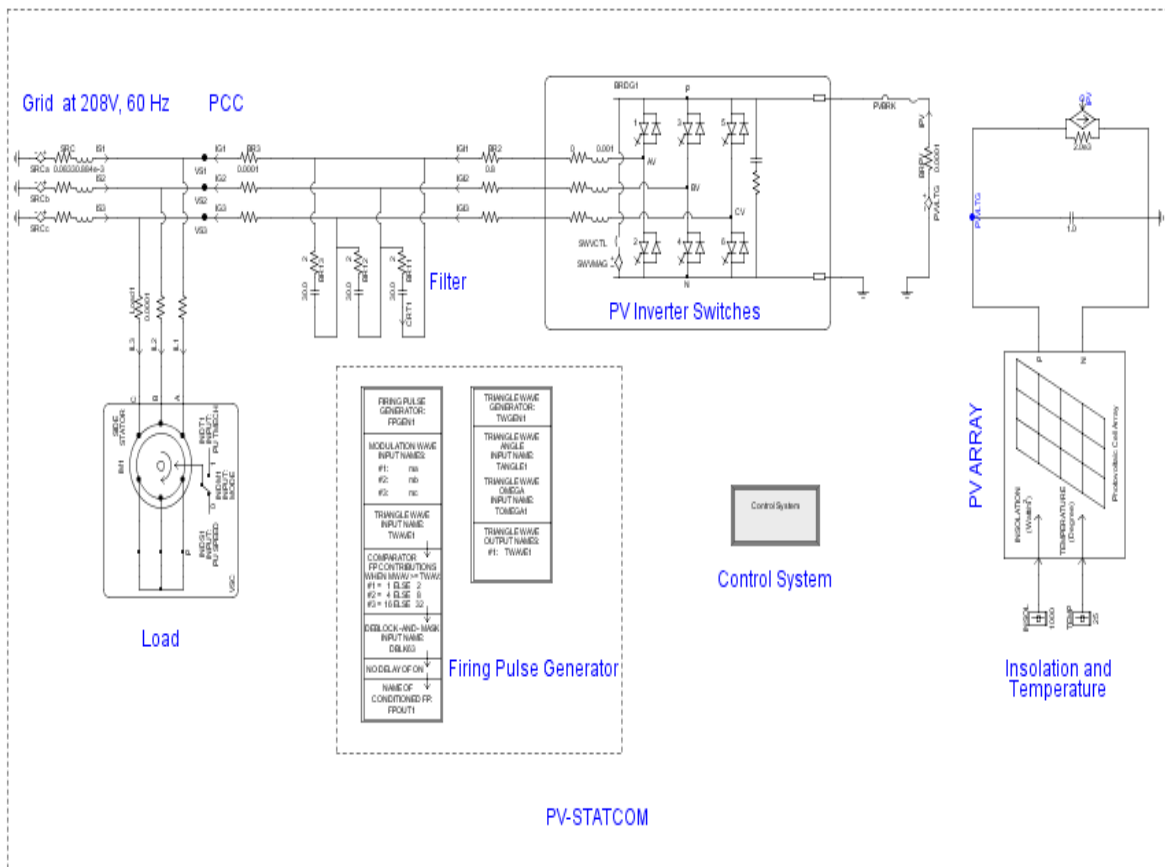
B.6 PWM Controller parameter

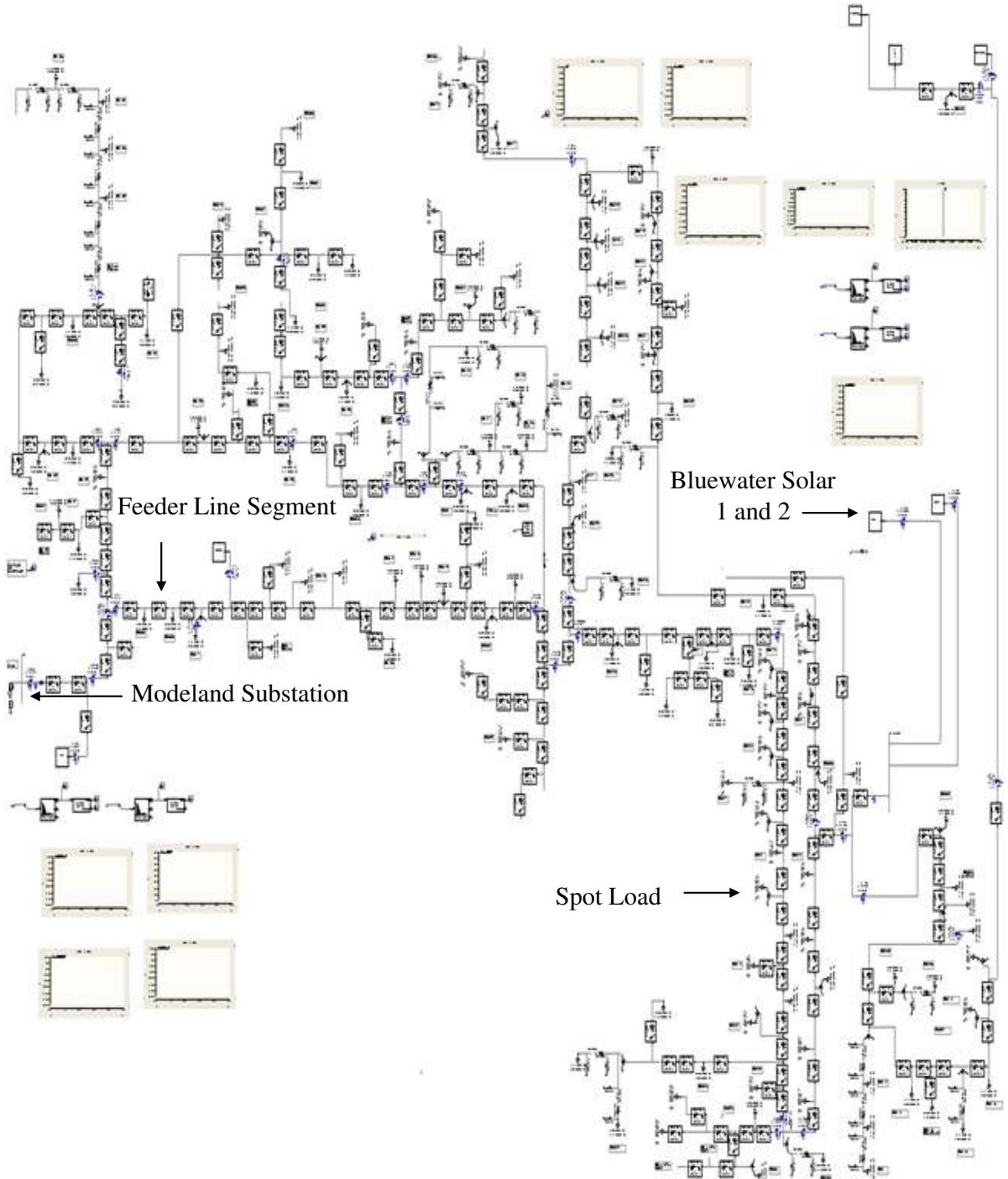|	
Current Control	$K_p = 2$, $Ti = 2$ ms
DC Bus Voltage Control	$G = -14$, $T_{id} = 1$sec, $T_{ld} = 0.067$, $T_{lg} = 0.0015$
AC Bus Voltage Control	$T_{iac} = 19.8$ μs
Switching Frequency	$f_{SW} = 6$ kHz
Controller Sampling Frequency	$f_{Sampling} = 20$ kHz

APPENDIX C

C.1 dSPACE Hardware System
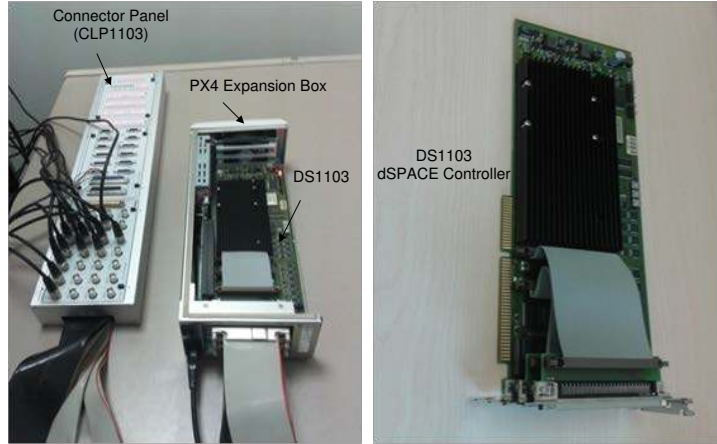
C.2 RTDS Hardware

APPENDIX D

D.1 Feeder M23 model in PSCAD

Feeder Line Segment

Modeland Substation

Bluewater Solar
1 and 2 →

Spot Load →

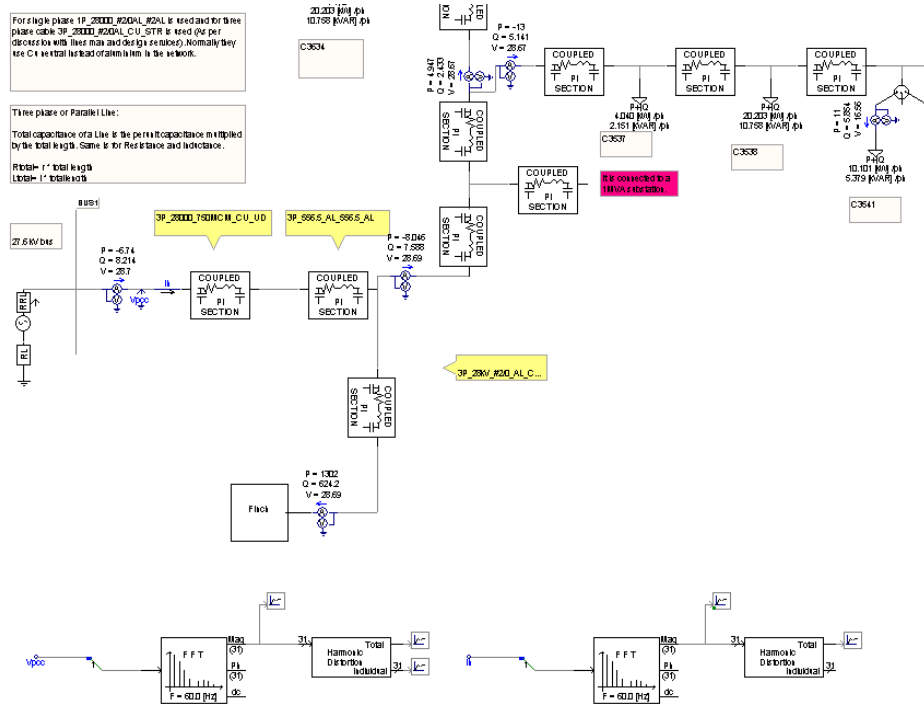# D.2 Snapshots of Different Segments of 96M23Feeder Modeled in PSCAD
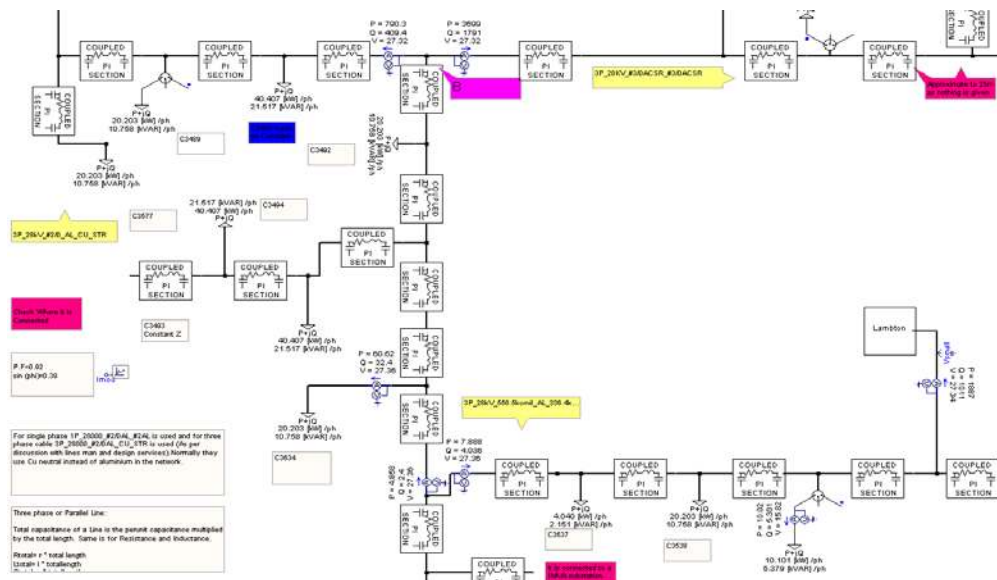

Figure D.1 Modeland Station Feeding 96M23

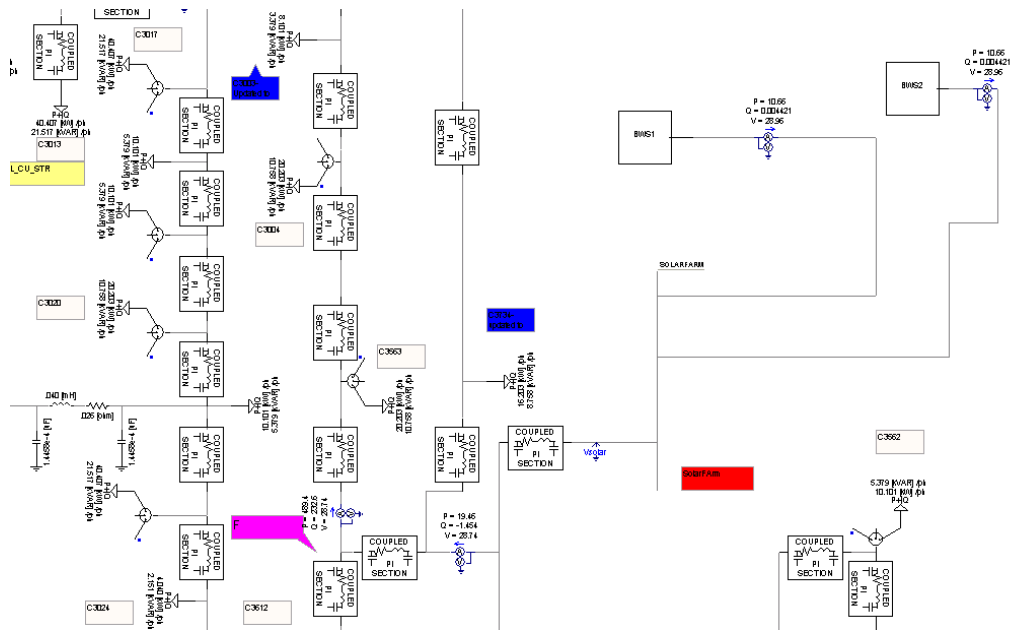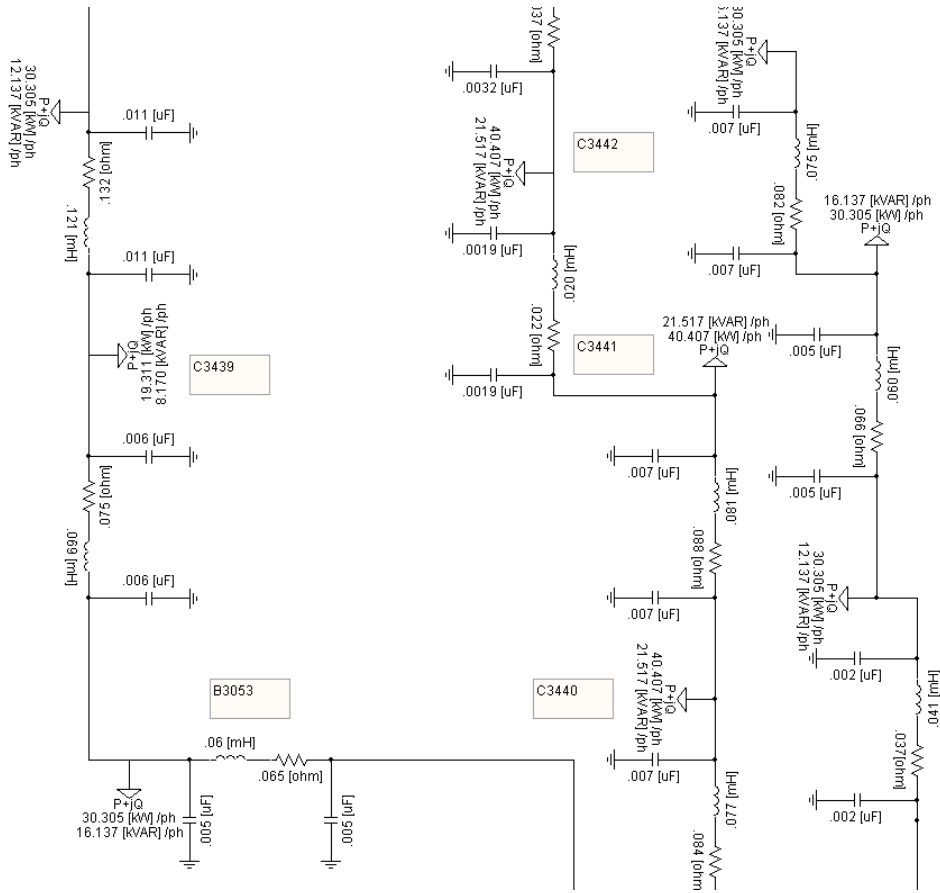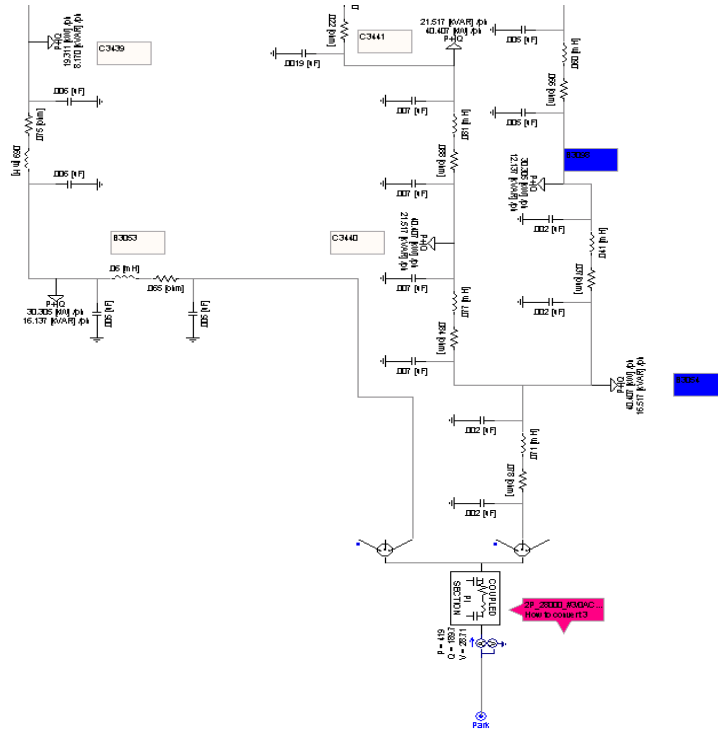**Figure D.2** London Line Area

Figure D.3 Lambton Mall

Figure D.4 Finch Residential Area-1

Figure D.5 Finch Residential Area-2

Figure D.6 Two Solar Farm connected to 96M23

Figure D.7 Confederation area

Figure D.8 Sarnia Airport

Figure D.9 Park Highland Residential Area
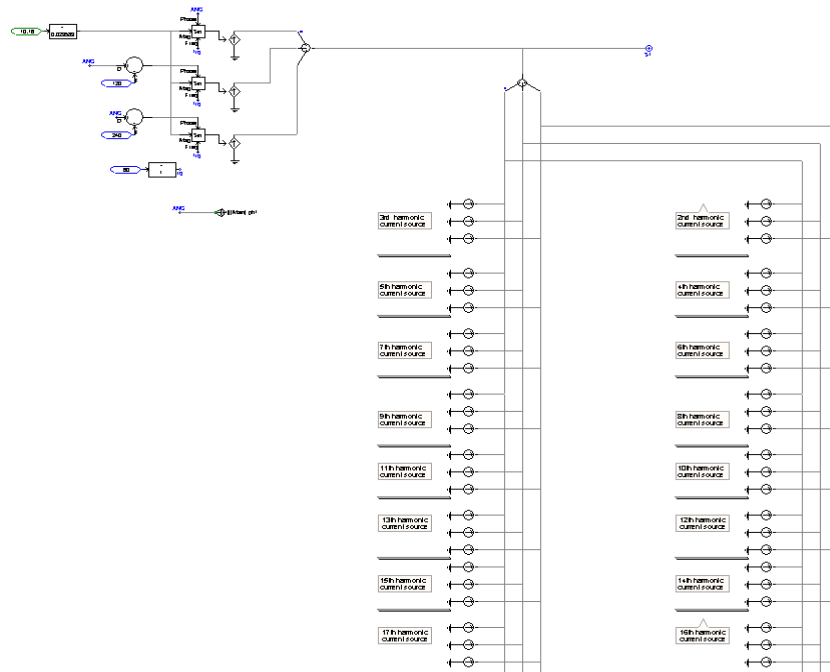
Figure D.10 PV Solar Farm as a harmonic current source

D.3 Feeder M27 model in PSCAD

Modeland Substation

Feeder Line Segment

Solar 3

Spot Load

Solar 6
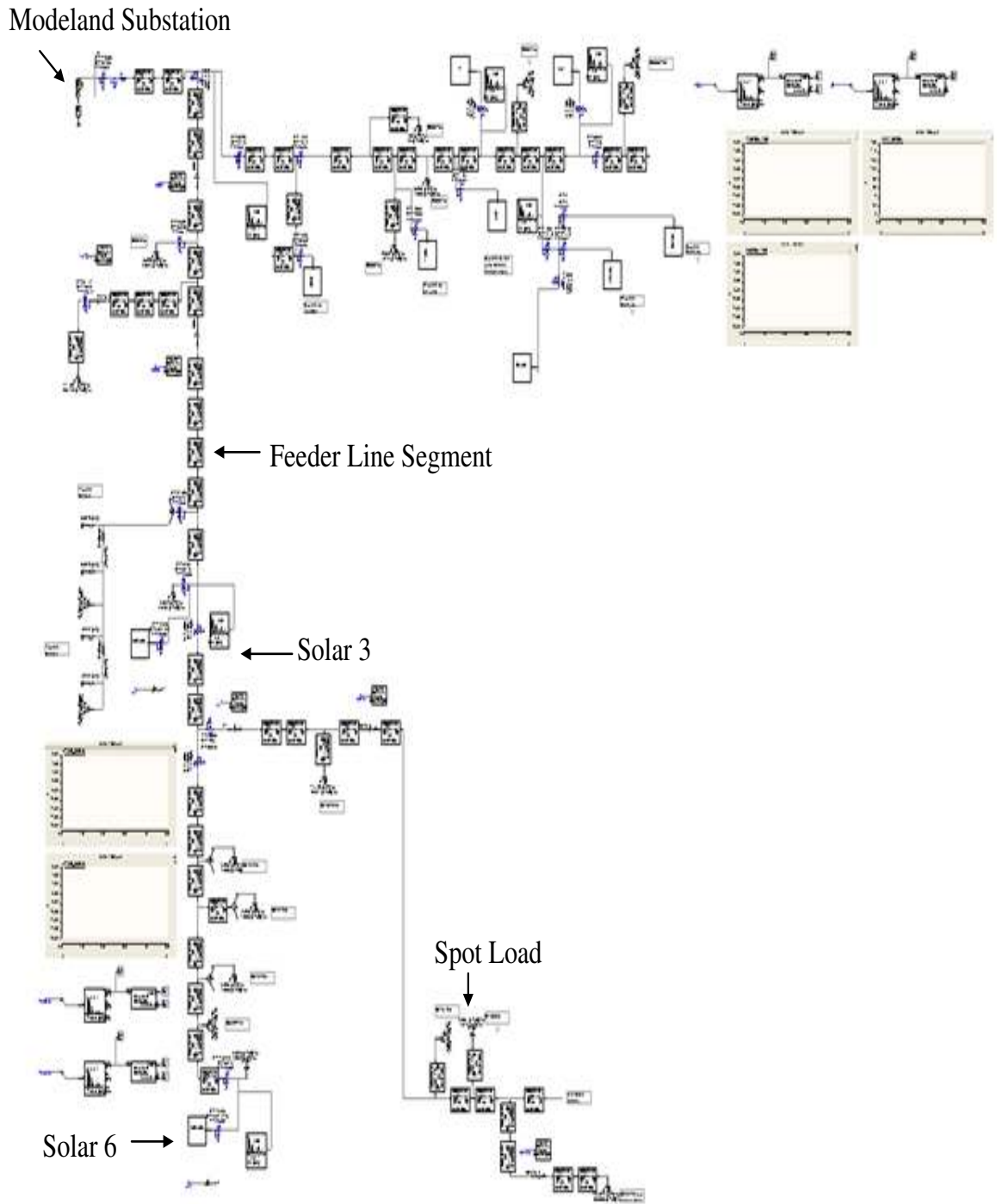
CURRICULUM VITAE

Name:	Byomakesh Das
Post-secondary Education and Degrees:	Biju Pattanaik University of Technology Bhubaneswar, Odisha, India 2001-2005 B.Tech.
	Western University London, Ontario, Canada 2010-2012 M.E.Sc.
Honors and Awards:	Natural Science and Engineering Research Council (NSERC) Industrial Post Graduate Scholarship 2011
Related Work Experience	Project Engineer SoftDEL Systems Pvt. Ltd 2006-2008
	Project Engineer Kyocera Corporation 2008-2009

Publications:

[1] R. K. Varma, E. M. Siavashi**,** B. Das and V. Sharma, "Real-Time Digital Simulation of PV Solar system as STATCOM (PV-STATCOM) for voltage regulation and power factor correction", in *Proc. 2012 IEEE EPEC* Conference, vol., no., pp.1-8.

[2] R.K. Varma, E.M. Siavashi, B. Das and V. Sharma, "Novel application of a PV solar plant as STATCOM (PV-STATCOM) during night and day in a distribution utility network: Part 2," in *Proc. 2012 IEEE T&D Conference and Exposition*, vol., no., pp.1-8.

[3] R. K. Varma, B. Das**,** I. Axente and T. Vanderheide, "Optimal 24-hr Utilization of a PV Solar System as STATCOM (PV-STATCOM) in a Distribution Network", in *Proc. 2011 IEEE PES GM,* vol., no., pp.1-8.